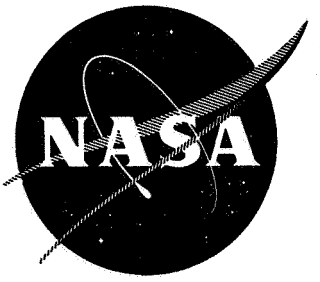

NASA CR-54813
AGC 9400-5

# DEVELOPMENT OF LIQUID OXYGEN/LIQUID HYDROGEN THRUST CHAMBER FOR THE M-1 ENGINE

by


R. J. Barsotti
S. C. Datsko
R. Louison
R. J. Kovach
D. J. Miller
W. P. Pulliam


Prepared for

National Aeronautics and Space Administration

Contract NAS 3-2555



AEROJET-GENERAL CORPORATION

SACRAMENTO, CALIFORNIA


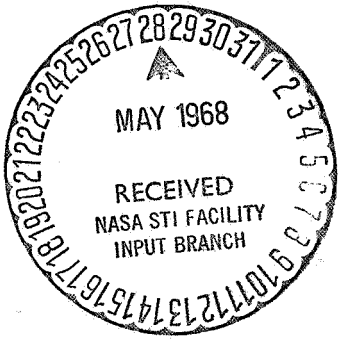

NOTICE

This report was prepared as an account of Government sponsored work. Neither the United States, nor the National Aeronautics and Space Administration (NASA), nor any person acting on behalf of NASA:

A.) Makes any warranty or representation, expressed or implied, with respect to the accuracy, completeness, or usefulness of the information contained in this report, or that the use of any information, apparatus, method or process disclosed in this report may not infringe privately owned rights, or

B.) Assumes any liabilities with respect to the use of, or for damages resulting from the use of any information, apparatus, method or process disclosed in this report.

As used above, "person acting on behalf of NASA" includes any employee or contractor of NASA, or employee of such contractor, to the extent that such employee or contractor of NASA, or employee of such contractor prepares, disseminates, or provides access to, any information pursuant to his employment or contract with NASA, or his employment with such contractor.

Requests for copies of this report should be referred to:

National Aeronautics and Space Administration
Office of Scientific and Technical Information
Attention: AFSS-A
Washington, D. C. 20546

NASA CR-54813
AGC 9400-5

TECHNOLOGY REPORT

# DEVELOPMENT OF LIQUID OXYGEN/LIQUID HYDROGEN THRUST CHAMBER FOR THE M-1 ENGINE

Prepared for

NATIONAL AERONAUTICS AND SPACE ADMINISTRATION

15 May 1968

CONTRACT NAS 3-2555

Prepared by:

AEROJET-GENERAL CORPORATION
LIQUID ROCKET OPERATIONS
SACRAMENTO, CALIFORNIA

AUTHORS: R. J. Barsotti
S. C. Datsko
R. Louison
R. J. Kovach
D. J. Miller
W. P. Pulliam

APPROVED: J. C. Moise
Manager
M-1 Program

Technical Management:

NASA LEWIS RESEARCH CENTER
CLEVELAND, OHIO

TECHNICAL MANAGER: W. A. Tomazic

APPROVED: W. A. Tomazic
M-1 Project Manager

## ABSTRACT

The current technology for large-scale liquid oxygen/liquid hydrogen thrust chamber designs is summarized. This information was obtained primarily from development testing of the M-1 thrust chamber assembly for the M-1 Engine Program, which was conducted at the Aerojet-General Corporation, Sacramento, California.

A thrust chamber using a coaxial element Rigimesh [R] face injector and an ablative-lined uncooled chamber was successfully designed and tested. The injector incorporates copper baffles to preclude instability. These baffles are cooled by a combination of convective and film cooling. The conical chamber has an inside diameter of 40-in. at the injector, a throat diameter of 30-in., and measures 30-in. from the injector to the throat. This thrust chamber was designed for the following operating conditions:

| | |
|---|---|
| Thrust | 1,500,000 lb with a 40:1 nozzle (or 1,200,000 lb with a 2:1 uncooled chamber) |
| $P_c$ (plenum) | 1000 psia |
| M.R. | 5.49 |
| $\dot{W}_o$ | 2872 lb/sec |
| $\dot{W}_f$ | 524 lb/sec |
| Contraction ratio | 1.74 |
| Characteristic Length | 42 inches |
| Specific Impulse | 432 sec |

The test results show that satisfactory start and shutdown transients as well as operation and performance were achieved with the first unit tested. The sea-level specific impulse achieved at a 2:1 expansion ratio was 306 sec and when extrapolated to a 40:1 altitude chamber results in a value of 430 sec. The M-1 coaxial element injector demonstrated a considerable margin of stability, both hydraulically and acoustically, at nominal design conditions.

---

R Registered Trademark of Aircraft Porous Media Corporation

TABLE OF CONTENTS

TABLE OF CONTENTS (Cont'd)

TABLE OF CONTENTS (Cont'd)

TABLE OF CONTENTS (Cont'd)

APPENDICES (Cont'd)

## LIST OF TABLES

## LIST OF FIGURES

## LIST OF FIGURES (Cont'd)

LIST OF FIGURES (Cont'd)

## LIST OF FIGURES (Cont'd)

LIST OF FIGURES (Cont'd)

## I. SUMMARY

The M-1 Thrust Chamber Assembly development program was undertaken to provide a unit for the 1,500,000 lb thrust liquid oxygen/liquid hydrogen M-1 Engine.

The following are the design criteria for the cooled thrust chamber assembly:

| | |
|---|---|
| Thrust | 1,500,000 lb |
| $P_c$ (plenum) | 1,000 psia |
| M.R. | 5.49 |
| $\dot{W}_o$ | 2872 lb/sec. |
| $\dot{W}_f$ | 524 lb/sec. |
| Contraction Ratio | 1.74 |
| Characteristic Length | 42-in. |
| Throat Area | 803-in.$^2$ |
| Nozzle Area Ratio | 40:1 |
| Length, Injector Face to Throat | 30-in. |
| Fuel Injector Temp. | 143°R |
| Specific Impulse | 430 sec. |

The thrust chamber assembly delineated in this report is one with an uncooled chamber. It was designed to obtain data regarding the starting, operation, performance, and stability parameters of the injector before any commitment was made for the much more expensive regeneratively-cooled chamber.

An injector with 3248 coaxial elements was selected. Each of these elements has a thrust of approximately 450 lb and they were designed to provide an injection velocity ratio (hydrogen velocity to oxygen velocity) of 18:1. The face of the injector is transpiration-cooled and the injector itself incorporates both convective-cooled and film-cooled copper baffles as well as a bolt-on oxidizer manifold. Other injector designs were considered, including multiorifice impinging jet injectors and 1184 coaxial element injectors featuring lower injection velocity ratios. Although some injectors were fabricated to these alternative designs, they were not subjected to test evaluation.

The selected 3248 coaxial element injector design appeared to be the most likely one for providing stability along with acceptable performance. This conclusion was based upon the results obtained from NASA for the J-2 engine development effort as well as the NASA in-house stability program (TND 3373).

An ablative-lined chamber was selected to establish injector performance and stability characteristics because this chamber provided the necessary operating duration without any compromise in the evaluation of either performance or stability. Other types of chambers were considered, including a film-cooled metal chamber, a heat-sink copper chamber, and a refractory-coated metal chamber.

A film-cooled metal chamber with a short duration capability also was fabricated for use in the stability evaluation. Its use permitted an investigation of whether the ablative-lined chamber dampened any of the pressure perturbations, which would affect the results of the stability evaluation.

The liquid hydrogen was pre-heated before entering the thrust chamber by adding gaseous hydrogen to simulate the temperatures expected at the outlet of the regeneratively-cooled chamber.

Thirty-five tests were conducted with the selected injector design using both ablative and stainless film-cooled chambers. Thirteen of these tests combined performance and stability evaluation. The operating conditions for these tests were as follows:

| | |
|---|---|
| $P_c$ (plenum) | 870 to 1040 psia |
| M.R. | 4.2 to 6.2 |
| $I_{sp}$ (extrapolated to 40:1 nozzle) | 426 to 434 seconds |
| Hydrogen Injection Temperature | 98 to 167°R |

The injector performance was slightly higher than the nominal PFRT requirements of 429 sec specific impulse (extrapolated to 40:1 altitude operation) and the characteristic exhaust velocity efficiency was approximately 96.5%.

Thrust chamber stability with respect to both low and high frequency instability appeared to be very satisfactory. Classic low frequency instability (chugging) occurred after the step in the start transient when ignition occurred; however, it immediately disappeared when the main oxidizer thrust chamber valve opened which increased both the chamber pressure and manifold pressure drop. No high frequency instabilities were noted during steady-state operation. Fuel temperature ranged from 98°R to 167°R during steady-state.

Therefore, the margin between 98°R and the design point temperature of 143°R indicated that the injector possessed an adequate stability margin. When fuel temperature was decreased, instability was noted at approximately 75°R to 80°R over a range of injector mixture ratios from 4.5 to 6.0. The temperature decrease rate was varied from 4-degrees/sec to 40-degrees/sec without affecting the accuracy of determining self-triggering temperature. Two tests were conducted. The fuel temperature was decreased until instability occurred; then, the fuel temperature was increased until stable operation had been regained.

Stable operation occurred when the fuel temperature reached approximately 100°R. The amplitudes of oscillation in the instabilities noted were sufficiently low so as not to cause any hardware damage. No high frequency instabilities were noted with start transient fuel temperatures higher than 65°R.

The start transient is slightly over 4.0 sec duration from Fire-Switch-one. It yielded shallow pressure rise rates and low magnitudes of applied thrusts, which resulted in very low torus inlet dynamic loads. The shutdown transient lasted approximately 1.0 sec. The peak axial accelerations, approximately two-thirds of the values predicted for the design load conditions along with inlet line dampers, yielded torus inlet dynamics loads that were approximately 20% of engine design values.

## II. INTRODUCTION

The work accomplished in the thrust chamber development for the M-1 Engine prior to phaseout of the program is described in this report. It presents both the design considerations and the test results.

The program to develop a thrust chamber assembly for the M-1 Engine was initially planned to be a trial-and-error approach as used in previous programs. The plan provided for testing several different injector configurations as well as several modifications of each configuration using uncooled and cooled chambers. The approach of selecting the single most likely design to provide the required reliability and performance was not adopted until during the design and hardware fabrication program phases. Acquisition of data from the J-2 Program as well as from smaller scale tests at the NASA/Lewis Research Center made this new approach appear practical.

Subsequent funding limitations resulting from the phaseout of the M-1 Engine Program necessitated that testing be limited to only a few tests with one injector and an uncooled chamber. An ablative-lined unit was selected to provide performance and stability data. A heat exchanger mixing gaseous hydrogen with liquid hydrogen was utilized to control the temperature of the injected hydrogen to simulate the injector temperatures created by a regeneratively-cooled chamber.

This report includes the design and fabrication information as well as the difficulties encountered with the injector, oxidizer manifolding, baffles, and uncooled chambers. Discussions of the untested designs as well as results of those tested also are included.

## III. HARDWARE DESIGN AND FABRICATION CONSIDERATIONS

### A. INJECTION CONCEPTS

#### 1. Coaxial Element Design

##### a. Designs Considered

In general, the elements considered consisted of two parts threaded together; an oxidizer tube or "post" and a fuel sleeve. The oxidizer tube was recessed within the fuel sleeve. This design provided a fuel injection annulus between the outside of the oxidizer tube and the inside of the fuel sleeve. The annulus was fed through four fuel sleeve feed holes having an effective area of at least four times the annulus area while the oxidizer tube was fed axially through the tube inlet end. A swirler in the oxidizer tube also was considered to whirl the oxidizer flow and provide conical spray injection.

The inlet ends of the oxidizer tubes were designed for welding, brazing, or a combination of threading and brazing into injector plates. Fuel sleeves were designed to be shouldered against the back of the injector face plates and welded or swaged into the front of the face plates.

The basic swirler type element is shown on Figure No. 1, where the oxidizer tube incorporated a 30-degree open cone swirler and the oxidizer tip was recessed 0.050-in.

The configruations shown on Figures No. 2 through No. 7 are modifications of the basic element design. The oxidizer tip of Figure No. 2 was chamfered at a 15-degree included angle and recessed 0.300-in. In Figure No. 3, the element differed from that shown on Figure No. 1 in that the oxidizer tip was recessed 0.300-in. while the element shown on Figure No. 4 differed in that the swirler was changed to a 60-degree open cone spray and the oxidizer tip recessed 0.100-in. The element of Figure No. 5 was identical to that of Figure No. 1 except that the oxidizer tip was recessed 0.150-in. The only physical change between the element shown on Figure No. 6 and that of Figure No. 3 was the method of fastening at the injector face. The counterbore in the oxidizer tip was the major modification applied to the element shown on Figure No. 7 in addition to a recess change to 0.202-in. The element shown on Figure No. 8 which was used in the 1184 element injector, was the same as that shown on Figure No. 7 except that the oxidizer tip was chamfered instead of counterbored. In addition, an orifice was added to the oxidizer tube inlet to increase pressure drop.

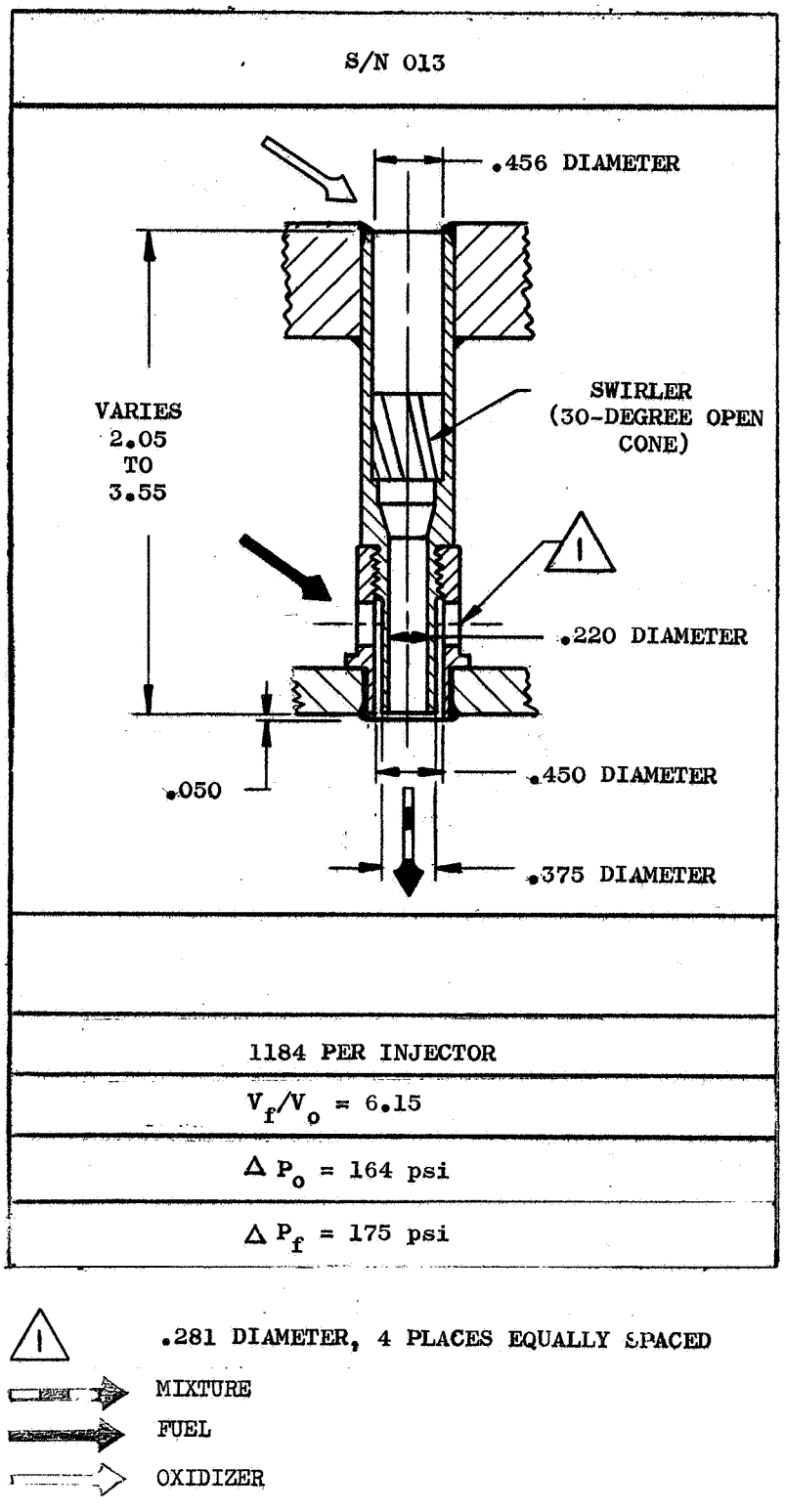


Figure 1. Basic Swirler Type Element, S/N 013

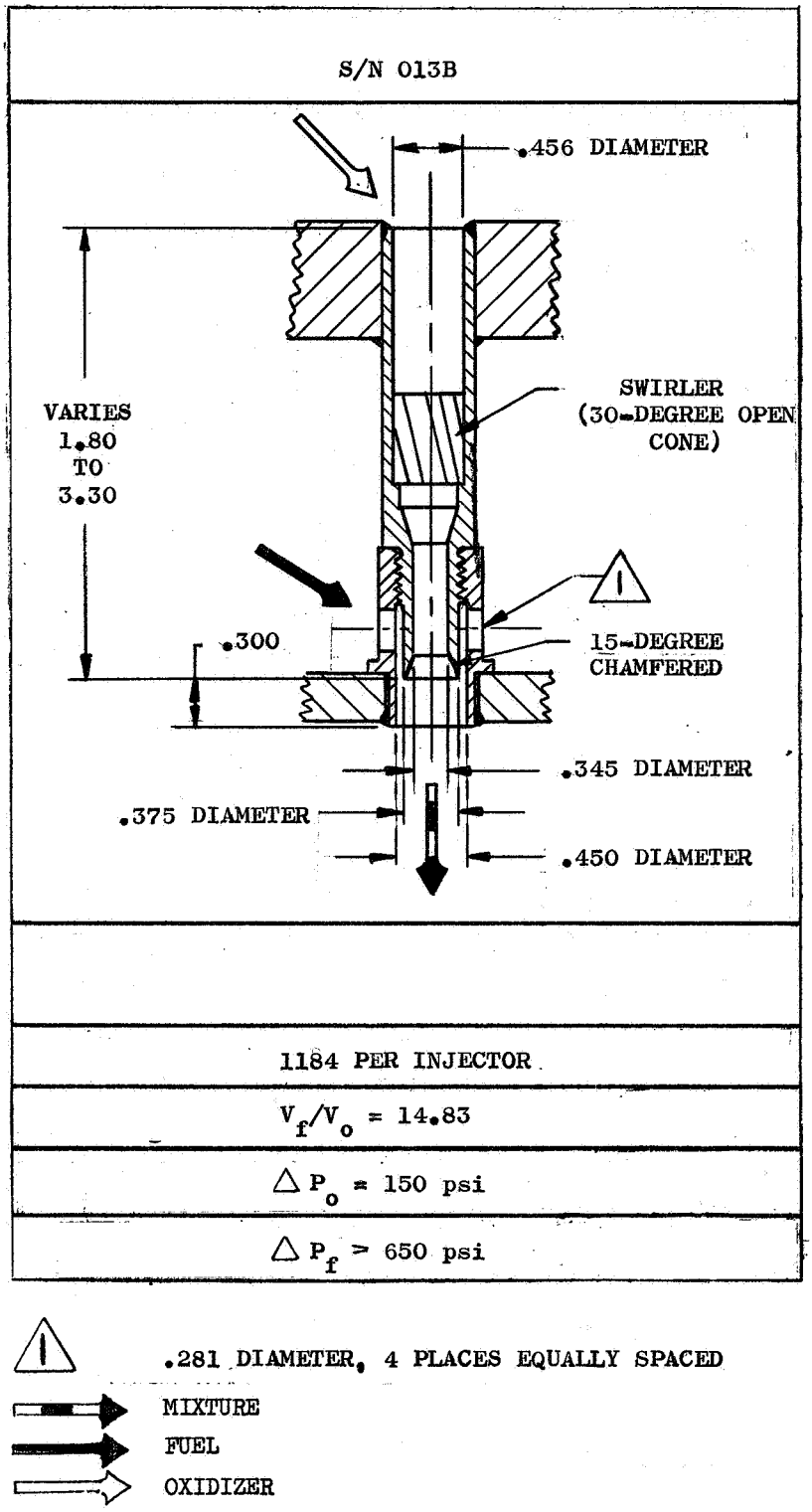


Figure 2. Basic Swirler Type Element, S/N 013B

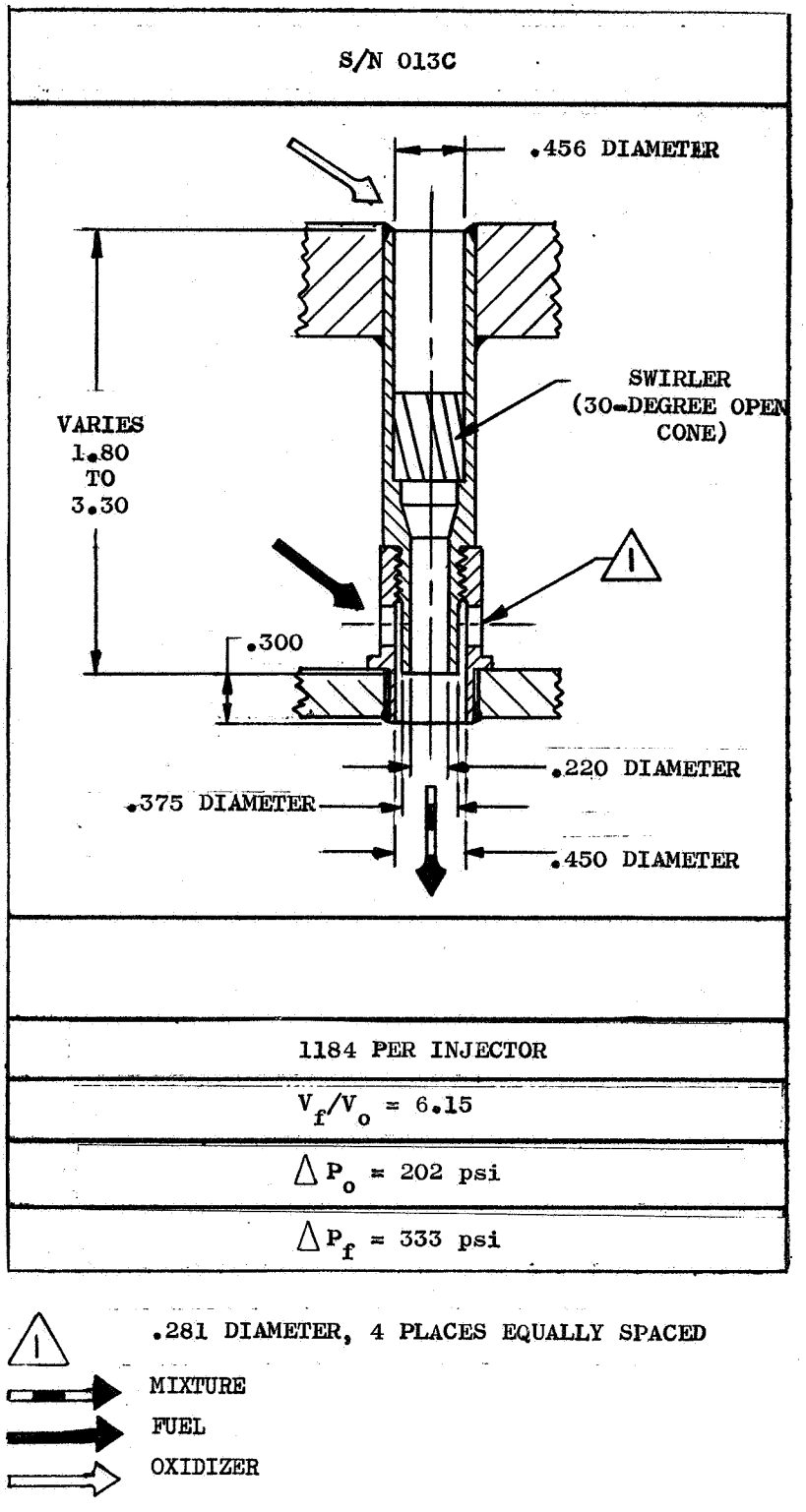


Figure 3. Basic Swirler Type Element, S/N 013C

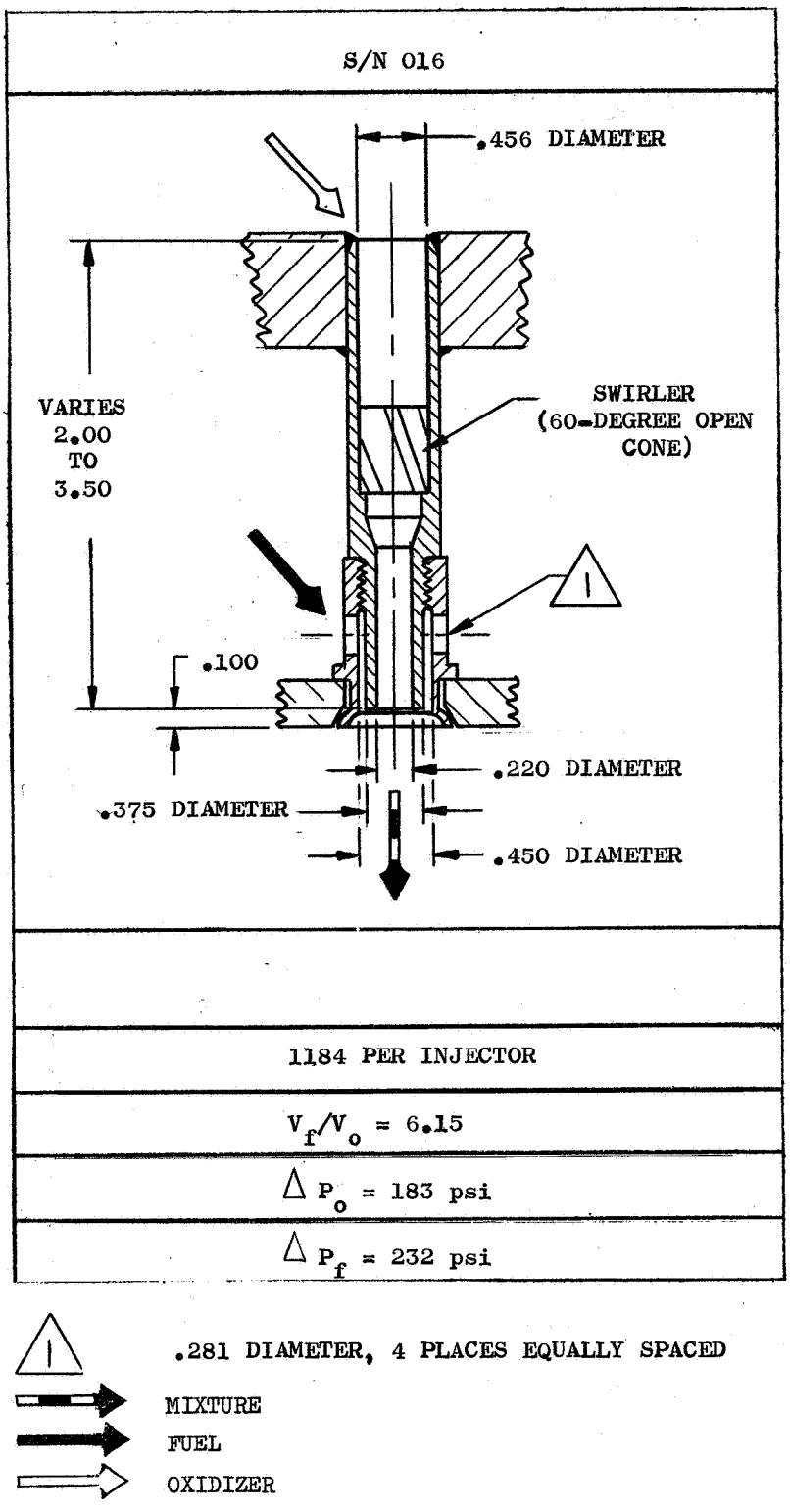


Figure 4. Basic Swirler Type Element, S/N 016

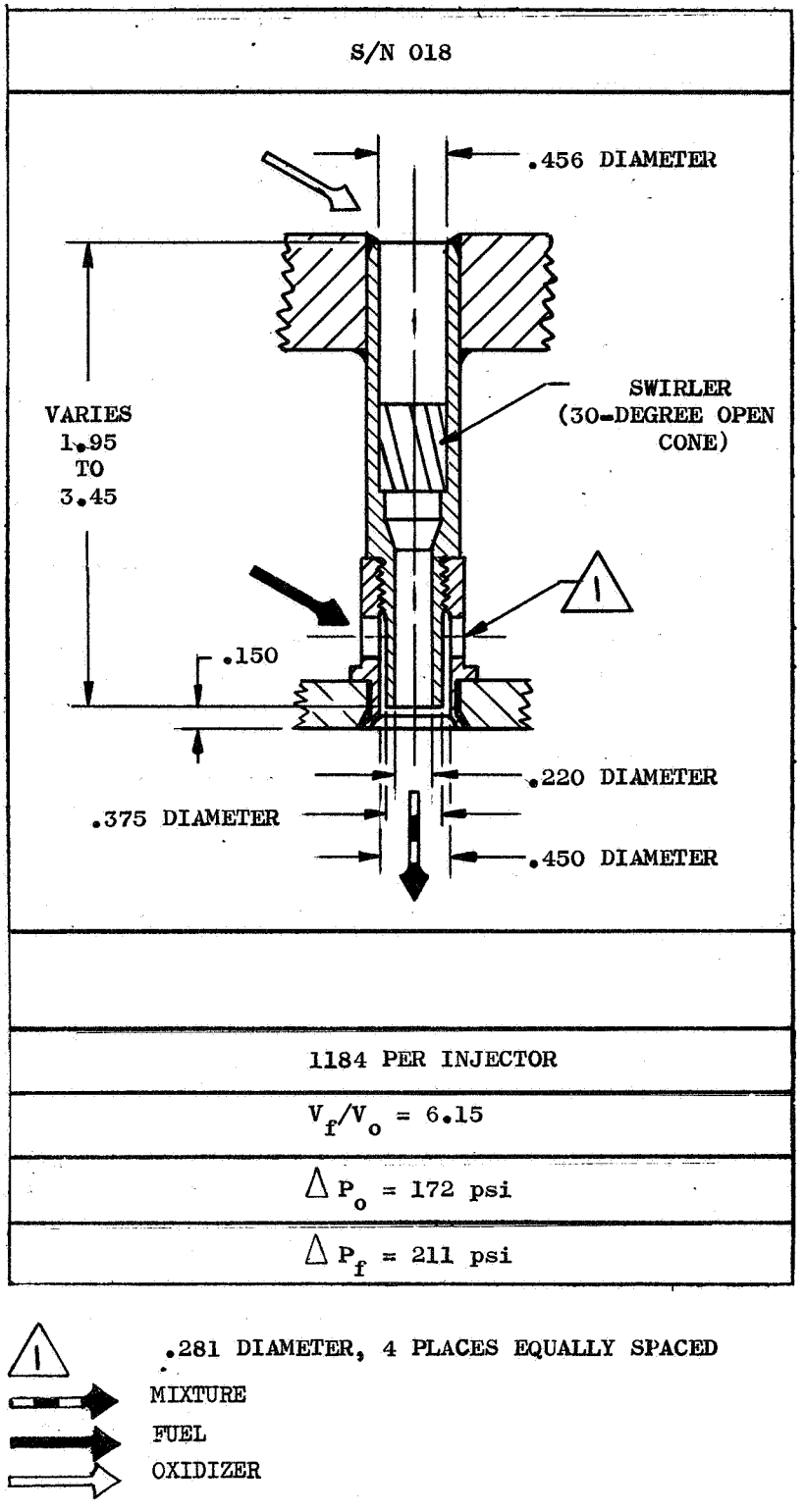


Figure 5. Basic Swirler Type Element, S/N 018

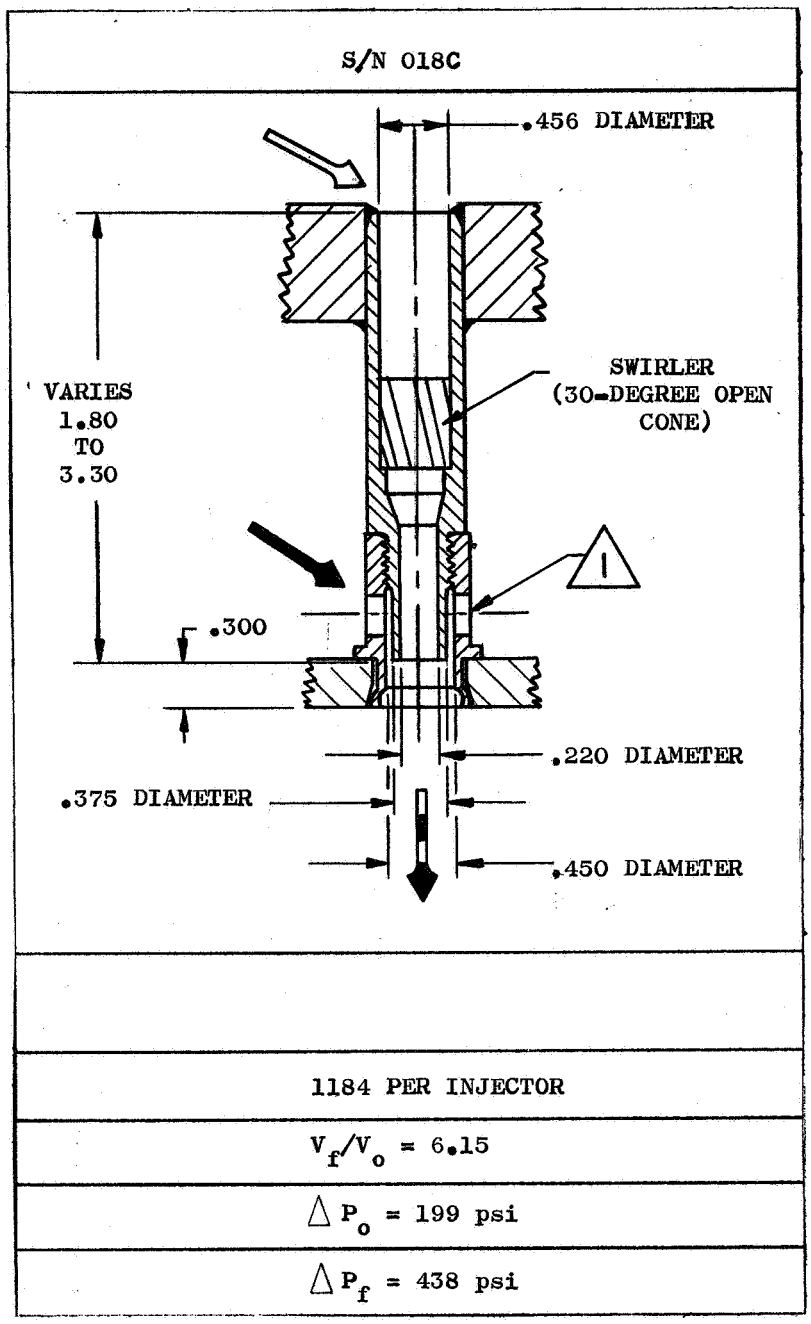


Figure 6. Basic Swirler Type Element, S/N 018C

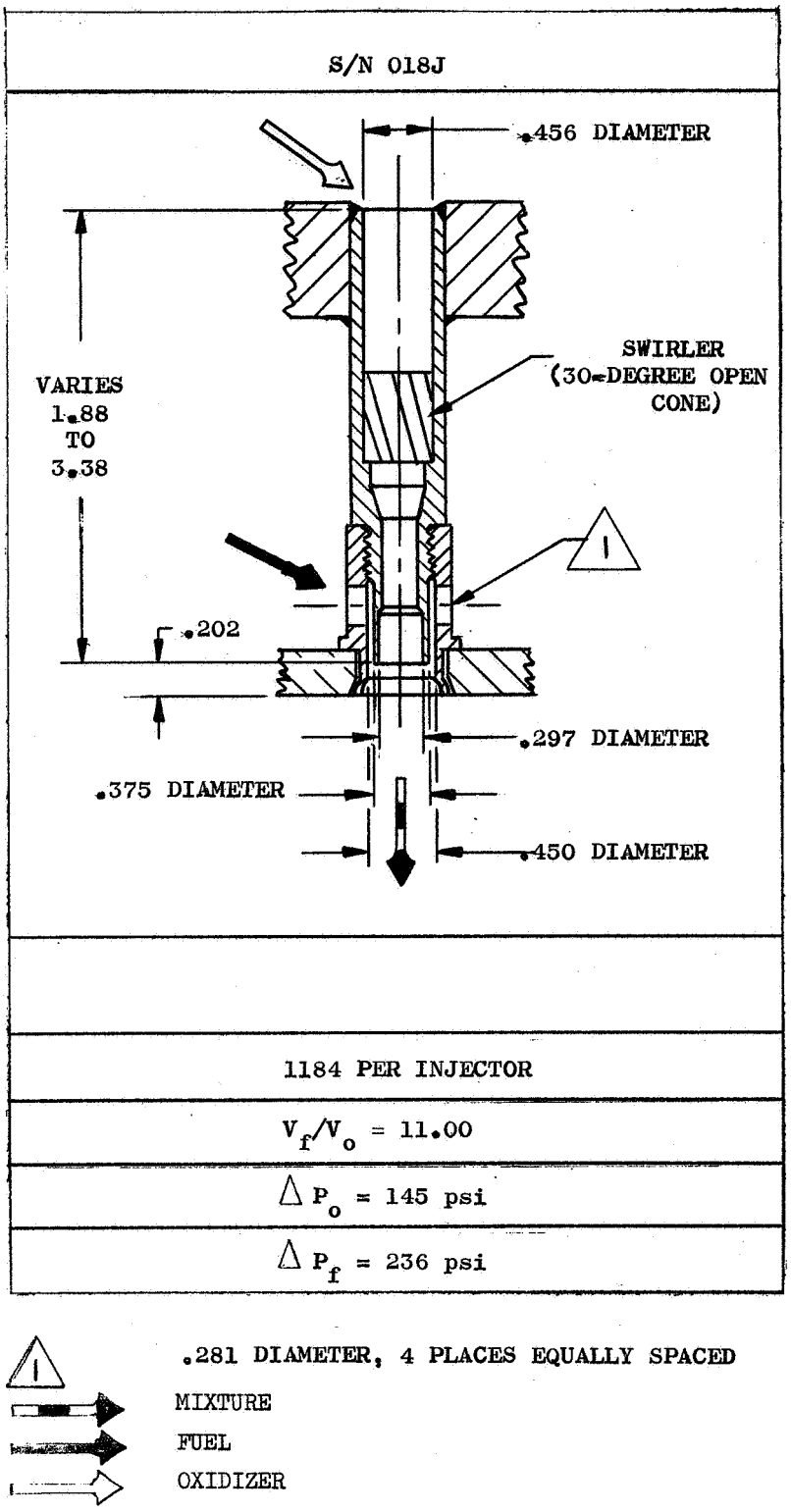


Figure 7. Basic Swirler Type Element, S/N 018J

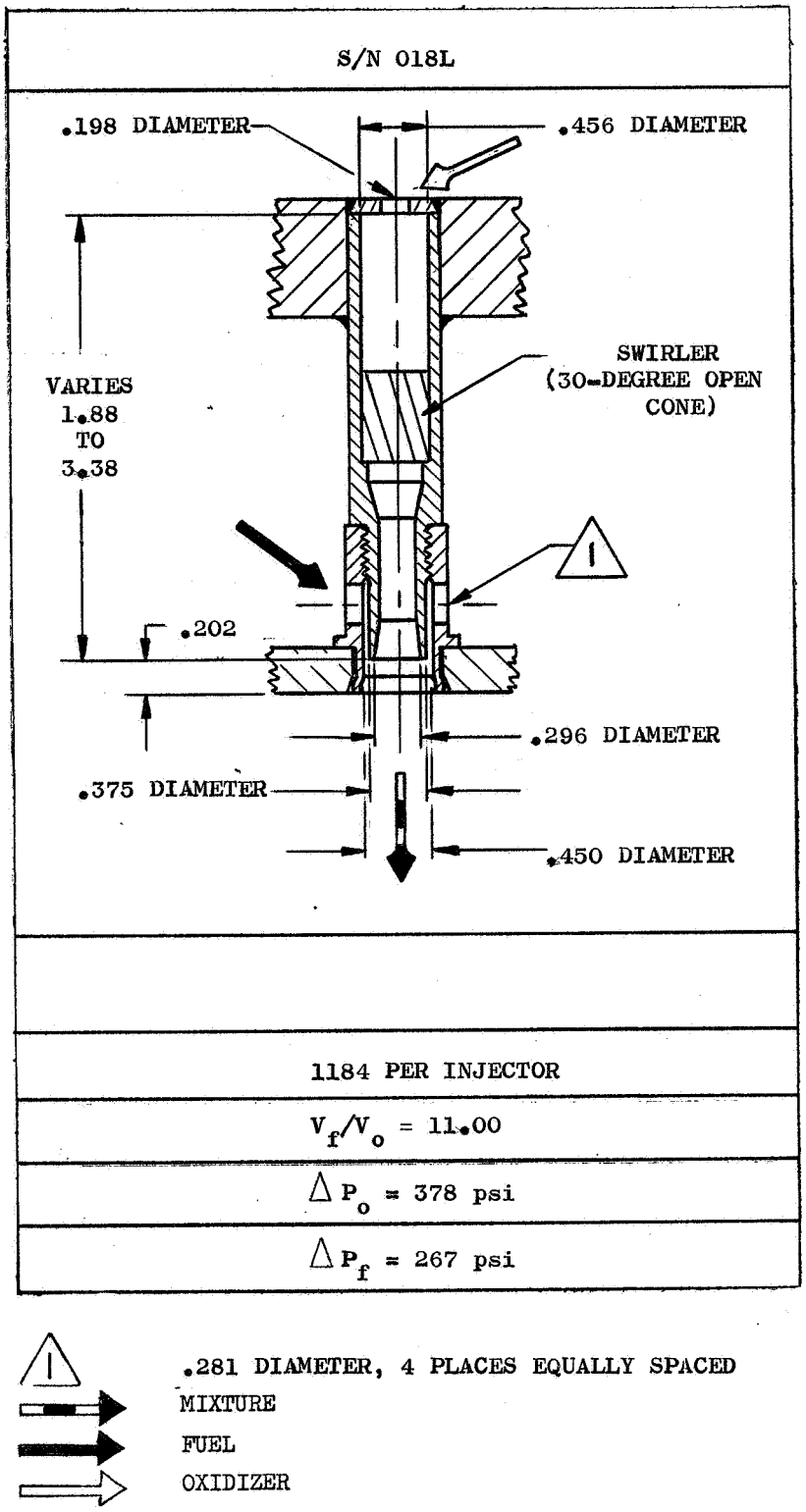


Figure 8. Basic Swirler Type Element, S/N 018L

Figure No. 9 depicts a one-piece, pre-mix type of design. The oxidizer tube is fed at the upstream end through four holes, which are tangential to the inside diameter. These holes are positioned to swirl the oxidizer so as to assure a hollow cone spray injection. Eight orifices, recessed approximately 0.3-in. from the injector face, were designed to impinge the fuel feed upon the oxidizer at a 45-degree angle. The oxidizer inlet end of this element was intended for brazing into the injector plate while the outlet or pre-mix chamber end was designed for shouldering and swaging.

b. Design Selected

The element selected for the limited phaseout program as well as use in the 3248 element injectors (S/N 012 and S/N 020) is shown on Figure No. 10. This element has no swirler, the oxidizer pressure drop is controlled through a small diameter orifice at the entrance to the tube, and the injection velocity ratio (fuel to oxidizer) increases to approximately 20. The oxidizer tube recess is 0.231-in.

The serial number shown at the top of Figures No. 1 through No. 10 is the identification number assigned to each element during development. This development was conducted as the M-1 Uni-Element Program.(1) Pertinent data is tabulated on each figure.

2. Fuel Manifold Description

The injector fuel manifold is formed in the large diameter, relatively shallow cavity between the aft side of the injector plate and the porous face plate sections (see Figure No. 11). Concentric baffle support rings and radial baffle support ribs divide the manifold into separate sections with the smallest support ring enclosing a single circular section at the injector center. Six, equally-spaced, radial support ribs extend from the inner ring to the outer ring. Twelve, equally-spaced, radial support ribs extend from the outer ring to the fuel ring at the injector periphery. The fuel ring is held away from the injector plate by the fuel ring support ribs and forms an annular opening between itself and the injector cavity wall.

Circumferential rows of coaxial injector element oxidizer posts pass through the fuel manifold from the injector plate to the injector face. Injector element fuel sleeves are assembled to the exit end of the oxidizer posts and aid in supporting the porous face plate sections. Appropriately shaped, pouous face plate sections are nested flush with the fuel ring and baffle supports to serve as the aft sides of the manifold sections.

(1) M-1 Uni-Element Program, Aerojet-General Report No. 8800-57, 15 February 1966

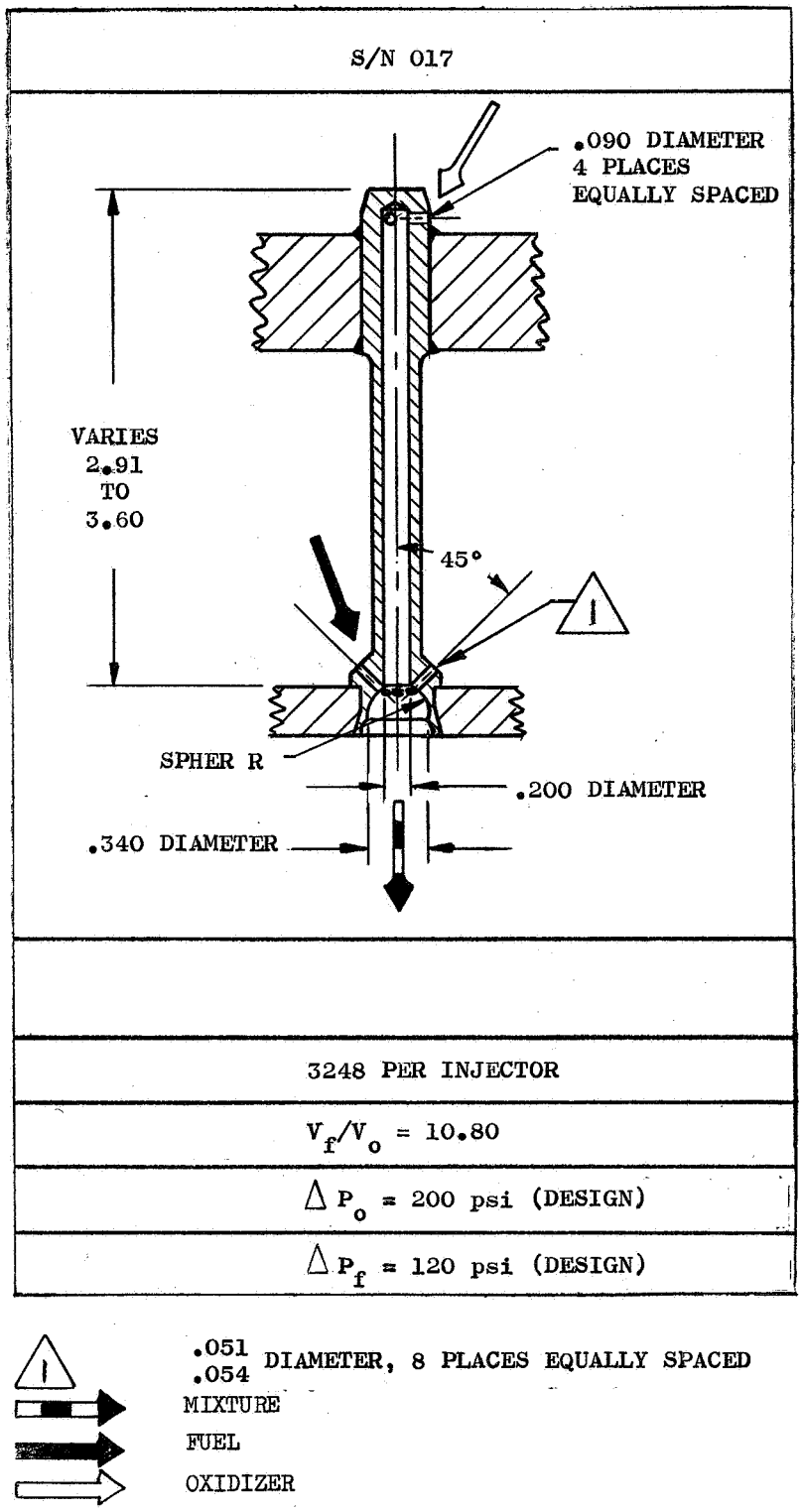


Figure 9. Basic Pre-Mix Type Element, S/N 017

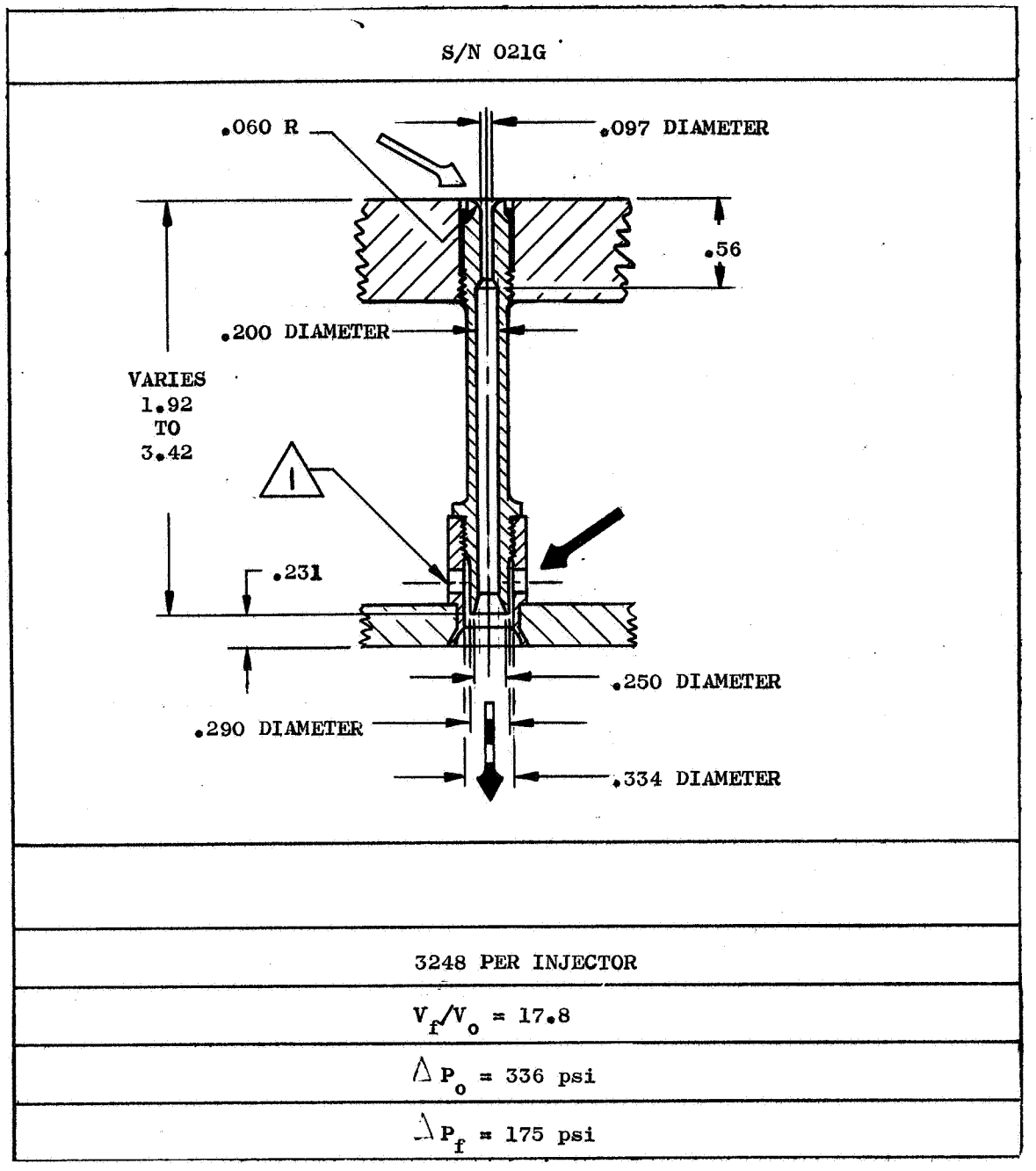


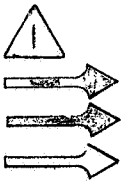

.141 DIAMETER, 4 PLACES EQUALLY SPACED
MIXTURE
FUEL
OXIDIZER

Figure 10. High-Velocity Ratio Type Element, S/N 021G

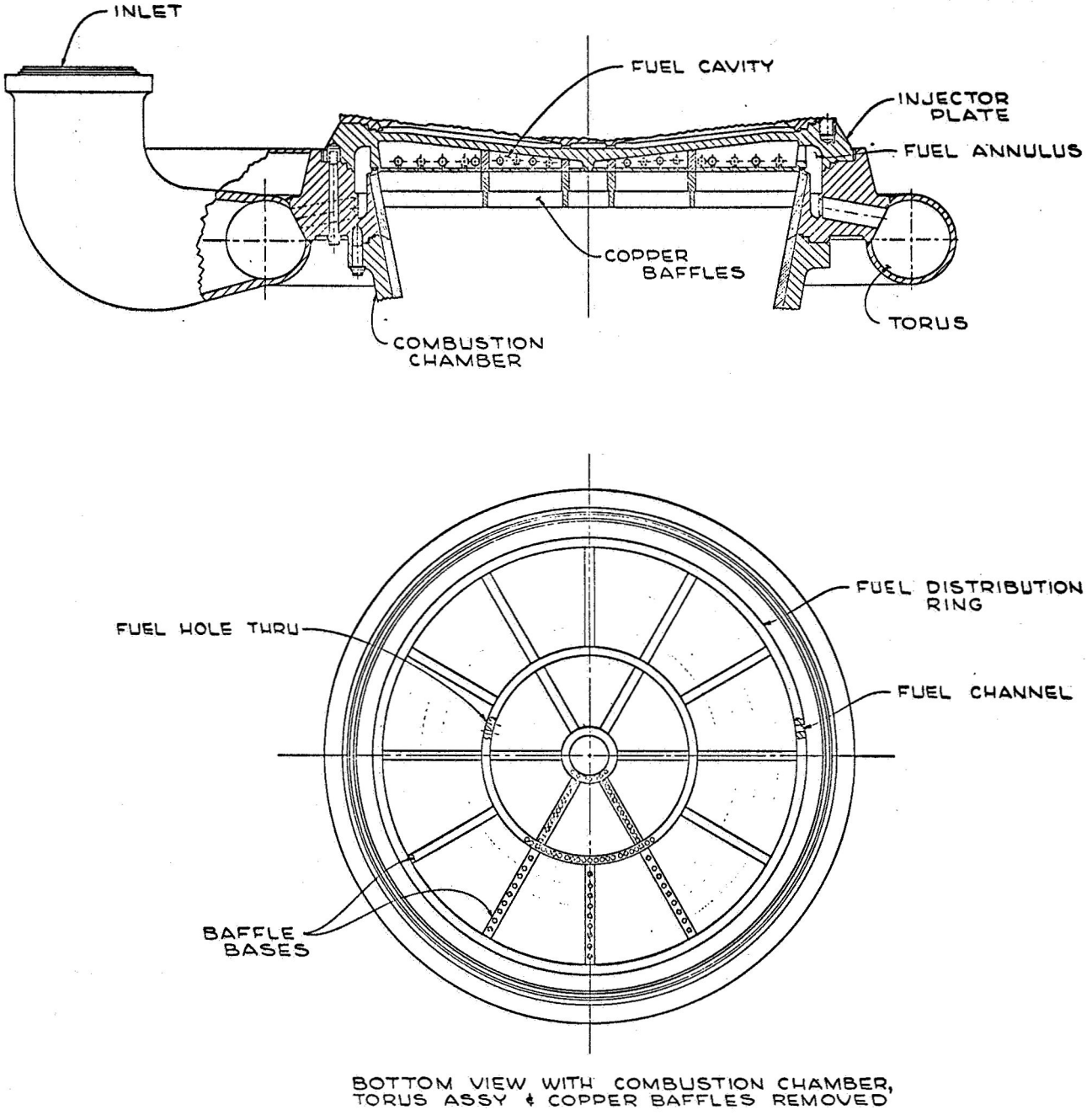


Figure 11. Injector Fuel Manifold

Fuel enters the annular area at the injector periphery, passes through the fuel ring, and makes a right-angle turn to flow into the twelve outer sections of the manifold. As the fuel flows toward the injector center through the bank of injector element oxidizer posts, a portion of the fuel is injected into the combustion chamber through each fuel sleeve. Large area, radially-drilled holes in the baffle support rings allow the fuel to flow through the rings to the inboard sections. The calculated pressure drop profile in the injector fuel circuit is shown on Figure No. 12. Test results are subsequently described in Section IV, A, 5 of this report. The radial distribution of the resultant oxidizer-fuel mixture ratio is shown on Figure No. 13.

3. Oxidizer Manifold Description

The injector oxidizer manifold is formed on the forward side of the injector plate between the injector plate and the oxidizer dome (see Figure No. 14). This manifold is divided into twelve sections by equally-spaced, radial ribs forged integrally with the dome. Small diameter, tubular baffles close the gap between the dome ribs and the injector plate to minimize circumferential flow between the sections. Circular ribs on both the injector and the dome interface form a small circular center section. Openings in the injector rib provide passages for the radial flow of oxidizer into this center section. The individual manifold sections are fed through twelve radial standpipes which support the external oxidizer dome torus. Circumferential rows of coaxial element oxidizer posts, which pass through the fuel manifold to the injector face, are assembled into the injector plate with the inlet ends exposed in the oxidizer manifold.

Oxidizer from the external oxidizer inlet torus enters the manifold sections through the radial standpipes. As the oxidizer flows through the manifold sections toward the center of the injector, a portion of each flow is injected into the combustion chamber through each oxidizer post. The calculated and actual pressure drop profile in the injector oxidizer circuit is as shown on Figure No. 15. The radial distribution of the resultant oxidizer fuel mixture ratio appeared on Figure No. 13.

4. Multi-Orifice Injector

a. Manifolding

The multi-orifice injector consists of a one-piece, 347 stainless steel forging having 23 concentric channels (11 oxidizer and 12 fuel) with propellant feed slots and 18, equally-spaced, radial ribs machined into the basic forging. Manifold covers are welded to the machined ribs to form pie-shaped fuel and oxidizer manifolds thereby enclosing the back side of the injector. Concentric ring face plates are welded to the machined lands to form propellant channels. Then, the orifice pattern is drilled into the face plates to complete the injector (see Figure No. 16).

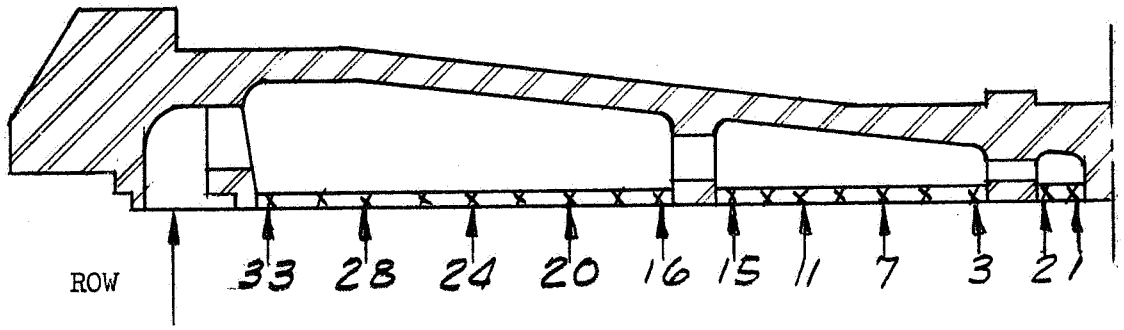


| PLENUM PRESSURE TO FACE PRESSURE | | | | | | | | | | | |
|---|---|---|---|---|---|---|---|---|---|---|---|
| ROW | 33 | 28 | 24 | 20 | 16 | 15 | 11 | 7 | 3 | 2 | 1 |
| $\Delta P$ ROW METHOD | 208 | 186 | 170 | 157 | 142 | 123 | 112 | 106 | 100 | 87.5 | 86 |
| $\Delta P$ "AVERAGING" | 158 | — | — | — | — | 109 | — | — | — | — | 86 |

Figure 12. Fuel Injector Design Pressure Profile

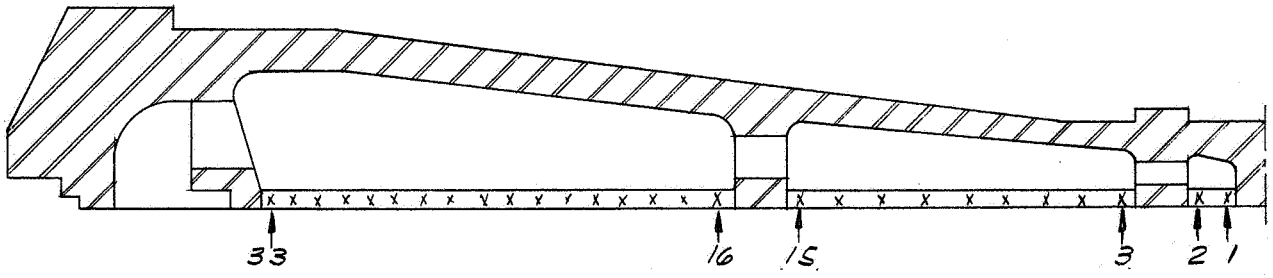


| ROW NO | 1 | 2 | 3 | 4 | 5 | 6 | 7 | 8 | 9 | 10 | 11 | 12 | 13 | 14 | 15 | 16 | 17 | 18 | 19 | 20 | 21 | 22 | 23 | 24 | 25 | 26 | 27 | 28 | 29 | 30 | 31 | 32 | 33 |
|---|---|---|---|---|---|---|---|---|---|---|---|---|---|---|---|---|---|---|---|---|---|---|---|---|---|---|---|---|---|---|---|---|---|
| M.R. | 6.87 | 7.20 | 6.94 | 6.90 | 6.85 | 6.47 | 6.47 | 6.85 | 6.56 | 6.56 | 6.47 | 6.36 | 6.25 | 6.24 | 6.10 | 6.25 | 6.18 | 6.02 | 6.02 | 5.92 | 5.97 | 5.74 | 5.69 | 5.64 | 5.96 | 5.90 | 5.81 | 5.75 | 5.64 | 5.62 | 5.58 | 5.44 | 5.44 |

Figure 13. Element Design Mixture Ratio Distribution

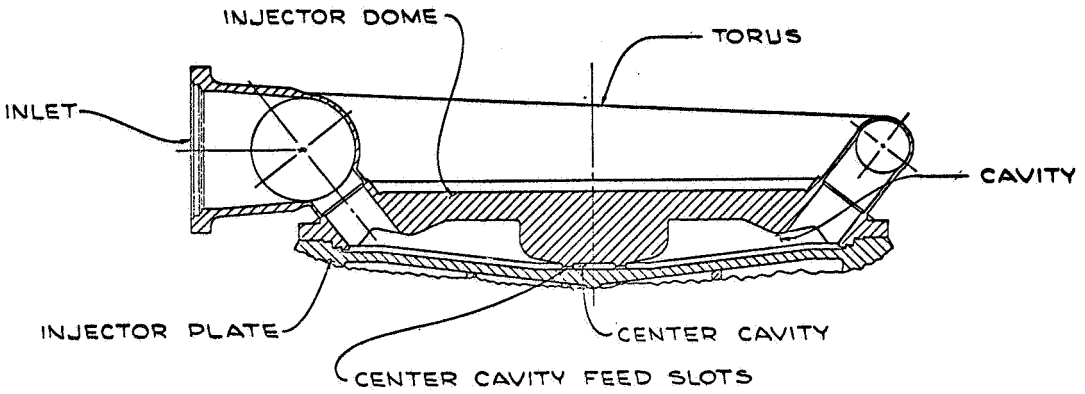


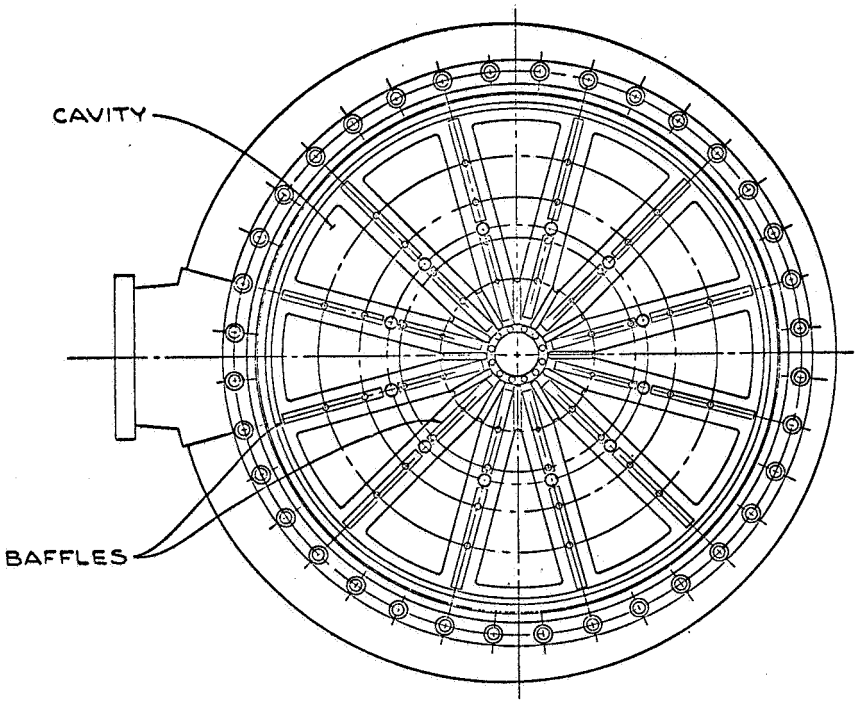


BOTTOM VIEW WITH
INJECTOR PLATE REMOVED

Figure 14. Injector Oxidizer Manifold

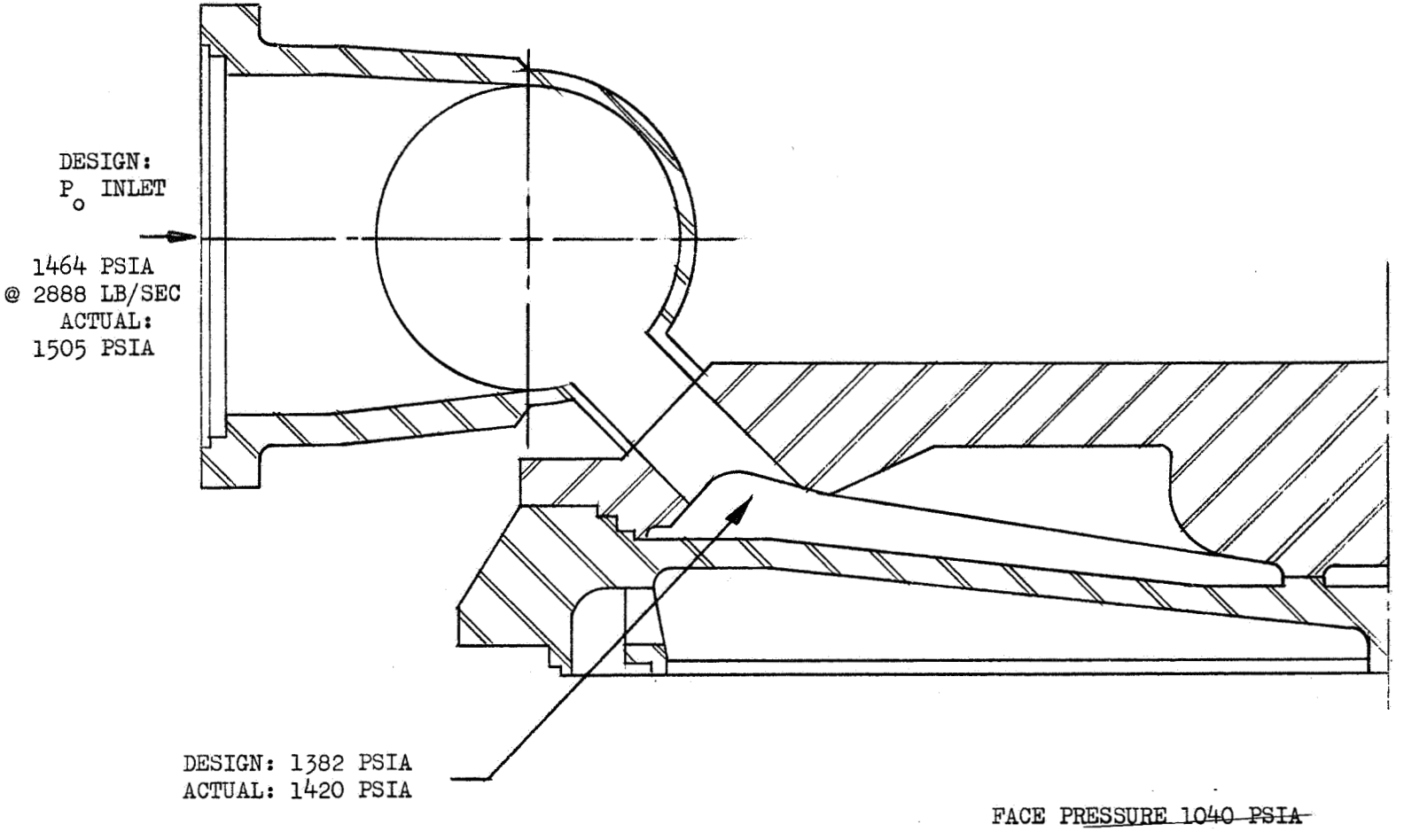


Figure 15. Pressure Drop Profile, Injector Oxidizer Circuit

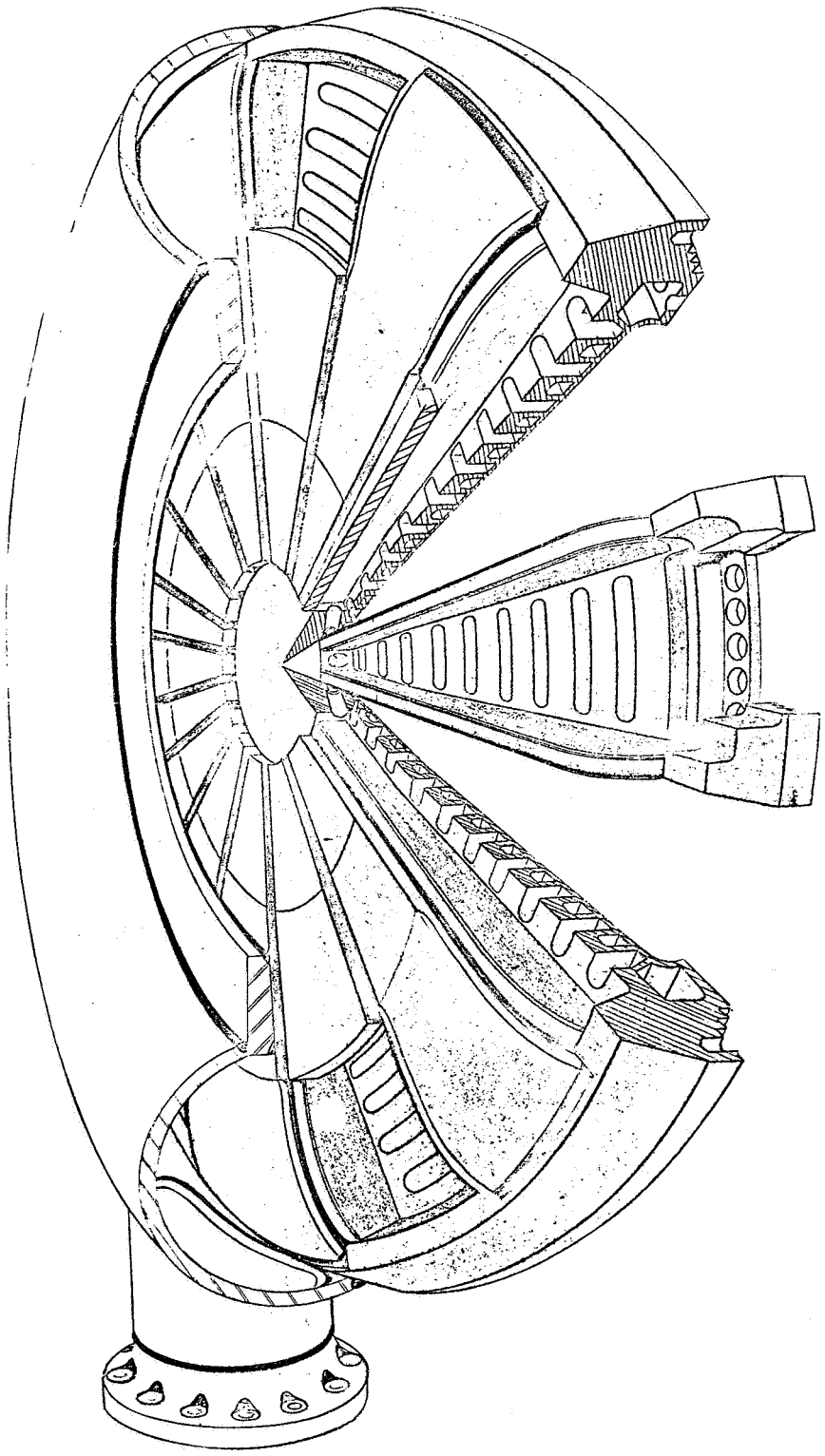

Figure 16. Multi-Orifice Injector

The nine, pie-shaped, oxidizer manifolds are fed radially from an external torus mounted to the outer circumference of the injector. The initial constant velocity oxidizer torus is fabricated as a half-circle, which is explosively formed from 347 stainless steel plate. This design was changed for future units to a full-round torus with nine spouts to feed the manifolds, and reduces the torus weight by 350 lb (see Figure No. 17).

The fuel manifolds are fed radially from the chamber/injector interface, which contains an annular channel for fuel distribution from the combustion chamber to the injector.

The initial design investigation for the optimum number of channels ranged from 17 to 34 channels. These channel numbers were derived from the successful Titan first-stage injectors. The investigation showed that the channel land heights were proportional to channel number while maintaining design velocities and pressure drops. For example, using 31 channels and maintaining design velocities and pressure drops, the maximum land height is 3-1/4-in. From Titan experience, the channel land heights in this region have caused the land to crack during face plate installation. If the land thickness was increased considerably, the cracking could be eliminated. However, to maintain the design parameters, the channel land thickness for this concept could not be increased to eliminate possible cracking. In an effort to keep land thicknesses to a minimum, a maximum channel height limitation of approximately 1.5-in. was imposed. The higher the number of channels, the more feed slots were required and this reduced the strength of the basic plate. Twenty-three channels were calculated to be optimum from the standpoints of velocity, propellant distribution, pressure drop, and maintaining of the channel land heights limitation.

The 17-channel design was not satisfactory because channel land thickness would be excessive. This could possibly cause injector face erosion.

The number of wedge-shaped manifolds to be used were varied from 12 to 24 similar to the successful Titan I injectors; however, when too few manifolds are used, the unfed distance increases to a point that channel depths become excessive in order to retain design velocities. While the unfed distance was reduced as the number of manifolds became greater, the increased number of ribs obstructed the required feed slot areas to the channels. Eighteen equally-spaced wedge manifolds (nine fuel and nine oxidizer) permitted the injector design to remain within the design parameters.

The ribs, which are machined in the basic forging, serve as structural members and become the walls of the manifolds. This avoids inter-channel welding in the feeding manifolds. A foot is incorporated at the base to give the rib a "T" cross-section which increases its bending strength.

NOTES: 1. REMOVE ALL BURRS AND SHARP EDGES EQUIV. TO .005/.015 R UNLESS OTHERWISE NOTED.
2. INTERPRET DRAWING PER STANDARDS PRESCRIBED IN MIL-D-70327.
3. CLASSIFICATION OF CHARACTERISTICS PER ▲ E-W-XXII DENOTED BY ⓒ CRITICAL Ⓜ MAJOR / NO SYMBOL MINOR.
4. CLEAN PER MSFC-SPEC-164, TYPE III, CLASS I.
5. PRESERVE / PACKAGE PER MSFC-DWG-NO. 10419900, FOR OXYGEN SYSTEM REQUIREMENTS.
6. BRAZE PER CONTRACT ENGINEER.
7. FLANGES ARE STILL ACCEPTABLE AFTER USE OR AFTER WELDING IF THIS DIA IS Ⓒ .015.
8. THIS SURFACE ⌐.010 NEW FLANGES, ⌐.015 AFTER USE OR AFTER WELDING.
9. FLANGES ARE STILL ACCEPTABLE AFTER USE OR AFTER WELDING IF THIS DIA IS Ⓒ .015.
10. THIS SURFACE ⌐.010 NEW FLANGES, ⌐.015 AFTER USE OR AFTER WELDING.
11. THESE SURFACES TO BE FREE OF SCRATCHES, DENTS, STEPS, OR FLAWS EXCEEDING SURFACE ROUGHNESS NOTED.
12. HYDROTEST:
A. PROOF / LEAK TEST THE OXIDIZER / FUEL CIRCUITS AT THE FOLLOWING PRESSURES / GIMBAL LOADS SIMULTANEOUSLY.
(1) PROOF: a) 1490 PSIG / 1510 K LBS (PER COGNIZANT ENGR.)
b) 1490 PSIG / 1890 K LBS
(2) LEAK: 1118 PSIG / 1450 K LBS.
(B) BACKFLUSH BOTH CIRCUITS AT 5 TO 100 PSIG UNTIL FREE OF FOREIGN MATERIAL.
(C) FOR OBTAINING Kw VALUES USE THE FOLLOWING:
OXIDIZER - DENSITY 70.0 LB/FT³
FUEL - DENSITY 2.3 LB/FT³
(D) RECORD THE FOLLOWING PRESSURE DROPS:
FUEL - INLET TO P_B, INLET TO P_J1, P_J1 TO P_C
13. SURFACE ROUGHNESS TO BE "63" UNLESS OTHERWISE NOTED.
▲ MARK PER ASD 5215 C WITH PATENT NO. 2,992,840.
15. ALL FILLET RADII TO BE .005/.015 R EXCEPT AS NOTED
16. ALL CONICAL GROOVE DIM'S APPLY AT 68° ± 5°F.

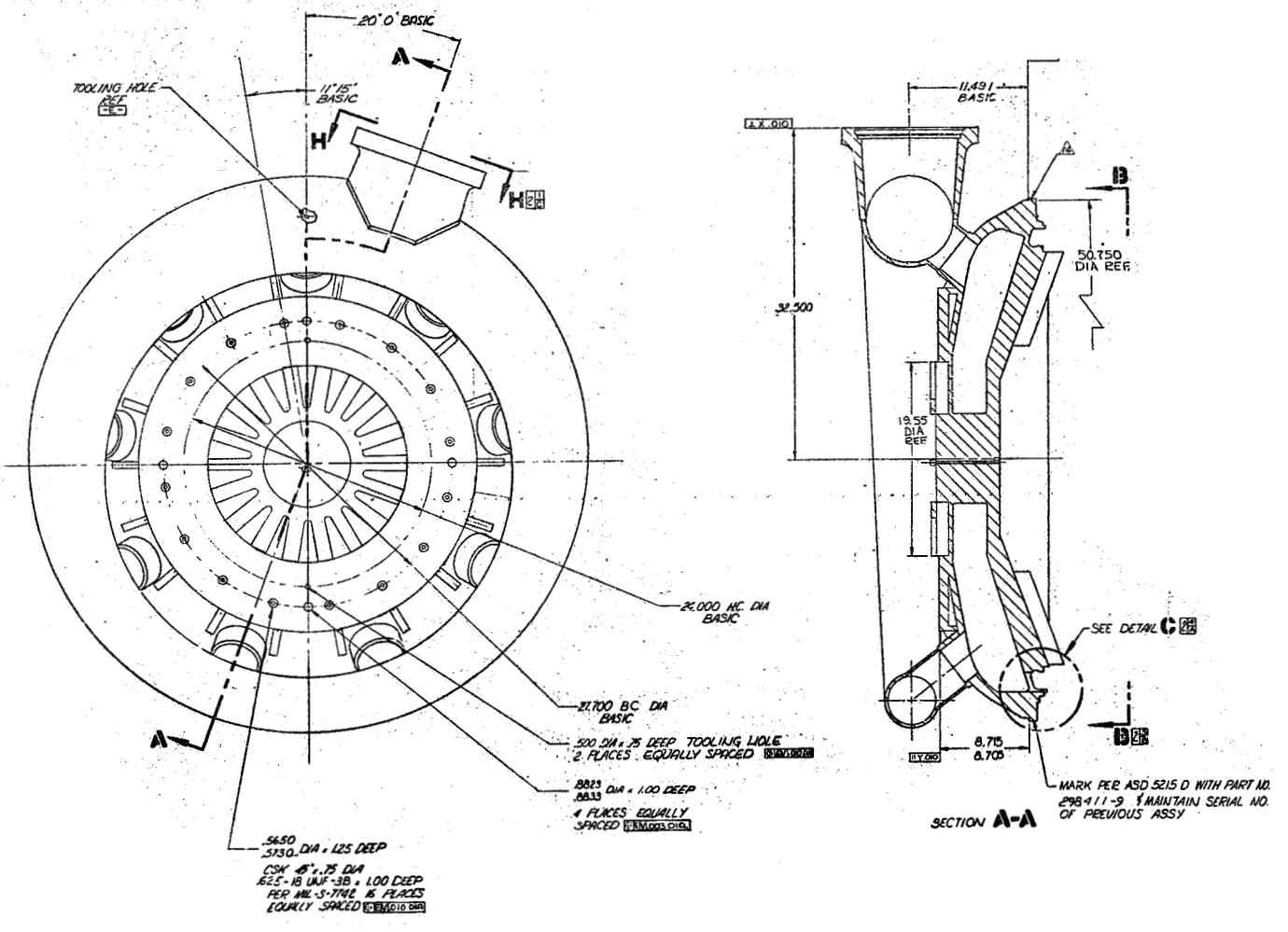


Figure 17. Thrust Chamber Injector

The injector has a dished face which was selected upon the basis of successful Aerojet-General experience.

Propellant distribution and $\Delta P$ were the main design parameters. The $\Delta P$ limits were: $\Delta P_o$ = 395 psi and $\Delta P_f$ = 202 psi. In designing to these limits, calculations were based upon constant propellant velocities in manifolds and the manifold velocities were not to exceed one-half the propellant velocities in the orifices. The surface area method ($lb/sec/in.^2$ of injector face) was applied for propellant distribution.

Constant mixture ratio was obtained except at the periphery and baffle locations where mixture ratio was reduced to protect the chamber tubes and baffles.

The following velocities were used:

Oxidizer Manifolds = 30 FPS

Fuel Manifolds = 230 FPS

Fuel Channels = 165 FPS

Oxidizer Channels = 30 FPS

The actual $\Delta P$'s from hydrotesting, inlet to Pc, were:

$\Delta P$ Oxid. = 232 psi

$\Delta P$ Fuel = 213 psi

b. Injector Patterns

No single injector pattern has evolved that will serve as a universal pattern for all liquid engines. Each new injector requires its own development program; however, several general concepts were developed that can be used in initial pattern design.

The items to be considered are the types of orifice impingement (if any), impingement distance from the face, angle of impingement, orifice diameter, length-to-diameter ratio of the orifice, and random versus systematic arrangement of the orifices. One of the first considerations of a multi-orifice injector is selecting the type of orifice impingement.

Using these considerations as well as Aerojet-General experience, the initial injector pattern selected was a like-on-like fuel and like-on-like oxidizer with each oxidizer pair radially aligned with every fuel pair. Both the fuel and oxidizer pairs were arranged in a double row per channel (see Figure No. 18).

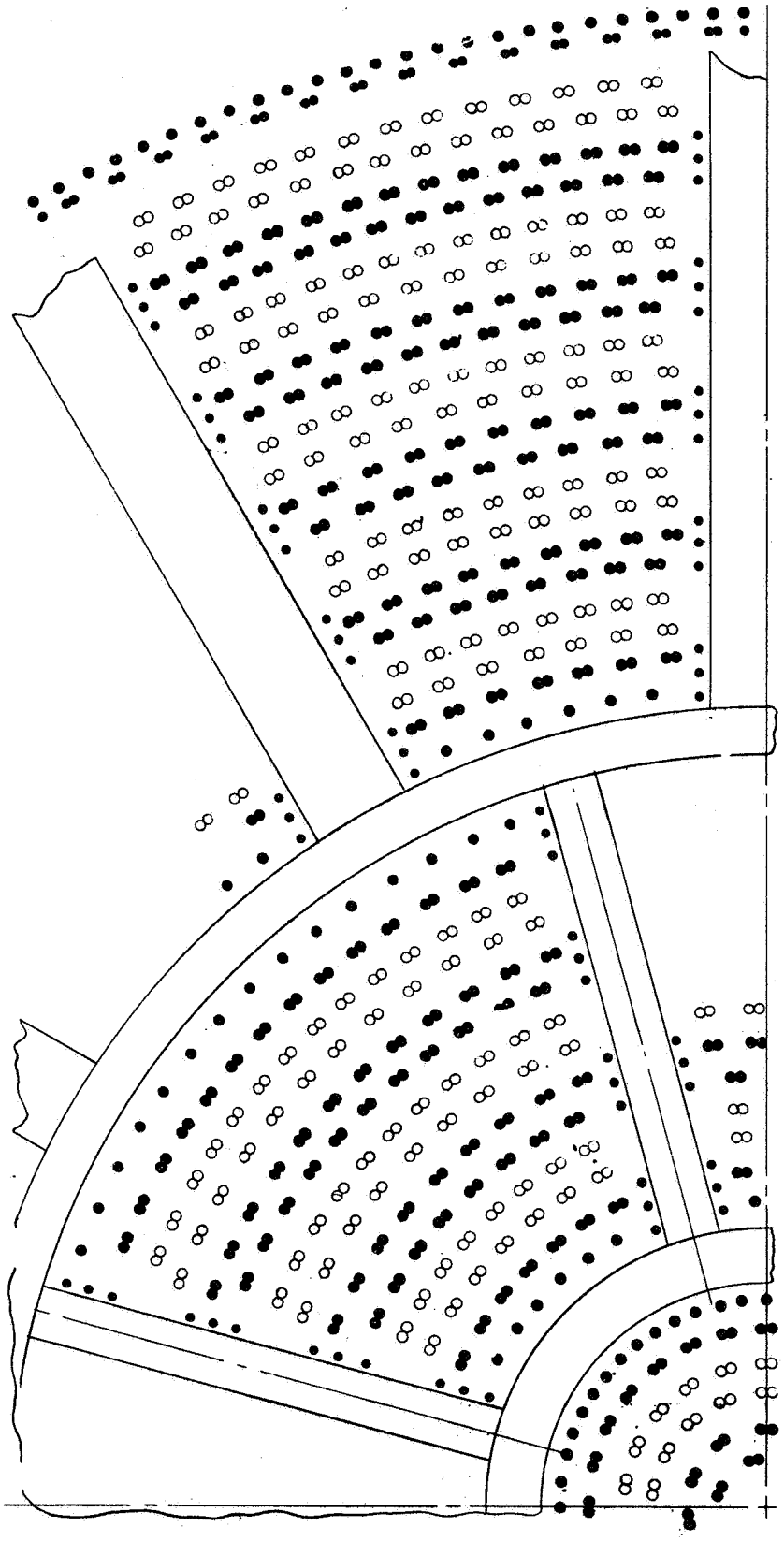

Figure 18. Multi-Orifice Injector Pattern, MALL-24-1

The second design selected was like-on-like fuel impinging pairs and showerhead oxidizer orifices (see Figure No. 19).

The third pattern selected was an all-showerhead one which was to be used for an injector incorporating pre-drilled face plates (see Figure No. 20).

c. Baffles

It was decided to use baffles in the initial M-1 injectors in an attempt to minimize combustion stability problems. The baffle system selected consisted of radially-oriented, bolt-on stainless steel blades that are film-cooled with fuel. Baffle simplicity without impairing injector serviceability also was emphasized.

An investigation showed that baffles could be externally cooled, which eliminated the time and effort required to design and fabricate an intricate convectively-cooled or regeneratively-cooled baffle with an untested configuration. Flexibility was desirable because the configuration could be established only by test firing. This flexibility could best be achieved if the baffles were removable. However, the use of removable baffles implied a weight penalty of as much as 25%. This weight penalty could be nullified by using permanent baffles after the configuration needed for combustion stability was established by test firing.

The baffles for the initial injector firings were designed to withstand the maximum shock loading that could occur as a result of detonation in a baffle compartment providing that the compartment contained the optimum gas mixture and the ignition source was from an adjacent compartment.

Many baffle configurations were proposed and examined. It was found that most baffle configurations were combinations of radial vanes and circumferential rings. The final baffle configuration for all M-1 multi-orifice injectors was as recommended in Appendix A and shown in Figure No. 21. While baffle length cannot be determined analytically, experience indicated for the chosen configuration that a six-inch long baffle system would be adequate to suppress the spinning tangential mode of instability.

The baffle system, which is shown on Figure No. 21, consists of 347 stainless steel bolted-on baffles. Type 347 stainless steel was selected because of cost considerations. Only the more expensive high nickel content materials have better oxidation resistance at elevated temperatures. Twelve radially-aligned outer blades are bolted to 12 equally-spaced bases, that have been welded to the face of the injector. After the blades are bolted in place, the inner assembly is bolted to the twelve outer radial blades. The inner assembly is composed of six equal radially-aligned blades welded in place between two concentric rings of 5-in. and 20-in. diameters. The entire baffle system is cooled by a film of fuel flowing through orifices spaced at close intervals along both sides and adjacent to all of the baffles.

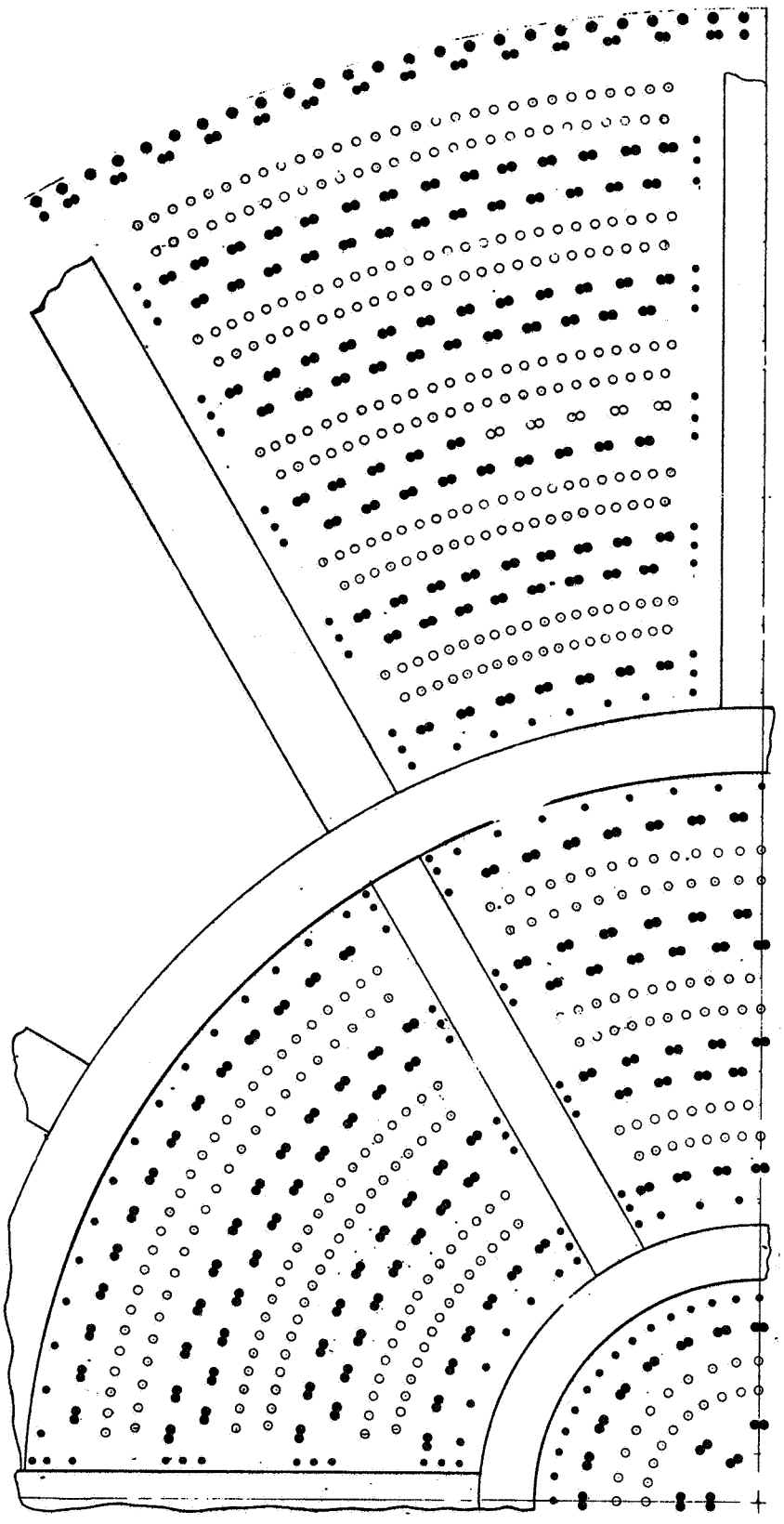

Figure 19. Multi-Orifice Injector Pattern, MALL-23-1

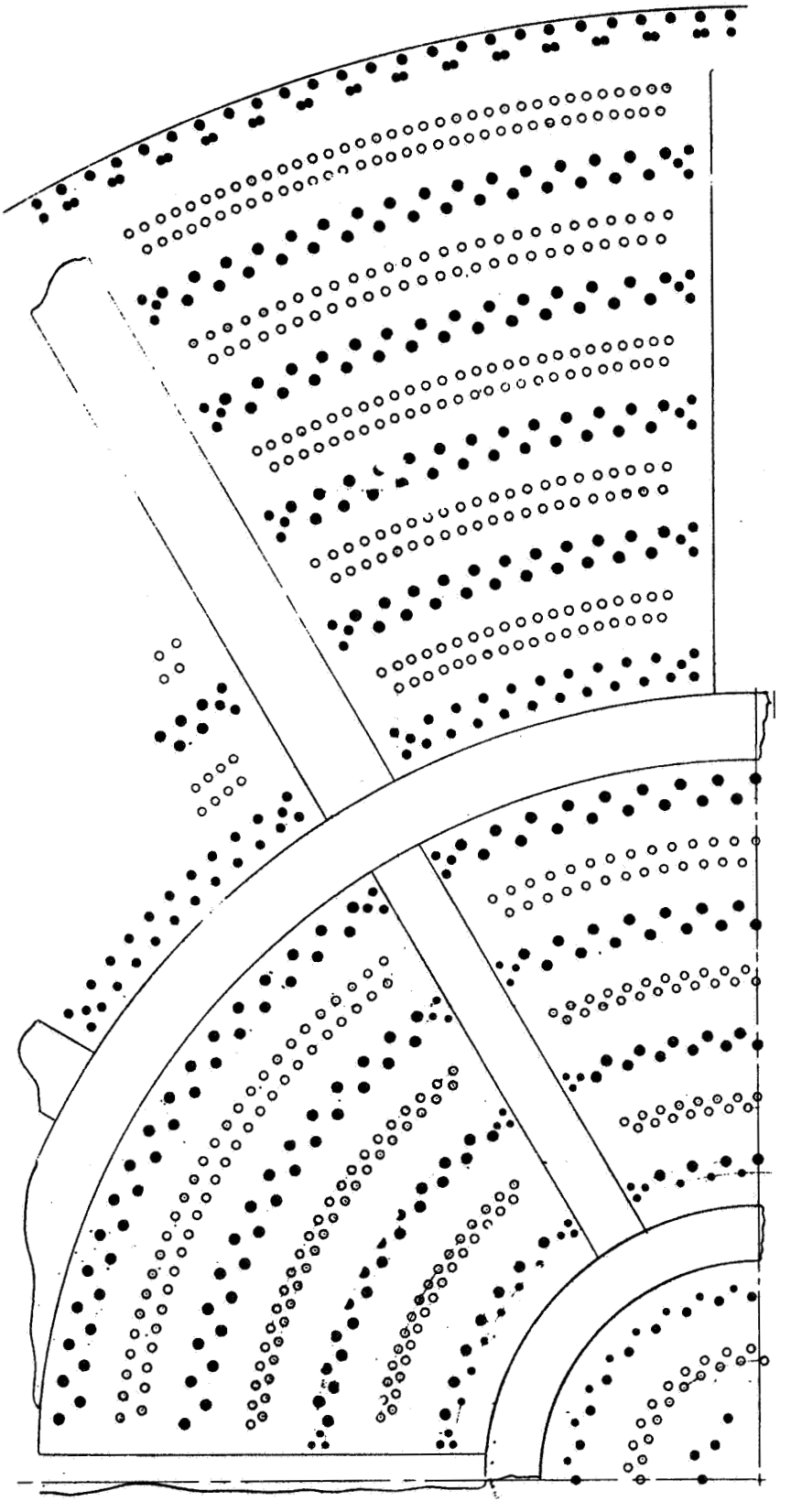

Figure 20. Multi-Orifice Injector Pattern, MAM-22-1

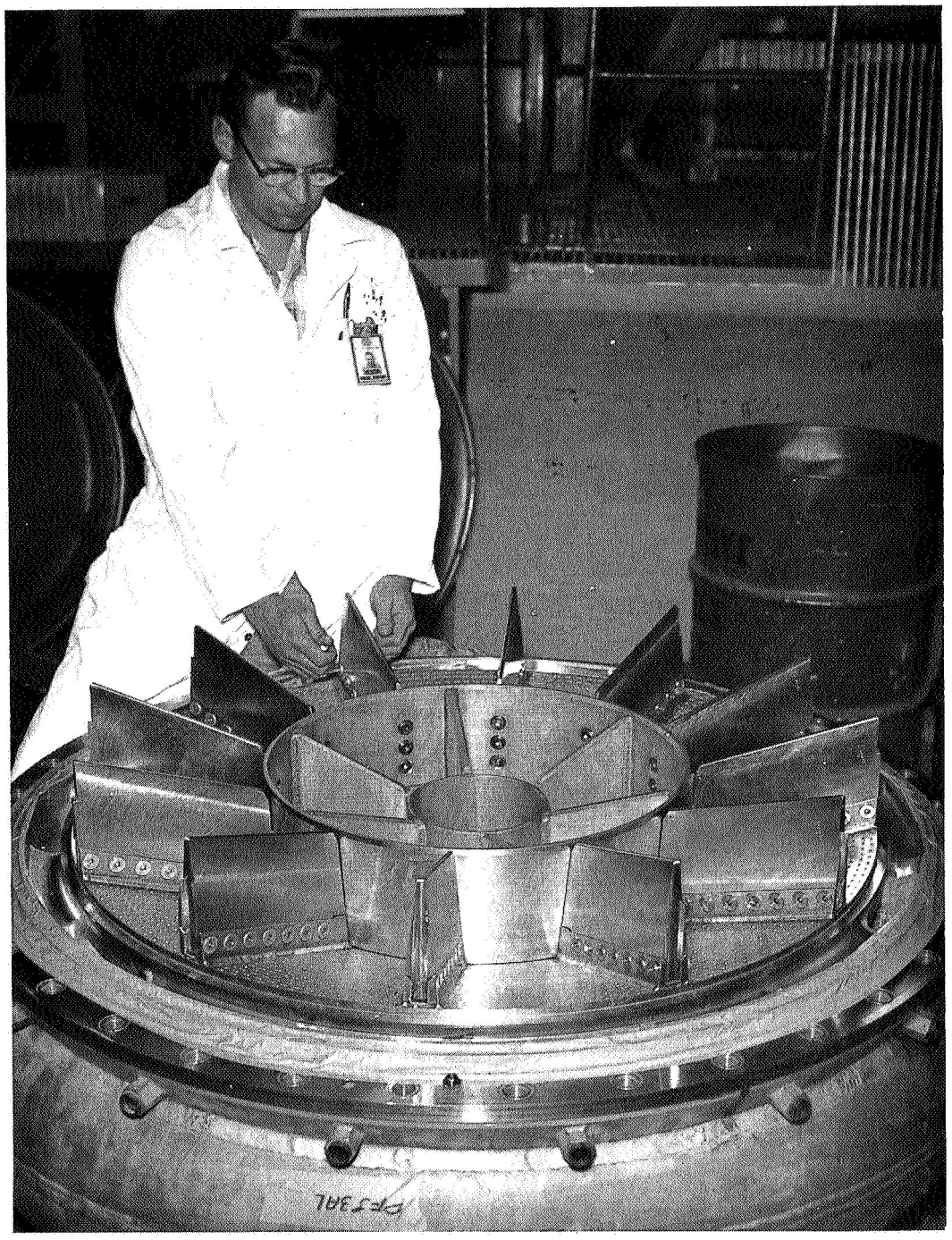

Figure 21. Multi-Orifice Injector Assembly with Baffles

## B. PERFORMANCE

The injector and chamber configurations are both significant in achieving high percentages of specific impulse. The injector must be designed to provide for uniform propellant distribution near the design mixture ratio and rapid mixing of the propellants. The chamber must be of sufficient length to assure that the gases passing through the throat are completely combusted and mixed with the excess fuel. Also, it should be of sufficient contraction ratio to limit those losses caused by combustion at high velocities to reasonable values.

The ensuing discussion contains the design information used in determining the injector configuration selected to provide high performance. An evaluation of the performance data obtained also is presented. The chamber parameters considered in assuring that the performance data obtained with the uncooled chamber would be applicable to a regeneratively-cooled unit also are delineated.

### 1. Injector Considerations

Only the coaxial injector concept is discussed because the multi-orifice concepts were discontinued prior to any performance testing.

#### a. Elements

Primary control over propellant distribution and mixing is achieved through the injector orifice or element. The design of the orifice or element is of prime consideration as regards performance.

At the time that the design of the first M-1 coaxial injectors was initiated, little information was available regarding the effect of injector parameters upon performance. Qualitative data obtained through discussions with the Pratt & Whitney personnel responsible for the development of the RL-10 Engine indicated that performance had been improved by installing swirlers within the oxidizer elements. These swirlers caused the oxidizer to be injected as a conical spray. This information was incorporated into the initial M-1 element designs (Figures No. 1 through No. 8) and fabrication of the injectors was initiated. This fabrication was of designs with 1184 and 3248 elements respectively, because no data was available regarding the effect of element number or thrust-per-element. Figure No. 22 shows the element injector pattern. Designs with as many as 5000 elements were considered; however, space within the selected injector diameter was not adequate for the practical application of this number of elements.

While these initially selected designs were being fabricated, data became available regarding Rocketdyne experience with the J-2 Engine. It differed from the RL-10 results in that the J-2 conclusions were that higher performance could be obtained if the propellant injection was recessed within the injector face and the swirlers eliminated.

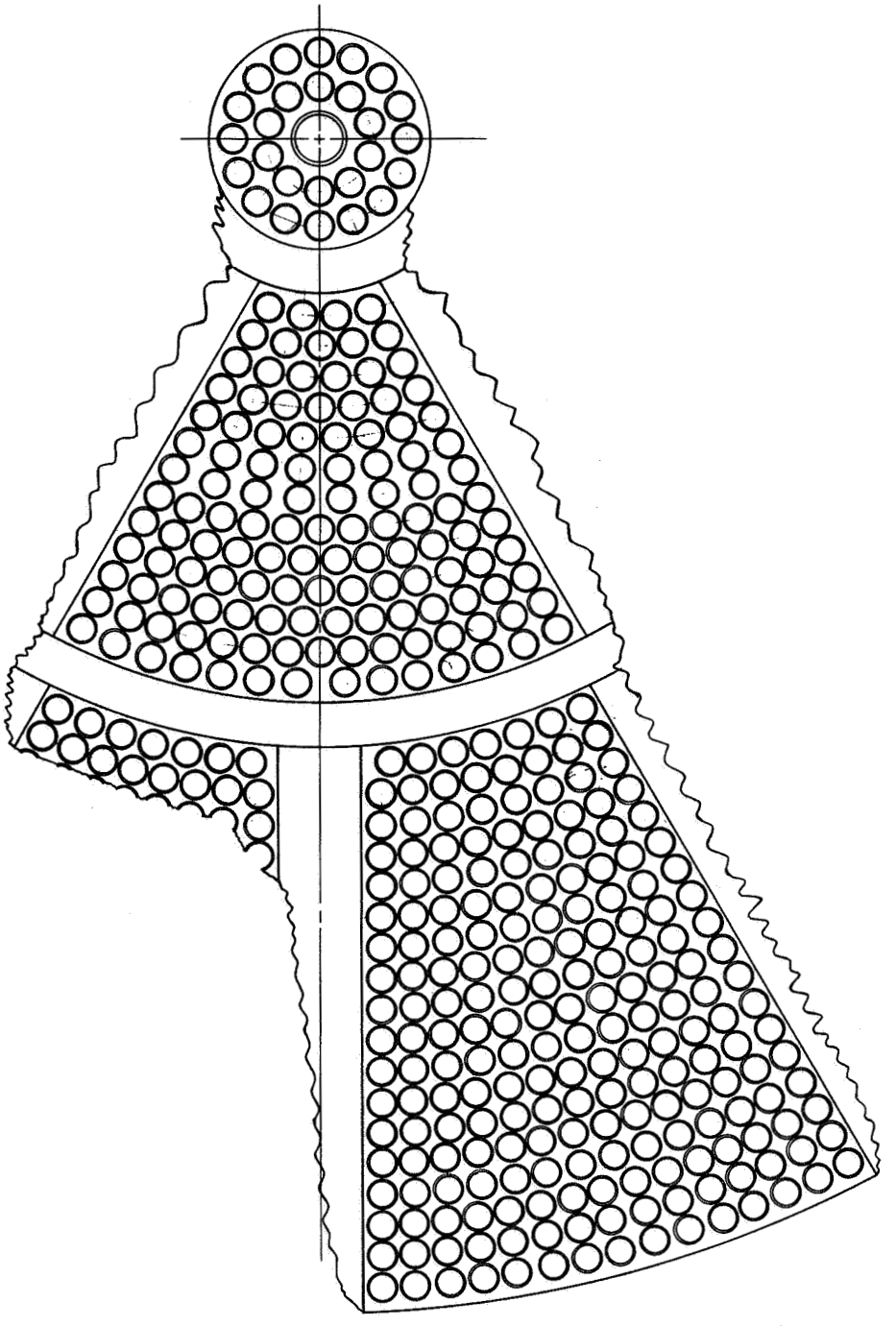

Figure 22. 3248 Injector Element Pattern

These factors, along with stability criteria discussed, resulted in the final element design shown on Figure No. 10.

b. Manifolding

The injector manifolding is secondary in establishing performance by the control of propellant distribution. By using relatively large volumes and low propellant velocities in the manifolds (see Figure No. 23 and No. 24), it is possible to provide uniform propellant distribution while maintaining all orifices or injection elements the same size. Also, by varying element sizing or pressure drop on an individual basis, a design with a minimum manifold volume can be derived. In most injector designs, as in the case with the M-1 Engine injector, a compromise between same sized or varying sized elements is reached because of factors other than performance which must be considered in the designs. Large manifolds tend to extend both start and shutdown transients because they require relatively long times to fill and drain. During these periods, local adverse mixture ratio and pressure drop can exist and result in local erosion or combustion oscillations.

Smaller manifolds result in larger manifold pressure drops, which necessitates an increase in pump discharge pressures or a reduction in injection element pressure drops to compensate for this in an engine system. Increasing pump discharge pressures tend to reduce system performance. Reducing injection pressure drops tends to make a unit more susceptible to combustion oscillation as well as making it more difficult to assure adequate dispersion and mixing of the propellants.

c. Heat Transfer

(1) Injector Face

Based upon results from the J-2 and RL-10 engine programs, a porous face was selected for the M-1 coaxial injectors. Rigimesh material with a porosity of 300 CFM of air at 20 psi pressure differential demonstrated adequate cooling in uni-element and NASA Lewis Research Center multi-element model tests. Therefore, this material was used in construction of the injector.

(2) Baffles

The original plan was to establish injector and baffle configurations which would be compatible with stability. After the number, location, and required length of the baffles was determined, the cooling requirements would be ascertained and incorporated. As a result, the initial baffles were made of solid stainless steel cooled by film coolant (13% of the fuel flow injected from the face of the injector). This configuration was readily adaptable to changes in baffle length which could be established only through experimentation.

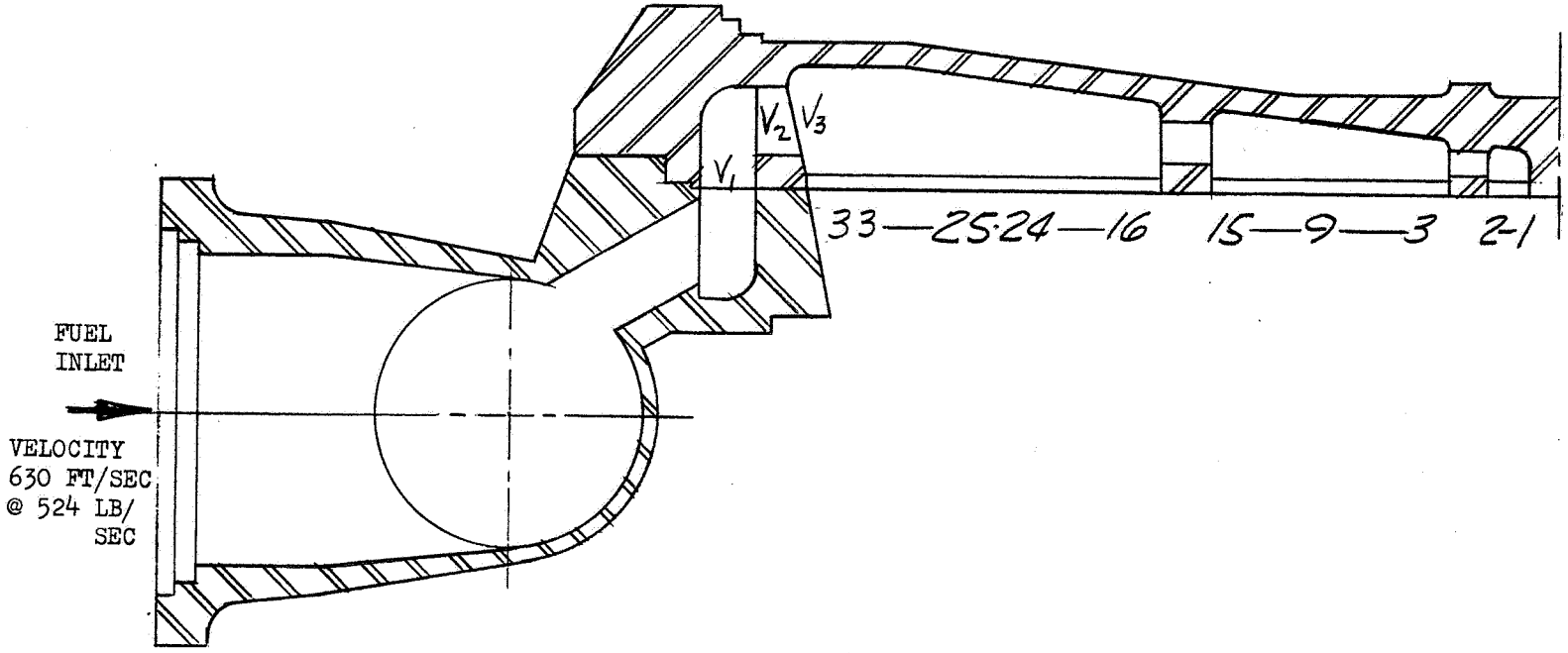


| MANIFOLD VELOCITY- FUEL | | | | | | | | | | | | |
|---|---|---|---|---|---|---|---|---|---|---|---|---|
| ROW NO | 33 | 25 | 24 | 16 | 15 | 9 | 3 | 2 | 1 | $V_1$ | $V_2$ | $V_3$ |
| VELOCITY FT/SEC | 368 | 336 | 321 | 268 | 255 | 163 | 90.2 | 386 | 365 | 212 | 440 | 156 |

Figure 23. Manifold Velocity, Fuel

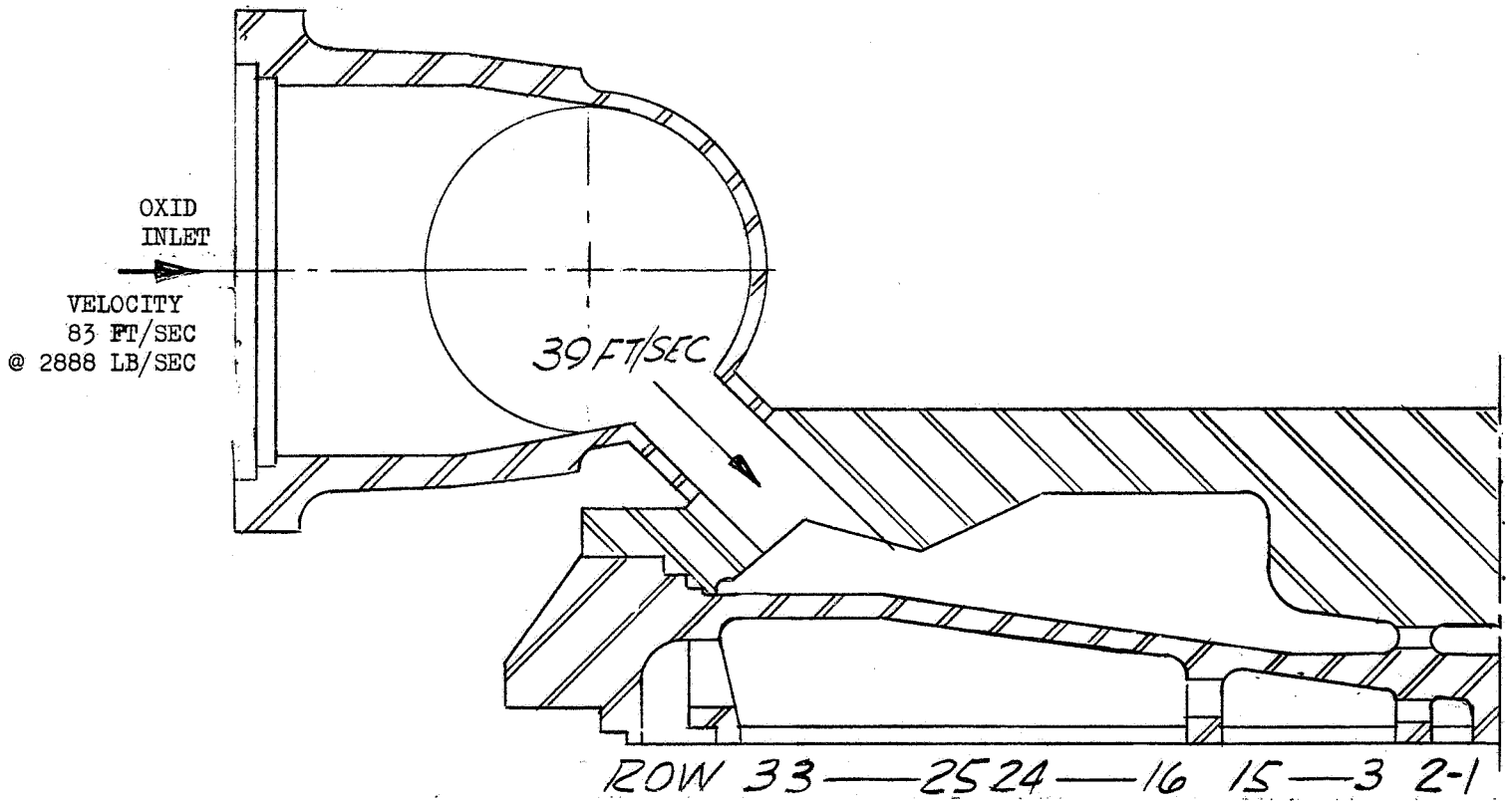


| ROW NO | 33-25 | 24-16 | 15-3 | 2-1 |
|---|---|---|---|---|
| MANIFOLD VELOCITY FT/SEC | 25 | 26 | 28 | 40 |

Figure 24. Manifold Velocity, Oxidizer

As discussed in Section III,C,1 of this report, a baffle length of 3-1/2-in. to 4-in. was selected and an evaluation of cooling methods was initiated. Transpiration cooling using Rigimesh, porous metal baffles, and a combination of convective-cooling and film-cooling using copper baffles with internal cooling passages were analytically evaluated. These analyses showed that either type of cooling method could be successful; however, the copper baffle would require more coolant flow.

The Rigimesh baffle surface temperatures were calculated using the Rannie[2] correlation and assuming that the wall surface temperature is the same as the coolant discharge temperature:

$$\frac{Tg - Twg}{Twg - Tc} = 37E \left(\frac{Gc}{Gg}\right) Re^{0.1} Pr \left[1 + \frac{Cpc}{Cpg} \left(1.18 (Re)^{0.1} - 1.0\right)\right]$$

Equation (1)

where:

Cpc = specific heat of coolant

Cpg = specific heat of combustion gas

E = effectiveness (experimental constant 0.85)

Gc = coolant mass velocity parallel to wall lb/sec - unit area

Pr = Prandtl number

Re = Reynolds number

Tg = combustion or recovery temperature

Tc = coolant inlet temperature

Twg = temperature, heated surface

Gg = combustion gas mass velocity parallel to wall lb/sec - unit area

Using the correlation of Equation (1), the results shown on Table I were obtained.

(2) Rannie, W. D., A Simplified Theory of Porous Cooling, Jet Propulsion Laboratory, Report No. 4-50

TABLE I

RIGIMESH BAFFLE SURFACE TEMPERATURES
FOR VARIOUS COOLANT FLOW RATES
AND ENVIRONMENT AT THE BAFFLE SURFACE

| % Fuel Used as Coolant | Wall Environment Based on Local Mass Velocity (Gg) Multipliers of | Surface Temperature °F 1.0 | 1.5 | 2.0 |
|---|---|---|---|---|
| 2 | | 1350 | 1950 | 2450 |
| 4 | | 640 | 1030 | 1420 |
| 6 | | 325 | 700 | 1020 |

Table I indicates that the wall temperatures using stainless steel Rigimesh would be adequately low using less than 4% of the fuel as coolant. The following equation[3] was used to establish a temperature profile within the Rigimesh for pressure drop calculations:

$$t_x = (t_2 - t_o^1)\left[ e^{-\varepsilon_w \delta(1 - \frac{x}{\delta})} \right] + t_o^1 \quad \text{for } 0 \leq x \leq 8 \qquad \text{Equation (2)}$$

where:

$$\varepsilon_w = \frac{G\, C_p}{K_w\,(1-P)}$$

G = mass flow rate of coolant per unit area

Cp = specific heat of coolant

Kw = thermal conductivity of wall

P = void fraction of material

$\delta$ = plate thickness

x = distance from cold surface

t = temperature

It was determined that the temperature of the material to within 0.02-in. to 0.03-in. of the hot gas wall remained at the temperature of the entering coolant.

(3) Schneider, P. J., Conduction Heat Transfer, Addison-Wesley, 1957

Recognizing that the environment at the hot-gas side wall surface had an appreciable effect on the distribution and was not well established, it was decided to test a model baffle in a scale injector at the NASA Lewis Research Center. These tests showed that pressure drops through the Rigimesh became excessive as the coolant flow approached design values which made the use of the available Rigimesh baffles impractical. As a result, it was decided to revert to the cooled copper baffle. Calculations had shown that a design such as that illustrated on Figure No. 25 would be satisfactory. This analysis used a modified Bartz equation for calculation of the gas-side heat transfer coefficient.

$$h_g = \frac{c_g H}{D_e^2} \left( \frac{\mu^{0.2} C_p}{P_r^{0.6}} \right)_{T_{am}} \left( \frac{W}{A} \right)^{0.8} \left( \frac{T_{fs}}{T_{am}} \right)^{0.8} \qquad \text{Equation (3)}$$

where:

$D_e$ = equivalent or hydraulic diameter of a baffle compartment

$h_g$ = gas-side heat transfer coefficient

$H$ = an empirical correction factor

$C_g$ = Bartz constant = 0.026

$\mu$ = Viscosity

$P_r$ = Prandtl number

$W$ = weight flow into baffle compartment

$A$ = baffle compartment cross-sectional area

$T_{fs}$ = gas-side film temperature

$T_{am}$ = arithmetic mean temperature bulk fluid to baffle surface

The liquid-side heat transfer coefficient was calculated using both the correlation of McCarthy and Wolf as well as one supplied by the NASA Lewis Research Center.

The McCarthy and Wolf correlations:

$$h_L = \frac{0.025 K_b}{D_e} \left( Re_b \right)^{0.8} \left( Pr_b \right)^{0.4} \left( \frac{T_{w1}}{T_b} \right) - 0.55 \qquad \text{Equation (4)}$$

The correlation supplied by the NASA Lewis Research Center is:

$$h_L = \frac{0.023\ K_f}{D_e} \left( Re_f \right)^{0.8} \left( Pr_f \right)^{0.4} \left( \frac{\rho_o}{\rho wl} \right)^{-0.4} \quad \text{where } Re_f = \frac{\rho b V D_e}{\mu}$$

Equation (5)

where:

$h_L$ = liquid-side film coefficient
$D_e$ = equivalent or hydraulic diameter of coolant passage
$K_b$ = thermal conductivity of coolant at bulk conditions
$K_f$ = thermal conductivity of coolant at film conditions
$Re_b$ = Reynolds number at coolant bulk conditions
$Pr_f$ & $Pr_b$ = Prandtl number at film and coolant bulk conditions
$T_{wl}$ = Temperature of wall at coolant surface
$T_b$ = bulk coolant temperature
$\rho b$ = density of coolant at bulk conditions
$\rho wl$ = density of coolant at coolant surface
$\mu_f$ = viscosity at film temperature
$V$ = velocity coolant

Film cooling effectiveness was calculated using a modified Hatch and Papell correlation:

$$\frac{dT_f}{dx} = \frac{AB(T_r - T_f)}{W^{0.875}}$$

Equation (6)

where:

$$A = \frac{h_g\ \pi D_e}{C_p}$$

$$B = 1.628 \left(\frac{V_g}{V_c}\right) \left(\frac{C_p}{K}\right) \left(\frac{1}{\pi D_e}\right)^{0.125}$$

$x$ = distance from film coolant injection point

$V_g$ = velocity of combustion gases

$V_e$ = velocity of film coolant

$T_r$ = recovery temperature

and other terms as defined previously.

In these analyses the correction factor (H) in the gas-side coefficient equation was assumed to be 1.0, although previous tests with injectors using storable propellants have shown values as high as 2.0.

Because the hardware used with the Rigimesh baffle was available, model tests were conducted. It was found that a design such as that shown on Figure No. 25 was required to prevent erosion of the model baffle. This design was selected for testing with the full-scale injector.

2. Chamber Considerations

a. Cooling

Initial M-1 program planning was based upon determining performances during tests of 20 sec duration with regeneratively-cooled chambers. However, in order to phase out the program within available funds and in a minimum time, it was necessary to delete the regeneratively-cooled chambers from the program. In addition, it appeared that performance could not be adequately established using the film-cooled chambers planned for use in the stability evaluation; the film cooling requirement was several times that of the cooled chamber. Available information did not permit sufficiently accurate performance corrections to account for losses caused by this additional film coolant. Therefore, an ablative-lined chamber with the same amount of film cooling as a regeneratively-cooled one was selected for performance testing. This ablative liner necessitated a change in the location of the film coolant holes from the gasket holder to the injector face, but it did not appear that this change would significantly affect performance determinations. Figure No. 26 shows the mixture ratio in relationship to predicted measured vacuum specific impulse for both regenerative and ablative chambers.

A heat transfer analysis was performed to estimate the thermal response of the M-1 ablative liner at three chamber locations for each of the four planned 5 sec duration firings (TS-1 to FS-2). Each firing period included a 1.1 sec fuel lead, during which no combustion occurs, as well as start-up and shutdown (after FS-2) transients of approximately 1.5 sec and 0.8 sec duration respectively. The chamber pressure builds up and decays during the latter times. A firing period of 5 sec duration gives approximately 2.5 sec of steady-state operation.

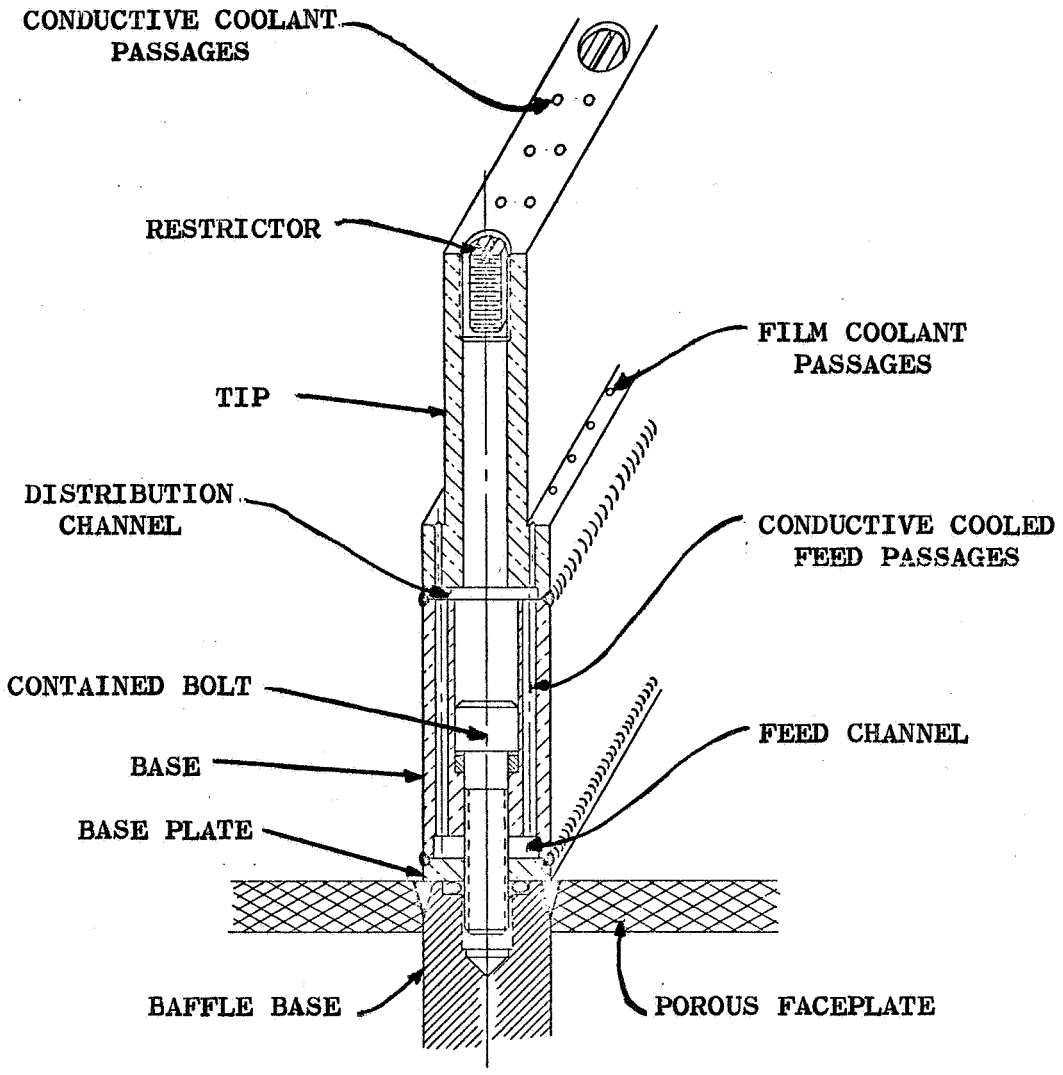


Figure 25. Bolt-On Copper Baffle Assembly

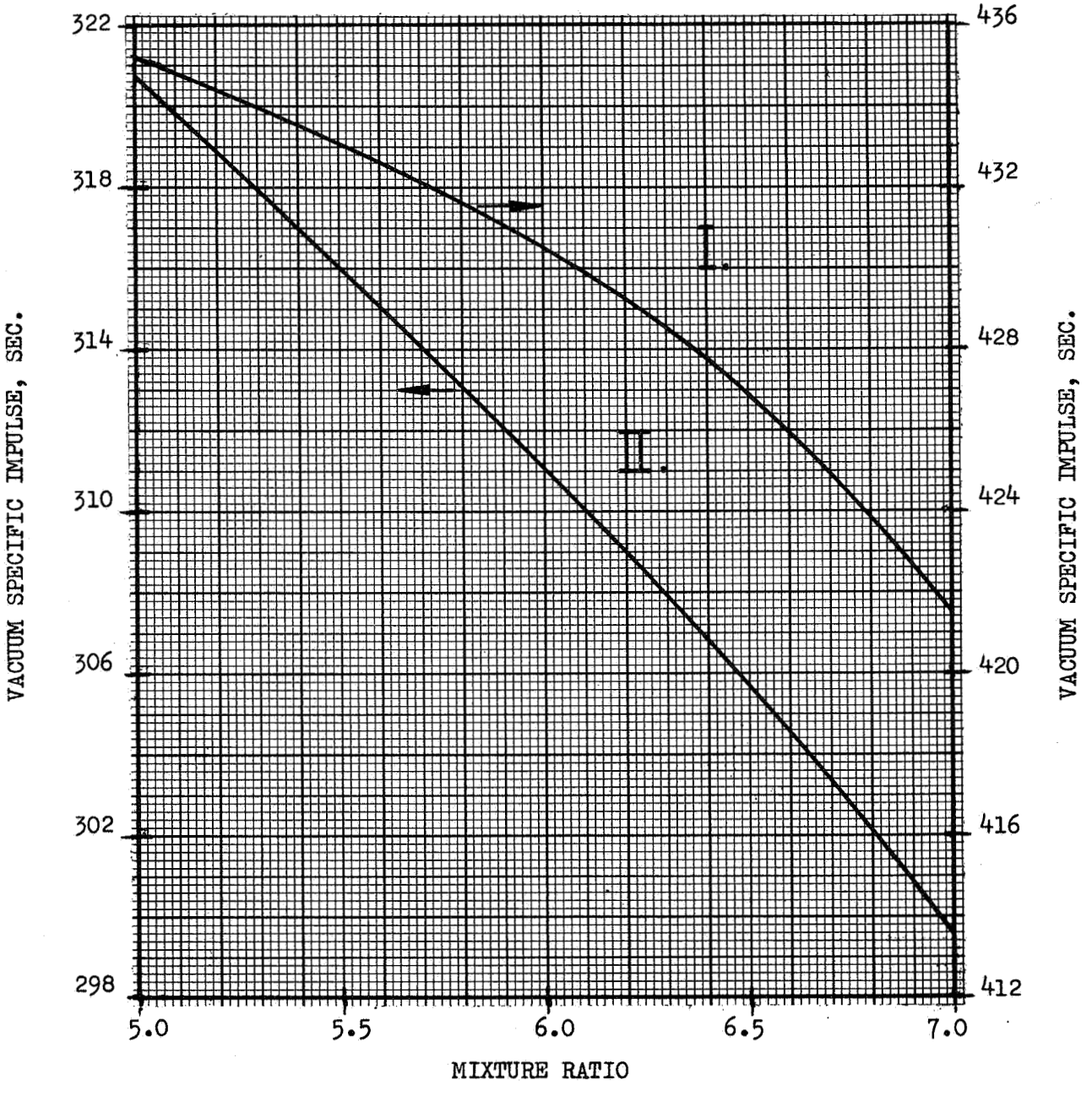


I. REGENERATIVE CHAMBER 3% FILM COOLING,
$A_e/A_t$ = 40.0

II. ABLATIVE CHAMBER 3% FILM COOLING,
$A_e/A_t$ = 2.08

Figure 26. Predicted Measured Vacuum Specific Impulse vs Mixture Ratio (2:1 and 40:1 Nozzles)

The initial liner design was composed of compression-molded billets constructed from high silica fabric impregnated with a modified phenolic high char resin system. It was manufactured "in-house." A ring of WBC-6301 was used as an ablative build-up material behind the liner of the fuel flange and torus assembly. The WBC-6301 is a rubber modified, silica-reinforced phenolic similar to the liner materials used for the Apollo and Transtage ablative chambers. The build-up and liner material are bonded to provide good thermal contact. The reinforcing fiber orientation for the liner material is 35-degrees to the normal direction. This ablative chamber assembly is shown on Figure No. 27 while the dimensions of the ablative components as well as the steel pressure vessel used in this analysis are given on Table II. Also it was assumed in this analysis that no supplemental film cooling is used.

TABLE II

ABLATIVE LINER AND SHELL THICKNESS

| Location | Liner Material | Liner Thickness, in. | Steel Shell Thickness, in. |
|---|---|---|---|
| Injector | WBC-2230 & -6301 | 0.86 | 0.22 |
| Axial Distance 13.31-in. | WBC-2230 | 1.26 | 1.00 |
| Throat | WBC-2230 | 1.75 | 0.90 |

The computations were performed by means of computer program 8059.[4]. This program accounts for convective heat transfer from the propellant gases to the liner surface as well as radiation heat transfer from the gas-side and ambient-side of the chamber wall to the environment. The temperature response of the liner and steel shell is calculated as well as charring and dimensional ablation during the fire and soak periods. A heat blockage effect, which accounts for the diffusion of the ablative liner off-gases into the boundary layer, was accounted for by means of the equation suggested by MacFarland.[5] Thermal properties used for the analysis are the best estimates from the available data and are listed on Table III. These data were obtained from the manufacturer, Western Backing Corporation, as well

(4) Analytical Study to Extend the Capabilities of the Aerojet-General Ablation Digital Computer Program, Aerojet-General Report No. 9140-64-1R, Contract NAS 9-2832, November 1964

(5) MacFarland, B., Joerg, P., and Taft, M., Criteria for Plastic Ablation Materials as Functions of Environmental Parameters: Part 1 - Results of Analytical Studies, ASD-TR-61-439, Part 1, Contract No. AF 33(616)-7401, May 1962

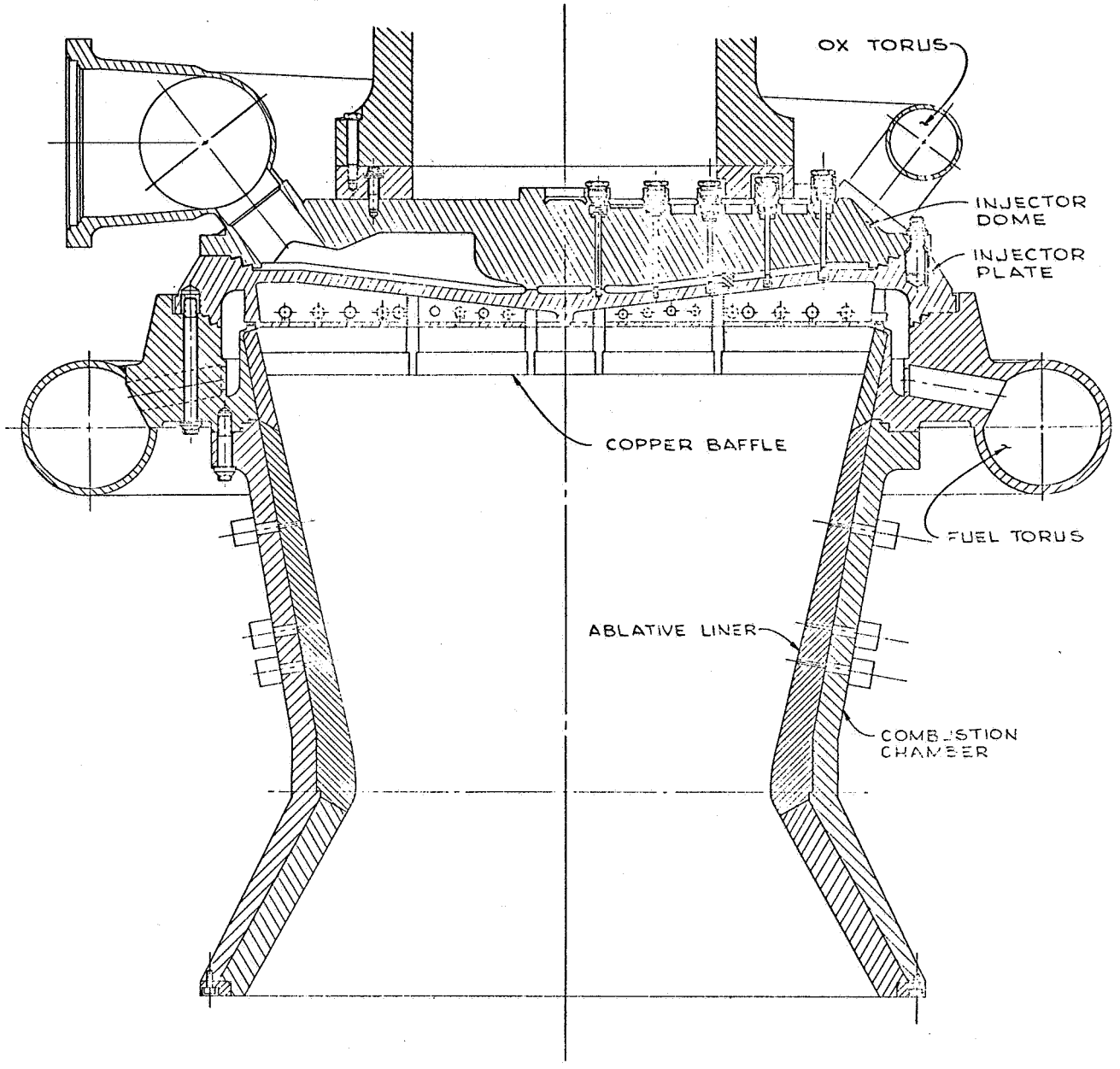


Figure 27. Ablative Chamber Assembly

as thermal analysis personnel at Aerojet-General, Azusa Plant. The gas-side heat transfer coefficient was calculated using the simplified Bartz correlation.(6) The start-up and shutdown transient chamber conditions were obtained from computer program No. 109, runs 8850-004 and 8840-00B, respectively.

TABLE III

M-1 ABLATIVE LINER THERMAL PROPERTIES

| Liner Material | WBC-2230 | WBC-6301 |
|---|---|---|
| Type of material | Silica-reinforced phenolic | Rubber-modified, silica-reinforced phenolic |
| Laminate Properties | | |
| Conductivity, Btu/in.-sec-°R | $6.5 \times 10^{-6}$ | $4.0 \times 10^{-6}$ |
| Specific Heat, Btu/lb-°R | 0.25 | 0.3 |
| Heat of Char, Btu/lb | 374 | 374 |
| Char Temperature, °R | 1460 | 1460 |
| Char Properties | | |
| Conductivity, Btu/in.-sec-°R | $1.3 \times 10^{-5}$ | $1.1 \times 10^{-5}$ |
| Specific Heat, Btu/lb-°R | 0.25 | 0.3 |
| Heat of Ablation, Btu/lb | 2600 | 2600 |
| Ablation Temperature | 4660 | 4660 |

Estimated temperature profiles and surface recession for the ablative liner at the injector (13.31-in. downstream from the injector face) and at the throat are shown on Figures No. 28, No. 29, and No. 30. The temperature profiles shown are at FS-2 and at the end of a 30 sec soak period. The liner char depth for the total firing time is given on Table IV.

TABLE IV

PREDICTED M-1 ABLATIVE LINER CHAR DEPTHS

| Chamber Location | Firing Duration, sec | Char Depth, in. |
|---|---|---|
| Injector | 20* | .387 |
| Axial Distance 13.31-in. | 20 | .447 |
| Throat | 20 | .475 |

*Four 5 sec duration firings including transients

(6) Bartz, D. R., "A Simple Equation for Rapid Estimation of Rocket Nozzle Heat Transfer Coefficients," Jet Propulsion, (1):49:51, 1957

The temperature profiles shown on Figures No. 28, No. 29, and No. 30 along with the char depth predictions of Table IV indicate that the ablative liner will protect the steel chamber walls from excessive temperature for four, 5 sec firings provided that the combustion is stable and there is no severe oxidizer streaking from the injector.

Although this method of analysis was used with good success in predicting the thermal response of the lower pressure, lower temperature Transtage and Apollo ablative liners, wherein little or no dimensional ablation occurred, it required experimental verification for conditions where substantial dimensional ablation was anticipated (see Section IV,C,3 for test results).

b. Contour

Because the M-1 film-cooled chamber was designed as a workhorse to be used for injector and baffle development, it was unnecessary to extend the chamber beyond a 2:1 expansion ratio. This chamber has an internal contour identical to the 14:1 regeneratively-cooled chamber (converging half angle, 10°56').

(1) Ablative Chamber

The ablative-lined combustion chamber was fabricated by modifying a 32.00-in. diameter throat, film-cooled, steel chamber to a 30.00-in. diameter throat with an ablative liner thickness at the throat of 1.500-in. minimum. This 1.500-in. liner thickness at the throat guarantees that a minimum of four, 5 sec firings would be possible using one chamber only. The propellant flow rates were adjusted to reflect the change in throat diameter while maintaining the design chamber plenum pressure at 1000 psia.

Two sets of four pressure pick-ups were added at the aft end of the nozzle to ascertain what portion of the measured thrust could be attributed to the pressure acting upon the ablative liner aft support ring. One set of pressure pick-ups was located in line with an injector baffle while the second set of pressure pick-ups was located between the injector baffles. The difference in pressure readings at similar pick-up points would indicate the baffle influence (see Table VII, Item 36).

(2) Film-Cooled Chamber

A heat transfer study was performed utilizing the design requirements of the gas-side wall temperature (2260°R) and the mean wall temperature (1460°R, or less) for a duration of 5 sec. This study indicated that film cooling would be required in two locations; in the torus and flange assembly as well as in the lower chamber.

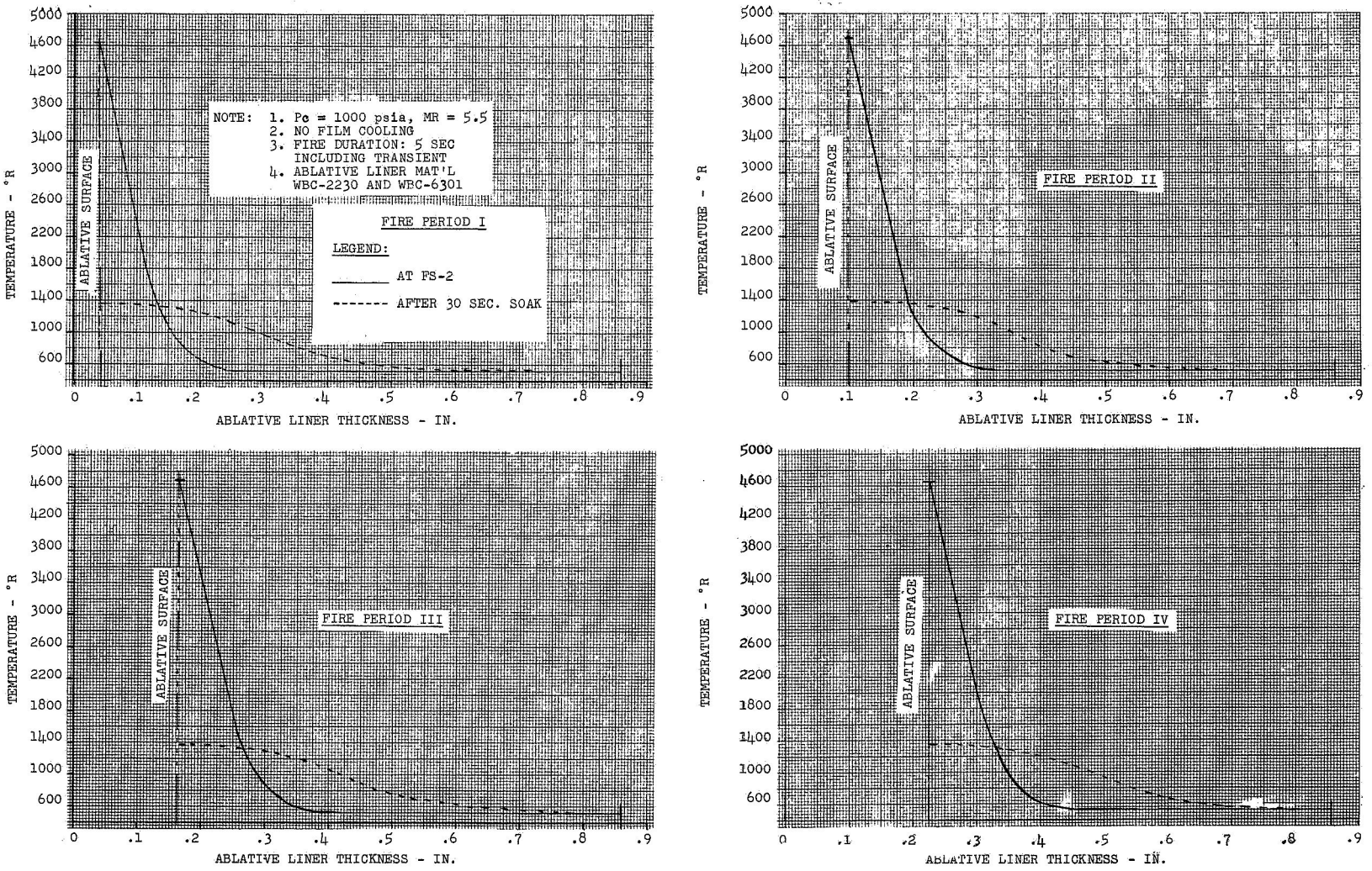


Figure 28. Estimated Temperature Profiles and Surface Recession for the Ablative Liner at Injector Face

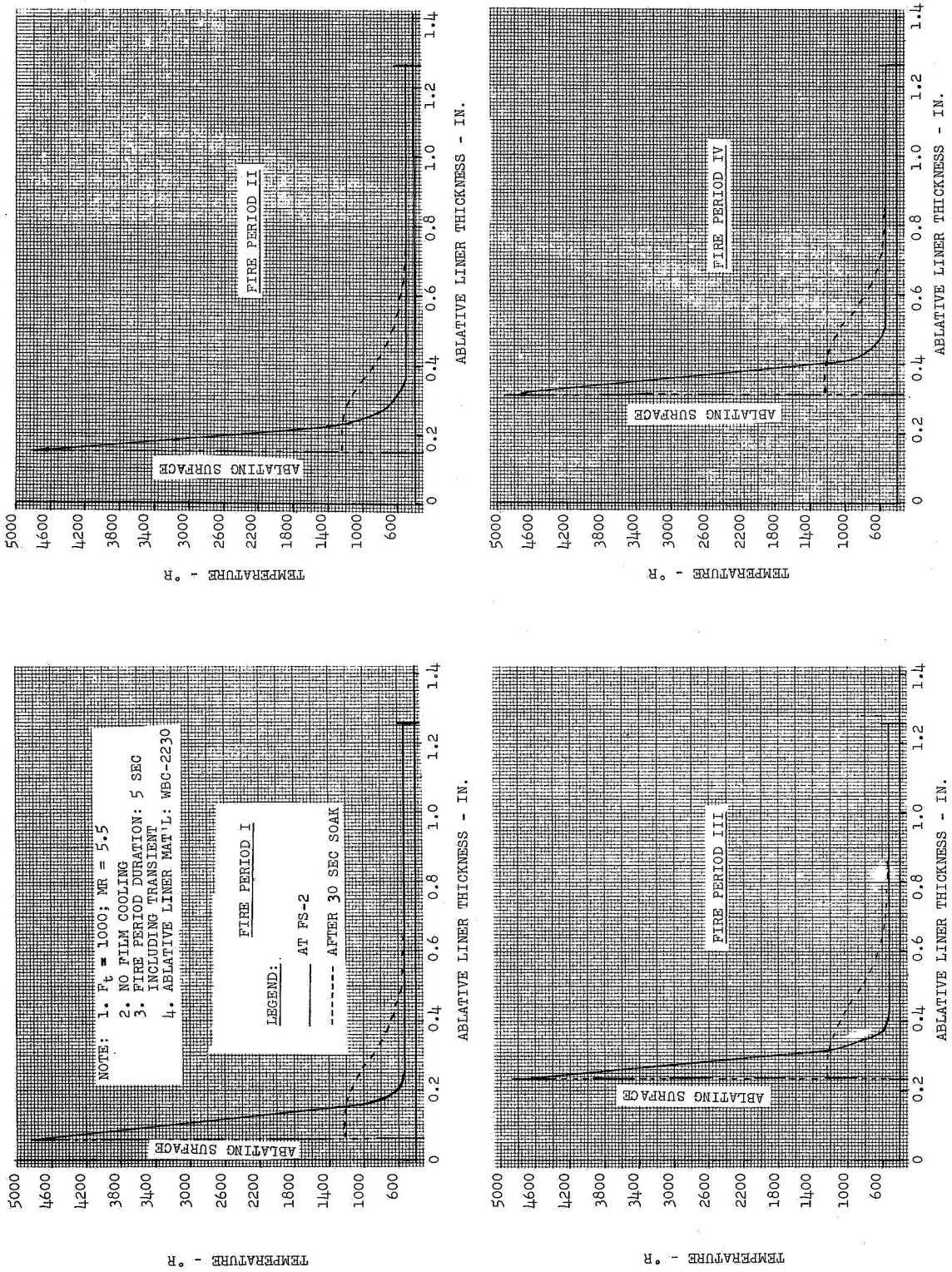


Figure 29. Estimated Temperature Profiles and Surface Recession for the Ablative Liner, 13.31-in. from Injector Face

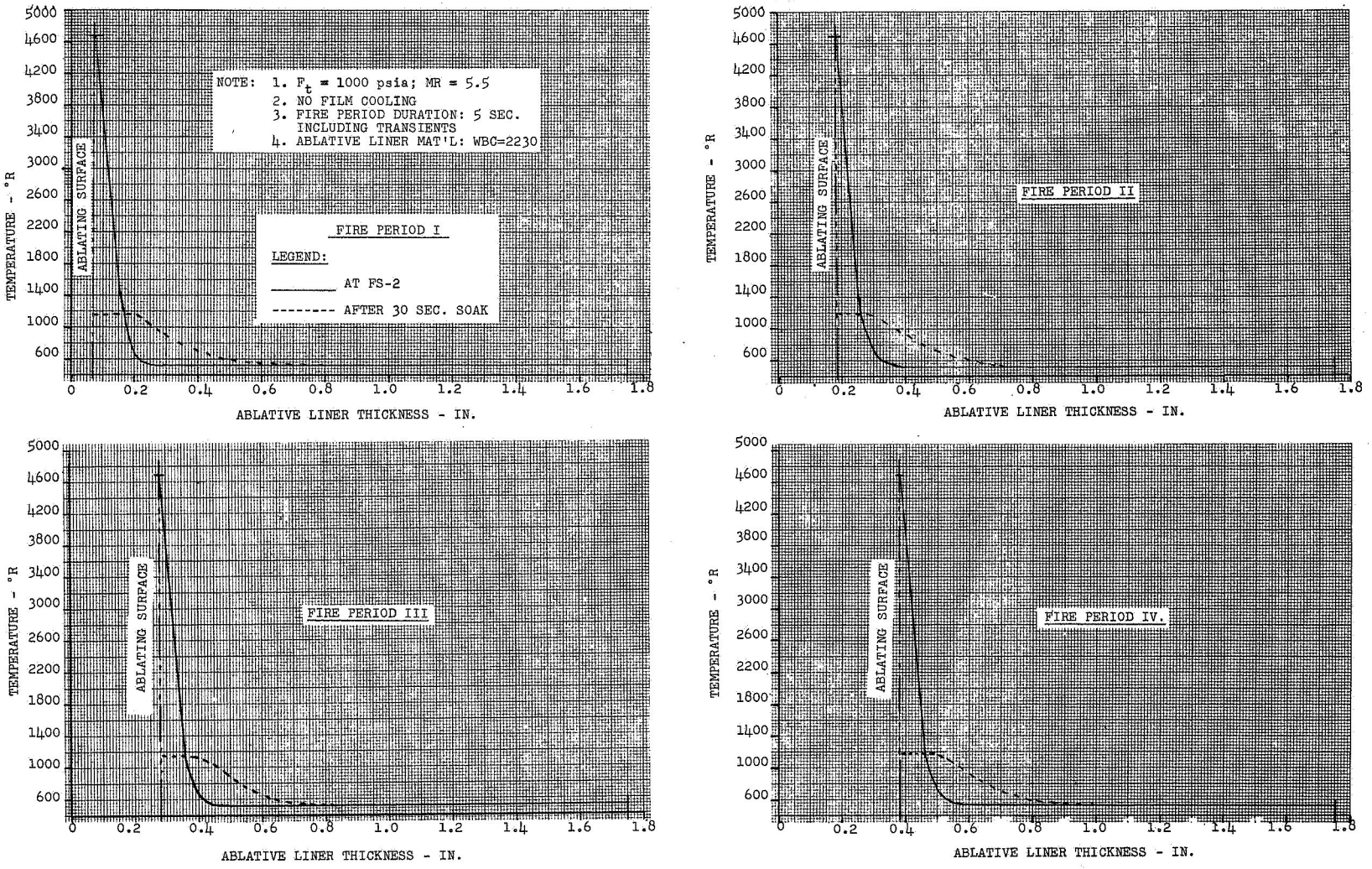


Figure 30. Estimated Temperature Profiles and Surface Recession for the Ablative Liner at Throat

The torus and flange assembly is film-cooled by means of orifices drilled adjacent to the injector/chamber interface. Approximately 6% of the total fuel flow is required.

The lower chamber is cooled by means of 360 small coolant tubes staggered in two rows of 180 each. An alternative method consists of a series of orifices in a coolant ring which is welded to the chamber contour approximately 15-in. upstream of the throat. Approximately 5% of the total fuel flow is required. A small manifold welded to the chamber and fed from the main fuel torus provides the coolant for either method.

## C. COMBUSTION STABILITY

Combustion instability has been a serious problem in the development of all high-thrust, large diameter thrust chambers. The combination of analytical and empirical design methods available at the time that the M-1 thrust chamber design was initiated were not adequate for assurance that the unit would operate stably. This section summarizes the analyses conducted as well as the experimental evidence drawn upon to arrive at intermediate and final designs for the baffles, the injection elements, and the propellant manifolding. A description of the instrumentation used to establish the stability characteristics of the tested designs also is included.

### 1. Baffles

The high frequency combustion stability characteristics of the M-1 thrust chamber were analyzed using the Sensitive Time Lag Theory. The results of this analysis are presented on Figures No. 31 and No. 32. The details of the analysis are presented in Appendix A.

This analysis (see Figure No. 31) showed that the thrust chamber would be sensitive to those tangential modes lying between the third and sixth as well as being sensitive to the first and second radial modes. To preclude these modes from occurring, the baffle pattern shown on Figure No. 33 was selected. The resultant stability and operating zones are shown on Figure No. 32.

Although not completely quantitative, the method of analysis used served to indicate the number as well as the locations of the necessary baffle spokes and hubs. However, this analysis did not provide any indication of the appropriate lengths for these baffle components (see Appendix A). Available data from Aerojet-General's Titan, Gemini, and Apollo programs as well as Rocketdyne's Atlas and F-1 programs were studied. This information indicated that the baffle lengths should be approximately 4-in.

However, the indicated available data were not for a thrust chamber of M-1 size nor for its propellant combination; therefore, a conservative 6-in. length was selected for the initial design. These first

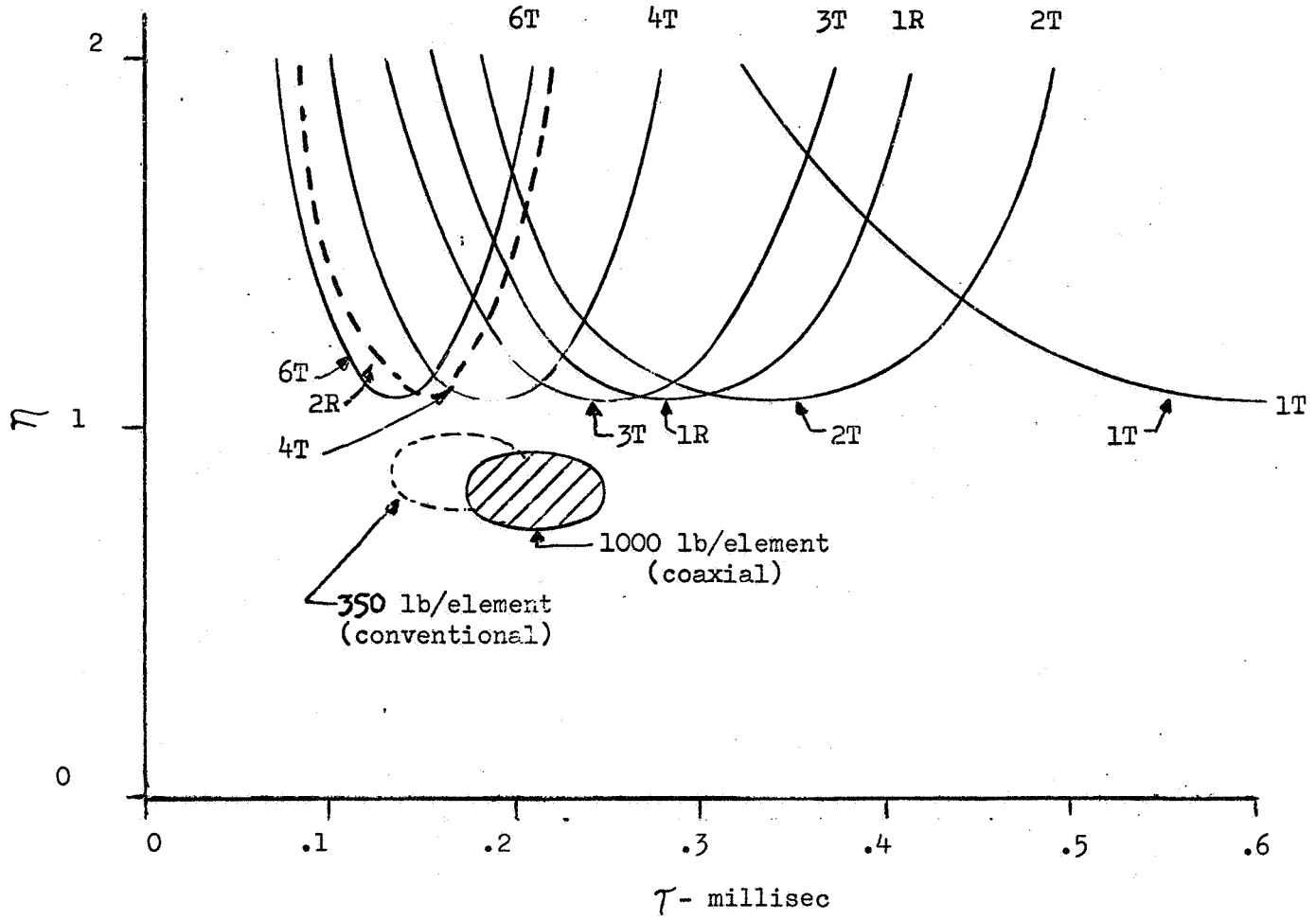


KEY: 1T = first tangential mode
2T = second tangential mode
3T = third tangential mode
4T = fourth tangential mode
6T = sixth tangential mode
1R = first radial mode
2R = second radial mode

Figure 31. M-1 Thrust Chamber Instability Zones Without Baffles

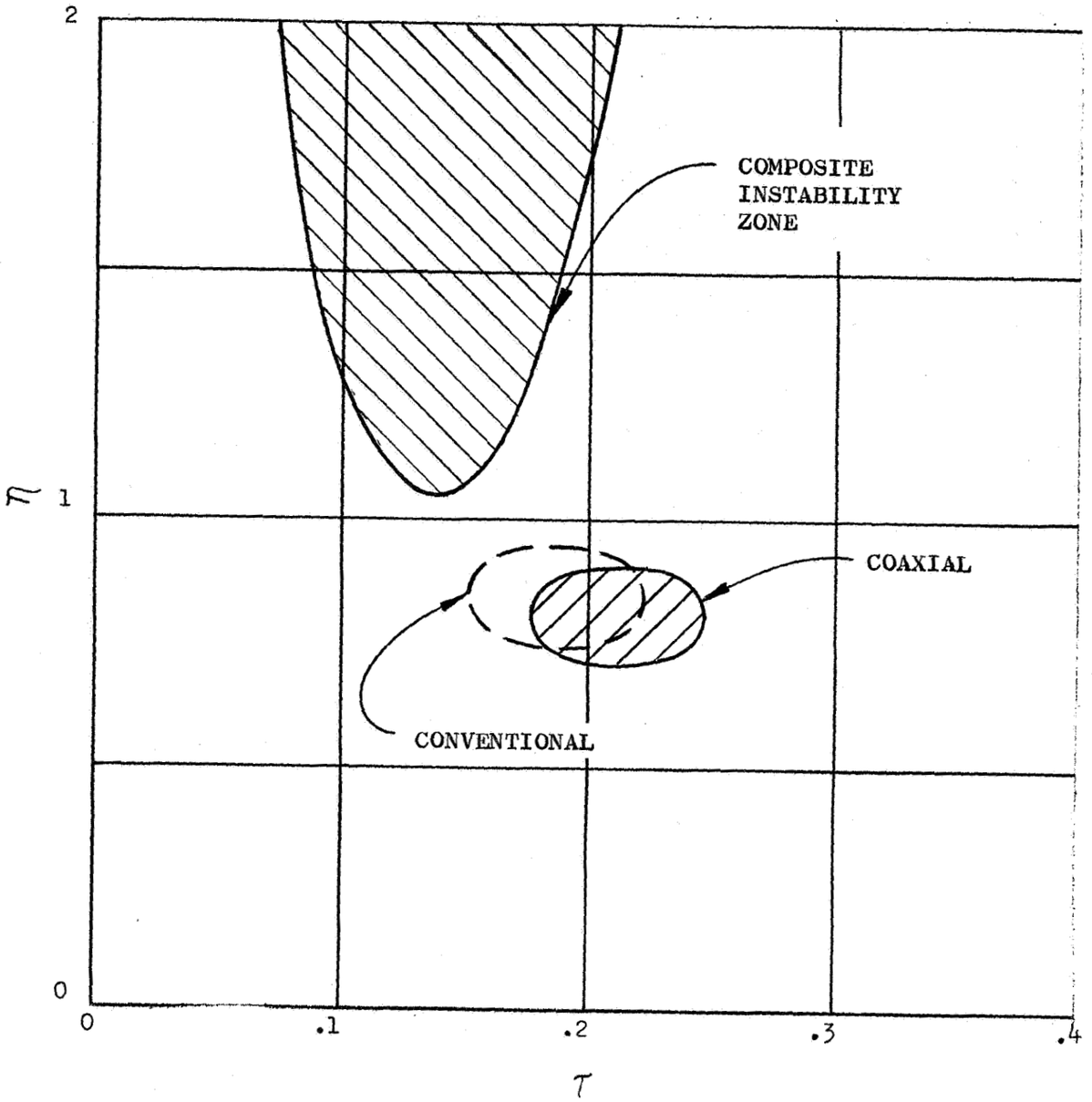


Figure 32. Baffled Chamber Instability Zone

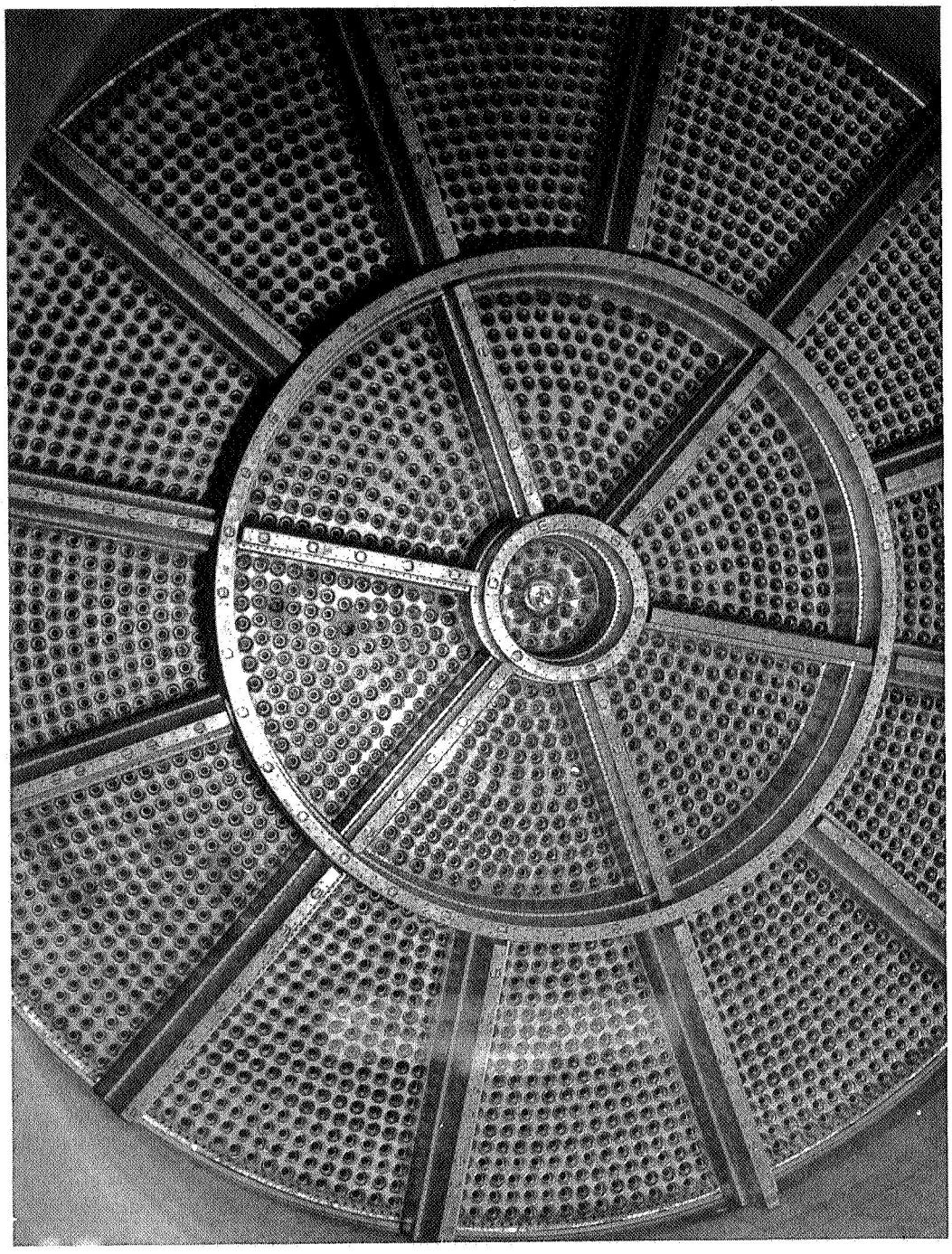

Figure 33. M-1 TCA Coaxial Injector

baffles were solid pieces of stainless steel alloy because this design facilitated fabrication, which permitted early testing of the thrust chamber. The baffles were film-cooled by hydrogen which was injected as a barrier between the combustion gases and the metal.

While the injector was being fabricated, additional data became available concerning cooling problems and acoustical damping[7] at various baffle lengths. This information showed that cooling requirements grew significantly severe as baffle lengths increased over 4-in. In addition, a baffle length of 6-in. did greatly increase acoustical damping when compared to a 4-in. baffle. As a result, it was decided to limit the length of the cooled baffle design to be tested to 3-1/2-in. to 4-in.

2. Element

Data available at the initiation of the M-1 program indicated that larger thrust-per-element units tended to have greater resistance to high frequency combustion instability. Although the 3248 element design would tend to provide higher performance, it appeared that the 1184 element design could give adequate performance with a greater stability margin.

While the initial units were being fabricated, an evaluation of data obtained at the NASA Lewis Research Center as well as J-2 engine data showed that stability margins were increased with coaxial injectors by increasing the ratio of the hydrogen to oxygen velocity ratio. The NASA data indicated that a minimum velocity ratio of 7.0 was required for stability with 421 element, 11-in. diameter, 20,000 lb thrust injectors. However, it was believed that this value should be increased as the flow-per-element became greater. The velocity ratio was increased to a practical maximum of 18.0 for the final M-1 design.

3. Manifold

Data obtained by the NASA Lewis Research Center indicated that division of the injector manifolds into compartments by radial separators improved resistance to instability. Therefore, the M-1 injector incorporated this concept. The radial baffle bases formed the compartments in the fuel manifold as can be seen on Figure No. 11. The oxidizer manifold was divided into twelve compartments by separators as shown on Figure No. 14.

4. Instrumentation

a. Injector

Nine instrumentation ports were provided in the fuel manifold. Three temperature sensing probes, two low-frequency response

(7) M-1 Ambient Acoustic Tests, Aerojet-General Report No. TCER-019, 18 May 1968

pressure transducers measuring magnitude of pressure, and two high-frequency response pressure transducers located 70-degrees apart were utilized. One of the fuel manifold high-frequency response pressure transducers was in line with an oxidizer manifold and a chamber pressure high-frequency response pressure transducer.

Twelve, equally-spaced instrumentation ports were provided in the oxidizer manifold; one port per compartment. Three temperature sensing probes, three low-frequency response pressure transducers (one measuring torus pressure), and two high-frequency response pressure transducers located 30-degrees apart were utilized.

b. Chamber

The chamber was instrumented along its circumference at different axial locations by using high-frequency response pressure transducers. Kistler helium bleed transducers were used in the ablative-lined chamber and water-cooled Photocon transducers were used with the film-cooled stainless chambers. The ablative and stainless chamber instrumentation locations as well as the installation dimensions are shown on Figures No. 34 and No. 35.

## D. STRUCTURAL DESIGN AND FABRICATION

### 1. Structural

#### a. Element Plate and Radial Dome Bolts

##### (1) Method of Analysis

A composite structural analysis of the 2:1 uncooled injector and thrust chamber assembly was performed to determine the structural effects of individual structural components upon the entire structure.

Various assumptions pertaining to loading conditions and geometrical configurations were analyzed to find the most severe loading conditions. These analyses included considerations of a temperature change on the radial dome bolts as well as the absence of a temperature change. Also, the existence of radial shear reactions between injector and the fuel torus flanges was considered as well as the absence of such shear.

A mathematical model was prepared utilizing the 1040 thin shells of revolution computer program and the ring equations. The resulting system of discontinuity equations, which describe the loading and geometry was then solved for loads and deflections by using the AS71U utility package for solution of large simultaneous equations.

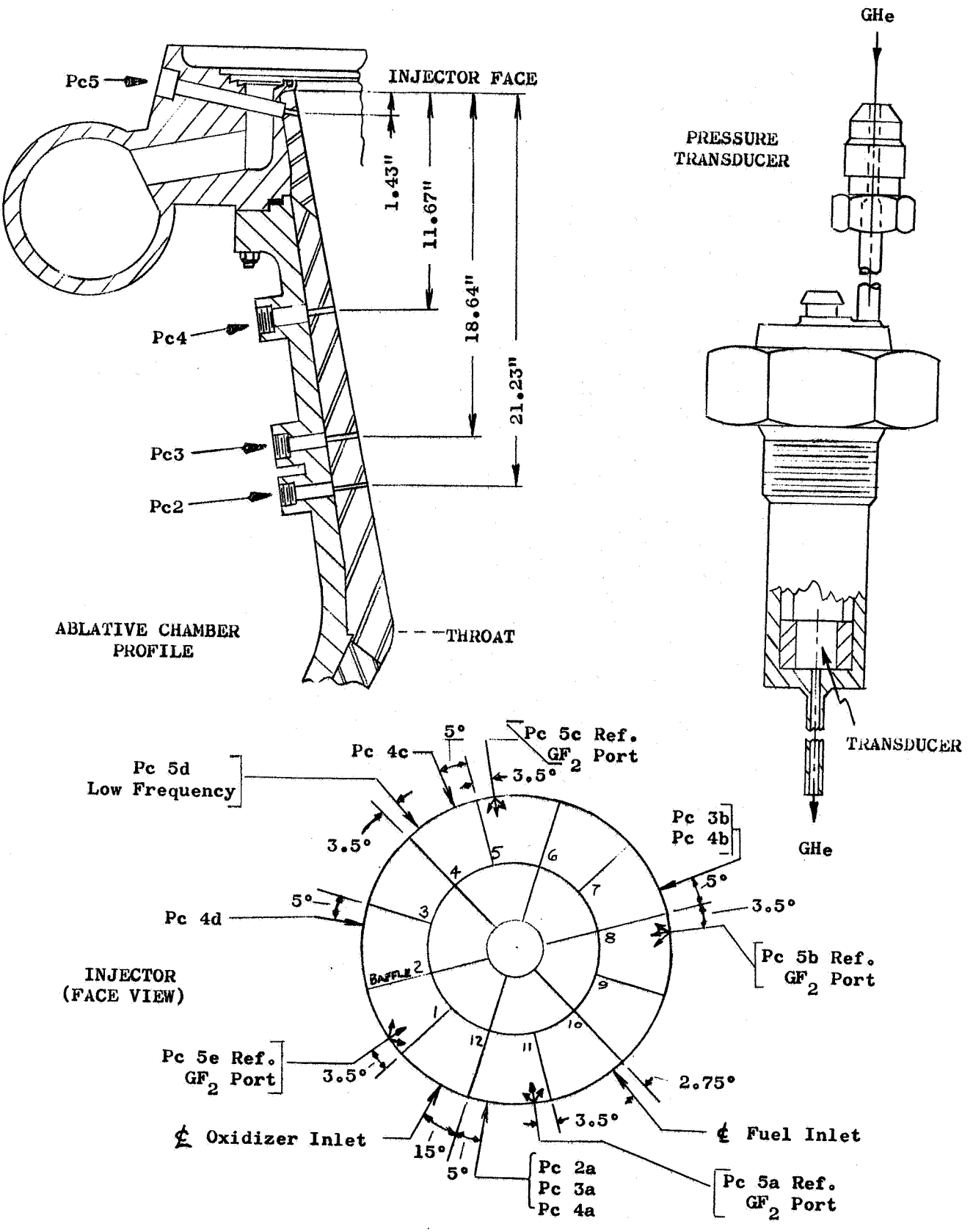


Figure 34. High-Frequency Response Pressure Transducer Instrumentation, Ablative Chamber

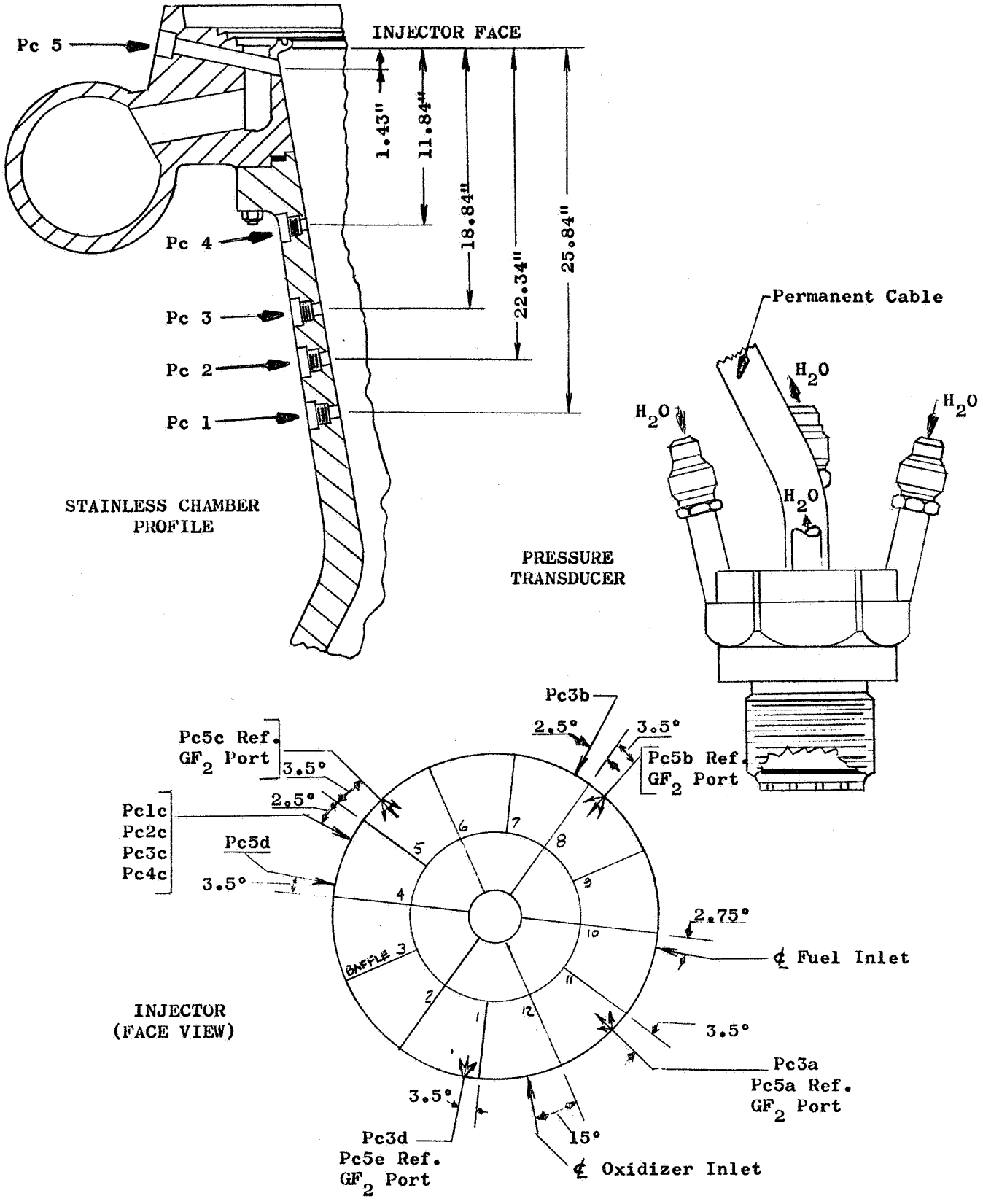


Figure 35. High-Frequency Response Pressure Transducer Instrumentation, Stainless Steel Chamber

(2) Severest Loading Condition

The operating pressures and thrust for this condition are as follows:

P = 1040 psia Chamber

P = 1428 psia Oxygen

P = 1240 psia Fuel

T = 1,057,000 lb Thrust
(Temperatures for 5 sec)

(3) Analysis Summary

Assuming that the radial dome bolts are cold and a radial shear reaction exists between the injector and fuel torus flanges, the maximum values of elastic bending and tension stress on the injector element plate are 72,000 psi and 33,000 psi, respectively, at the junction of the injector plate with the injector flange. Because the maximum stress is caused by bending, it occurs on an outside surface that has been subjected to considerable cooling. Therefore, a margin of safety was calculated based upon the ultimate strength of stainless steel Type 347 at 160°R ($F_{tu}$ = 160,000 psi). Using a bending modulus of 1.3 and a factor of safety of 1.5, the margin of safety was calculated to be 0.15. This calculated margin of safety is conservative because 90% of the injector element plate stress is caused by thermal gradients and 347 stainless steel is an extremely ductile material (e = 50% @ room temperature). It can withstand a great amount of thermal strain. A plastic analysis, preferably in a computerized form, is necessary to determine the state of stress that exists. The current elastic analysis indicates that the element plate is subject to localized stresses which are above the yield point but below the ultimate strength of the material.

The critical set of radial dome bolts are those located at a radius of 16.95-in. The stresses are a maximum when the bolts are assumed to be cold and with a radial shear load between the injector and fuel torus flanges. Maximum stress under these conditions is 153,000 psi plus 11,000 psi as a result of pre-torque. This stress level is for the most current configuration as well as a torque on the injector-to-dome studs of 670 ft-lb.

This analysis is conservative because of the assumptions made. If it is assumed that the bolts are at room temperature instead of 175°R, the stress is decreased from 153,000 psi to 115,000 psi. In reality, only a partial radial shear load exists between the injector and fuel torus flanges. The relative displacement of the two flanges is such that the bolts have to bear against the side of the bolt holes before a radial shear reaction can be developed. Without a radial shear reaction, the bolt stress can be reduced from 153,000 psi to 147,000 psi.

b. Elements

The critical load, as pertains to the elements, occurs in those elements that are adjacent to the baffle bases. It is caused by restrained thermal contraction resulting from a temperature change of 60°R, assuming that the element is fully-cooled before the heavier bases are cooled sufficiently to contract. Tensile tests indicate that the maximum load which can be sustained by the flared end fitting is 900 lb at room temperature. This value has been scaled upward in proportion to the ratio of yield stresses at 140°R and room temperature to a design value of 1300 lb. A 1300 lb load produces a minimum margin of safety to yield in the minimum area, excepting the flare, of 0.77. The stresses in the flared segment will exceed the yield stress, but this is an isolated condition and does not limit the fatigue life of the part from a practical aspect.

The brazed connection at the injector plate end of the element is subject to high tensile stresses because of the restrained radial shrinkage of the plate in relationship to the element. Based upon elastic theory, these stresses are in excess of the material strength; however, they are actually of a lesser value because of post-elastic behavior. Tests have demonstrated that the joint is satisfactory.

c. Rigimesh Support

The combination of a complicated geometry and indefinite overly-redundant support conditions prevent an exact analysis of the stresses in the Rigimesh face plate. The principal load is a restrained thermal contraction that produces high tensile stresses in the plate in all directions. The worst result from this is the possibility that the face plate would become disconnected from the baffle bases. This extreme condition was investigated and it was found that the flared ends of the injector elements provide sufficient support against the differential pressure force across the plate.

d. Torus and Dome

The design loads for the oxidizer torus are an internal pressure of 2130 psi, proof, a uniform temperature change of 60°R, and the dynamic load reactions at the inlet flange. Design proof pressure is 1.2 times the design limit pressure; design ultimate is 1.6 times the limit. The frequency of the dynamic loads is taken as 20 cps and the length of a full-duration firing as 400 sec. The order of magnitude of the critical dynamic loads lies between 100,000 in.-lb and 200,000 in.-lb for moment and 10,000 lb for direct loads. These are limit values; ultimate loads are 1.5 times the limit.

The pressure stresses at the base of the standpipes are calculated using standard models for a fixed-end tube. The stresses at the upper end of the standpipes and around the inlet flange are found by applying stress intensification factors based upon existing literature reporting the results of full-scale tests of pipe intersections.

The temperature (shrinkage of torus) stresses in the standpipes are calculated as for a rigid ring on an elastic foundation of numerous small beam elements. The rigid ring concept is modified at local intersections through the use of a digital computer solution for shells of revolution replacing the standpipes with a pair of large conical segments to estimate the affects of cross-section deformations. The results of this analysis were authenticated by a favorable comparison between predicted deflections and the results of chill tests of a torus-dome assembly.

The reactions in the standpipes resulting from loads applied at the inlet flange are calculated on the same assumptions as the temperature stresses. Existing data[8] is used to calculate the stresses at the inlet flange. This data includes stress intensification factors based upon an extensive series of tests made with piping ties.

All of the above analyses result in stresses calculated upon the basis of elastic theory and which, when totaled, far exceed the yield stress of the material in local areas. However, these calculated elastic stresses can be used to predict the low cycle fatigue life of the oxidizer torus assembly using the method presented in the A.S.M.E. Nuclear Pressure Vessel Code (Article 4) in conjunction with Narkl's data[9]. These analyses result in a predicted minimum fatigue life of one full-duration firing. The critical area is the intersection of the inlet flange and the oxidizer torus.

e. Chamber

Stress analyses were made for both the ablative-lined chamber design and the film-cooled metal chamber. Both chamber designs were found to be structurally adequate for the static test firing planned to be accomplished in Aerojet-General's Test Stand H-8. The major loads on the chamber are those resulting from the internal chamber pressure and those caused by the external support struts. The strut loads are expected to reach a maximum of $\pm$ 50,000 lb per strut during the start transient phase of the firing. They will be considerably less than this during the steady-state portion of the test. A summary of minimum margins of safety for the chamber as well as the other related components investigated, is shown on Table V.

(8) Narkl, A.R.C., "Fatigue Tests for Piping Components," Trans. ASME, 1952
(9) Ibid.

TABLE V

SUMMARY

MINIMUM MARGINS OF SAFETY

| Description | Drawing | Design Condition | Type Stress | M.S. |
|---|---|---|---|---|
| Ablative Chamber w/Reinforcing Rings | 1120379 | Strut Load = ± 50,000; Static Wall Pressure | Membrane & Bending | -0.05 (y)* |
| Forward Ablative Liner | 1120825-19 | Static Wall Pressure | Compression | 0.04 (u)** |
| Film Cooled Chamber | 293837 | Strut Load = ± 50,000 Static Wall Pressure | Membrane & Bending | 0.75 (y) |
| Support Clevis | 286293 | Strut Load = ± 50,000 | Tension | 0.16 (y) |
| Gasket Holder Tip | 1120497 | Temp. Gradient and p = 415 psi | Compression & Bending | -0.46 (u) |
| Gasket Holder Stem | 1120497 | Temp. Gradient and p = 415 psi | Compression & Bending | -0.17 (y) |
| Fuel Torus Inlet | 284890 | Dynamic Loads; Operating Pressure | Membrane & Bending | 0.28 (u) |
| Bolts, Fuel Valve to Torus | 284841 | Dynamic Loads; Operating Pressure | Tension | 1.02 (y) |

* (y) Margin of Safety based on yield strength
** (u) Margin of Safety based on ultimate strength

The ablative-lined chamber design uses two reinforcing rings in the throat area to help react the indicated strut loads. These rings are required to help absorb the imposed loads because of the reduction in chamber wall thickness by machining to permit the assembly of the ablative liner. Positive margins of safety, based upon material yield strength, were exhibited for all loading cases except the situation where the strut loads act in radially opposite directions. However, the analytical methods used were conservative. A more extensive analysis would show these margins to be positive also. For example, each of the following factors would result in lower calculated stresses if they were considered in the analysis: the maximum strut loads superimposed upon the pressure distribution which exists in the start transient phase of firing (distribution not known) instead of the steady-state condition; and the loads as acting for a short duration of time rather than as being static.

In addition to the analysis made for the basic chamber, the other portions of the ablative chamber assembly investigated include the liners, bosses, clevises, and aft retaining ring. All of these items were found to be satisfactory.

The basic structural difference between the film-cooled metal chamber and the ablative design is that the film-cooled version does not have reinforcing rings. Instead, reinforcing pads are utilized to distribute the strut loads over a sufficiently large shell area so that no further chamber reinforcement is required. All positive margins of safety are indicated for this design.

Analysis indicates that yielding will occur in the outer fibers of the gasket holder stem because of the combined effect of differential pressure and a thermal gradient. The extent of this yielding depends primarily upon the amount of radial clearance between the gasket holder tip and the injector rim (radial tolerance ranges from 0-in. to 0.030-in.). Once the tip has deflected sufficiently to contact the injector rim, it will receive support from this surface, thereby reducing further yielding. Any yielding which does occur, even with maximum tolerances, is not expected to impair the proper functioning of the gasket holder.

f. Seals

The M-1 program design goal of component and system seals acceptance is "no leakage allowed." Testing is performed with gas and leakage being determined by visual observation of the bubbles escaping when the part is submerged under water or with soap solution around the joints and pressurized to the leak test pressure for two minutes. A leakage rate of one bubble in two minutes is approximately equivalent to $1 \times 10^{-3}$ cc/sec.

(1) Double Conoseals* and Vent Ports

Metallic Conoseals were selected for the engine design phase to meet the leakage requirement as well as other design objectives for the seals (i.e., vibration load, thermal cycling, and environment requirements).

A double Conoseal is used to increase the reliability as well as to monitor the leakage. This double Conoseal consists of two seals of different diameters. The seal grooves are concentric to each other; therefore the cavity between the seals is readily accessible to the leak monitoring port. In this way, the leakage through the smaller primary seal can be monitored. Two monitoring ports are provided so that the improper seating of the seals during installation can be detected by pressurizing the cavity between the seal. Both ports are necessary for this purpose because an improperly seated seal can block the monitoring port, thereby giving an indication during a leakage test. This problem is minimized with the two ports which are located 180-degrees apart.

(2) Radial Bolt Seals

Bolts are passed through the oxidizer dome and threaded into the plate to add additional structural rigidity to the plate to which the elements are attached. Initial designs required an aluminum crush washer beneath the bolt head to prevent the leakage of oxidizer to the atmosphere. However, these seals proved to be unsatisfactory. The dome was then modified to accept a conical copper gasket beneath the bolt head, but this too, was inadequate. The final design (see Figure No. 36) consisted of enclosing the bolt head inside a boss which was then sealed with a standard Voishan** seal thereby permitting loading of the seal independently of the bolt limitations.

2. Fabrication

a. Oxidizer Post Attachment

The fabrication of integral injector bodies/oxidizer posts utilizing electrochemical (ECM) or electrical discharge machining (EDM) was not attempted because it was not possible to obtain forgings and castings of the size required that did not have blowholes or inclusions. If an inclusion existed in a machined oxidizer post, it could mean that the entire injector would have to be scrapped or as a minimum, it would necessitate that the bad post be replaced using conventional welding or brazing. As a result of this consideration as well as the questionable cost advantage to be gained from integral fabrication, it was decided to fabricate and install the oxidizer posts separately.

*Registered Trademark of the Aeroquip Corp.
**Registered Trademark of Voi-Shan Manufacturing Co.

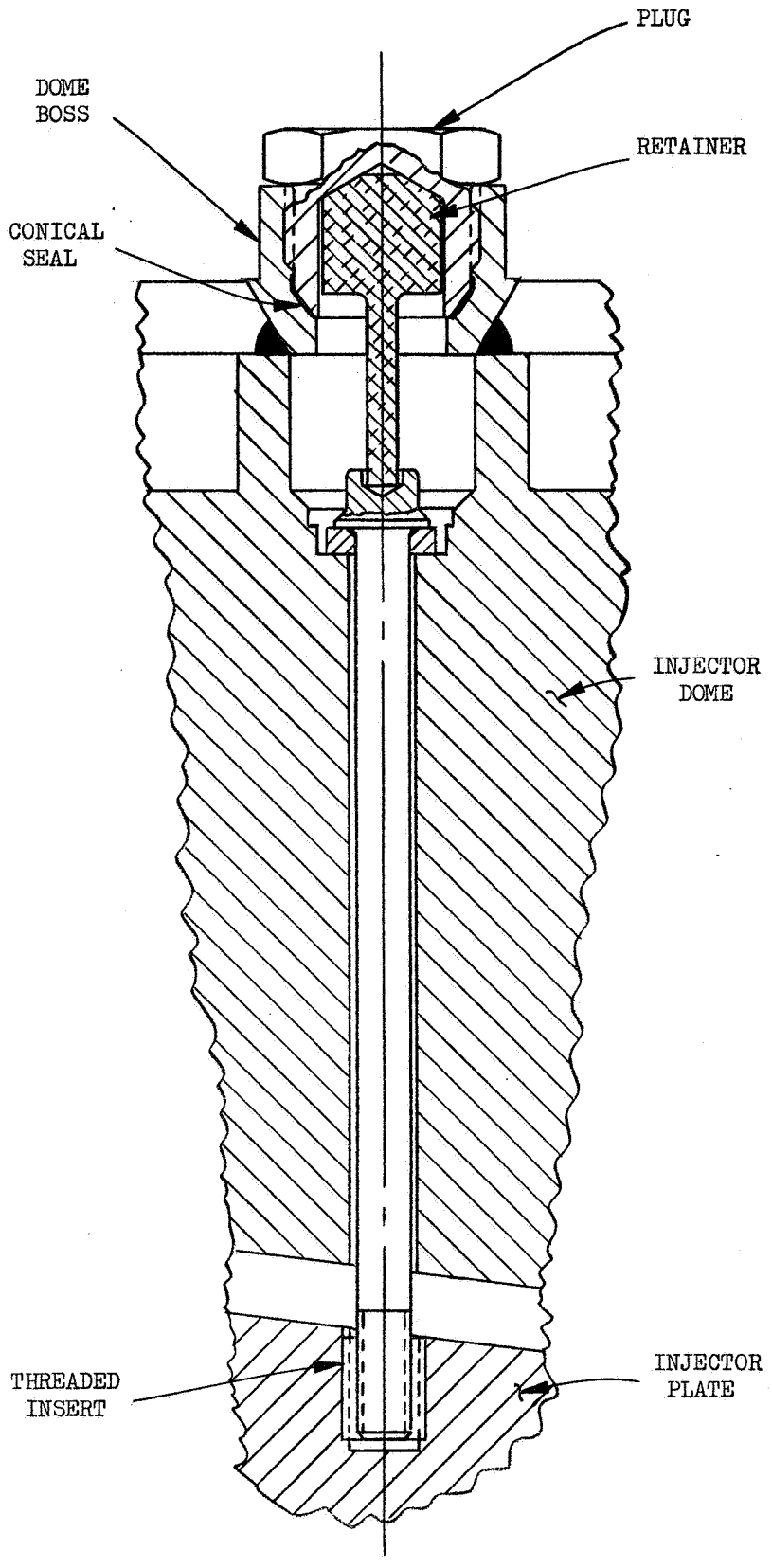


Figure 36. Radial Bolt Seal

(1) Joint Selection

For the initial injectors, the oxidizer injection elements were welded to the element plate on the oxidizer dome side. Cracking and failure of similar welds was experienced during a gas generator test; therefore, a braze joint was added on the fuel manifold side. This was modified in the final design wherein the element was threaded into the plate and sealed by a copper braze. Braze gaps varied from .001-in. to .003-in. Leakage checks after chilling the brazed assembly in a liquid nitrogen bath indicated that the joints were satisfactory.

(2) Brazing Difficulties

Both injectors fabricated with the final element joint design required two braze cycles because subsequent to these furnace cycles, it was discovered that the surfaces to a depth of approximately 0.030-in. had been carburized. A review of fabrication procedures showed that the plate had been mounted on spacers relatively close to a graphite supporting plate. It also was found that the hydrogen for the brazing atmosphere could very easily become stagnated. The graphite plate was encased in stainless alloy and the hydrogen manifolding modified. Treatment of the part for 20 hours at 1900°F in dry hydrogen removed the embrittling effects of the carburization. The process appeared to be a combination of carbon removal and diffusion in the interior of the part.

b. Rigimesh Face Attachment and Flow Tests

The selected baffle arrangement effectively divided the injector into 19 individual compartments, each bounded by baffle bases or the injector periphery. It was decided to machine 19 pieces of Rigimesh to fit individual compartments. Thus Rigimesh would then be welded to the injector periphery or the baffle bases completely around its perimeter. Stress analysis of the resultant structure showed that the calculated deflection of the Rigimesh at the center of each compartment could be undesirable.

Further support of the Rigimesh was needed. Two methods were considered: the addition of supports between the injection elements similarly to that found in the RL-10 injector or the Rigimesh could be supported by means of the injection elements. It was decided to provide Rigimesh support through the elements because the number of parts would be reduced and the flow area available between elements was already limited.

This support could be accomplished by welding the trailing end of the fuel sleeve to the Rigimesh or either upsetting or swedging this end over the Rigimesh. The swedging method was selected as being the most economical. In addition, Rocketdyne had reported successful use of this method for J-2 hardware. Swedging tooling and control procedures were developed to provide a consistent product. While this tooling was being perfected, one injector was fabricated with a welded joint at this location.

During fabrication of the injectors selected for testing, it was noted that holes through the Rigimesh were being elongated during the peripheral welding. Visual observation of the injectors showed that the contact between the swedged element and the Rigimesh was not consistent from element to element or around the circumference of the element. However, the test results indicated that these differences had no significant affect upon the injector function.

Some discoloration of the Rigimesh was noted in the initial injectors fabricated. Although this tendency was substantially reduced by passivating the Rigimesh upon its receipt, a method for checking the Rigimesh flow after the injector was completed seemed desirable. To accomplish this, the cavity between the Rigimesh and the injector plate was pressurized with either air or nitrogen. Then, a small diameter tube, which was connected to a calibrated flowmeter (a Rotameter was used), was pressed against the exposed Rigimesh face. In this way, both local and total Rigimesh flow rates were established.

c. Copper Baffles

Each bolt-on copper baffle was consisted of three pieces as shown on Figure No. 25. These are a thin base plate which is mated to the injector face, an intermediate base containing 0.080-in. diameter convection coolant holes, and a tip containing a combination of convection coolant and film cooling holes.

The initial fabrication sequence consisted of welding the base and base plate together, installing the contained bolts, and welding on the tip. The coolant and bolt holes as well as the feed passages were premachined. Prior to welding, the passages were packed with Fuller's earth. A check of completed units by means of a temperature-sensitive coating subjected to heating and cooling of the baffles by alternately flowing hot and cold water showed some plugging of the 0.080-in. holes. Removal of the base plate permitted the determination that weldment had fallen through to restrict the passages. The restricting metal was removed mechanically. The fabrication process was revised to require installation of the tip and reaming of the passages prior to installation of the base plate.

Although minor rework of weld defects was occasionally required, these sequences permitted successful fabrication of baffles with uniform passages.

d. Ablative Liner

Two fabrication methods were used in the construction of the ablative liners. Ablative liner No. 1 was fabricated using compression molded billets manufactured "in-house." These billets were of controlled fiber orientation and individual rings were cut from them. Later, these

rings were bonded to form a rough combustion chamber liner. The rough liner assembly was then contour-machined on the inside diameter and match-machined on the outside diameter to provide a line-to-line fit with the steel combustion chamber shell (see Figures No. 37, No. 38, and No. 39). This is a similar construction method to that used for the successfully-fired Titan IIA subscale chambers.

The construction method used for liners No. 2 and No. 3 consisted of tape-wrapping the net to the surface of a mandrel having the same contour as the chamber. Then, the liner underwent hydroclave curing. These liners were manufactured by Haveg Industries, Inc. of Santa Fe Springs, California. After curing, the liners were contour-machined at the throat and match-machined on the outside diameter. In this way, a line-to-line fit with the steel chamber liner was provided (see Figures No. 38, No. 39 and No. 40). This fabrication method is used for many ablative-lined liquid and solid rocket engine chambers.

A comparison between the two fabrication techniques used shows that the net tape-wrapping offers greater advantages. There is minimum material waste, a single curing cycle completes the part, more rapid fabrication is possible, and there are substantially reduced tooling costs. This method is recommended for future ablative liner fabrication.

The tape-wrapped chamber liner design and the compression molded chamber liner design use a different liner interface angle at the torus-chamber joint, the forward chamber liner, and the aft chamber liner which is immediately aft of the throat. These angle differences result from the fiber orientation angles being different at these locations. An attempt was made to make these angles similar and the liners interchangeable; however, the tape-wrap angles required adjustment to prevent shifting of the fibers when the tape-wrapped nozzle liner assembly was cured.

e. Chamber

The chamber is comprised of two major components; the upper portion contains the torus and flange assembly while the lower portion is the lower chamber. Initially, the purpose of these two separate components was to allow fabrication of the torus and flange assembly from stainless steel while the lower chamber would be made from mild steel to reduce costs. However, the design selected consisted of both components being made from 347 stainless steel.

The upper portion has a 62-in. diameter torus of constant cross-section made from 8-in. diameter schedule 80, CRES 347 stainless steel pipe which is rolled, but on a bias, and welded to the flange. The flange has a 5-in. deep annular cavity with a width of 1.20-in. on an average diameter of 43.8-in. This cavity is connected to the torus by 36, 2-in. diameter fuel passages, which have a 1.50-in. diameter orifice to simulate the regeneratively-cooled combustion chamber pressure drop.

NOTES:

1. INTERPRET DRAWING PER STANDARDS PRESCRIBED IN MIL-D-70327.
2. SURFACE ROUGHNESS TO BE 125 UNLESS OTHERWISE NOTED.
3. CLASSIFICATION OF CHARACTERISTICS PER MIL-W-9411 DENOTED BY (16)(CRITICAL),(15)(MAJOR) AND NO SYMBOL MINOR.
4. WIPE SURFACE CLEAN WITH "MEK" USING A CLEAN LINT FREE CLOTH.
5. PRESERVE AND PACKAGE PER FUSELAGE COMPONENT REQUIREMENTS OF MSFC DWG NO. 10419900.
6. TEMPORARY MARK PER ASD5215 WITH 1120825 AND APPLICABLE DASH NO.
7. MACHINE DETAIL PARTS FROM THE BILLETS AS INDICATED.
8. FOR DETAILS, ALL INSIDE DIAMETERS ARE TO BE CONCENTRIC TO EACH OTHER WITHIN .010 TIR AND ALL OUTSIDE DIAMETERS WITHIN .03 TIR.
9. METHOD OF ASSEMBLING LINERS:
   - A. WIPE MATING SURFACES OF DETAILS CLEAN PER GEN NOTE 4.
   - B. PRIME MATING SURFACES WITH PHENOLIC RESIN.
   - C. LAY-UP FOUR PLYS OF ASBESTOS PHENOLIC FELT CUT FROM YARD GOODS AT EACH JOINT.
   - D. JOIN DETAILS, INSTALL ALLIGNMENT RINGS AND HOLD UNDER ONE PSI MINIMUM PRESSURE.
   - E. REMOVE ANY ASBESTOS PHENOLIC FELT PROJECTING INTO ONE INCH WIDE GROOVES.
   - G. PRIME GROOVE SURFACE WITH PHENOLIC RESIN.
   - H. WRAP ONE INCH WIDE GROOVES WITH ONE INCH WIDE ASBESTOS PHENOLIC TAPE .20 ABOVE SURFACE. DEBULK AS TAPE IS APPLIED WITH HEAT AND ROLLER.
   - I. INSTRUMENT WITH THERMOCOUPLES PER COGNIZANT ENGINEER.
   - J. OVER WRAP TAPED AREAS WITH A MINIMUM OF FIVE LAYERS OF MYLAR TAPE.
   - K. APPLY VACUUM BAG AND BLEEDER AS REQUIRED OVER ENTIRE ASSY.
   - L. CURE FOR ONE HOUR MINIMUM AT 300±10°F AND 28±2 IN. MERCURY UNDER 20,000 LB MINIMUM LOAD.
10. ON ASSEMBLY ALL INSIDE DIAMETERS ARE TO BE CONCENTRIC TO EACH OTHER WITHIN .020 TIR.
11. DO NOT REMOVE SHARP EDGES.
12. THIS SURFACE TO BE MACHINED ON NEXT ASSEMBLY.
13. REMOVED
14. IT IS PERMISSIBLE TO USE CERROBEND TO SUPPORT DETAILS DURING FABRICATION. THE USE OF ANY OTHER MEDIA MUST BE APPROVED BY ENGINEERING. DO NOT USE WATER TO REMOVE CERROBEND.

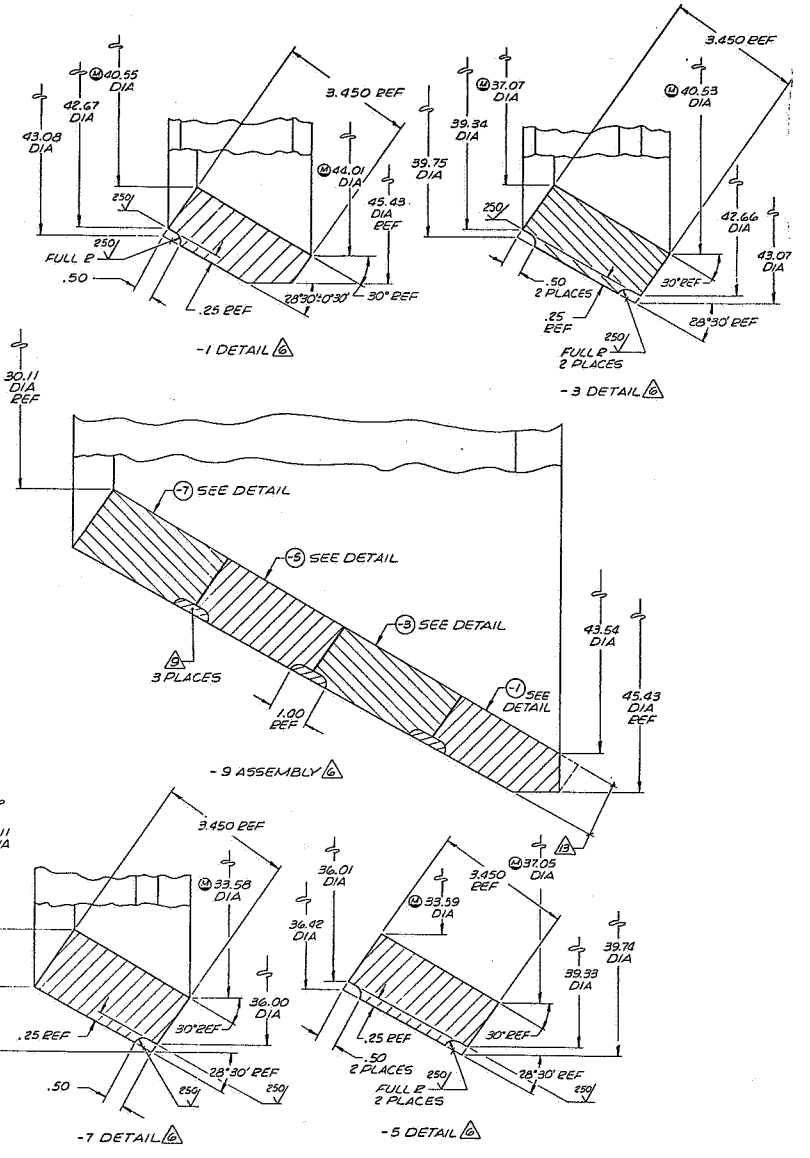


Figure 37. Combustion Chamber Ablative Liner

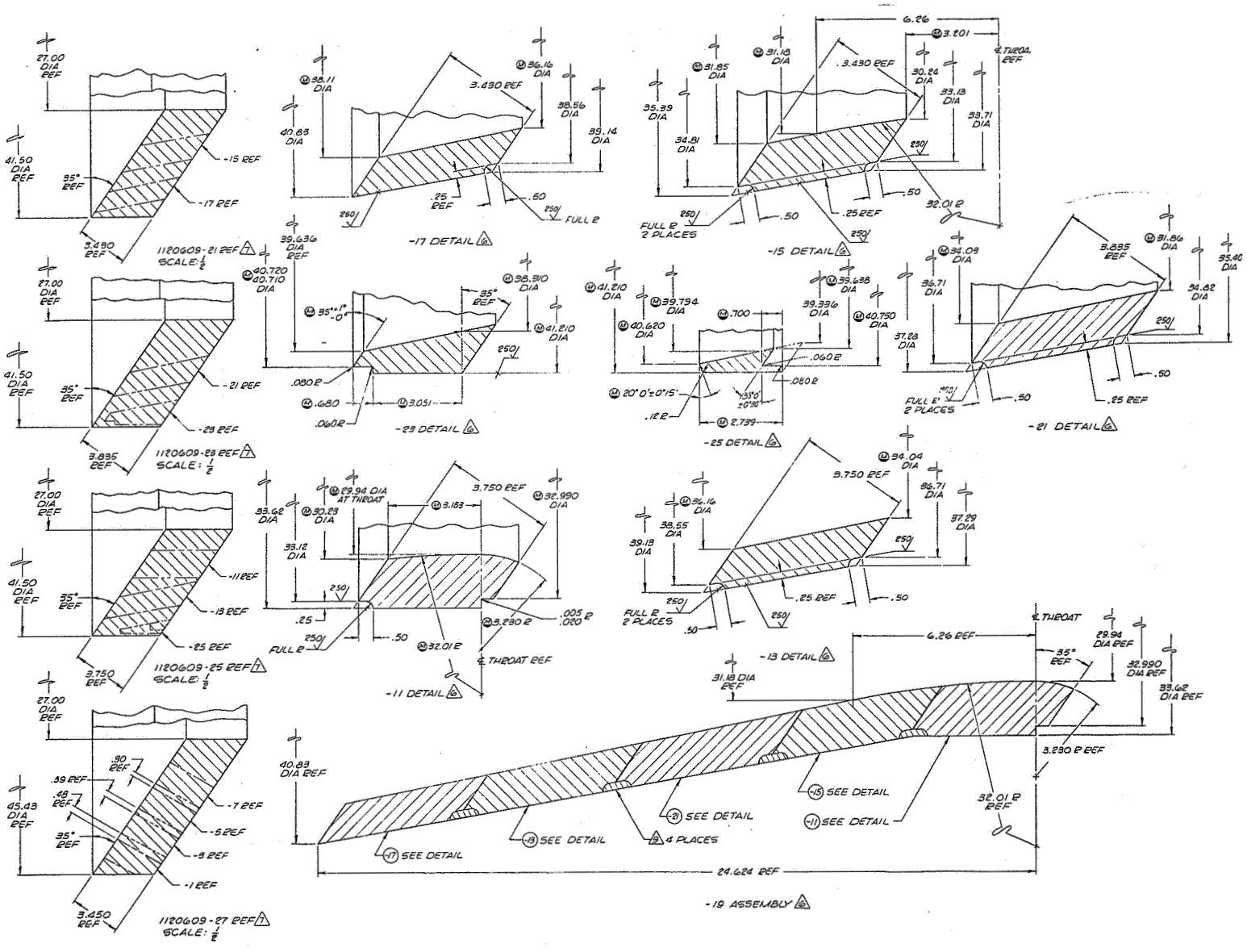


Figure 37. Combustion Chamber Ablative Liner

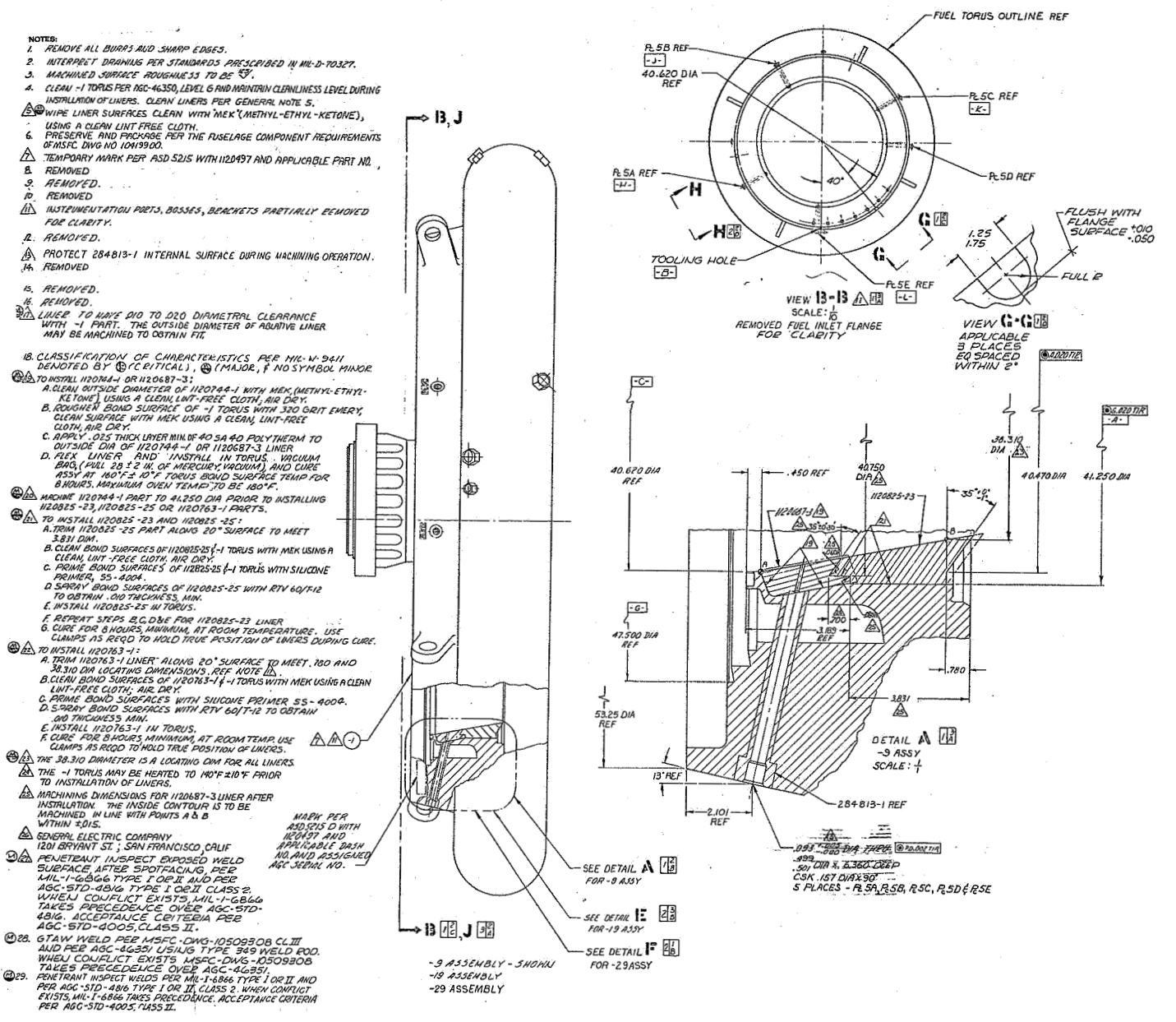


Figure 38. Thrust Chamber Assembly Torus

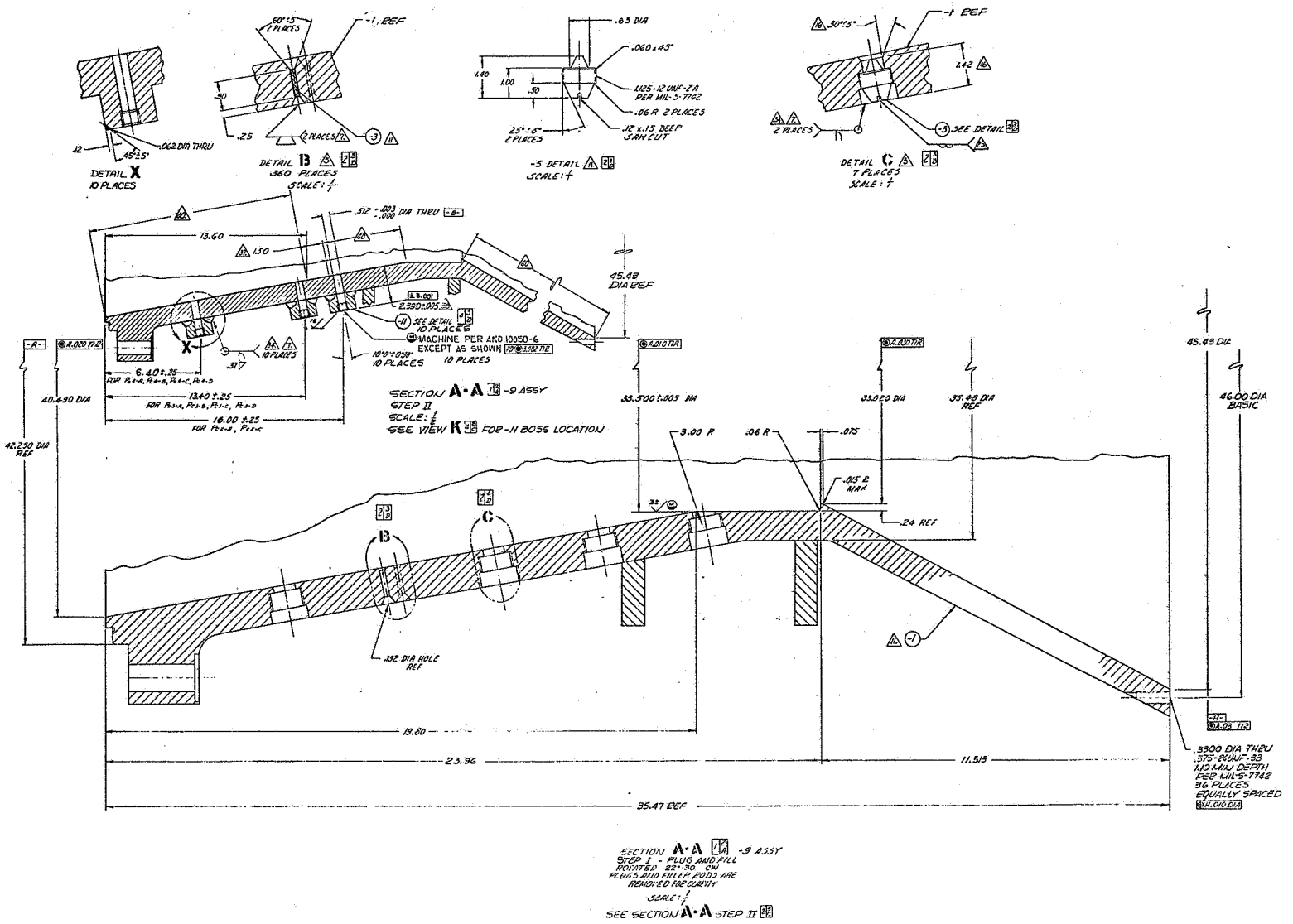


Figure 39. Ablative Combustion Chamber (Shell)
(Sheet 1)

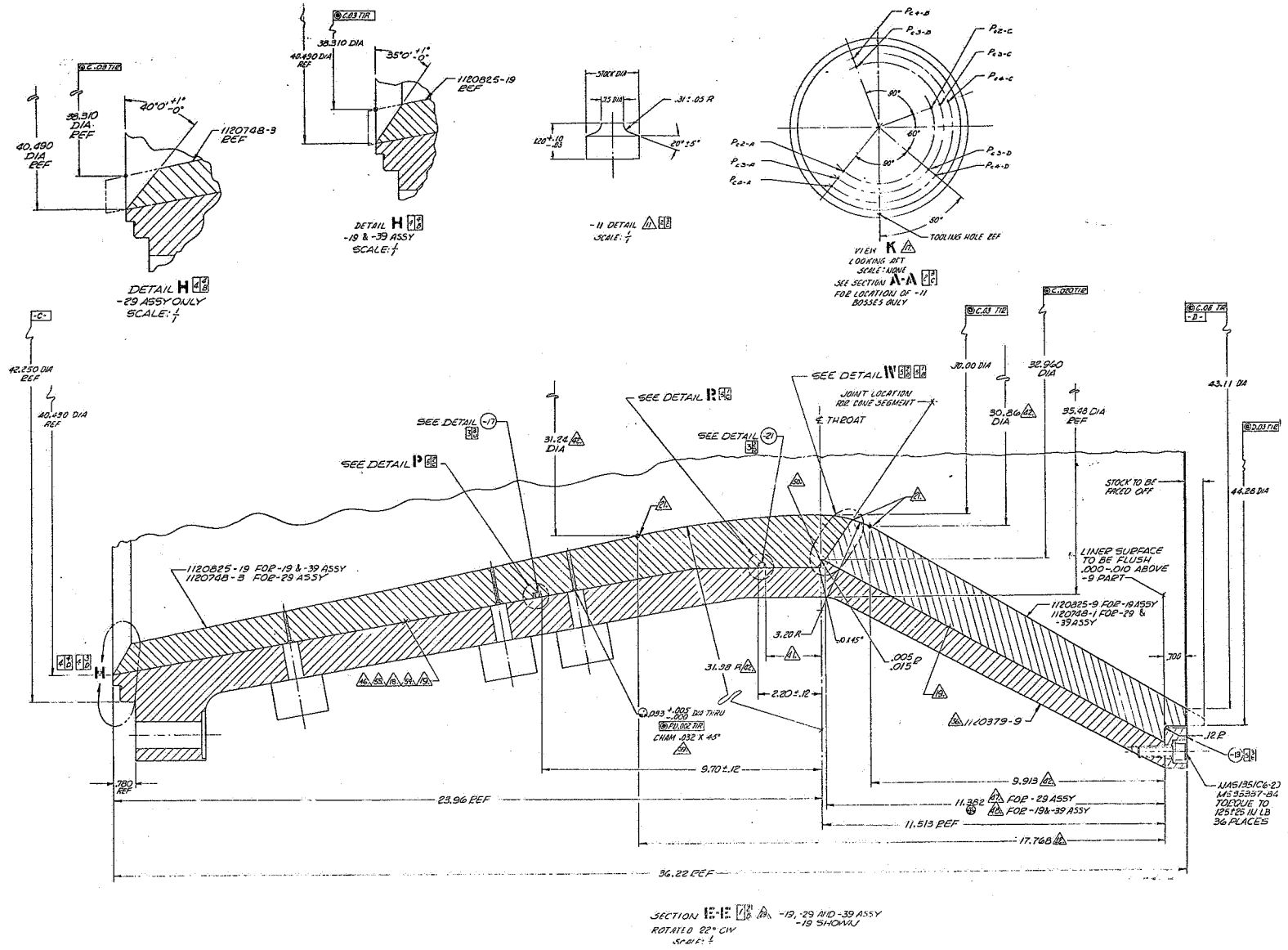


Figure 39. Ablative Combustion Chamber (Shell and Liner Assembly) (Sheet 2)

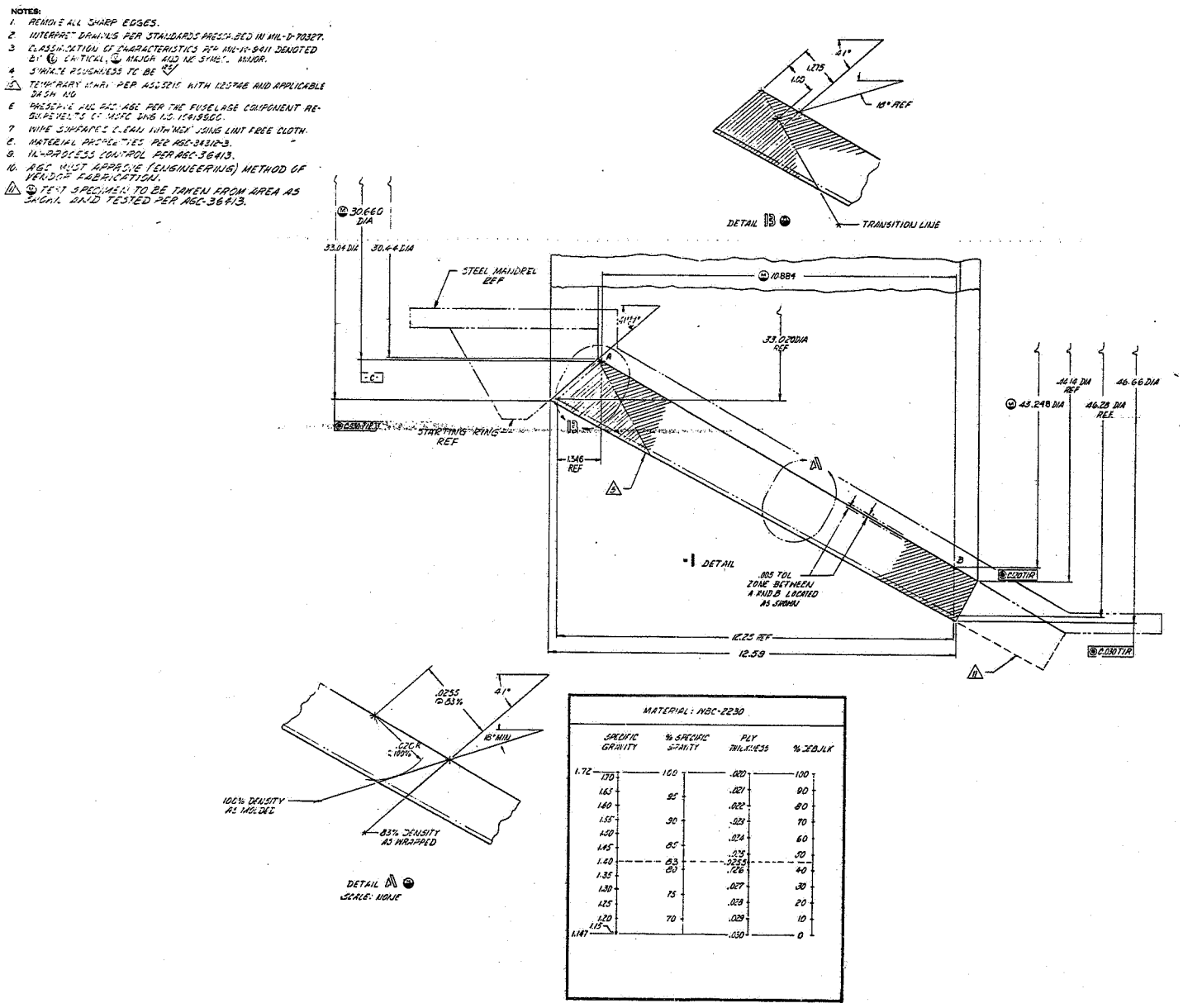


Figure 40. Combustion Chamber Ablative Liner

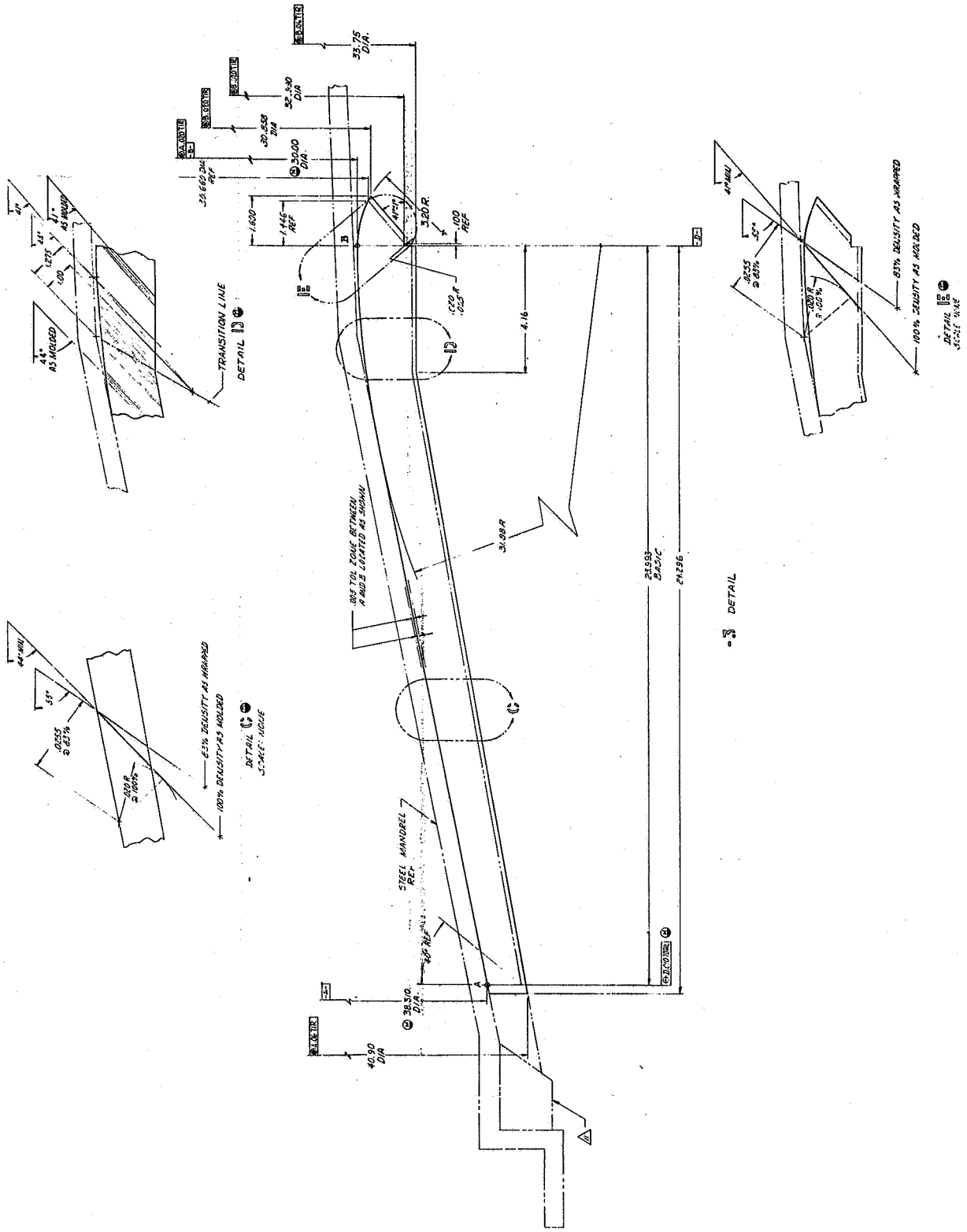


Figure 40. Combustion Chamber Ablative Liner

The lower portion is fabricated from three pieces of rolled and welded 347 stainless steel plate and one flange forging. The three cones as well as the flange are welded and contoured on the internal surface face only.

The ablative-lined combustion chambers (P/N 1120379-19 and -29) consist of an ablative liner, a steel outer shell, and an ablative liner aft support ring. The ablative liner is sealed to the steel outer shell with an ablative silicone rubber RTV-60, and has a joint angled 55-degrees with respect to the chamber centerline. This joint also is sealed with RTV-60. An O-ring was placed at the throat and at the center of the convergent portion of the shell between the ablative liner and the steel shell to close off any possible hot gas flow passage in the event a crack in the ablative liner should occur.

The steel outer shell for the ablative liner (P/N 1120379-9) was made from a film-cooled combustion chamber. This chamber was modified by plugging existing instrumentation ports, machining the inside diameter to accept an ablative liner, and adding gimbaling reaction blocks as well as throat reinforcing rings to provide greater structural rigidity to the chamber. In addition, bosses were added so that the required Kistler instrumentation could be installed.

Some difficulty was encountered when the chamber was machined internally. The lack of concentricity of the convergent portion of the chamber with the chamber flange resulted in a non-uniform wall thickness circumferentially.

A structural analysis of the modified combustion chamber was made. The non-uniformities were considered and the results showed that the modified chamber would withstand the 1500 psi proof load. These results were later verified when the modified chamber successfully passed proof, leakage, and flow tests using water.

The ablative liner aft support ring, which is bolted to the nozzle end of the chamber, assures that the seal and bond between the nozzle portion of the ablative liner and the steel shell is maintained during handling. The ablative liner is also protected from damage by the ring because it projects 0.050-in. beyond the ablative liner in the axial direction.

## IV. TEST RESULTS

### A. PERFORMANCE

#### 1. Injector Comparison

##### a. Baffle Film Cooling

Injector S/N 020 was used in thrust chamber assembly tests No. 1.2-05-EHM-006 through -010 as well as 1.2-07-EHM-001 through -004. Injector S/N 012 was used for the remaining tests, No. 1.2-07-EHM-005 through -025. In tests No. 1.2-07-EHM-017 through -025, the film-cooled combustion chamber was used in place of the ablative chamber.

It became evident during the initial testing with S/N 020 injector that the outer baffle legs were experiencing a greater amount of erosion (see Section IV,C) than were the inner baffle legs. This was particularly true of outer baffles No. 8 and No. 11. After test No. 1.2-05-EHM-008, these baffles were replaced by new ones which had the same coolant flow rate per unit area as did the individual inner baffle legs. This resulted in a 7% film coolant flow rate increase for the outer baffle leg.

The flow rate of all twelve of the S/N 012 injector outer baffles was increased 7% and the outer 2 in. of each baffle had a flow rate increase of 15%.

##### b. Element Flow Characteristics

Each oxidizer post (oxidizer portion of the element) for S/N 020 injector was water-flow tested prior to installation because of manufacturing irregularities, which resulted in deviations from the specifications. This testing was for the purpose of verifying that each post provided an acceptable spray pattern and a pressure drop of 150 $\pm$ 10 psi. However, this individual flow testing was not done for the S/N 012 injector elements because there were no deviations from the manufacturing specifications.

##### c. Chamber Wall Streaking

Tests with the ablative-lined chamber indicated that S/N 020 injector possessed streaking characteristics (see Section IV,C) while S/N 012 provided an even propellant distribution. This latter characteristic resulted in uniform erosion of the liner.

#### 2. Instrumentation Error Estimate

The primary calculated performance characteristics (specific impulse, characteristic exhaust velocity, and mixture ratio) involve direct measurement of thrust, propellant weight flows, chamber face pressure, and chamber throat area. The expected error for these calculated performance

parameters are listed on Table VI along with the estimated errors for the directly measured parameters. The estimate of measurement accuracy is obtained by combining expected calibration and dynamic errors by root square summation.

3. Steady-State Performance

The primary objective of tests No. 1.2-05-EHM-006 through -010, 1.2-07-EHM-001 through -011, and 1.2-07-EHM-014 through -016 was to determine performance, both with and without baffles, at varying mixture ratios. In addition, tests No. 1.2-07-EHM-006 through -010 as well as tests No. 1.2-07-EHM-015 and -016 were combined performance and stability tests, which also permitted the stability limits to be ascertained. Table VII is a listing of all significant parameters for all full chamber pressure performance tests. Sample calculations (using data from test No. 1.2-05-EHM-006) of characteristic exhaust velocity ($\eta c^*$) and vacuum specific impulse efficiency ($\eta I_{sp}$) are presented as Appendix B.

4. Performance During Temperature Decrease

The objective of test No. 1.2-07-EHM-006 was to determine injector performance and then to check stability by decreasing the fuel temperature to its absolute minimum. Maximum test duration was approximately 11.0 sec (based upon previous test data) because of the gaseous hydrogen pressurant limitations. Therefore, a fuel injector temperature decrease rate of 40°/sec was selected.

Table VIII presents the presents the $\eta I_{sp}$ at 10-degree intervals for this test as well as tests No. 1.2-07-EHM-007 through -009, -015, and -016. Instability, which is defined as oscillations in chamber pressure monitored at the $P_c3A$ and/or $P_c4C$ locations that are in excess of 100 psi peak-to-peak amplitude at 600 cps (minimum) for a duration of 0.030 sec (minimum), occurred during all of these tests at approximately 75°R to 82°R fuel injection temperature. Hardware inspection following most of these tests revealed that baffles had been loosened apparently as the result of the instabilities. There had been no apparent loosening of baffles during stable tests.

In test No. 1.2-07-EHM-007, the objective was to ascertain whether mixture ratio had any affect upon the fuel injection temperature at which spontaneous acoustic instability occurred.

TABLE VI

INSTRUMENT ERROR ESTIMATES

| MEASUREMENTS: | Error |
|---|---|
| Temperature: | |
| Thermocouple | |
| CC (-425°F to +100°F) | ±9.9°F |
| CA (-425°F to +100°F) | ±7.3°F |
| RTT | |
| -200°F to -300°F | ±0.44°F |
| -300°F to -435°F | ±0.50°F |
| +75°F to -435°F | ±1.77°F |
| -400°F to -435°F | ±0.24°F |
| -200°F to -435°F | ±0.85°F |
| Pressure: | |
| 2-Channel Average | ±0.30% |
| Single Channel | ±0.42% |
| PERFORMANCE: | |
| Derived Parameters: | |
| $I_{sp}$ | +0.96%<br>-0.97% |
| c* | +0.92%<br>-0.91% |
| Mixture Ratio | +1.39%<br>-1.72% |
| Thrust | ±0.5% |
| Total Weight Flow | +0.83%<br>-0.82% |
| Measured Parameters: | |
| Thrust, Sea Level | ±0.5% |
| Thrust, Chamber Pressure | ±0.42% |
| Oxidizer Flow Rate | ±0.95% |
| Fuel Liquid Flow Rate | +1.63%<br>-1.02% |
| Fuel Gaseous Flow Rate | ±3.0% |
| Fuel Total Flow Rate | +1.43%<br>-1.01% |

NOTES: A plus (+) sign means that the measured value is higher than the actual value by the amount of error indicated.
A minus (-) sign means that the measured value is lower than the actual value by the amount of error indicated.

TABLE VII
STEADY-STATE PERFORMANCE

| | | | | | | | | | | | | | | | | | | | |
|---|---|---|---|---|---|---|---|---|---|---|---|---|---|---|---|---|---|---|---|
| 1. Injector S/N | 020 → | | | | | | | | 012 → | | | | | | | ** → | ** → | ** → | ** → |
| 2. Test Series | 1.2-05-EHM → | | | | 1.2-07-EHM → | | | | | | | | | | | | | | |
| 3. Test Number | 006 | 008 | 009 | 010 | 001 | 002 | 003 | 004B | 005 | 006 | 007 | 008 | 009 | 010 | 011 | 014 | 014 | 015 | 016 |
| 4. Test Date | 7-20-66 | 7-28-66 | 8-4-66 | 8-4-66 | 8-23-66 | 8-23-66 | 8-25-66 | 8-26-66 | 9-30-66 | 10-19-66 | 11-17-66 | 11-21-66 | 11-23-66 | 11-30-66 | 1-11-67 | 1-25-67 | 1-25-67 | 1-31-67 | 3-17-67 |
| 5. Test Duration, sec | 6.56 | 7.63 | 7.49 | 7.01 | 7.48 | 7.49 | 10.04 | 7.60 | 8.71 | 10.25 | 9.36 | 10.87 | 10.92 | 15.07 | 8.51 | 12.04 | 12.04 | 13.97 | 13.60 |
| 6. Data Summary Period - sec | 6.0-6.6 | 6.7-7.6 | 6.5-7.5 | 6.7-7.1 | 6.8-7.6 | 7.1-7.6 | 8.4-10.0 | 6.6-7.6 | 6.4-7.2 | 6.6-7.4 | 6.8-7.5 | 6.9-7.7 | 6.4-7.1 | 14-15 | 6.5-8.5 | 7.0-8.0 | 11.0-12.0 | 7.0-8.0 | 7.4-8.4 |
| 7. $A_t$ (pre-test)-in.$^2$ | 704.04 | 705.56 | 706.67 | 706.86 | 710.44 | 709.03 | 711.96 | 715.27 | 717.50 | 723.74 | 706.90 | 705.56 | 707.40 | 707.99 | 707.99 | 704.917 | 704.917 | 709.177 | 706.970 |
| 8. $A_t$ (post-test)-in.$^2$ | 705.99 | 706.67 | 706.86 | 710.44 | 709.03 | 711.96 | 715.27 | 717.50 | 723.74 | 729.40 | 705.36 | 707.40 | 707.39 | 707.99 | 708.46 | 709.171 | 709.171 | 710.392 | 703.652 |
| 9. $A_t$ (data summary period)-in$^2$ | 705.74 | 706.56 | 706.85 | 710.31 | 709.14 | 711.74 | 714.82 | 717.17 | 721.24 | 726.37 | 706.11 | 706.38 | 707.61 | 707.99 | 708.34 | 708.64 | 708.91 | 710.24 | 704.03 |
| 10. PfJ - psia | 1274 | 1266 | 1283 | 1269 | 1250 | 1252 | 1254 | 1234 | 1240 | 1288 | 1192 | 1241 | 1215 | 1206 | 1266 | 1211 | 1247 | 1243 | 1187 |
| 11. PoJ - psia | 1432 | 1406 | 1418 | 1415 | 1308 | 1410 | 1408 | 1444 | 1433 | 1483 | 1280 | 1470 | 1357 | 1457 | 1465 | 1395 | 1396 | 1391 | 1250 |
| 12. Pc5D - psia | 1106 | 1100 | 1107 | 1098 | 1042 | 1079 | 1055 | 1078 | 1065 | 1108 | 1033* | 1118* | 1081* | 1122* | 1127* | 1084* | 1080* | 1084* | 1018* |
| 13. Pc4D - psia | - | - | - | - | - | - | - | - | - | - | 857 | 927 | 897 | 923 | 934 | 899 | 897 | 899 | 847 |
| 14. TfJ - °R | 154.3 | 133.4 | 132.5 | 135.9 | 139.0 | 143.2 | 139.6 | 139.7 | 127.2 | 128.2 | 130.1 | 129.1 | 136.3 | 97.8 | 136.3 | 143.8 | 166.9 | 158.9 | 142.6 |
| 15. $T_o$J - °R | 175.1 | 176.0 | 173.4 | 178.9 | 174.1 | 175.9 | 173.2 | 171.4 | 173.9 | 176.6 | 173.3 | 173.0 | 173.2 | 172.0 | 174.0 | 171.3 | 171.0 | 173.2 | 175.3 |
| 16. $\Delta$ Pf (injector) - psi | 168 | 166 | 176 | 171 | 208 | 173 | 199 | 156 | 175 | 180 | 159* | 123* | 134* | 84* | 139* | 127* | 167* | 159* | 169* |
| 17. $\rho$f (injector)-lb/ft$^3$ | 1.56 | 1.84 | 1.88 | 1.80 | 1.73 | 1.66 | 1.73 | 1.71 | 1.91 | 1.93 | 1.78 | 1.87 | 1.72 | 2.70 | 1.79 | 1.53 | 1.43 | 1.50 | 1.60 |
| 18. $\rho$f*$\Delta$Pf - lbm-lbf/in$^2$-ft$^3$ | 262.1 | 305.4 | 330.9 | 307.8 | 359.8 | 287.2 | 344.3 | 266.8 | 334.3 | 347.4 | 283.0* | 230.0* | 230.5* | 226.8* | 248.8* | 194.3* | 238.8* | 238.5* | 270.4* |
| 19. $\Delta$Po (injector) - psi | 326 | 306 | 311 | 317 | 266 | 331 | 353 | 366 | 368 | 375 | 247* | 352* | 276* | 335* | 338* | 311* | 316* | 307* | 232* |
| 20. $\rho$o (injector) lb/ft$^3$ | 70.32 | 70.08 | 70.57 | 69.58 | 70.33 | 70.14 | 70.58 | 70.95 | 70.51 | 70.08 | 70.39 | 70.70 | 70.51 | 70.70 | 70.50 | 70.9 | 70.9 | 70.6 | 70.0 |
| 21. $\rho$o*$\Delta$Po - lbm-lbf/in$^2$-ft$^3$ | 22924 | 21444 | 21947 | 22057 | 18708 | 23216 | 24915 | 25968 | 25948 | 26280 | 17386* | 24886* | 19461* | 23685* | 23829* | 22050* | 22404* | 21674* | 16240* |
| 22. Contraction Ratio | 1.714 | 1.711 | 1.711 | 1.703 | 1.705 | 1.699 | 1.692 | 1.686 | 1.677 | 1.665 | 1.713 | 1.712 | 1.709 | 1.708 | 1.707 | 1.707 | 1.706 | 1.703 | 1.718 |
| 23. Pc5D/P plenum | 1.0662 | 1.0683 | 1.0685 | 1.0691 | 1.0671 | 1.0688 | 1.0698 | 1.0709 | 1.0731 | 1.0741 | 1.0681 | 1.0695 | 1.0679 | 1.0769 | 1.0680 | 1.0674 | 1.0654 | 1.0657 | 1.0663 |
| 24. P plenum - psia | 1037 | 1030 | 1036 | 1027 | 976 | 1010 | 986 | 1007 | 992 | 1032 | 967 | 1046 | 1013 | 1042 | 1055 | 1016 | 1014 | 1017 | 955 |
| 25. $\dot{w}_f$ $H_2$ - lb/sec | 361.5 | 418.5 | 437.5 | 410.8 | 444.3 | 384.6 | 398.4 | 365.9 | 427.1 | 441.0 | 455.2 | 400.4 | 424.9 | 439.6 | 427.2 | 370.9 | 349.2 | 366.7 | 424.5 |
| 26. $\dot{w}_g$ $H_2$ - lb/sec | 91.0 | 75.9 | 79.6 | 80.5 | 92.4 | 81.6 | 86.2 | 79.5 | 72.4 | 78.8 | 87.6 | 79.0 | 89.2 | 44.2 | 87.6 | 91.8 | 119.5 | 109.9 | 98.9 |

* Pc5D injector face pressure calculated from Pc4D; therefore, plenum pressure is based upon this calculation.

** Without baffles

TABLE VII (CONT.)

| | Injector S/N | 020 | | | | | | | | 012 | | | | | | ** | ** | ** | ** | ** |
|---|---|---|---|---|---|---|---|---|---|---|---|---|---|---|---|---|---|---|---|---|
| | Test Series | 1.2-05-EHM | | | | 1.2-07-EHM | | | | | | | | | | | | | | |
| | Test Number | 006 | 008 | 009 | 010 | 001 | 002 | 003 | 004B | 005 | 006 | 007 | 008 | 009 | 010 | 011 | 014 | 014 | 015 | 016 |
| 27. | $W_f$ - lb/sec | 452.5 | 494.4 | 517.1 | 491.3 | 536.7 | 466.2 | 484.6 | 445.4 | 499.5 | 519.8 | 542.8 | 479.4 | 514.1 | 503.8 | 514.8 | 462.7 | 468.7 | 474.2 | 523.4 |
| 28. | $W_o$ - lb/sec | 2767 | 2610 | 2615 | 2624 | 2346 | 2666 | 2606 | 2770 | 2673 | 2729 | 2269 | 2714 | 2476 | 2718 | 2628 | 2632 | 2600 | 2582 | 2265 |
| 29. | M.R. | 6.12 | 5.28 | 5.06 | 5.34 | 4.37 | 5.72 | 5.38 | 6.22 | 5.35 | 5.25 | 4.18 | 5.66 | 4.81 | 5.39 | 5.20 | 5.69 | 5.55 | 5.44 | 4.33 |
| 30. | C* (measured)- ft/sec | 7315 | 7542 | 7522 | 7534 | 7725 | 7384 | 7337 | 7226 | 7255 | 7423 | 7813 | 7444 | 7711 | 7368 | 7530 | 7488 | 7539 | 7596 | 7774 |
| 31. | $N_2$ Diluent - % | 1.43 | 0.27 | 0 | 0 | 0.29 | 0.29 | 0.30 | 0.30 | 2.40 | 1.00 | 0.02 | 3.00 | 3.00 | 0.96 | 3.86 | 1.98 | 1.98 | 1.67 | 0.60 |
| 32. | $h\ I_{SP}$ | 1.0037 | 1.0039 | 1.0042 | 1.0039 | 1.0055 | 1.0037 | 1.0041 | 1.0032 | 1.0036 | 1.0037 | 1.0053 | 1.0033 | 1.0047 | 1.0022 | 1.0041 | 1.0037 | 1.0046 | 1.0046 | 1.0057 |
| 33. | C* (theo - $h,N_2$) - ft/sec | 7544 | 7749 | 7800 | 7741 | 7893 | 7652 | 7729 | 7528 | 7702 | 7744 | 7939 | 7628 | 7789 | 7711 | 7705 | 7636 | 7670 | 7699 | 7911 |
| 34. | $\eta$ C* (from Pc) -% | 96.9 | 97.4 | 96.5 | 97.4 | 97.9 | 96.5 | 95.0 | 96.0 | 94.2 | 95.9 | 98.4 | 97.6 | 99.0 | 95.6 | 97.7 | 98.1 | 98.3 | 98.7 | 98.3 |
| 35. | $\eta$ C* (from nozzle losses)-% | 96.2 | 96.9 | 96.7 | 97.0 | 97.2 | 96.5 | 96.8 | 96.3 | 96.5 | 96.8 | 97.0 | 96.4 | 97.1 | 96.0 | 96.9 | 96.0 | 96.3 | 96.7 | 97.2 |
| 36. | $F_{S.L.}$ (corrected)-lb | 964186 | 960541 | 972975 | 964812 | 911303 | 952269 | 951202 | 959481 | 965572 | 998925 | 887523 | 966305 | 930526 | 978743 | 981337 | 930155 | 931855 | 936885 | 880748 |
| 37. | $F_{VAC}$ - lb | 985814 | 982079 | 994603 | 986440 | 932931 | 973897 | 972830 | 981109 | 987200 | 1020553 | 909151 | 987933 | 952154 | 1000373 | 1002965 | 951783 | 953493 | 958513 | 902376 |
| 38. | $I_{SP}$ (measured-S.L.)-lb | 299.5 | 309.4 | 310.6 | 309.7 | 316.1 | 304.0 | 307.8 | 298.4 | 304.4 | 307.5 | 315.6 | 302.6 | 311.2 | 303.8 | 307.4 | 300.6 | 303.7 | 306.6 | 315.9 |
| 39. | $I_{SP}$ (measured-Vac)-lb | 306.2 | 316.4 | 317.5 | 316.6 | 323.6 | 310.9 | 314.8 | 305.1 | 311.2 | 314.1 | 323.3 | 309.4 | 318.4 | 310.5 | 314.2 | 307.6 | 310.7 | 313.7 | 323.7 |
| 40. | E.R. (expansion ratio) | 2.085 | 2.082 | 2.081 | 2.071 | 2.075 | 2.067 | 2.058 | 2.052 | 2.040 | 2.026 | 2.084 | 2.083 | 2.079 | 2.078 | 2.077 | 2.076 | 2.075 | 2.071 | 2.089 |
| 41. | $I_{SP_{VAC}}$ (theo - E.R., h)-sec | 384.4 | 356.6 | 358.5 | 355.8 | 363.5 | 352.0 | 355.2 | 346.2 | 354.8 | 355.3 | 364.5 | 353.0 | 360.7 | 355.0 | 357.4 | 352.7 | 354.2 | 355.2 | 364.1 |
| 42. | $I_{SP_{VAC}}$ (theo - E.R., $h,N_2$)-sec | 347.6 | 356.4 | 358.5 | 355.8 | 363.2 | 351.9 | 355.0 | 346.0 | 352.9 | 354.4 | 364.5 | 350.8 | 357.7 | 354.3 | 353.9 | 351.2 | 352.7 | 353.9 | 363.4 |
| 43. | $\eta\ I_{SP2:1}$ - % | 88.1 | 88.8 | 88.6 | 89.0 | 89.1 | 88.3 | 88.7 | 88.2 | 88.2 | 88.6 | 88.7 | 88.2 | 89.0 | 87.6 | 88.6 | 87.6 | 88.1 | 88.6 | 89.1 |
| 44. | $\eta\ C_{F2:1}$ (from Pc)-% | 91.2 | 91.4 | 92.1 | 91.2 | 91.2 | 91.8 | 93.7 | 92.2 | 93.7 | 92.8 | 90.3 | 90.6 | 90.0 | 92.0 | 91.1 | 89.5 | 89.8 | 90.0 | 90.8 |
| 45. | $\eta\ C_{F2:1}$ (from nozzle losses)-% | 91.9 | 91.9 | 91.8 | 92.0 | 91.9 | 91.9 | 91.9 | 91.9 | 91.7 | 91.8 | 91.7 | 91.8 | 91.9 | 91.6 | 91.9 | 91.6 | 91.8 | 91.9 | 91.9 |
| 46. | $\eta\ C_{F2:1}$ (from Pc-w/o geom)-% | 98.5 | 98.7 | 99.4 | 98.9 | 98.6 | 99.2 | 101.0 | 99.5 | 101.4 | 100.1 | 97.3 | 98.0 | 97.4 | 99.4 | 98.5 | 96.9 | 97.1 | 97.3 | 98.1 |
| 47. | $\eta\ C_{F2:1}$ (from nozzle losses-w/o geom)-% | 99.2 | 99.3 | 99.2 | 99.3 | 99.3 | 99.2 | 99.2 | 99.2 | 99.1 | 99.2 | 99.1 | 99.2 | 99.3 | 99.0 | 99.3 | 99.0 | 99.1 | 99.3 | 99.3 |
| 48. | $I_{SP_{VAC}}$ (predicted 40:1)-sec | 422.9 | 431.6 | 431.4 | 432.7 | 434.1 | 427.7 | 430.8 | 424.3 | 424.8 | 430.6 | 431.9 | 423.0 | 429.1 | 423.2 | 426.0 | 421.8 | 424.7 | 428.6 | 431.0 |
| 49. | $I_{SP_{VAC}}$ (theo - 40:1 -h)-sec | 453.2 | 456.7 | 457.2 | 456.5 | 457.5 | 455.1 | 456.5 | 452.4 | 456.3 | 456.7 | 456.9 | 455.1 | 457.6 | 455.6 | 456.9 | 455.2 | 456.1 | 456.6 | 455.6 |
| 50. | $I_{SP_{VAC}}$ (theo,40:1 -$h,N_2$)-sec | 451.2 | 456.3 | 457.2 | 456.5 | 456.9 | 454.7 | 456.1 | 452.0 | 452.2 | 455.0 | 456.8 | 450.4 | 452.2 | 454.0 | 450.4 | 452.2 | 453.1 | 453.9 | 454.4 |

* Pc5D injector face pressure calculated from Pc4D; therefore, plenum pressure is based upon this calculation. ** Without baffles.

TABLE VII (CONT.)

| | | | | | | | | | | | | | | | | | | | |
|---|---|---|---|---|---|---|---|---|---|---|---|---|---|---|---|---|---|---|---|
| Injector S/N | 020 → | | | | | | | | 012 → | | | | | | ** → | | | | |
| Test Series | 1.2-05-EHM → | | | | 1.2-07-EHM → | | | | | | | | | | | | | | |
| Test Number | 006 | 008 | 009 | 010 | 001 | 002 | 003 | 004B | 005 | 006 | 007 | 008 | 009 | 010 | 011 | 014 | 014 | 015 | 016 |
| 51. $\eta I_{SP_{40:1}}$ - % | 93.7 | 94.6 | 94.4 | 94.8 | 95.0 | 94.1 | 94.3 | 93.9 | 93.9 | 94.6 | 94.3 | 93.9 | 94.9 | 93.2 | 94.5 | 93.3 | 93.7 | 94.4 | 94.9 |
| 52. $\eta C_{F_{40:1}}$ (w/o Geom)-sec | 97.5 | 97.7 | 97.7 | 97.8 | 97.8 | 97.6 | 97.7 | 97.6 | 97.4 | 97.8 | 97.5 | 97.5 | 97.8 | 97.2 | 97.7 | 97.3 | 97.4 | 97.7 | 97.7 |
| 53. $I_{SP_{VAC_{2:1}}}$ | 331.7 | 342.6 | 343.9 | 342.7 | 350.5 | 336.7 | 340.9 | 330.5 | 337.3 | 340.3 | 350.3 | 335.3 | 344.9 | 336.6 | 340.4 | 333.7 | 336.6 | 339.9 | 350.4 |
| 54. $\eta I_{SP2:1}$ (w/o Geom)-% | 95.4 | 96.1 | 95.9 | 96.3 | 96.5 | 95.7 | 96.0 | 95.5 | 95.6 | 96.0 | 96.1 | 95.6 | 96.4 | 95.0 | 96.2 | 95.0 | 95.4 | 96.0 | 96.4 |
| CHAMBER LOSSES (2:1 and 40:1) | | | | | | | | | | | | | | | | | | | |
| 55. Friction - sec. | 0.6 | 0.6 | 0.6 | 0.6 | 0.6 | 0.6 | 0.6 | 0.6 | 0.6 | 0.6 | 0.6 | 0.6 | 0.6 | 0.6 | 0.6 | 0.6 | 0.6 | 0.6 | 0.6 |
| 56. Mixture Ratio Distribution-sec | 5.1 | 4.4 | 4.2 | 4.4 | 4.0 | 4.7 | 4.4 | 5.2 | 4.4 | 4.3 | 4.0 | 4.7 | 4.1 | 4.4 | 4.3 | 4.7 | 4.6 | 4.5 | 4.0 |
| 57. Energy Release - sec. | 7.4 | 6.2 | 6.9 | 5.7 | 5.5 | 7.1 | 6.4 | 7.1 | 7.3 | 6.4 | 6.5 | 7.3 | 5.5 | 9.1 | 6.0 | 8.8 | 7.8 | 6.3 | 5.7 |
| 58. Subtotal - sec. | 13.1 | 11.2 | 11.7 | 10.7 | 10.1 | 12.4 | 11.4 | 12.9 | 12.5 | 11.3 | 11.1 | 12.6 | 10.2 | 14.1 | 10.9 | 14.1 | 13.0 | 11.4 | 10.3 |
| NOZZLE LOSSES (2:1) | | | | | | | | | | | | | | | | | | | |
| 59. Friction - Sec. | 0.5 | 0.5 | 0.5 | 0.5 | 0.5 | 0.5 | 0.5 | 0.5 | 0.5 | 0.5 | 0.5 | 0.5 | 0.5 | 0.5 | 0.5 | 0.5 | 0.5 | 0.5 | 0.5 |
| 60. Geometry - sec. | 25.5 | 26.2 | 26.4 | 26.1 | 26.9 | 25.8 | 26.1 | 25.4 | 26.1 | 26.2 | 27.0 | 25.9 | 26.5 | 26.1 | 26.2 | 26.1 | 25.9 | 26.2 | 26.7 |
| 61. Mixture Ratio Distribution-sec | - | - | - | - | - | - | - | - | - | - | - | - | - | - | - | - | - | - | - |
| 62. Energy Release - sec. | 2.3 | 2.1 | 2.4 | 1.9 | 2.1 | 2.3 | 2.2 | 2.1 | 2.6 | 2.3 | 2.6 | 2.4 | 2.1 | 3.1 | 2.1 | 2.9 | 2.6 | 2.1 | 2.2 |
| 63. Subtotal - sec. | 28.3 | 28.8 | 29.3 | 28.5 | 29.5 | 28.6 | 28.8 | 28.0 | 29.2 | 29.0 | 30.1 | 28.8 | 29.1 | 29.7 | 28.8 | 29.5 | 29.0 | 28.8 | 29.4 |
| NOZZLE LOSSES (40:1) | | | | | | | | | | | | | | | | | | | |
| 64. Friction - sec. | 4.7 | 4.7 | 4.7 | 4.7 | 4.7 | 4.7 | 4.7 | 4.7 | 4.7 | 4.7 | 4.7 | 4.7 | 4.7 | 4.7 | 4.7 | 4.7 | 4.7 | 4.7 | 4.7 |
| 65. Geometry - sec. | 2.6 | 2.6 | 2.6 | 2.6 | 2.6 | 2.6 | 2.6 | 2.6 | 2.6 | 2.6 | 2.6 | 2.6 | 2.6 | 2.6 | 2.6 | 2.6 | 2.7 | 2.7 | 2.7 |
| 66. Mixture Ratio Distribution-sec. | 0.3 | 0 | 0 | 0.1 | 0 | 0.1 | 0.1 | 0.3 | 0.1 | 0.1 | 0 | 0.1 | 0 | 0.1 | 0.1 | 0.1 | 0.1 | 0.1 | 0 |
| 67. Energy Release - sec. | 7.6 | 6.2 | 6.8 | 5.7 | 5.4 | 7.2 | 6.5 | 7.2 | 7.7 | 5.7 | 6.5 | 7.4 | 5.6 | 9.3 | 6.1 | 8.9 | 7.9 | 6.4 | 5.7 |
| 68. Subtotal - sec. | 15.2 | 13.5 | 14.1 | 13.1 | 12.7 | 14.6 | 13.9 | 14.8 | 15.1 | 13.1 | 13.8 | 14.8 | 12.9 | 16.7 | 13.5 | 16.3 | 15.4 | 13.9 | 13.1 |
| TOTAL LOSSES | | | | | | | | | | | | | | | | | | | |
| 69. 2:1 - sec. | 41.4 | 40.0 | 41.0 | 39.2 | 39.6 | 41.0 | 40.2 | 40.9 | 41.7 | 40.3 | 41.2 | 41.4 | 39.3 | 43.8 | 39.7 | 43.6 | 42.0 | 40.2 | 39.7 |
| 70. 40:1 - sec. | 28.3 | 24.7 | 25.8 | 23.8 | 22.8 | 27.0 | 25.3 | 27.7 | 27.6 | 24.4 | 24.9 | 27.4 | 23.1 | 30.8 | 24.4 | 30.4 | 28.4 | 25.3 | 23.4 |

*Pc5D injector face pressure calculated from Pc4D; therefore, plenum pressure is based upon this calculation.

**Without baffles

TABLE VIII

PERFORMANCE DURING TEMPERATURE DECREASE

| | | | | | | | | | | | | | | | | | | | | |
|---|---|---|---|---|---|---|---|---|---|---|---|---|---|---|---|---|---|---|---|---|
| 1. Test Number | 1.2-07-EHM-006 → | | | | | | | | 007 → | | | | | | | 008 → | | | | |
| 2. Test Duration ($FS_1$ to $FS_2$) - sec. | 10.25 → | | | | | | | | 9.36 → | | | | | | | 10.87 → | | | | |
| 3. Data Time ($FS_1$+sec) | 8.04 | 8.30 | 8.61 | 8.85 | 9.06 | 9.19 | 9.25 | 9.31 | 8.09 | 8.30 | 8.63 | 8.92 | 9.05 | 9.33 | 8.35 | 8.89 | 9.53 | 10.05 | 10.42 | 10.61 |
| 4. $A_t$ at Data Time - $in.^2$ | 727.41 | 727.56 | 727.92 | 728.14 | 728.30 | 728.44 | 728.49 | 728.55 | 705.87 | 705.83 | 705.74 | 705.67 | 705.62 | 705.57 | 706.72 | 706.87 | 707.04 | 707.17 | 707.30 | 707.35 |
| 5. Expansion Ratio ($A_{exit}/A_t$) | 2.022 | 2.022 | 2.021 | 2.020 | 2.020 | 2.019 | 2.019 | 2.019 | 2.084 | 2.084 | 2.085 | 2.085 | 2.085 | 2.085 | 2.080 | 2.080 | 2.080 | 2.080 | 2.080 | 2.080 |
| 6. TfJ Decrease Rate Degrees/sec. | -38.2 | 32.7 | 35.7 | 33.0 | 23.8 | 28.6 | 27.2 | 28.6 | 39.0 | 39.0 | 37.5 | 34.0 | 36.4 | 29.0 | 18.5 | 18.5 | 15.7 | 19.2 | 16.5 | 12.6 |
| 7. TfJ - °R | 120 | 110 | 100 | 90 | 85.0 | 81.4 | 80.0 | 78* | 120 | 110 | 100 | 90 | 85.0 | 77.9* | 120 | 110 | 100 | 90 | 85.0 | 82.6 |
| 8. $W_f$ Storage Factor | .906 | .904 | .888 | .897 | .928 | .916 | .925 | .920 | .902 | .887 | .883 | .894 | .890 | .920 | .953 | .948 | .951 | .940 | .950 | .962 |
| 9. $\dot{W}_f$ Measured-lb/sec. | 544 | 534 | 544 | 543 | 545 | 542 | 538 | 541 | 556 | 555 | 559 | 555 | 550 | 549 | 491 | 488 | 491 | 486 | 479 | 484 |
| 10. $\dot{W}_f$ Injector-lb/sec | 495 | 483 | 483 | 487 | 506 | 497 | 498 | 498 | 501 | 493 | 494 | 492 | 489 | 505 | 463 | 463 | 467 | 457 | 455 | 465 |
| 11. $\dot{W}_o$ - lb/sec | 2744 | 2733 | 2758 | 2759 | 2764 | 2756 | 2757 | 2772 | 2288 | 2276 | 2300 | 2320 | 2313 | 2346 | 2717 | 2722 | 2724 | 2735 | 2754 | 2745 |
| 12. M.R. | 5.55 | 5.66 | 5.71 | 5.67 | 5.46 | 5.54 | 5.54 | 5.57 | 4.57 | 4.61 | 4.66 | 4.72 | 4.73 | 4.65 | 5.80 | 5.88 | 5.83 | 5.98 | 6.05 | 5.90 |
| 13. $F_{s.l.}$ (measured) corrected)-lb | 988900 | 9[illegible]96 | 969720 | 972620 | 968938 | 961140 | 955311 | 938040 | 883160 | 882200 | 873680 | 882680 | 874187 | 880500 | 958890 | 959990 | 961590 | 952670 | 953180 | 945323 |
| 14. $F_{vac}$ (measured)-lb. | 1010530 | 1002320 | 991350 | 994250 | 990562 | 982764 | 976935 | 959670 | 904790 | 903830 | 895310 | 904310 | 895810 | 902130 | 980520 | 981620 | 983220 | 974300 | 974803 | 966946 |
| 15. $I_{sp_{vac}}$ (measured) -sec. | 311.99 | 311.4 | 305.88 | 306.30 | 302.62 | 301.80 | 300.36 | 293.48 | 324.41 | 324.07 | 320.45 | 321.58 | 319.42 | 316.42 | 307.86 | 308.20 | 308.12 | 305.23 | 303.54 | 300.81 |
| 16. $I_{sp_{vac}}$ (Theo -$A_e$/ $A_t$-sec | 351.3 | 350.3 | 349.9 | 350.2 | 352.30 | 351.42 | 351.52 | 351.0 | 361.1 | 360.8 | 360.4 | 359.9 | 359.50 | 360.5 | 350.6 | 349.9 | 350.3 | 349.1 | 347.80 | 349.30 |
| 17. $I_{sp_{vac}}$ (theo -$A_e$/ $A_t,N_2$-sec. | 350.6 | 349.5 | 349.2 | 349.5 | 351.40 | 350.82 | 350.72 | 350.3 | 361.1 | 360.8 | 360.4 | 359.9 | 359.50 | 360.5 | 348.4 | 347.7 | 348.1 | 346.9 | 346.00 | 347.50 |
| 18. Enthalpy Correction Factor | 1.0031 | 1.0026 | 1.0022 | 1.0019 | 1.0018 | 1.0016 | 1.0016 | 1.0014 | 1.0042 | 1.0036 | 1.0030 | 1.0024 | 1.0022 | 1.0018 | 1.0029 | 1.0026 | 1.0022 | 1.0018 | 1.0015 | 1.0015 |
| 19. $I_{sp_{vac}}$ (theo -$A_e$/ $A_t,N_2$,HO - sec. | 351.7 | 350.4 | 350.0 | 350.1 | 352.03 | 351.38 | 351.28 | 350.8 | 362.6 | 362.1 | 361.5 | 360.8 | 360.29 | 361.1 | 349.4 | 348.6 | 348.9 | 347.5 | 346.52 | 348.02 |
| 20. Nozzle Geometry Loss - sec. | 25.9** | 25.8** | 25.8** | 25.8** | 25.90 | 25.92 | 25.92 | 25.9** | 26.7 | 26.7 | 26.6 | 26.6 | 26.60 | 26.6 | 25.7 | 25.6 | 25.7 | 25.6 | 27.52 | 25.67 |
| 21. $I_{sp_{vac}}$ (theo - $A_e$/ $A_t,N_2$,h, 30.1°sec | 325.8** | 324.6** | 324.2** | 324.3** | 326.13 | 325.46 | 325.36 | 324.9** | 335.9 | 335.4 | 334.9 | 334.2 | 333.69 | 334.5 | 323.7 | 323.0 | 323.2 | 321.9 | 321.00 | 322.55 |
| 22. $\eta I_{sp}$ - % | 95.76** | 95.93** | 94.35** | 9445** | 92.79 | 92.73 | 92.32 | 90.33** | 96.58 | 96.62 | 95.69 | 96.22 | 95.72 | 94.60 | 95.11 | 95.42 | 95.33 | 94.82 | 94.56 | 93.259 |

* Temperature at initiation of instability

** Actual geometry loss unknown due to loss of ablative liner downstream of throat at $FS_1$ + 7.95 sec.

TABLE VIII

PERFORMANCE DURING TEMPERATURE DECREASE

| Test Number | 1.2-07-EHM-006 | | | | | | | | 007 | | | | | | 008 | | | | | |
|---|---|---|---|---|---|---|---|---|---|---|---|---|---|---|---|---|---|---|---|---|
| Test Duration ($FS_1$ to $FS_2$) - sec. | 10.25 | | | | | | | | 9.36 | | | | | | 10.87 | | | | | |
| 23. Pc4D-psia | 1102*** | 1088*** | 1094*** | 1089*** | 1078*** | 1072*** | 1066 | 1062*** | 848 | 849 | 841 | 846 | 840 | 827 | 921 | 920 | 916 | 911 | 911 | 906 |
| 24. Pplenum-psia | 1028 | 1013 | 1016 | 1008 | 996 | 989 | 983 | 979 | 956 | 957 | 948 | 954 | 947 | 932 | 1039 | 1038 | 1034 | 1028 | 1028 | 1023 |
| 25. C*(measured) ft/sec | 7434 | 7383 | 7347 | 7280 | 7146 | 7160 | 7087 | 7023 | 7779 | 7870 | 7697 | 7781 | 7481 | 7444 | 7423 | 7413 | 7381 | 7330 | 7113 | 7254 |
| 26. $h_{C*}$ | 1.0013 | 1.0011 | 1.0010 | 1.0008 | 1.0012 | 1.0007 | 1.0007 | 1.0006 | 1.0018 | 1.0015 | 1.0013 | 1.0010 | 1.0009 | 1.0008 | 1.0012 | 1.0011 | 1.0010 | 1.0008 | 1.0006 | 1.0006 |
| 27. C*(theo-h,$N_2$) ft/sec | 7678 | 7650 | 7640 | 7648 | 7693 | 7669 | 7669 | 7669 | 7884 | 7878 | 7868 | 7856 | 7863 | 7866 | 7595 | 7576 | 7586 | 7552 | 7542 | 7569 |
| 28. $\eta$ C* - % | 96.8 | 96.5 | 96.2 | 95.2 | 92.9 | 93.4 | 92.4 | 91.6 | 98.6 | 99.8 | 97.8 | 98.9 | 95.1 | 94.6 | 97.7 | 97.8 | 97.2 | 97.0 | 94.3 | 95.7 |
| 29. $\%\dot{W}_f$ (element) | - | - | - | - | - | - | - | 89.79 | - | - | - | - | - | 89.79 | - | - | - | - | - | 89.79 |
| 30. $V_f/V_o$ (element) | - | - | - | - | - | - | - | 7.65 | - | - | - | - | - | 8.98 | - | - | - | - | - | 7.14 |

***Pc5D - Face pressure

TABLE VIII

PERFORMANCE DURING TEMPERATURE DECREASE

| | | | | | | | | | | | | | | | | | | | | |
|---|---|---|---|---|---|---|---|---|---|---|---|---|---|---|---|---|---|---|---|---|
| 1. | Test Number | 1.2-07-EHM-009 → | | | | | | 010 → | | | 015B → | | | | | 016 → | | | | |
| 2. | Test Duration($FS_1$ to $FS_2$) - sec. | 10.92 → | | | | | | 15.07 → | | | 13.972 → | | | | | 13.596 → | | | | |
| 3. | Data Time $FS_1$ + sec. | 7.72 | 8.25 | 8.72 | 9.28 | 9.58 | 10.13 | 9.67 | 10.83 | 11.32 | 10.67 | 11.59 | 12.19 | 12.97 | 13.38 | 9.88 | 10.53 | 11.47 | 12.21 | 13.37 |
| 4. | $A_t$ at Data Time-$in.^2$ | 707.72 | 707.76 | 707.80 | 707.85 | 707.88 | 707.92 | 707.99 | 707.96 | 707.95 | 709.99 | 710.10 | 710.17 | 710.27 | 710.32 | 704.94 | 704.71 | 704.39 | 704.13 | 703.73 |
| 5. | Expansion Ratio ($A_{exit}/A_t$) | 2.079 | 2.079 | 2.079 | 2.079 | 2.078 | 2.078 | 2.078 | 2.078 | 2.078 | 2.072 | 2.071 | 2.071 | 2.071 | 2.071 | 2.087 | 2.087 | 2.088 | 2.089 | 2.090 |
| 6. | TfJ Decrease Rate-Degrees/sec. | 19.6 | 18.8 | 19.6 | 18.5 | 16.7 | 16.7 | 4.97 | 4.3 | 4.97 | 14.5 | 12.5 | 16.6 | 12.8 | 11.0 | 13.1 | 14.3 | 10.8 | 9.8 | 6.2 |
| 7. | TfJ -°R | 120 | 110 | 100 | 90 | 85.0 | 75.8* | 90 | 85.0 | 81.8* | 120 | 110 | 100 | 90 | 85.4 | 120 | 110 | 100 | 90 | 79.6 |
| 8. | $W_f$ Storage Factor | .950 | .946 | .941 | .944 | .949 | .954 | .984 | .986 | .986 | .963 | .963 | .950 | .960 | .965 | .967 | .958 | .967 | .968 | .981 |
| 9. | $\dot{W}_f$ Measured-lb/sec. | 527 | 530 | 539 | 551 | 528 | 533 | 500 | 504 | 499 | 489 | 485 | 491 | 479 | 477 | 535 | 534 | 541 | 530 | 534 |
| 10. | $\dot{W}_f$ Injector-lb/sec. | 501 | 501 | 506 | 520 | 501 | 509 | 492 | 497 | 491 | 471 | 467 | 466 | 460 | 460 | 517 | 512 | 524 | 513 | 524 |
| 11. | $W_o$-lb/sec | 2478 | 2468 | 2469 | 2462 | 2489 | 2498 | 2719 | 2712 | 2706 | 2595 | 2638 | 2606 | 2635 | 2618 | 2251 | 2261 | 2268 | 2267 | 2301 |
| 12. | M.R. | 4.94 | 4.93 | 4.88 | 4.74 | 4.97 | 4.91 | 5.52 | 5.46 | 5.51 | 5.51 | 5.65 | 5.59 | 5.81 | 5.68 | 4.35 | 4.42 | 4.33 | 4.42 | 4.39 |
| 13. | $F_{SL}$(measured corrected)-lb | 929640 | 924100 | 925500 | 925520 | 922491 | 904050 | 975730 | 970342 | 967210 | 934846 | 926627 | 923067 | 929296 | 919537 | 880429 | 878270 | 875115 | 875402 | 875129 |
| 14. | $F_{vac}$(measured)-lb. | 951270 | 945730 | 947130 | 947150 | 944114 | 925680 | 997360 | 991966 | 988840 | 956470 | 948250 | 944691 | 950920 | 941160 | 902053 | 899894 | 896739 | 897026 | 896752 |
| 15. | $I_{sp_{vac}}$(measured)-sec. | 319.33 | 318.75 | 318.36 | 317.62 | 315.47 | 307.85 | 310.60 | 309.22 | 309.30 | 311.67 | 305.20 | 307.26 | 307.03 | 305.47 | 325.63 | 324.28 | 320.93 | 322.48 | 317.21 |
| 16. | $I_{sp_{vac}}$ (theo-$A_e/A_t$)-sec. | 357.8 | 358.0 | 358.3 | 359.5 | 357.75 | 358.1 | 352.9 | 353.70 | 353.0 | 353.25 | 352.00 | 352.25 | 350.30 | 351.40 | 361.80 | 361.50 | 362.00 | 361.50 | 361.50 |
| 17. | $I_{sp_{vac}}$ $A_t$, $N_2$)-sec | 355.7 | 355.9 | 356.2 | 357.4 | 354.95 | 356.0 | 352.2 | 353.63 | 352.3 | 352.00 | 351.00 | 351.25 | 349.30 | 350.50 | 361.50 | 361.00 | 361.14 | 360.80 | 361.00 |
| 18. | Enthalpy Correction Factor | 1.0038 | 1.0033 | 1.0029 | 1.0024 | 1.0020 | 1.0015 | 1.0019 | 1.0018 | 1.0016 | 1.0031 | 1.0026 | 1.0022 | 1.0018 | 1.0017 | 1.0045 | 1.0039 | 1.0034 | 1.0027 | 1.0022 |
| 19. | $I_{sp_{vac}}$ (theo-$A_e/A_t$,$N_2$, h)-sec. | 357.0 | 357.1 | 357.2 | 358.3 | 355.66 | 356.5 | 352.9 | 353.63 | 352.9 | 353.09 | 351.91 | 352.02 | 349.93 | 351.09 | 363.13 | 362.41 | 362.37 | 361.77 | 361.79 |
| 20. | Nozzle Geometry Loss-sec. | 26.4 | 26.4 | 26.4 | 26.5 | 26.4 | 26.4 | 25.9 | 26.0 | 25.9 | 25.95 | 25.88 | 25.90 | 25.70 | 25.80 | 26.95 | 26.90 | 26.99 | 26.90 | 26.90 |
| 21. | $I_{sp_{vac}}$ (theo-$A_e/A_t$,$N_2$,h,30.1°)sec | 330.6 | 330.7 | 330.8 | 331.8 | 329.26 | 330.1 | 327.0 | 327.63 | 327.0 | 327.14 | 326.03 | 326.12 | 324.23 | 325.29 | 336.18 | 335.51 | 335.38 | 334.87 | 334.9 |
| 22. | $\eta I_{sp}$-% | 96.59 | 96.39 | 96.24 | 95.73 | 95.81 | 93.26 | 94.98 | 94.38 | 94.50 | 95.27 | 93.61 | 94.22 | 94.78 | 93.91 | 96.86 | 96.65 | 95.69 | 96.30 | 94.71 |

TABLE VIII

PERFORMANCE DURING TEMPERATURE DECREASE

| | Test Number | 1.2-07-EHM-009 | | | | | 010 | | | 015B | | | | 016 | | | | |
|---|---|---|---|---|---|---|---|---|---|---|---|---|---|---|---|---|---|---|
| | Test Duration ($FS_1$ to $FS_2$)-sec | 10.92 | | | | | 15.07 | | | 13.972 | | | | 13.596 | | | | |
| 23. | Pc4D-psia | 892 | 889 | 890 | 888 | 888 | 852 | 929 | 927 | 922 | 898 | 897 | 885 | 890 | 886 | 842 | 834 | 844 | 840 | 838 |
| 24. | Pplenum-psia | 1007 | 1004 | 1005 | 1003 | 1003 | 962 | 1049 | 1047 | 1041 | 1015 | 1014 | 1000 | 1006 | 1002 | 949 | 940 | 951 | 947 | 945 |
| 25. | C*(measured) ft/sec | 7710 | 7708 | 7708 | 7662 | 7639 | 7304 | 7461 | 7436 | 7416 | 7570 | 7460 | 7442 | 7437 | 7580 | 7786 | 7696 | 7728 | 7722 | 7582 |
| 26. | $h_{C*}$ | 1.0016 | 1.0014 | 1.0012 | 1.0010 | 1.0008 | 1.0007 | 1.0008 | 1.0008 | 1.0007 | 1.0013 | 1.0011 | 1.0011 | 1.0008 | 1.0007 | 1.0044 | 1.0016 | 1.0014 | 1.0011 | 1.0009 |
| 27. | C*(theo-h,$N_2$) ft/sec | 7764 | 7763 | 7769 | 7792 | 7763 | 7761 | 7678 | 7690 | 7681 | 7704 | 7648 | 7660 | 7612 | 7637 | 7923 | 7891 | 7901 | 7887 | 7887 |
| 28. | $\eta C^*$ - % | 99.3 | 99.2 | 99.2 | 98.3 | 98.3 | 94.2 | 97.2 | 96.7 | 96.5 | 98.3 | 97.5 | 97.0 | 97.5 | 99.0 | 98.2 | 97.5 | 97.6 | 97.8 | 96.1 |
| 29. | $\%\omega_f$ (element) | - | - | - | - | - | 89.79 | - | - | 89.79 | - | - | - | - | 91.72 | - | - | - | - | 91.72 |
| 30. | $V_f/V_o$ (element) | - | - | - | - | - | 8.55 | - | - | 8.15 | - | - | - | - | 8.06 | - | - | - | - | 9.80 |

*Temperature at initiation of instability

The primary objective of test No. 1.2-07-EHM-008 was to determine whether the fuel injection temperature decrease rate affected the temperature at which instability occurs. A review of gaseous hydrogen pressurant limitations data indicated that this test duration could be increased to 13 sec; therefore, a fuel injection temperature decrease rate of 20°/sec was designated. As a secondary objective, this test would serve to determine the effect of mixture ratio upon the temperature at which instability occurs.

In test No. 1.2-07-EHM-009, the primary objective was to decrease the fuel injection temperature until instability occurred and then to increase the temperature at the rate of 55°/sec until stability was recovered. This fast rate would minimize the duration of the instability. Recovery from instability (combustion similar to steady-state conditions) appeared to occur at 100°R and 4.35 MR with a temperature increase rate of 54°/sec.

Fuel injection temperature was decreased at the rate of 5°/sec until instability occurred in test No. 1.2-07-EHM-010. Then, the temperature was increased at the rate of 55°/sec until recovery, which occurred at 101.5°R and 4.63 MR with an actual temperature increase rate of 55.3°/sec.

The effect of the shorter (0.5-in.) baffles upon combustion smoothness and performance was investigated during test No. 1.2-07-EHM-011.

The objective of test No. 1.2-07-EHM-014 was to ascertain whether a higher fuel injection temperature had any affect upon performance.

Tests No. 1.2-07-EHM-015 and -016 served to permit determination of stability limits without baffles. It was found that the instabilities were approximately five times greater in magnitude without the baffles than with them.

Injector S/N 012 and the film-cooled chamber were used in tests No. 1.2-07-EHM-019 through -025. These tests were for the purpose of evaluating the effects upon stability of wall materials as well as the relative location of the chamber wall with respect to the injector periphery. The first two tests, -019 and -020, were conducted using inserts, which were metal pieces bolted to the fuel torus beneath the gasket holder. These inserts simulated the relative location of the chamber wall with respect to the injector periphery in the same way as was found during the stability testing with the ablative chamber.

Warm oxygen (210°R to 240°R as compared with 175°F) and the chamber inserts were used for tests No. -021 and -022 of this series. The chamber inserts were omitted and a normal oxygen temperature was used in tests No. -023 and -025.

Generally, the stability of several hardware configurations with varying propellant feed conditions was evaluated. This evaluation consisted of establishing the hydrogen injection temperature at which instability was self-triggered and, in some instances, the hydrogen injection temperature at which instability was self-damping.

The hardware variations tested were limited to chamber and baffle changes using a single injector design. These variations consisted of:

- an ablative chamber with approximately 3.7% of the fuel injected as film coolant from the injector periphery (this unit was tested with both short 1/2-in. and long 3-1/2-in. baffles).

- a steel chamber with inserts at the periphery extending from the injector face downstream approximately 6 in. (In addition to film coolant from the injector face, an approximately 8.0% secondary film coolant was injected approximately 13.6 in. above the throat.)

- the above steel chamber with the inserts removed and with an additional 5.0% of the fuel injected at the injector end of the chamber between the injector film cooling and the chamber wall as film cooling.

Different densities of the oxidizer were used as the propellant variations. These differences were obtained by permitting the propellant to warm in the tank prior to testing. The oxidizer injection densities varied from approximately 56 lb/cu ft to 71 lb/cu ft. Fuel density variations were achieved by injecting gaseous hydrogen into the liquid stream during the test.

The effect of hydrogen inlet temperature upon $\eta I_{sp}$ and $\eta c^*$ is illustrated on Figures No. 41 and No. 42. They show that performance decreases approximately 1% as the hydrogen injection temperature decreases from 167°R to 90°R. As the temperature at which instability is self-triggered (75°R to 85°R) is approached, the rate of performance change in relationship to temperature increases. From 90°R to 80°R, a change of approximately 5% occurs during the 10 degrees difference. It is interesting to note that the "knee" of each curve on Figure No. 41 occurs at a velocity ratio of approximately 10.

Figure No. 43 is a plot of the hydrogen injector temperature at which instability is self-triggered in relationship to injector mixture ratio. The approximate hydrogen injection temperature at which recovery from instability occurred also is shown. Careful study of these data indicates that none of the changes in hardware or test conditions had any appreciable affect upon the conditions at which instability was self-triggered.

Figure No. 44 is a plot of the element injection velocity ratio (injection velocity of the hydrogen divided by the injection velocity of the oxidizer) versus the hydrogen injection temperature at instability. Again, recovery from instability data is included. It can be seen that the injector is stable above 85°R with velocity ratios above 10 at nominal mixture ratio for any of the variations tested.

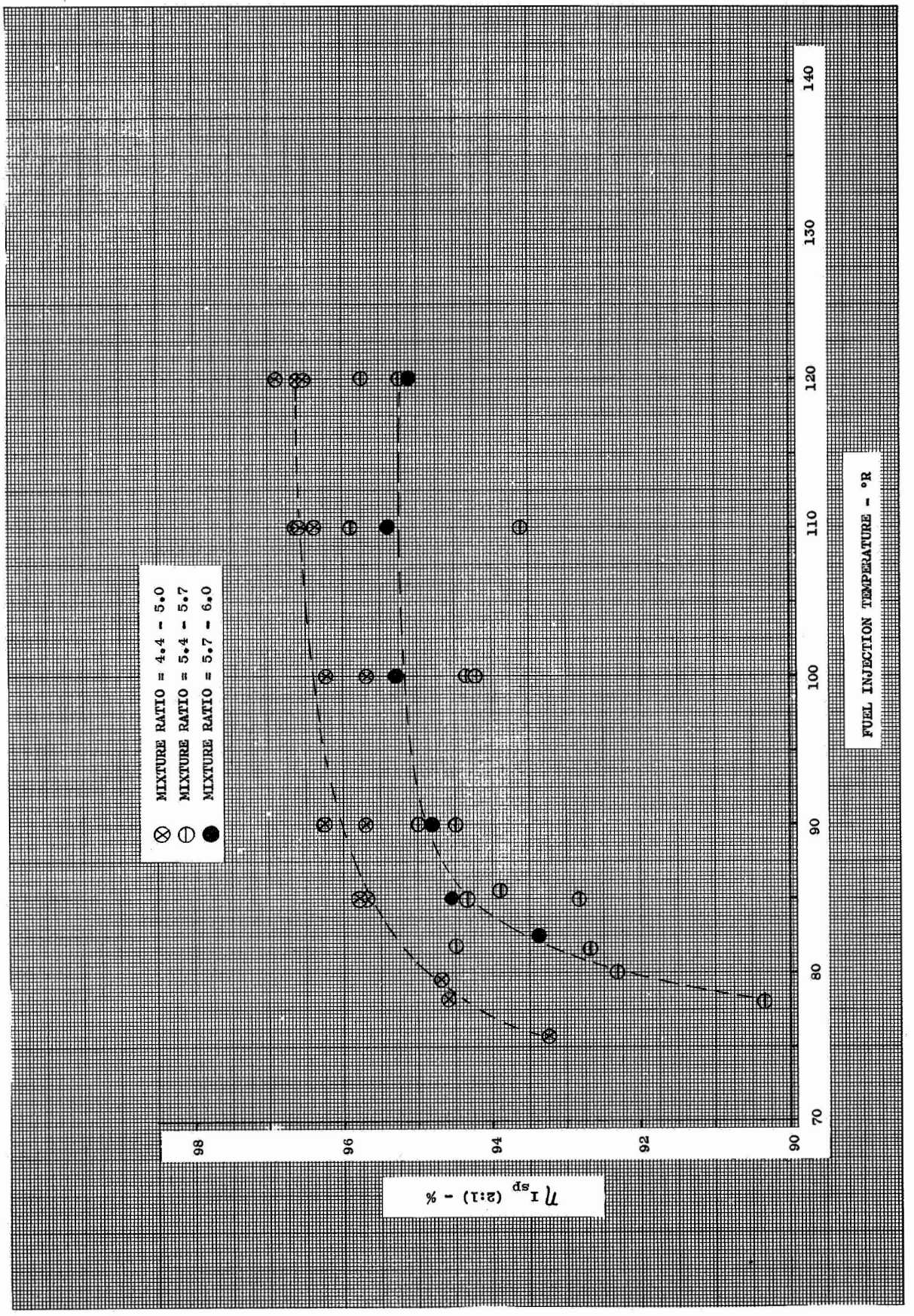


Figure 41. $\eta I_{sp}$ 2:1 vs. Fuel Injection Temperature

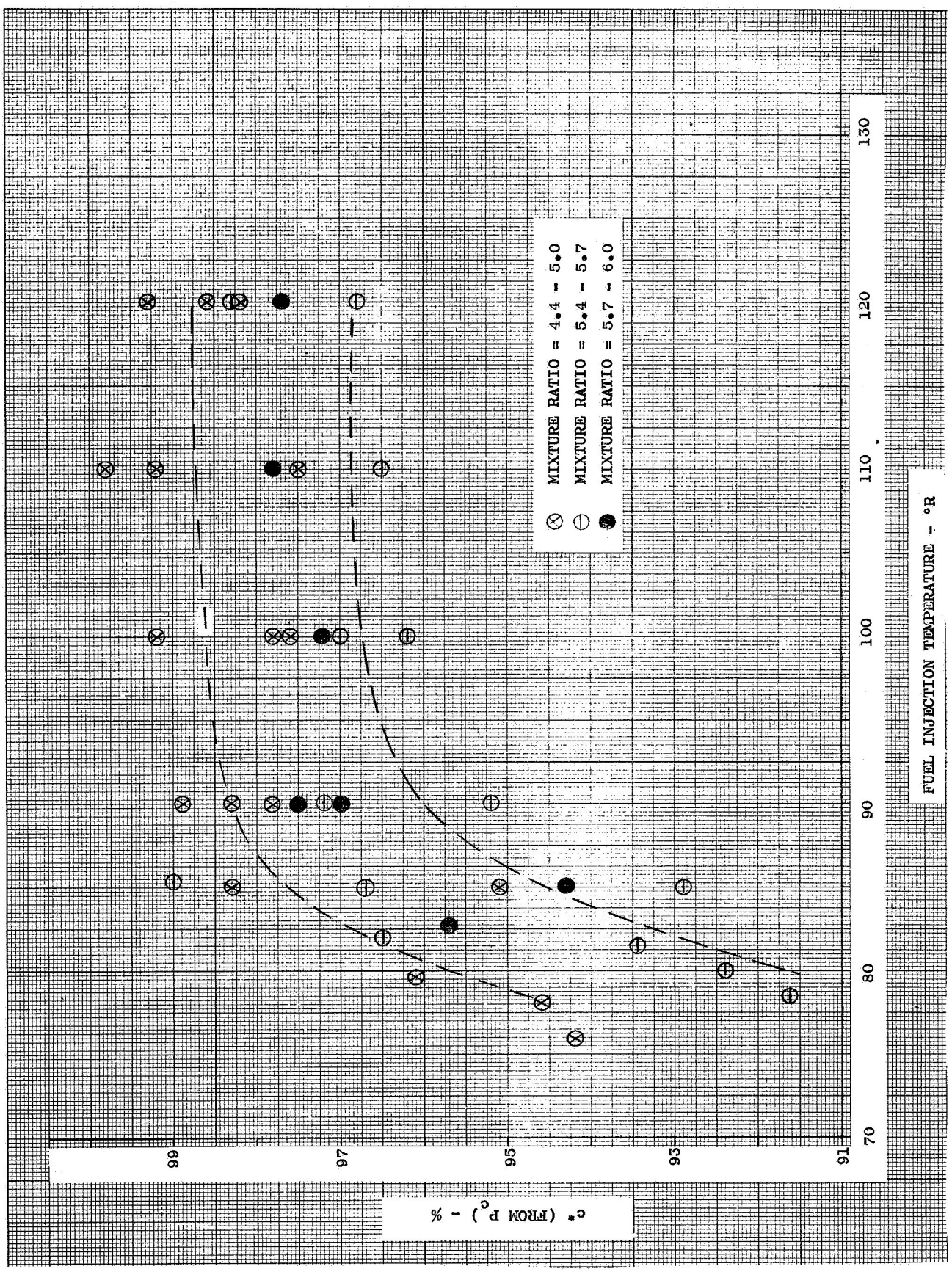


Figure 42. c° (From $P_c$) vs. Fuel Injection Temperature

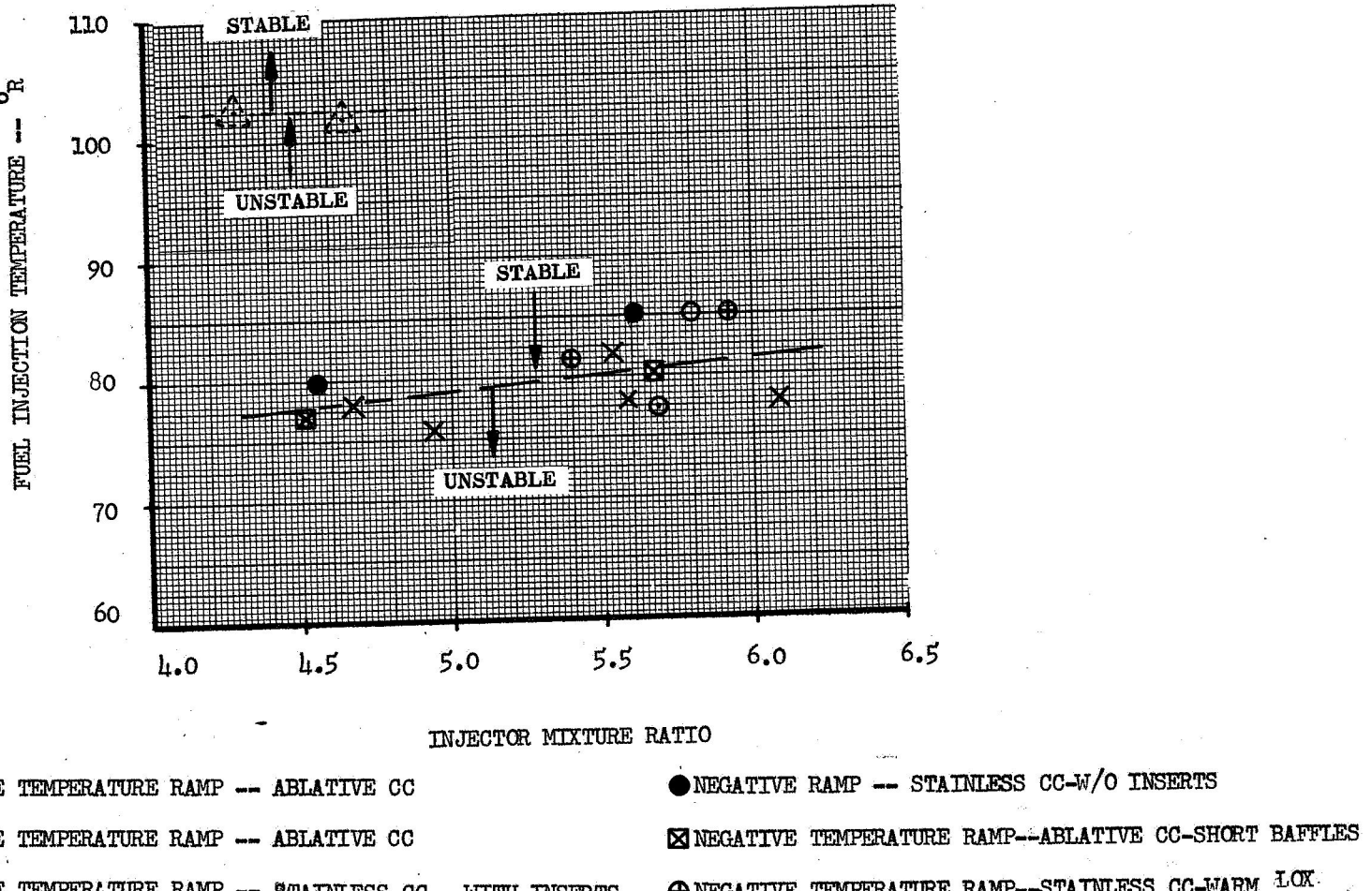


Figure 43. Hydrogen Injection Temperature vs. Mixture Ratio

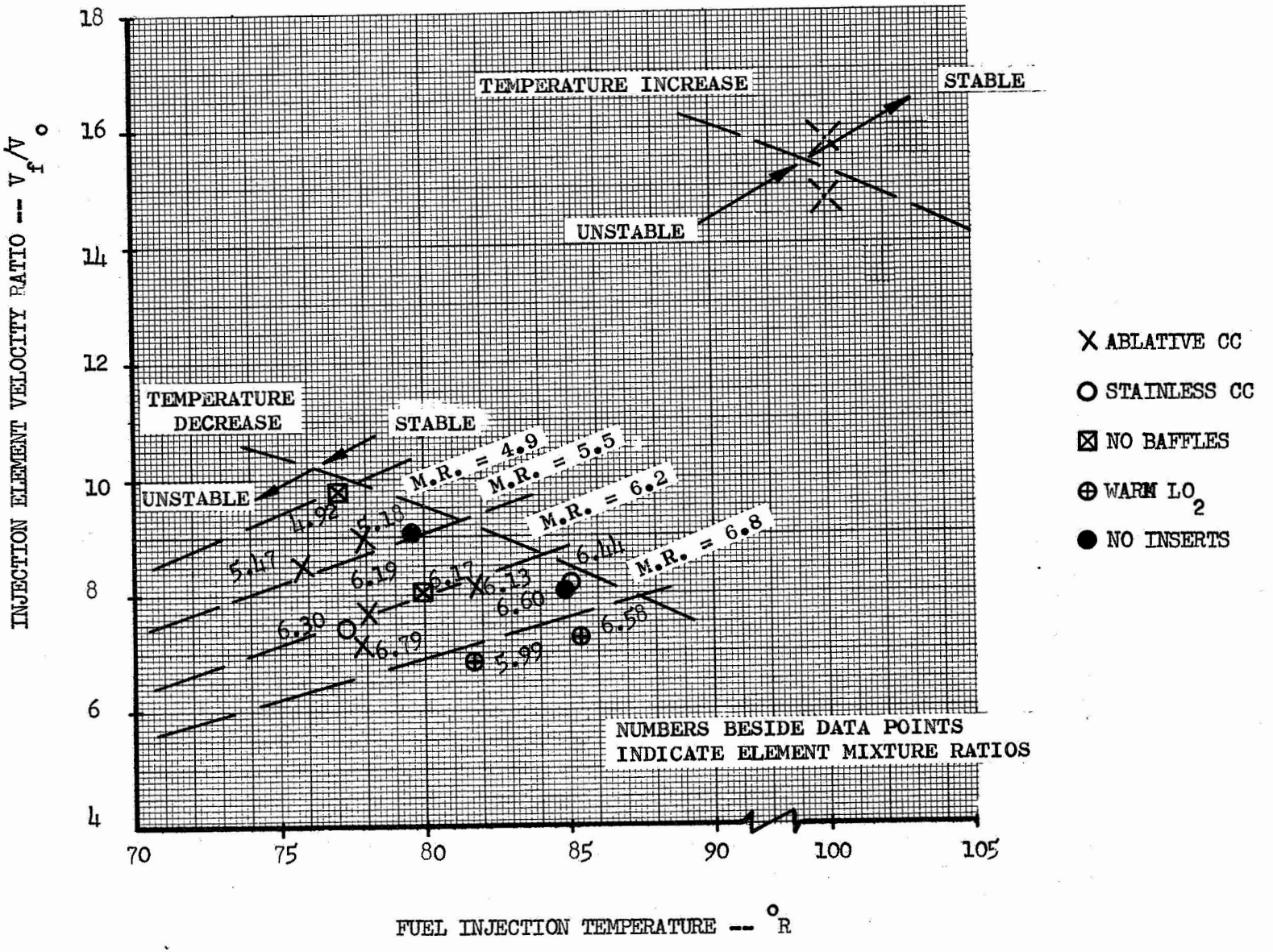


Figure 44. Injection Element Velocity Ratio vs. Fuel Injection Temperature

By applying the data from Figures No. 41 and No. 44, it is possible to obtain performance at the point of instability for the various conditions. These data indicate that the instability starts at high combustion efficiencies with the lower mixture ratios.

Sample calculations (using data from test No. 1.2-07-EHM-006) for $\eta I_{sp}$ are presented in Appendix C, wherein the items listed correspond with those of Table VIII. These items are those not defined in Appendix B.

5. Hydraulic Analysis of the Fuel Injector

Two different methods for calculating the fuel injector manifold pressure profile were investigated. The first method was a row-by-row method based upon the following assumptions:

ROW RESISTANCE SCHEMATIC

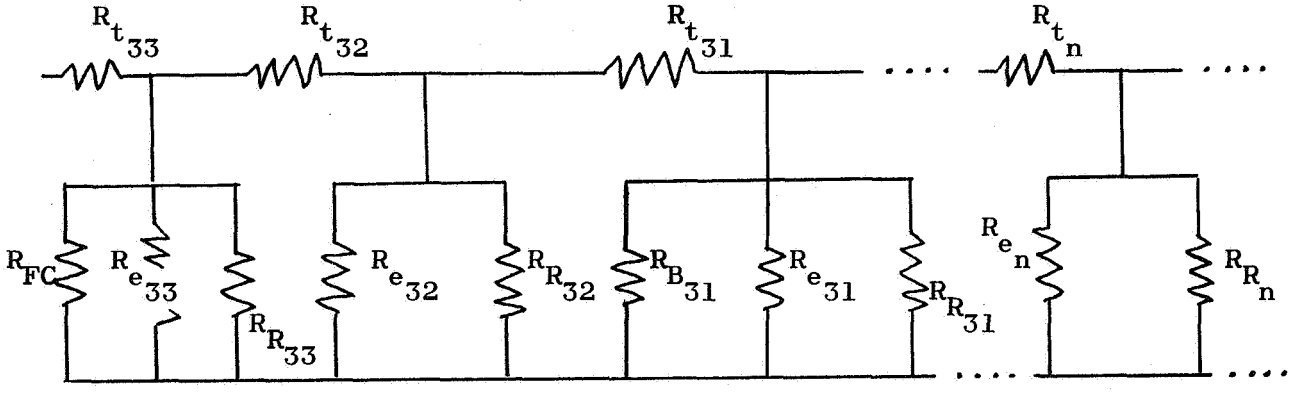


$R_t$ = resistance past the tubes

$R_{FC}$ = resistance chamber wall film cooling (row 33 only)

$R_e$ = resistance elements

$R_r$ = resistance of Rigimesh

$R_B$ = resistance of baffle cooling [Rows 31, 27, 23, 19, outer ring (between 16 and 15), 14, 11, 8, 5, and inner ring (between 3 and 2)]

$$\Delta P = \frac{\dot{w}^2}{\rho} \qquad \text{Equation (7)}$$

Where:

$R_B$ and $R_{FC}$ were obtained from the equation:

$$K = 1.41 + 1.57e^{-0.38L/D} + F\frac{L}{D}, \text{ empirically determined} \qquad \text{Equation (8)}$$

$R_e$ was obtained from single element testing

$R_R$ was calculated using the following equation:

$$\dot{w} = 0.0361\ (SCFM)\sqrt{\frac{\Delta P_{inj}}{\Delta P_{air}} \times S.G._M}\left(\frac{A_R}{144}\right) \qquad \text{Equation (9)}$$

$R_t$ was obtained by analyzing for flow through staggered tubes by using the following equation:(10)

$$\Delta P = 4F\frac{\dot{w}^2}{2g\rho A^2} \qquad \text{where}$$

$$f = \left[0.23 + \frac{0.110}{(X_t - 1)^{1.08}}\right]\left(\frac{E_o \dot{w}}{\mu A}\right)^{-0.15} \qquad \text{Equation (10)}$$

It was conservatively assumed that all adjacent tube rows were staggered. Table IX shows analysis results based upon 524 lb/sec fuel weight flow and 1040 psia injector face pressure. From this table, it is found that the flow distribution is as follows:

| Rows | 1-2 | 3-15 | 16-24 | 25-33 |
|---|---|---|---|---|
| No. of Elements | 26 | 750 | 996 | 1476 |
| % Total Flow Rate | 0.532 | 17.108 | 27.221 | 44.921 |
| Total Flow Rate (lb/sec) | 2.79 | 89.65 | 142.64 | 235.39 |
| Flow Rate/Element (lb/sec) | 0.1072 | 0.1195 | 0.1432 | 0.1595 |

| | Ablative Chamber | | Steel Chamber (3.5-in. Baffles) | |
|---|---|---|---|---|
| | 3.5-in. Baffles | 0.5-in. Baffles | With Inserts | Without Inserts |
| Total Rigimesh Flow, % | 2.56 | 2.56 | 2.56 | 2.56 |
| Total Baffle Flow, % | 3.93 | 2.00 | 3.93 | 3.93 |
| Primary Chamber Film Cooling, % | 3.72 | 3.72 | 3.72 | 8.72 |
| Secondary Chamber Film Cooling, % | -- | -- | 8.00 | 8.00 |
| Total Element Flow, % | 89.79 | 91.72 | 81.79 | 76.79 |

(10) McAdams, W. H., Heat Transmission, McGraw-Hill, 1954

TABLE IX

M-1 INJECTOR S/N 020 WITH FILM COOLING
FLOW RATE PER ROW

| Row No. | $\dot{w}_o$, % | $(\dot{w}_f)_E$, % | $(\dot{w}_f)_B$, % | $(\dot{w}_f)_R$, % | $\dot{w}_f$, % | $MR_E$** |
|---|---|---|---|---|---|---|
| 1 | 0.27 | 0.211 | -- | 0.009 | 0.220 | 7.03 |
| 2 | 0.43 | 0.321 | -- | 0.015 | 0.336 | 7.35 |
| Inner Ring | -- | -- | 0.313 | -- | 0.313 | -- |
| 3 | 0.66 | 0.519 | -- | 0.021 | 0.540 | 6.98 |
| 4 | 0.83 | 0.642 | -- | 0.018 | 0.660 | 7.09 |
| 5 | 0.99 | 0.783 | 0.143 | 0.020 | 0.946 | 6.94 |
| 6 | 1.16 | 0.936 | -- | 0.024 | 0.960 | 6.80 |
| 7 | 1.32 | 1.071 | -- | 0.026 | 1.097 | 6.76 |
| 8 | 1.32 | 1.047 | 0.141 | 0.034 | 1.222 | 6.92 |
| 9 | 1.32 | 1.075 | -- | 0.045 | 1.120 | 6.74 |
| 10 | 1.82 | 1.479 | -- | 0.036 | 1.515 | 6.75 |
| 11 | 1.98 | 1.637 | 0.164 | 0.040 | 1.841 | 6.64 |
| 12 | 2.14 | 1.807 | -- | 0.043 | 1.850 | 6.50 |
| 13 | 2.31 | 1.971 | -- | 0.048 | 2.018 | 6.43 |
| 14 | 2.48 | 2.135 | 0.175 | 0.050 | 2.360 | 6.38 |
| 15 | 2.31 | 2.016 | -- | 0.087 | 2.103 | 6.29 |
| Outer Ring | -- | -- | 0.845 | -- | 0.845 | -- |
| 16 | 2.56 | 2.181 | -- | 0.083 | 2.264 | 6.44 |
| 17 | 2.92 | 2.520 | -- | 0.060 | 2.580 | 6.36 |
| 18 | 2.92 | 2.560 | -- | 0.080 | 2.640 | 6.26 |
| 19 | 3.30 | 2.906 | 0.445 | 0.069 | 3.420 | 6.23 |
| 20 | 3.30 | 2.955 | -- | 0.075 | 3.030 | 6.13 |
| 21 | 3.66 | 3.225 | -- | 0.075 | 3.300 | 6.23 |
| 22 | 3.66 | 3.331 | -- | 0.089 | 3.420 | 6.03 |
| 23 | 4.03 | 3.745 | 0.507 | 0.088 | 4.340 | 5.91 |
| 24 | 4.02 | 3.798 | -- | 0.102 | 3.900 | 5.81 |
| 25 | 4.71 | 4.173 | -- | 0.097 | 4.270 | 6.20 |
| 26 | 4.71 | 4.230 | -- | 0.110 | 4.340 | 6.11 |
| 27 | 5.10 | 4.632 | 0.561 | 0.107 | 5.300 | 6.04 |
| 28 | 5.10 | 4.680 | -- | 0.120 | 4.800 | 5.98 |
| 29 | 5.50 | 5.093 | -- | 0.117 | 5.210 | 5.93 |
| 30 | 5.50 | 5.170 | -- | 0.130 | 5.300 | 5.84 |
| 31 | 5.89 | 5.573 | 0.635 | 0.132 | 6.340 | 5.80 |
| 32 | 5.89 | 5.650 | -- | 0.150 | 5.800 | 5.72 |
| 33 | 5.89 | 5.720 | (3.724)* | 0.356 | 9.800 | 5.65 |
| Total | 100.00 | 89.792 | 7.653 | 2.556 | 100.00 | -- |

*Chamber wall fuel film cooling.
**Local element mixture ratio for over-all MR = 5.49.

From Table IX, it is seen that the tube bank and element pressure drop is 213 psi. The fuel manifold inlet loss is 18 psi; therefore, the loss from PfJ transducer location to face pressure is 231 psi. The tube bank and manifold inlet loss from PfJ to row 1 is 145 psia.

The second method for calculating the pressure profile was to determine the manifold loss (tube bank) using average areas between tubes and averaging the pressure drops for both in-line and staggered tubes. The following equations were utilized:(11)

$$P = 4fN \frac{\rho V^2}{2g} \quad \text{where:} \qquad \text{Equation (11)}$$

$$\text{in-line tubes} \quad f = \left[ 0.044 + \frac{0.08X_L}{(X_t-1)^n} \right] \left( \frac{D_o G}{\mu} \right)^{-0.15}$$

$$M = 0.43 + \frac{1.13}{X_2}$$

$$\text{staggered tubes} \quad f = \left[ 0.23 + \frac{0.11}{(X_t-1)^{1.08}} \right] \left( \frac{D_o G}{\mu} \right)^{-0.15}$$

From Table X, the tube bank and inlet loss is 87 psi with the total injector loss 173 psi (assuming the element drop at row 1 equal to 86 psi).

At 524 lb/sec, the average $\rho\Delta P$ for S/N 020 injector is 340 lbm-lbf/in.$^2$ft$^3$ (see Appendix B). Therefore, normalizing this to design conditions results in a fuel injector pressure drop of 202 psi as compared to calculated losses, using the row-by-row and averaging methods of 231 psi and 173 psi, respectively.

6. Verification of Fuel Flowmeter Accuracy

The fuel flowmeter was not calibrated for cryogenics; therefore, the water calibration error estimates were based upon best engineering judgement (see Section IV,A,2). Two methods for determining the fuel flowmeter accuracy (element flow values from single-element testing and a mixer energy balance) follow. These data are from test No. 1.2-07-EHM-002.

(11) Kreith, F., Principles of Heat Transfer, International Text Book Co., 1958

TABLE X

INJECTOR PRESSURE PROFILE COMPARISON OF
ROW-BY-ROW AND AVERAGING METHODS

| | Row-by-Row Method - Pressure Loss, psi | Averaging Method - Pressure Loss, psi |
|---|---|---|
| Manifold Inlet | 18 | 15 |
| Element Row | | |
| 33 | 4.5 | |
| 32 | 4.7 | |
| 31 | 5.6 | |
| 30 | 4.1 | |
| 29 | 4.3 | |
| 28 | 3.8 | |
| 27 | 4.4 | |
| 26 | 3.4 | |
| 25 | 4.0 | 44 |
| 24 | 3.8 | |
| 23 | 3.9 | |
| 22 | 3.0 | |
| 21 | 3.9 | |
| 20 | 2.9 | |
| 19 | 4.0 | |
| 18 | 2.7 | |
| 17 | 4.9 | |
| 16 | 3.2 | |
| Baffle Base | 17.3 | 5 |
| 15 | 1.6 | |
| 14 | 2.9 | |
| 13 | 2.6 | |
| 12 | 2.5 | |
| 11 | 2.5 | |
| 10 | 2.5 | |
| 9 | 0.8 | |
| 8 | 1.2 | 23 |
| 7 | 2.0 | |
| 6 | 2.0 | |
| 5 | 2.0 | |
| 4 | 1.0 | |
| 3 | 1.3 | |
| Baffle Base | 10.9 | |
| 2 | 1.3 | |
| 1 | 1.5 | |
| Total | 145 | 87 |
| Row 1 Element | 86 | 86 |
| Total Injector Drop | 231 | 173 |

a. Single-Element Test

From single-element testing:

$K_W$ (1 element) = 0.0701 $\frac{lb^{1/2}\text{-in.}}{sec}$, see Section IV,E for definition of $K_W$

Therefore, the average element pressure drop equals:

$$\Delta P = \left(\frac{\frac{466 \times 0.898}{3248}}{0.0701}\right)^2 \frac{1}{0.0256} = 132 \text{ psi}$$

From Table IX, it is assumed that the average element weight flow occurs in row 18. From the row-by-row calculations, the tube bank pressure loss from row 18 to the manifold inlet is 62 psi at 466 lb/sec. Therefore, the calculated fuel injector pressure loss, utilizing an element flow constant, equals 194 psi.

The average manifold loss using "averaging" calculations equals:

$$\Delta P = \frac{72}{2} + 15 \left(\frac{466}{524}\right)^2 = 40 \text{ psi}$$

Therefore $\Delta P_{TOTAL}$ = 172 psi

The measured PfJ - Pc5D pressure drop for test No. 1.2-07 EHM-002 was 173 psi. This method of confirming the liquid hydrogen weight flow was considered less accurate because of the inaccuracies of calculated pressure losses.

b. Hydrogen Mixer Energy Balance

An energy balance check of the mixer follows:

where: $\dot{w}_f h_{mix} = \dot{w}_{GH_2} h_g + \dot{w}_{LH_2} h_L$ Equation (12)

Given: $T_{LH_2}$ = 49.6°R $h_{LH_2}$ = -30 B/lb

$T_{GH_2}$ = 523.5°R $h_{GH_2}$ = 1770 B/lb

$P_{MIXER}$ = 1615 psia

Therefore: $466.2\ h_{MIX} = 81.6\ (1770) + 384.6\ (-30)$

$h_{MIX} = 285$ B/lb

Thus, $T_{MIX} = 142.5°R$ at 1615 psia

The steady-state measured average fuel injector temperature was 143.2°R.

B. COMBUSTION STABILITY

The stability of the M-1 thrust chamber with respect to both low-frequency and high-frequency oscillations appears to be very good. During the two steps in the starting transient, some low-frequency oscillation (chugging) existed, but it disappeared as chamber pressure increased. These instabilities occurred at a chamber pressure of 250 psia and a frequency of 220 cps as well as a chamber pressure of 450 psia and a frequency of 250 cps.

The high-frequency stability aspect also was very encouraging in that a wide departure from the nominal operating conditions was required for pressure oscillations to be sustained.

1. Low-Frequency Stability

The possibility of sustained low-frequency stability was investigated analytically by means of a simplified approach.(12) This analysis was based upon the following major assumptions:

a. The frequency of oscillation is sufficiently low so that the wave effects in the combustion chamber can be neglected.

b. The combustion process can be represented by a single, constant time lag between the injection and combustion of each propellant and the injection element.

c. The resonance properties of the feed lines make no significant contribution to the dynamic behavior of the system. As a result, the maximum gain caused by resonance is assumed for all frequencies.

It should be noted that, while the above conservative assumptions indicate the theoretical possibility of low frequency instability, this instability may not be possible experimentally.

The first assumption is valid for frequencies below 100 cps, but it can be used up to 400 cps with reasonable accuracy.

(12) An experimental Investigation of Combustion Stability Characteristics at High Chamber Pressure, Final Report, Phase II, Aerojet-General Report No. 11741/SA6-F, Vol. 1, 25 August 1966

The second assumption was expected to give the best results in this application with the time lag based upon the oxidizer because it constitutes the greater portion of the weight flow.

The third assumption is highly conservative because it does not allow for phase stabilization. The resonant properties of the feed system are known to have a significant affect upon the dynamic behavior of the system, especially those feed system elements that are nearest to the injector. However, it was beyond the scope of the investigation undertaken to consider these effects.

This analysis, together with the occasional oscillations appearing on the test records, indicates that the M-1 thrust chamber can operate in the phase-stabilized region (one, wherein the resonant modes of the feed system do not couple with the combustion process because the combustion process total time lag falls between resonances) at steady-state conditions. Start transient data indicate that the M-1 engine passes through a low frequency stability boundary at a chamber pressure of 450 psia to 500 psia. This is primarily the result of low oxidizer weight flow and low oxidizer injection pressure drop. However, it is not known whether the apparent boundary results from phase stabilization caused by a changing total time lag or from gain stabilization caused by the increasing injection pressure drop.

The calculated stability limit for steady-state operation at nominal conditions is shown on Figure No. 45. The stability limit curve defines the neutral stability condition; above and to the right of it is the stable region (gain stabilized region), while below and to the left of it is the region wherein instability is possible (phase stabilized region). This particular stability limit curve is not altered significantly by the nominal range of mixture ratio variation or by the expected range of total time lag (1 millisec to 25 millisec). The nominal operating zone is based upon an L* of 40 in. to 42 in., a chamber pressure of 1000 psia to 1100 psia, an oxidizer injector pressure drop of 250 psia to 325 psia, and a fuel injector pressure drop of 160 psia to 170 psia.

The analytical results indicate that there is sufficient gain for the system to be unstable (see Figure No. 45). However, when the system was tested, it was stable as regards low frequency oscillations during steady-state, which indicates that it was phase-stabilized.

2. High-Frequency Stability

a. General Characteristics

The high-frequency instability occurred in a specific regime when the hydrogen temperature was lowered. As the temperature was ramped downward, instability occurred at a hydrogen temperature of approximately 80°R. However, the instability disappeared as the temperature was increased to approximately 100°R. Thus, the normal operating hydrogen temperature of 140°R provides a good margin of safety for high-frequency stability.

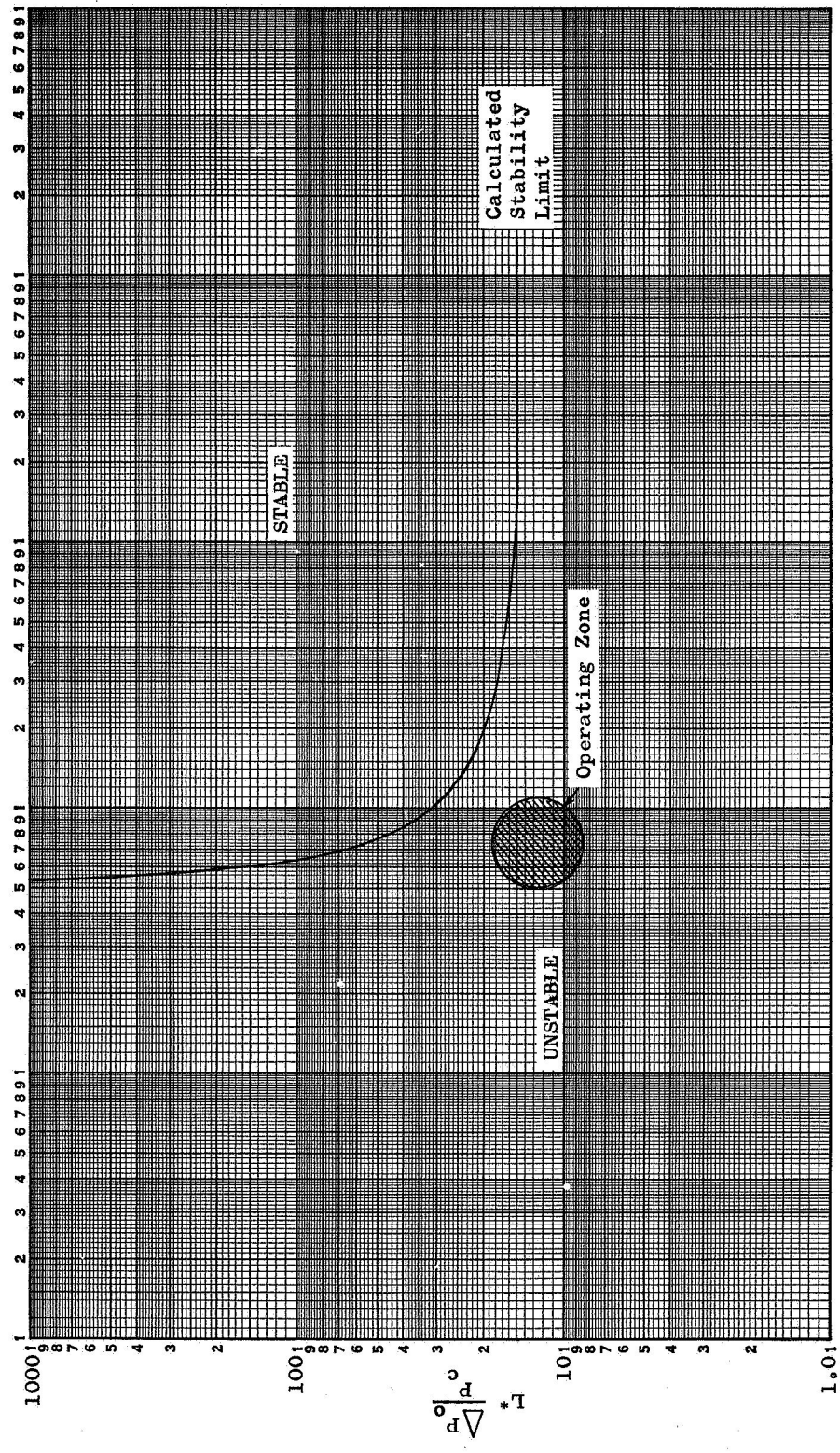


Figure 45. Amplitude vs. Frequency

Experimentally, the appearance of high-frequency instability could be directly related to hydrogen temperature; however, the factor often used in stability correlations is the injection velocity ratio (fuel/oxidizer). In the case of the M-1 injector, with its coaxial elements, it is hard to obtain a valid value of the velocity ratio because of the difficulty in obtaining actual pressures and temperatures at the injector face. However, despite this uncertainty, comparing the velocity ratio at the time of instability from one test to another yields relative values. Special care is needed in obtaining the data, particularly as regards the hydrogen temperature ramping rate. Stability limit velocity ratios were calculated for tests No. 1.2-07-EHM-006, -008, and -010, which had temperature ramping rates of 30°/sec, 17°/sec, and 5°/sec, respectively. The velocity ratios were 7.5, 7.8, and 7.9, which shows good consistency.

It was observed that the amplitude of the random combustion noise increased as hydrogen temperature decreased. This is illustrated by Figure No. 46. When the hydrogen temperature was decreased and then increased again during the same test (No. 1.2-07-EHM-009), the noise level first increased and then decreased (Figure No. 47). However, the amplitude was not unique for a given temperature, which indicated a dependence upon some other factor, such as mixture ratio or injection velocity.

As the noise level increased, a high order combustion disturbance was often observed. This disturbance was characterized by a sharp rise in chamber pressure (as much as 30% within 0.1 millisec). It appeared to be of a random nature in that it did not occur at any particular hydrogen temperature or combustion noise level. During one test, no disturbance was observed although the hydrogen temperature was lowered to 60°R. The stability of the thrust chamber in response to these disturbances was a function of the baffle system used as subsequently discussed.

b. Early Long Baffle Testing

The dynamic pressure data from the early 3-1/2-in. long baffle tests (No. 1.2-07-EHM-006 through -010) showed that no clearly periodic oscillations dominated and that the phase was continually changing, which indicated a possibility of numerous close frequencies. For this reason, the oscillations were analyzed for their spectral content. As a result, many peaks were observed between 6000 cps and 8000 cps. This is the resonant frequency range of the early helium bleed transducers; therefore, a detailed analysis was accomplished to determine the resonant frequencies as well as gain factors for the transducers actually used. This analysis is presented as Appendix D. It was found that the transducers had a gain factor of approximately 5 for frequencies of approximately 7000 cps. The amplitudes were corrected using this result as shown on Figure No. 48. However, this correction did not qualitatively alter the spectral content and it was concluded that one of the two major resonances in this high-frequency range represents a true combustion response.

TEST 1.2-07-EHM-025

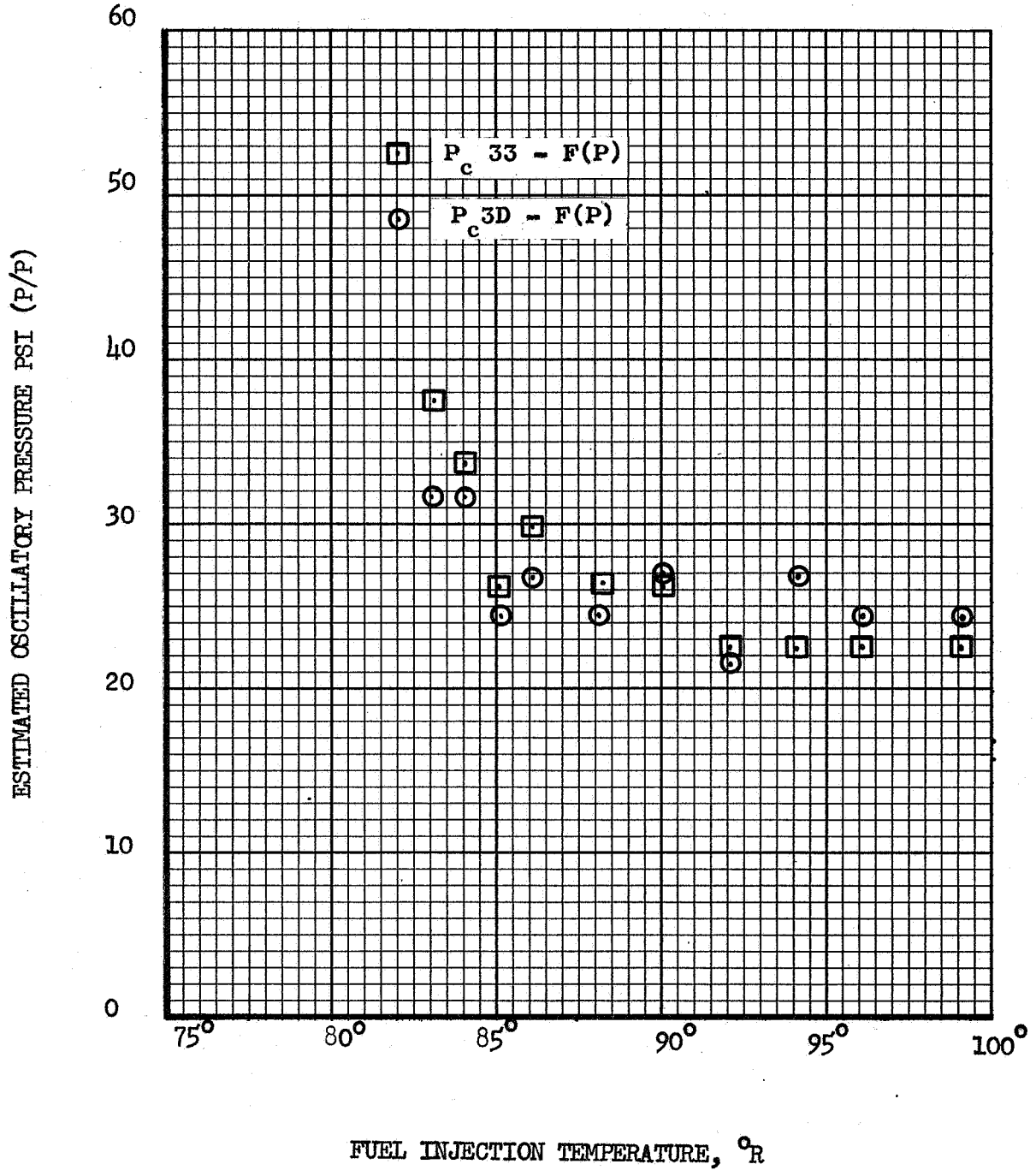


Figure 46. Estimated Oscillatory Pressure vs. Fuel Injection Temperature (Test 1.2-07-EHM-025)

TEST 1.2-07-EHM-009

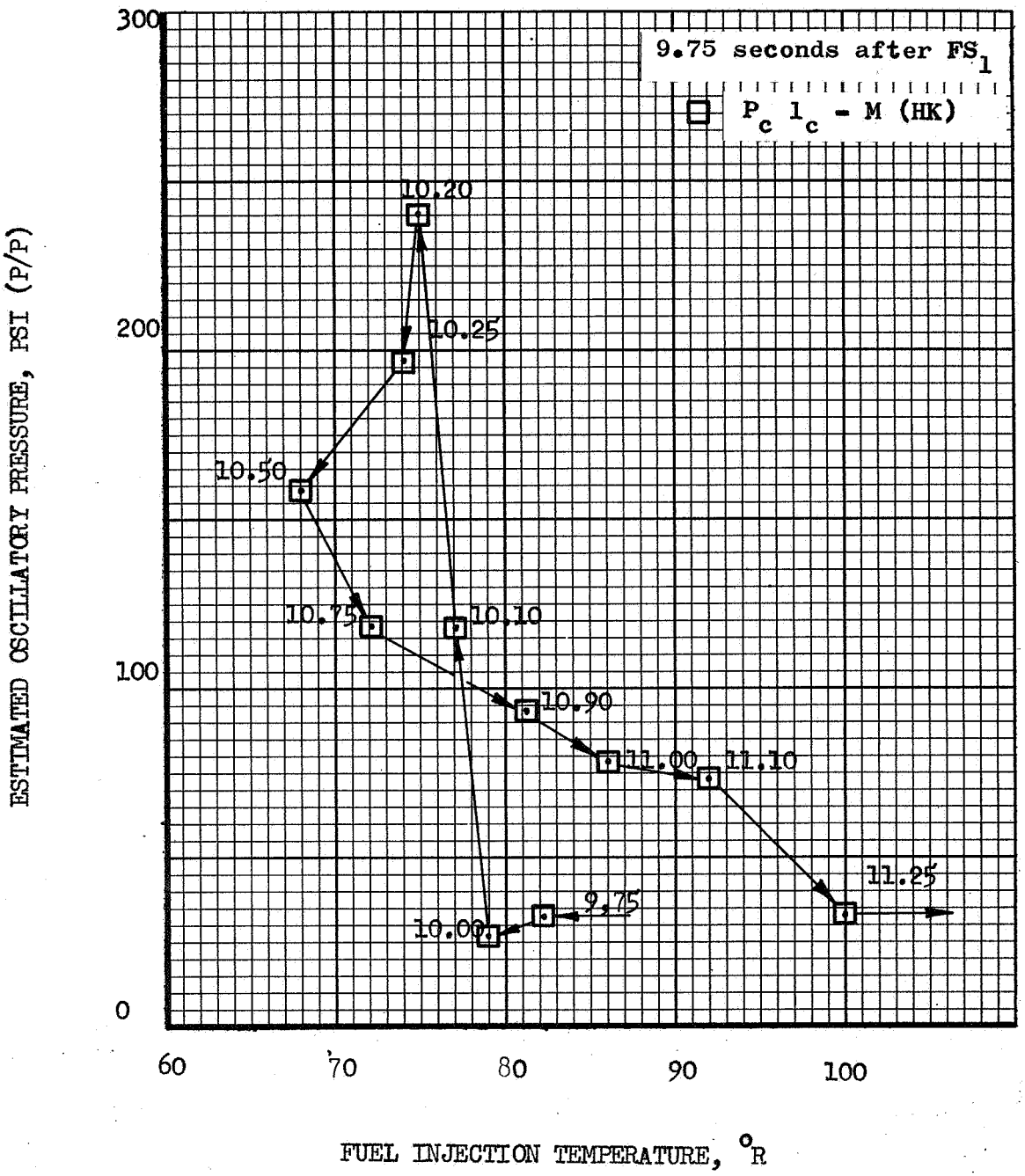


Figure 47. Estimated Oscillatory Pressure vs. Fuel Injection Temperature (Test 1.2-07-EHM-009)

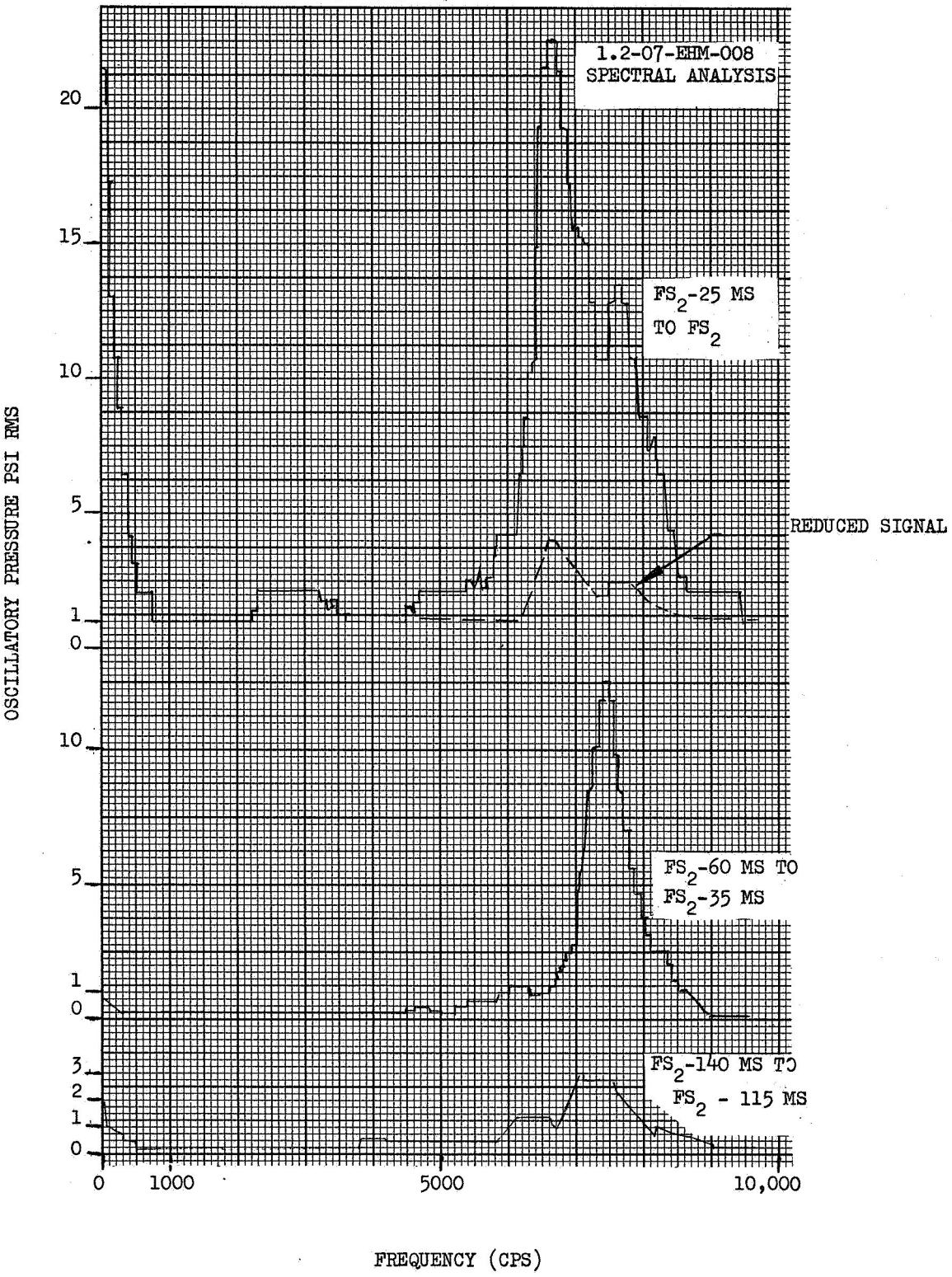


Figure 48. Oscillatory Pressure vs. Frequency

c. Short Baffle Testing

Tests No. 1.2-07-EHM-011 through -016 were performed with 1/2-in. baffles. When the hydrogen temperature was reduced during these tests, a well-ordered, high-amplitude, high-frequency (2700 cps) instability was observed, as illustrated by Figure No. 49. This resonant frequency of 2700 cps compared favorably with that predicted from the stability analysis (see Appendix A). However, there was not sufficient instrumentation to discriminate between the fourth tangential mode (2690 cps) and the combined first radial-first tangential mode (2700 cps) although the combined mode is more likely in view of its better spatial coupling with the injector design. A list of frequencies for various chamber modes is included on Table XI.

d. Recent Long Baffle Testing

Tests No. 1.2-07-EHM-017 through -025 were fired with a steel chamber, which included Photocon instrumentation, and with 3-1/2-in. long baffles. The Photocon pressure transducers had a resonant frequency of approximately 22,000 cps, with a flat response to approximately 10,000 cps. The dynamic pressure data obtained were similar to that from the early long baffle tests except that the spectral plots showed a wider range of coupling (see Figure No. 50). The sample times for the spectral analysis were selected to show the following:

- the combustion noise level.
- the nonlinear perturbation and the preferred decay frequency of the chamber.
- the increased noise level following the perturbation.
- the increase in noise level with the subsequent hydrogen temperature reduction.

From Figure No. 50, it appears that the baffles blocked the 2700 cps instability that was experienced during the short baffle tests. The high noise level accompanying the low hydrogen temperature, which was originally thought to be an instability, may be the result of poor mixing associated with the low hydrogen temperature, low hydrogen velocity, or both. Further analysis is required to define this mechanism more completely.

3. Conclusions

The M-1 thrust chamber is quite stable in the design temperature, pressure, and mixture ratio regime. Also, it is still very durable in low hydrogen temperature operation. The combustion resonant frequency is approximately 2700 cps and is well handled by the 3-1/2-in. long baffle. Dynamic stability has been implied by the successful damping of a previously existing instability by raising the hydrogen temperature above 100°R; however, it has not been demonstrated using the more conventional pulsing techniques.

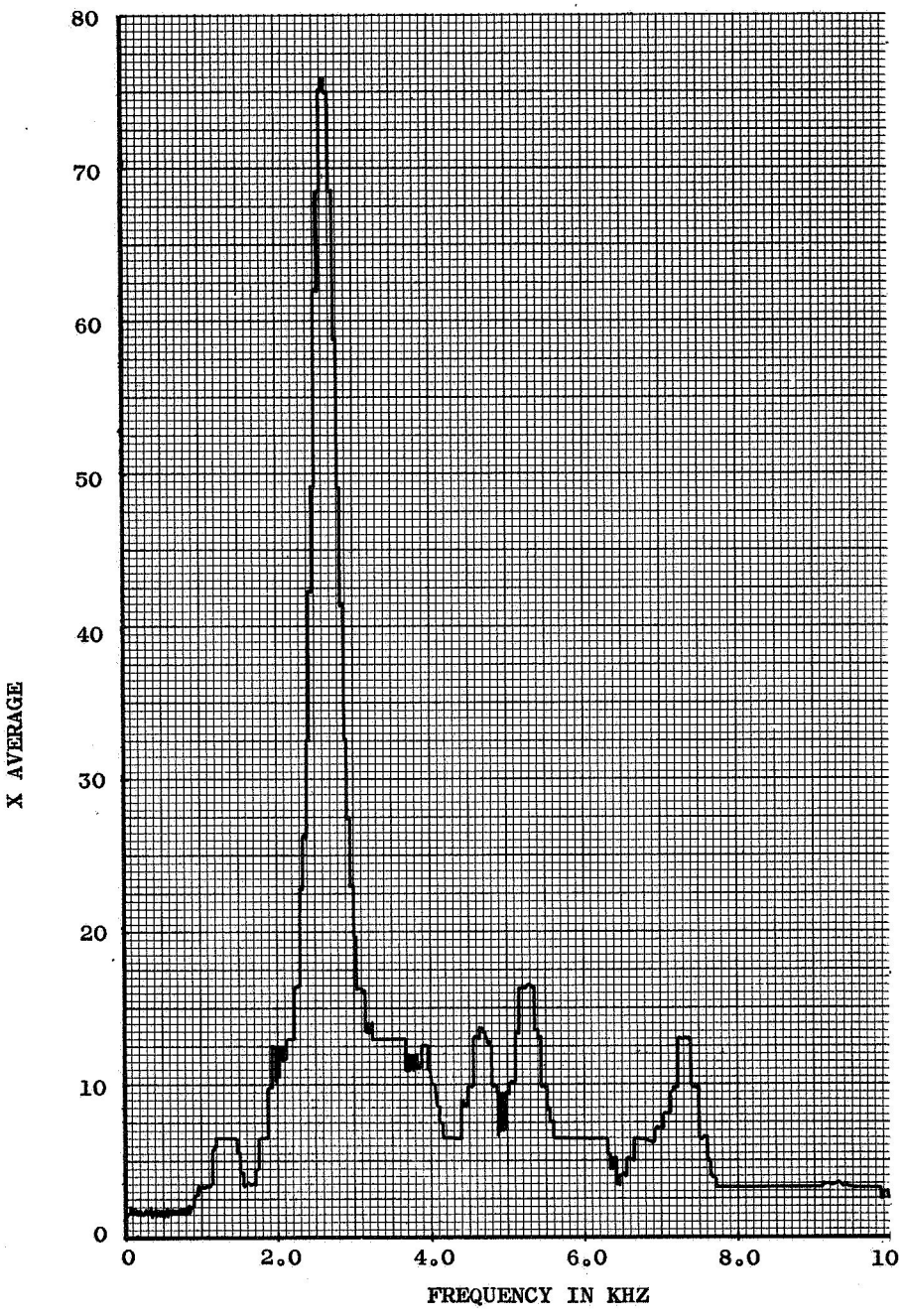


PC4C-M (HK) PSI RMS

TEST NO. 1.207-EHM-015B TEST DATE: 1-31-67
SPECTRUM SWEEP RANGE - 0 to 20 KHZ
DATA SAMPLE TIME - $FS_2$ -025 sec to $FS_2$ ($FS_2$ = 13.970 sec)
EFFECTIVE BAND WIDTH - 352 HZ
SPECTRUM SWEEP RATE - 1.0 sec
DATE PLOTTED - 2-16-67
COMPUTER PROGRAM NO. - 2902 REQUEST NO. - 5025

Figure 49. Frequency Curve for Test No. 1.2-07-EHM-015B

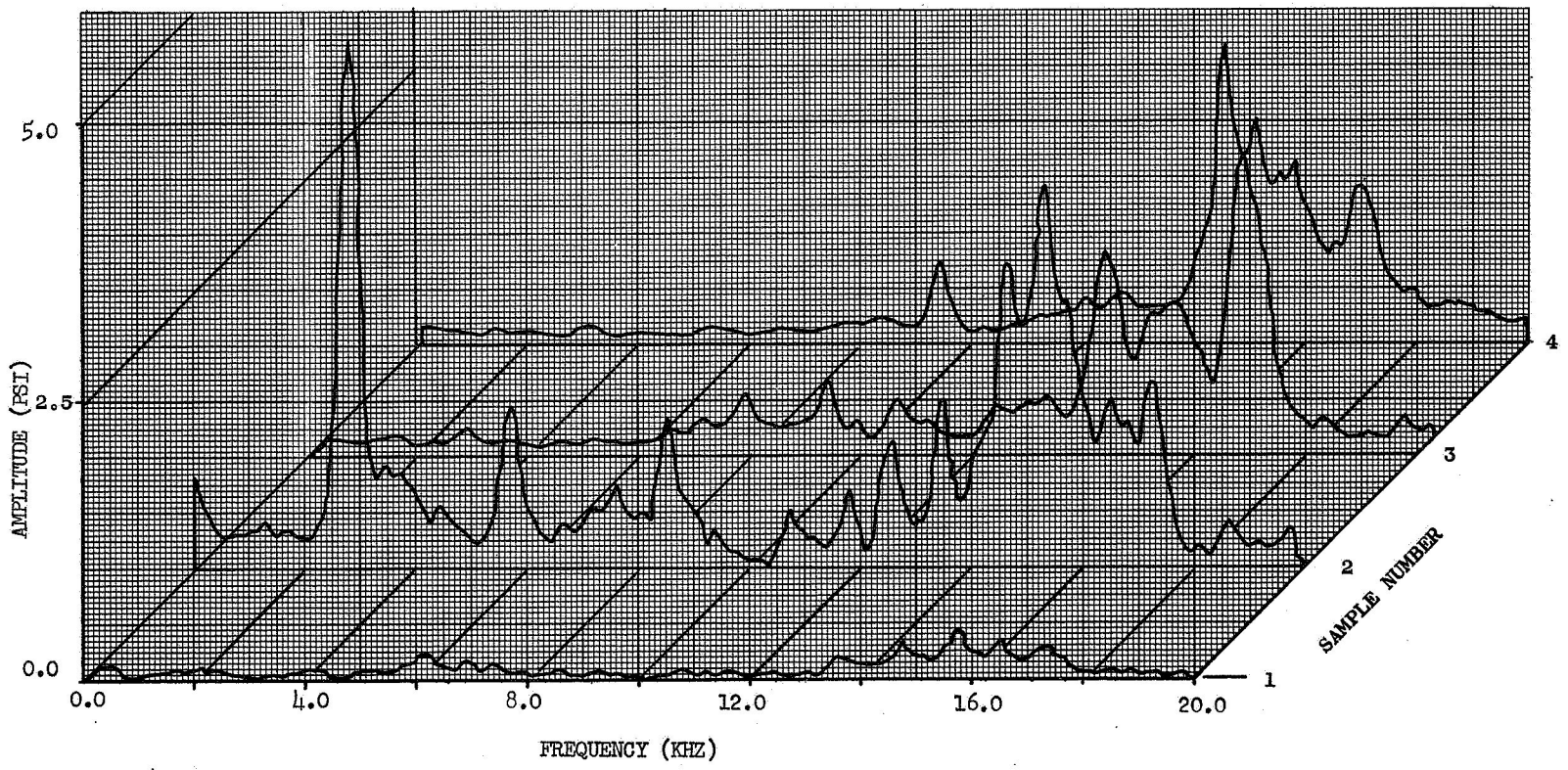


TEST NO. 1.2-07-EHM-020 (Pc1C)

| SAMPLE NO. | SAMPLE TIME (SEC) |
|---|---|
| 1 | $FS_2$ -.066 to $FS_2$ -.041 |
| 2 | $FS_2$ -.044 to $FS_2$ -.016 |
| 3 | $FS_2$ -.016 to $FS_2$ +.009 |
| 4 | $FS_2$ +.009 to $FS_2$ +.034 |

Figure 50. Amplitude vs. Frequency

TABLE XI

FREQUENCIES FOR VARIOUS CHAMBER MODES

ACOUSTIC MODES:

| Mode | Frequency, cps | Mode | Frequency, cps | Mode | Frequency, cps |
|---|---|---|---|---|---|
| 1T | 930 | 1R | 1940 | 3T+2R | 5740 |
| 2T | 1540 | 1T+1R | 2700 | 4T+2R | 6420 |
| 3T | 2130 | 2T+1R | 3395 | 5T+2R | 7080 |
| 4T | 2690 | 3T+1R | 4055 | 6T+2R | 7725 |
| 5T | 3250 | 4T+1R | 4700 | 3R | 5150 |
| 6T | 3800 | 5T+1R | 5325 | 1T+3R | 5925 |
| 7T | 4340 | 6T+1R | 5940 | 2T+3R | 6665 |
| 8T | 4880 | 7T+1R | 6545 | 3T+3R | 7380 |
| 9T | 5420 | 8T+1R | 7145 | 4T+3R | 8080 |
| 10T | 5950 | 2R | 3550 | 4R | 6750 |
| 11T | 6490 | 1T+2R | 4315 | 1T+4R | 7520 |
| 12T | 7040 | 2T+2R | 5045 | 2T+4R | 8275 |

POCKET MODES:

| Mode | Frequency, cps |
|---|---|
| Tangential in 1 outer pocket | 3800 |
| Tangential in 1 inner pocket | 4250 |
| 1R in outer pockets | 3200 |
| 1R in inner pockets | 3980 |

NOTE: Calculations are based upon a speed of sound of 5300 ft/sec and a chamber diameter of 40 in.

C. HEAT TRANSFER

1. Injector Face

The tests of injector S/N 020 showed that coolant flow through the Rigimesh face was adequate at steady-state as well as peripheral and nominal operating conditions. Figures No. 51 through No. 54 show representative sections of the face of this injector after the tests and indicated steady-state exposure times*. Operating conditions can be obtained from Table VII. It is apparent that no erosion or significant heat marking of the face occurred.

The test results with injector S/N 012 are not as conclusive although adequacy is indicated. Severe heat marking and significant erosion occurred on portions of this injector during its second test (No. 1.2-07-EHM-006). There were no heat marking or erosion during the initial test. No significant increase in heat marking or erosion was displayed in the tests following -006. This indicates that the erosion could have resulted from abnormal conditions encountered during that one test. The abnormal condition in test No. -006 was the lowering of the hydrogen inlet temperature to approximately 54°R after instability appeared at approximately 80°R. This would increase the fuel density and adversely affect fuel flow distribution, causing overheating. No instability occurred in the first test. In subsequent tests, temperatures were not permitted to decrease below 65°R. Figures No. 55 through No. 59 show portions of the injector after test No. 1.2-07-EHM-010. The darker areas on Figures No. 55, No. 56, and No. 57 indicate the eroded and heat marked zones. Note that, in Figure No. 58, erosion or heat marking are not apparent in the center portions of the injector. Similar zones can be seen on subsequent photographs used to illustrate baffle erosion. Figure No. 59 is an enlarged view showing typical worst-case erosion in these darkened areas.

This injector experienced a total of 13 instabilities. Figure No. 60 shows the injector face after the final test No. 1.2-07-EHM-025. Minor increase in face damage over that of test No. 1.2-07-EHM-010 (Figures No. 49 and No. 53) is evident in the inner baffle compartments.

With available analysis methods, a cause for the erosion sustained in test No. 1.2-05-EHM-006 could not be established. However, analysis of the flow and cooling characteristics of the Rigimesh did indicate that an increase in the gas-side heat transfer coefficient or a decrease in coolant flow resulting from chamber pressure oscillations is required to initiate the erosion. This increase in coefficient could result from locally high velocities resulting from unstable combustion or either steady or intermittent combustion within the element recess. The potential affects of unstable operation were discussed in Section IV,B of this report.

*Steady-state exposure time is defined as test duration above 90% of chamber pressure.

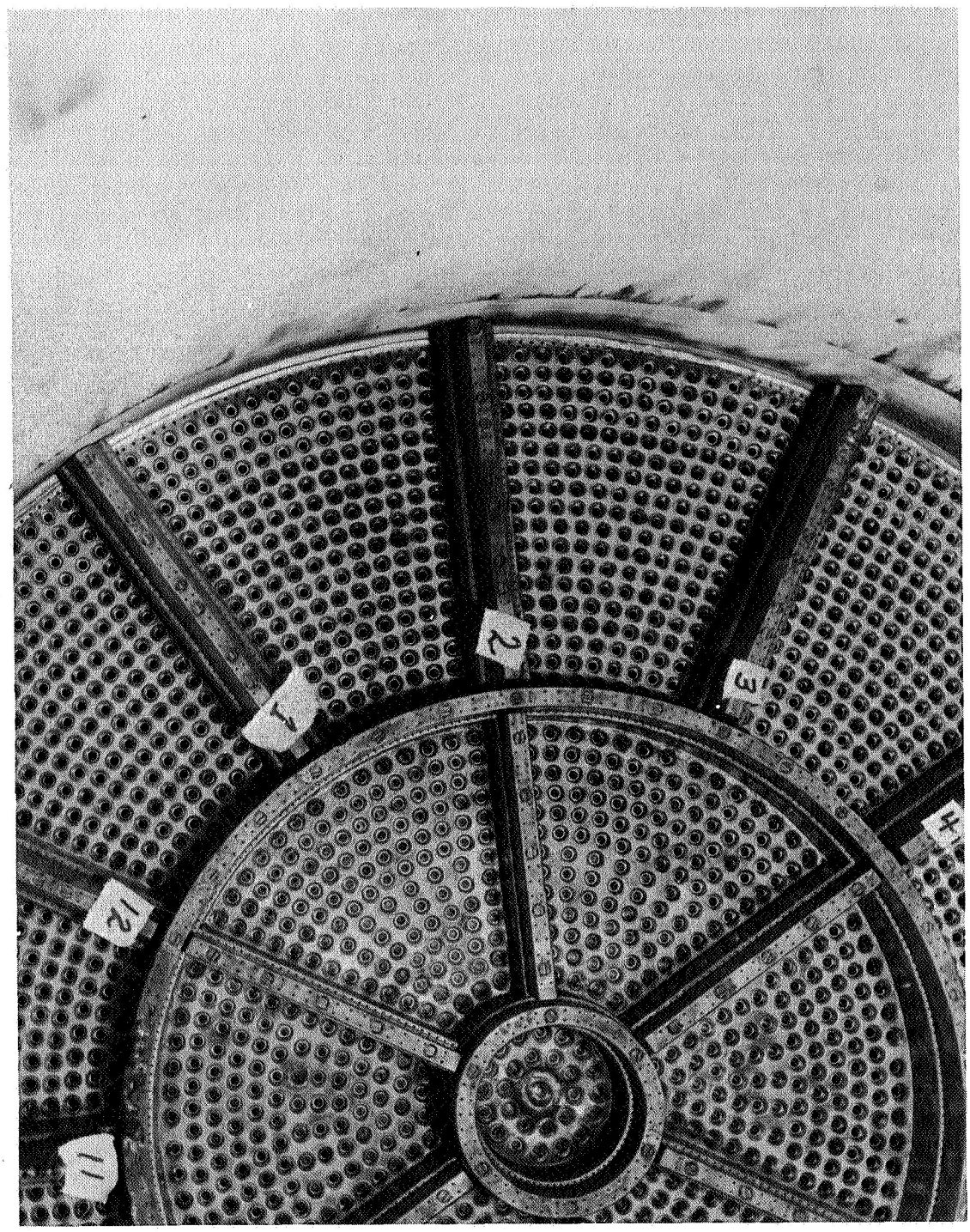

Figure 51. S/N 020 TCA Injector after 2.7 sec of Testing

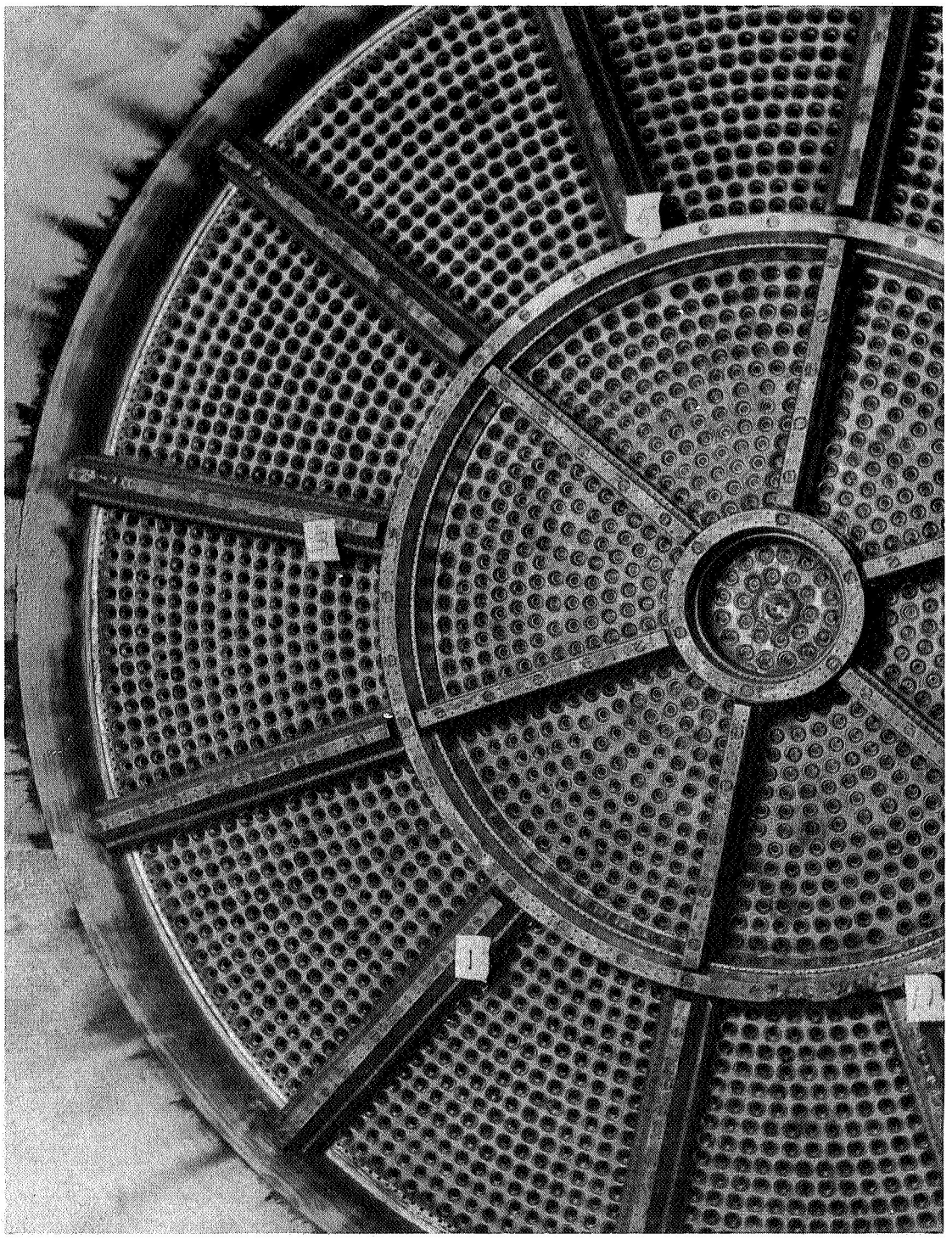

Figure 52. S/N 020 TCA Injector after 6.4 sec of Testing

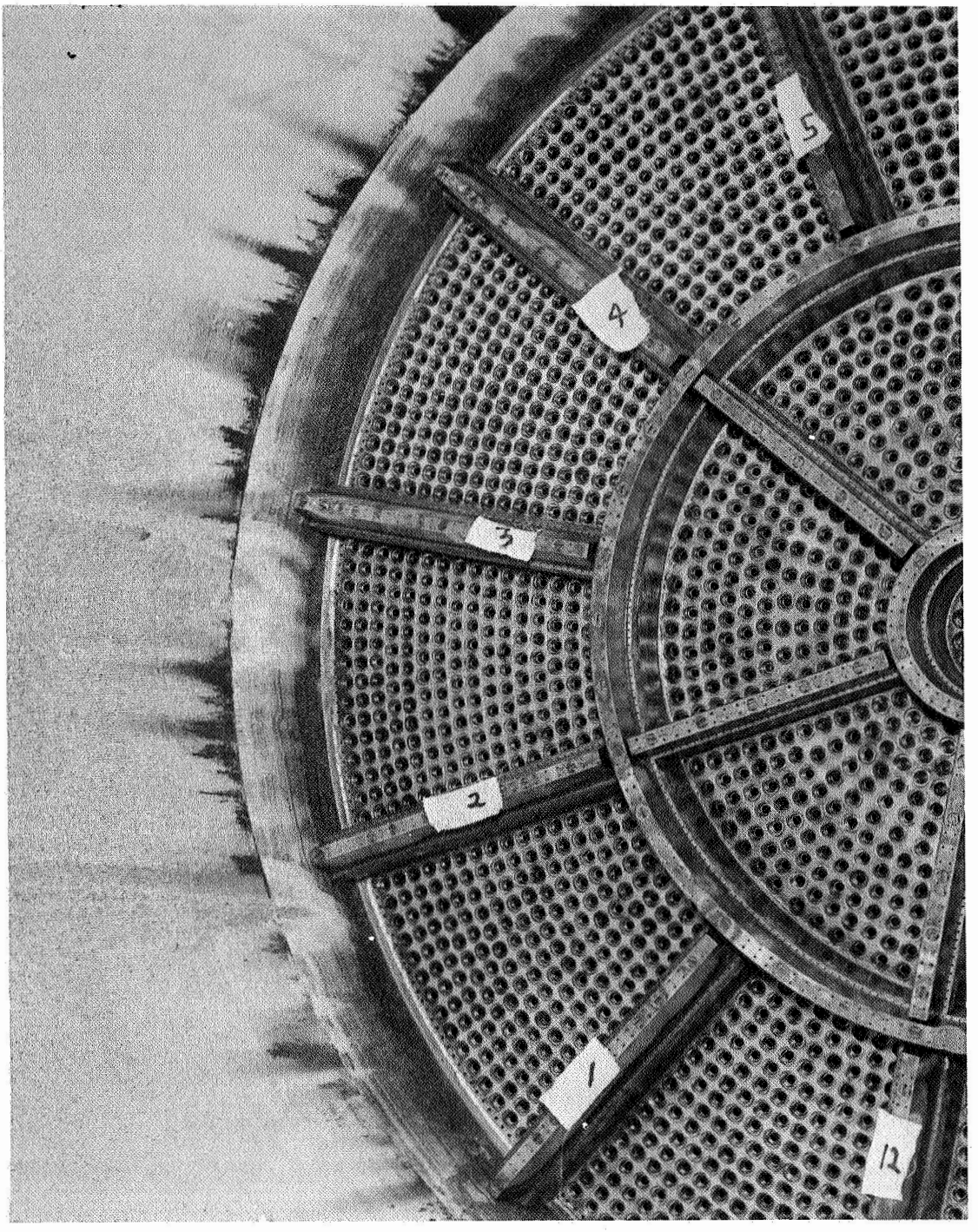


Figure 53. S/N 020 TCA Injector after 10.0 sec of Testing

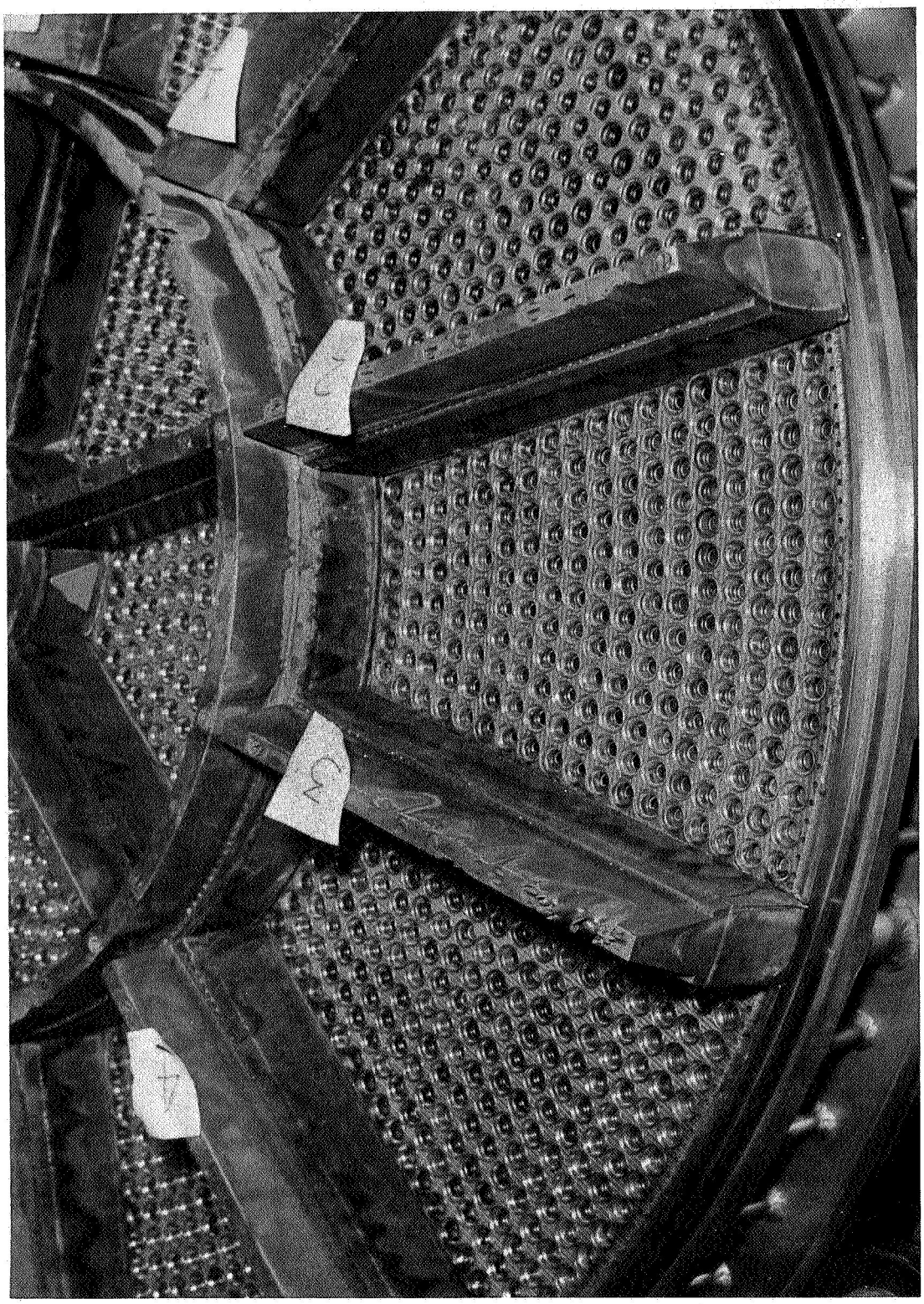

Figure 54. S/N 020 TCA Injector after 30.1 sec of Testing

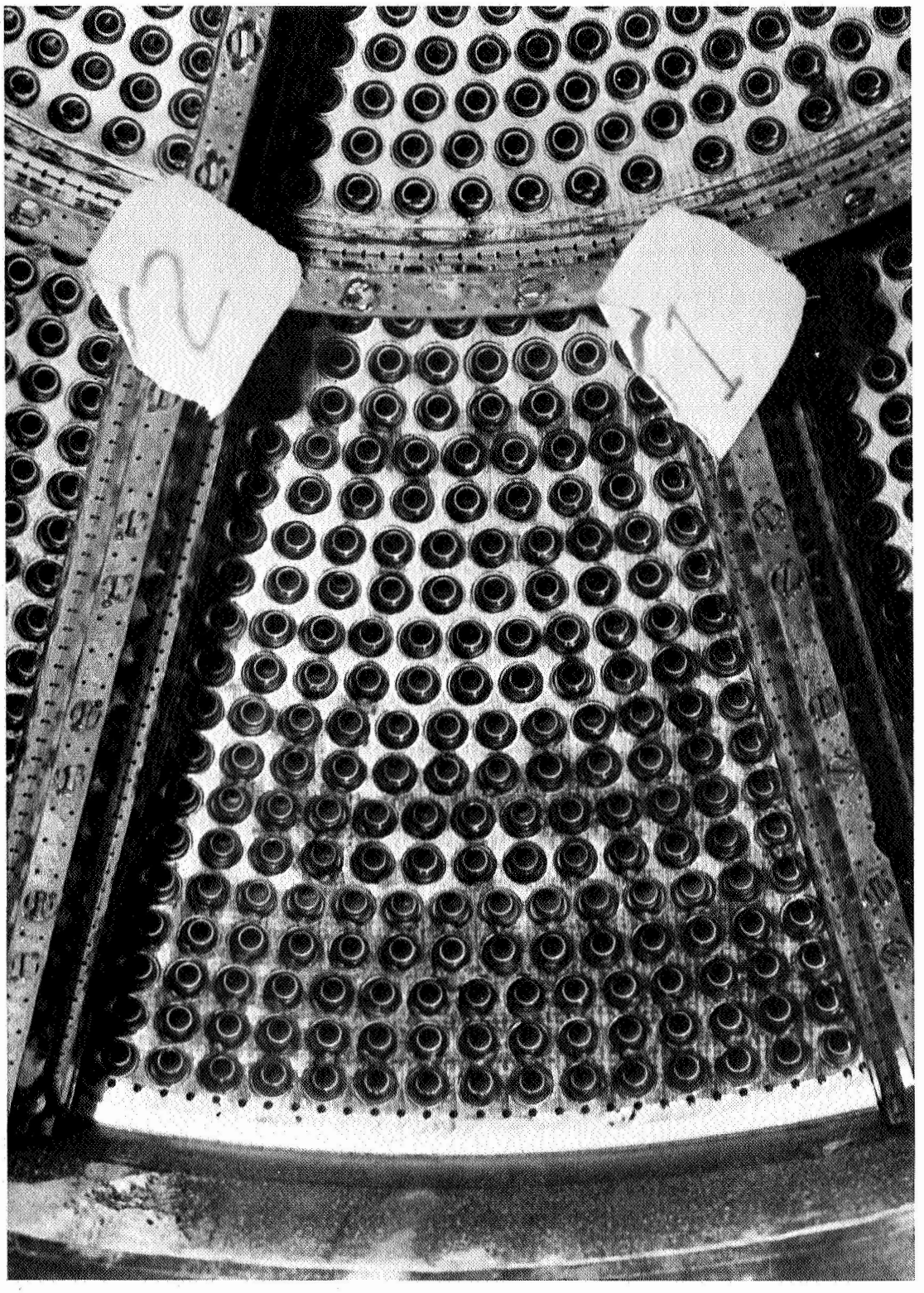

Figure 55. S/N 012 TCA Injector after Testing

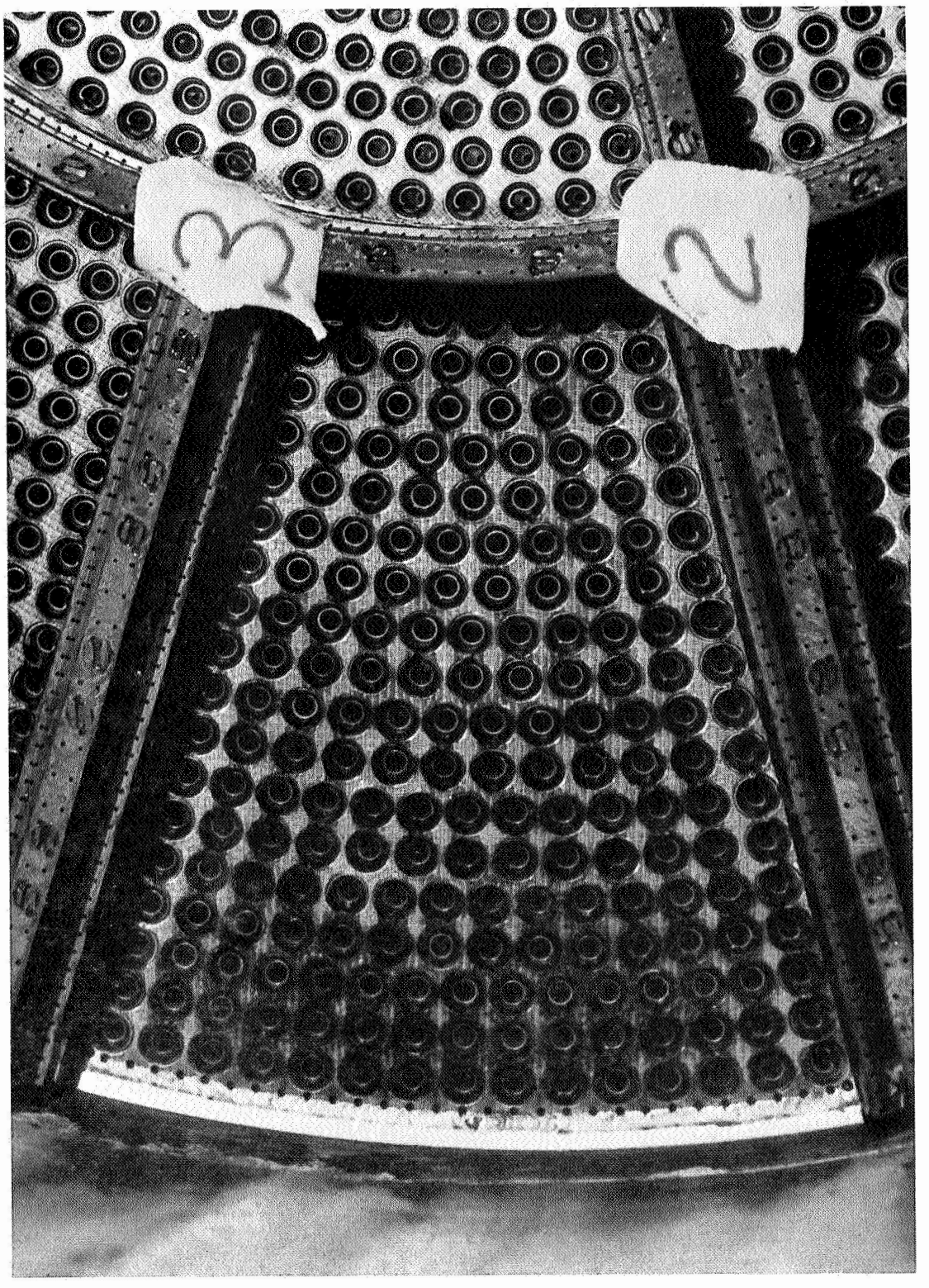

Figure 56. S/N 012 TCA Injector after Testing

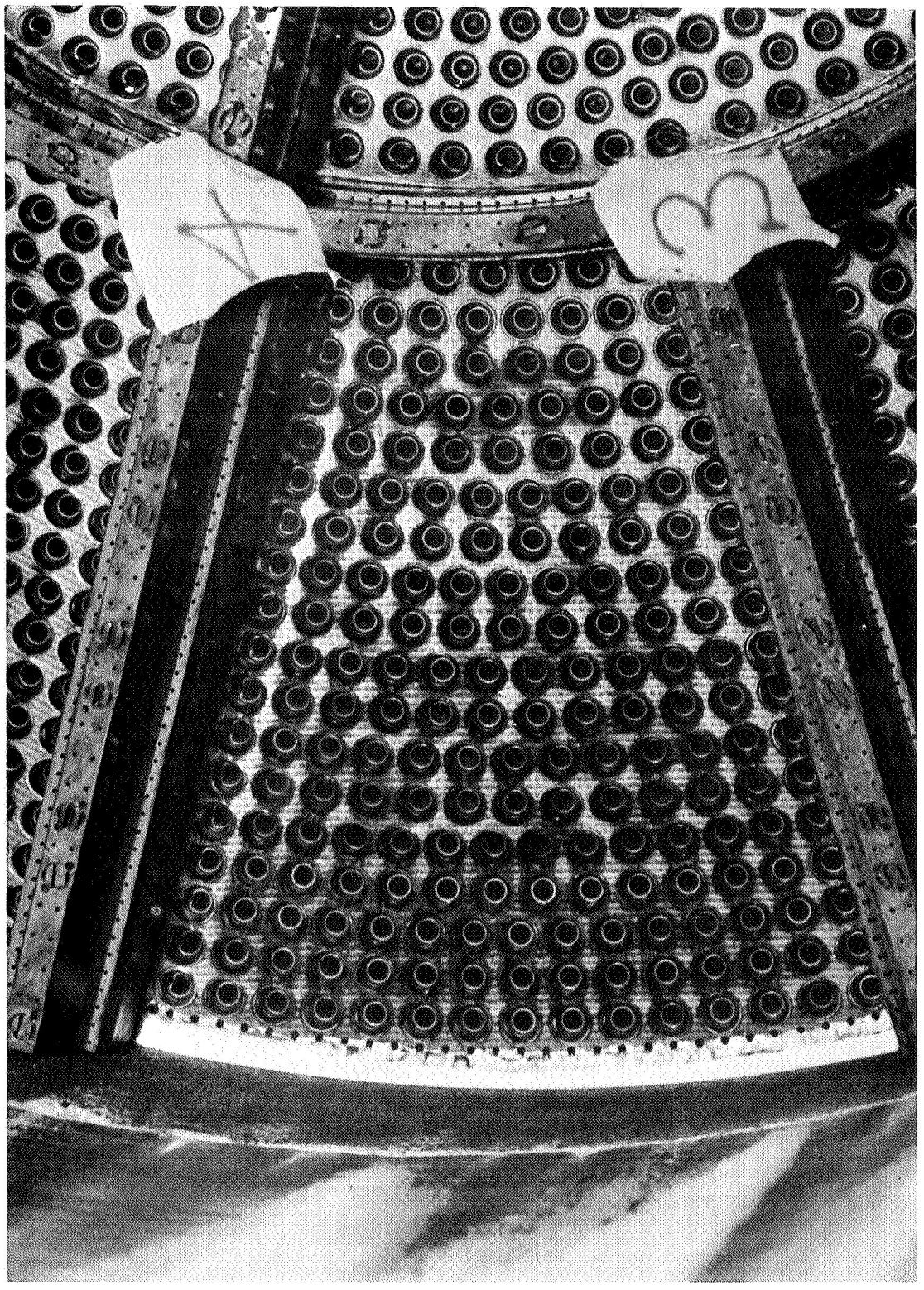

Figure 57. S/N 012 TCA Injector after Testing

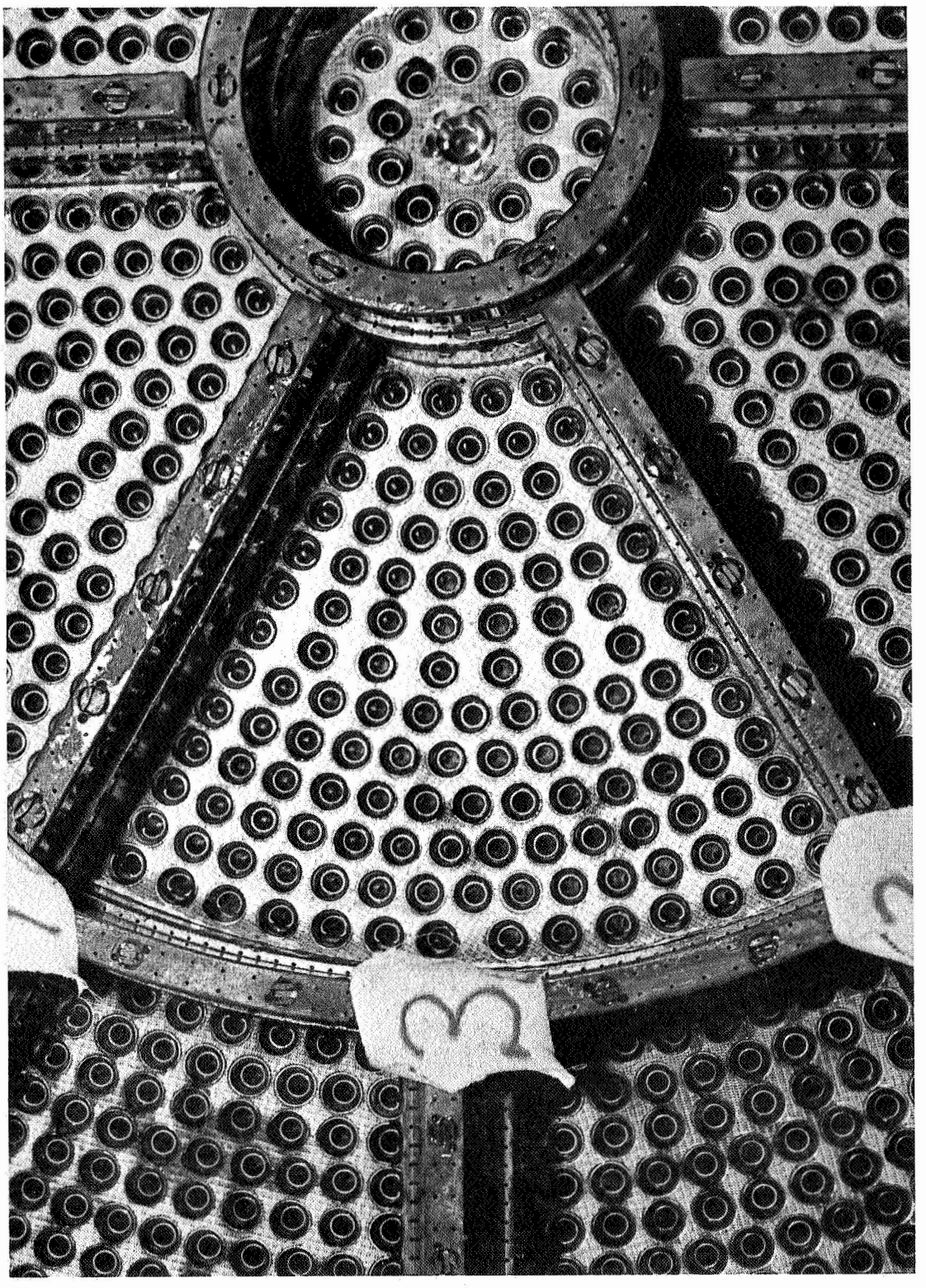

Figure 58. S/N 012 TCA Injector after Testing

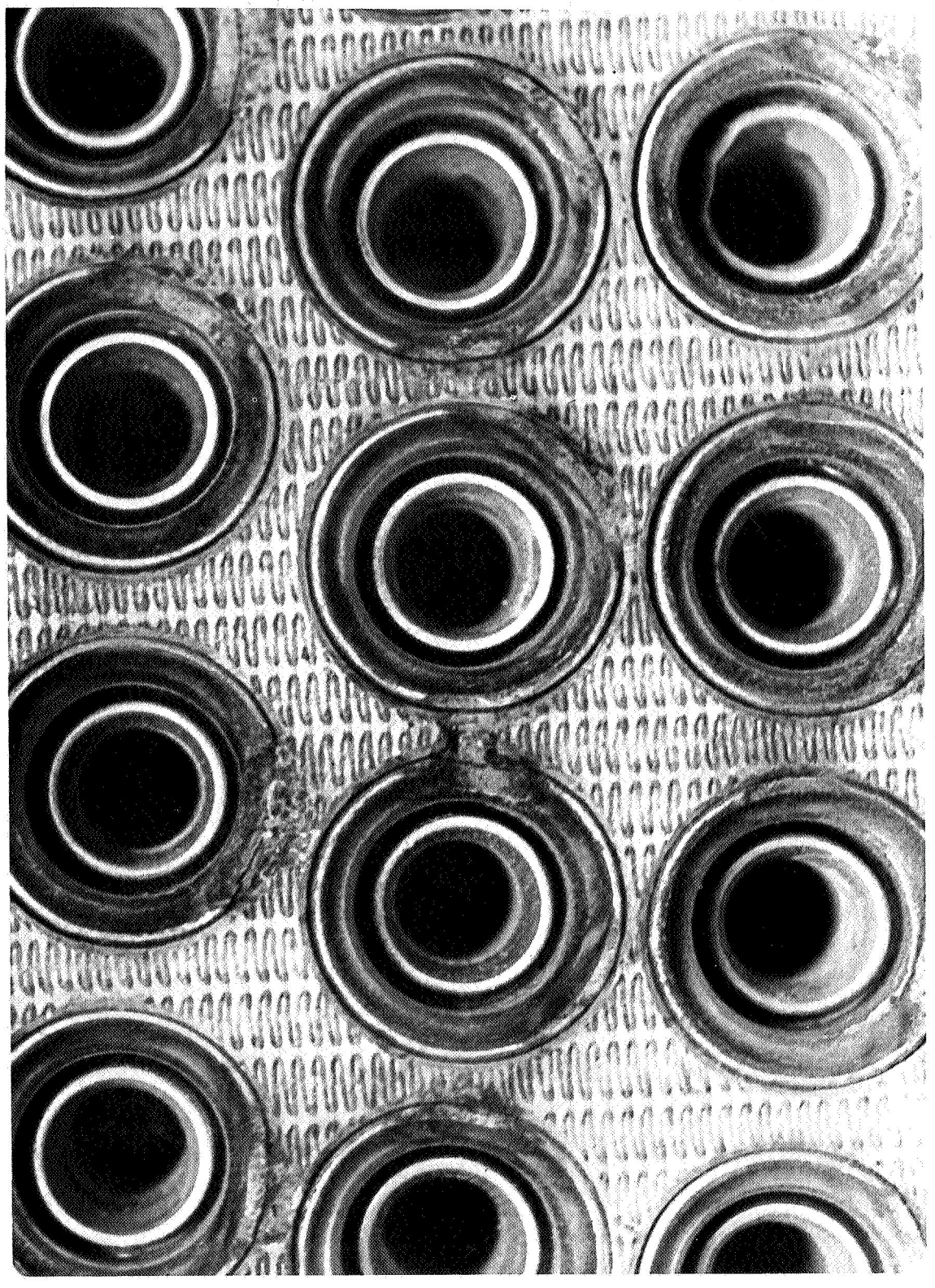

Figure 59. S/N 012 TCA Injector after Testing

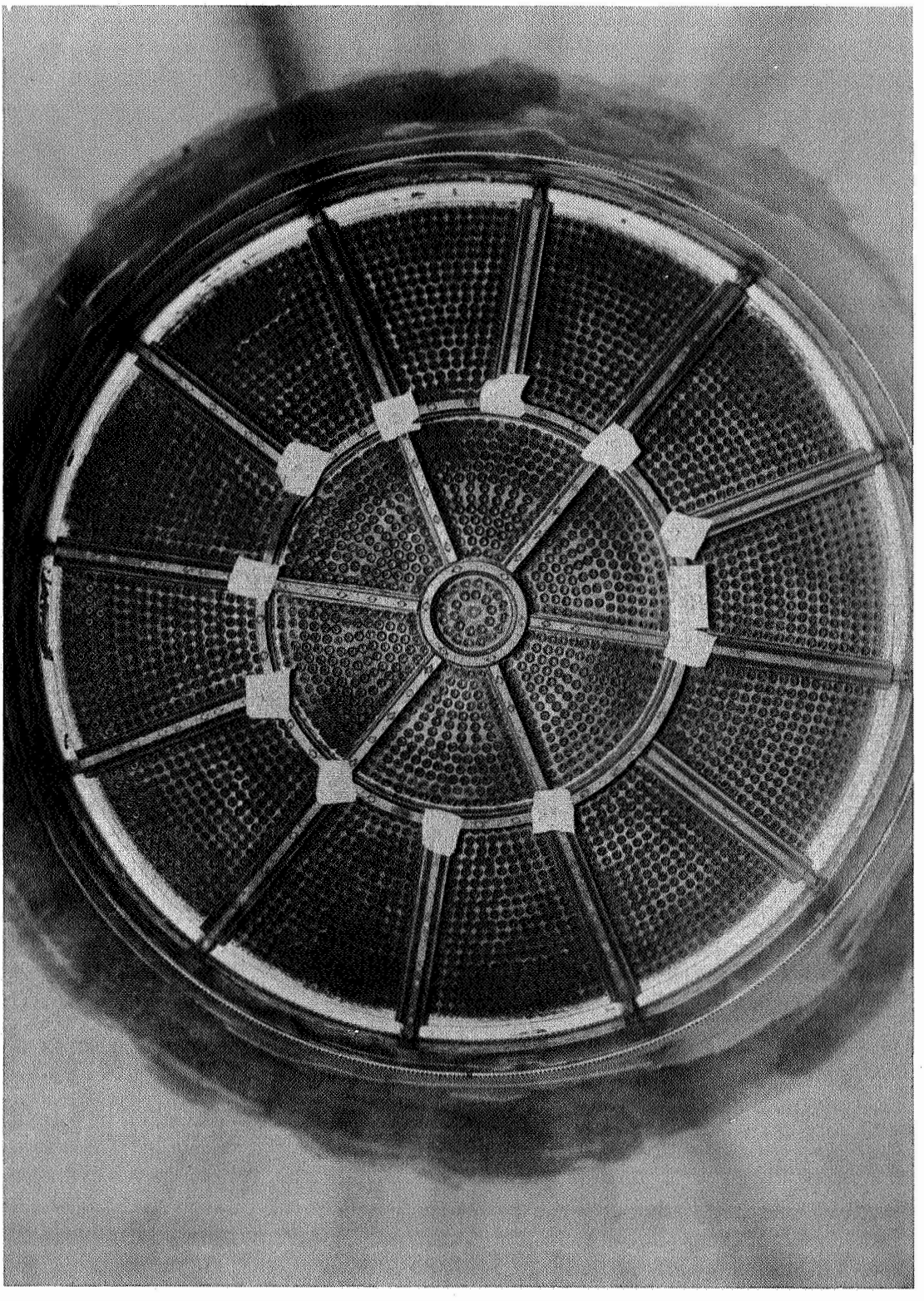

Figure 60. S/N 012 TCA Injector after Final Test

2. Baffles

The test results indicate that the cooling for the outer baffle legs was marginal. Substantial erosion occurred during the tests with injector S/N 020 and minor erosion occurred on the injector S/N 012 baffles. Figures No. 61 through No. 70 show typical baffle appearances after the tests and indicated accumulated durations at steady-state. Operating conditions can be found in Table VII.

Figures No. 61 and No. 62 show injector S/N 020 baffles after the initial test at rated thrust. No erosion occurred during the initial partial thrust start transient evaluation tests. As can be seen from the figures, erosion was quite severe on some portions of the baffles while completely absent on other portions. On Figure No. 61, the most severely eroded is baffle 8 with baffle 7 showing no erosion, while baffle 6 shows severe erosion on the outer 2 in. with little or no erosion inboard. Erosion of the outer ring baffle can be seen adjacent to baffle 11 and between baffles 8 and 9 as well as 9 and 10. It also can be seen that no erosion of the ring occurred between baffles 3 and 8. The same type of scattered erosion can be observed on Figure No. 62 with baffle 11 being severely eroded, 10 being severely eroded at the periphery, and 12 showing very little erosion. It can be noted on both figures that the inner ring and inner baffle legs show no erosion.

Figure No. 63 shows these same baffles after the next steady-state test (No. 1.2-05-EHM-008). Test No. 1.2-05-EHM-007 was shut down manually before steady-state was reached as a result of the indicated fuel flow drop being misinterpreted. It can be noted in this figure that only minor increases in the erosion appear to have occurred. No erosion is yet evident on the inner ring and leg baffles or on outer baffle 7. Prior to the next test, outer leg baffles 8 and 11 were removed and replaced by legs with the film cooling and tip injection holes in the outer 2 in. opened to increase this area by approximately 15%.

Figure No. 64 shows the same area of the injector after the next test. There was no major change in the previously eroded areas and no significant new areas of erosion can be seen. The relatively minor erosion of the new baffles 8 and 11 also can be seen.

Figure No. 65 shows the same areas of the injector and baffles after five additional tests (tests No. 1.2-05-EHM-010 and 1.2-07-EHM-001 through -004). This photograph was taken after the hardware was removed from the stand and the ablative combustion chamber had been removed. Definite indications of melting of the copper and resolidifying downstream are shown on baffle 8 and on the ring between baffles 8 and 9. There is an absence of

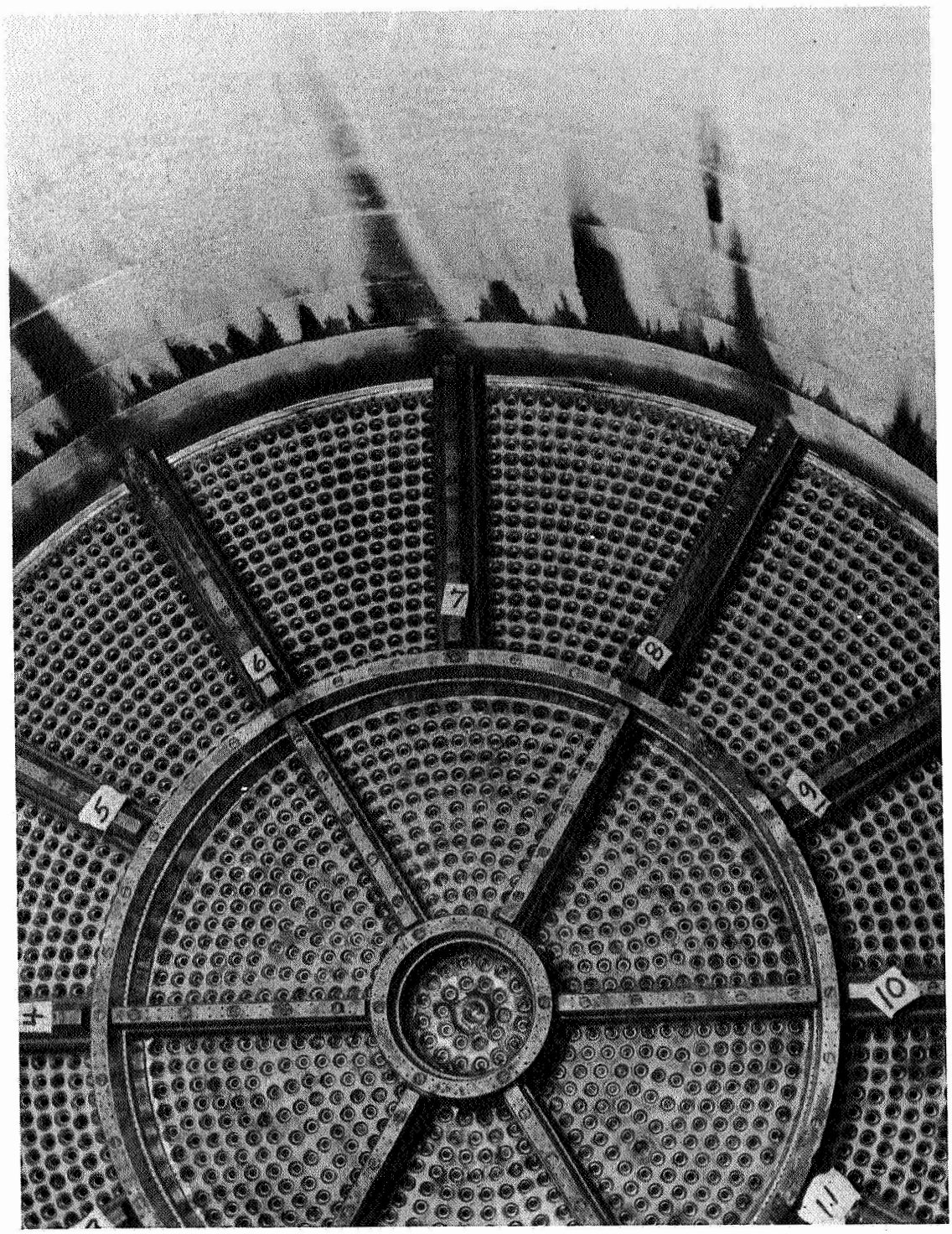


Figure 61. S/N 020 Injector Baffles after Initial Test at Rated Thrust

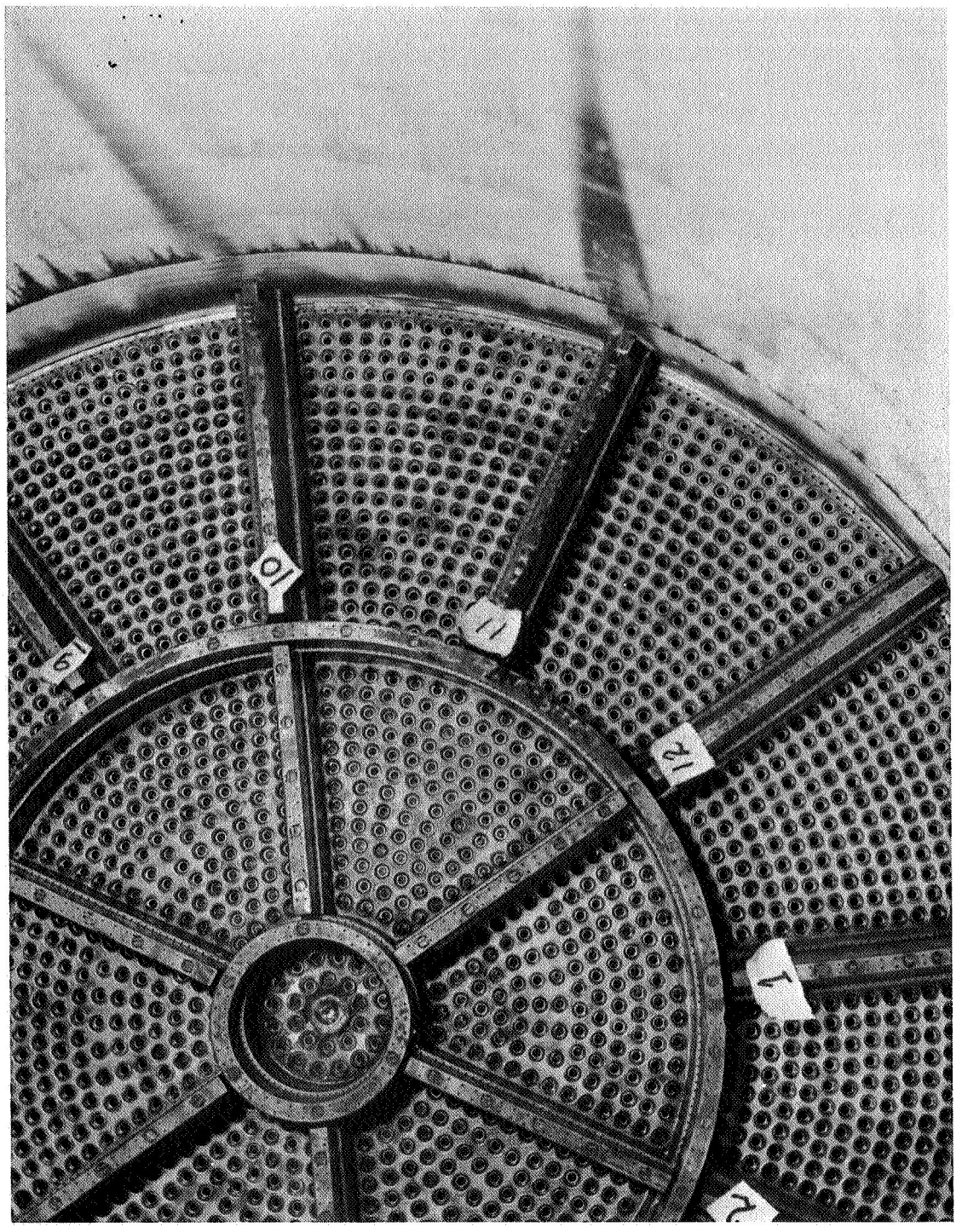

Figure 62. S/N 020 Injector Baffles after Initial Test at Rated Thrust

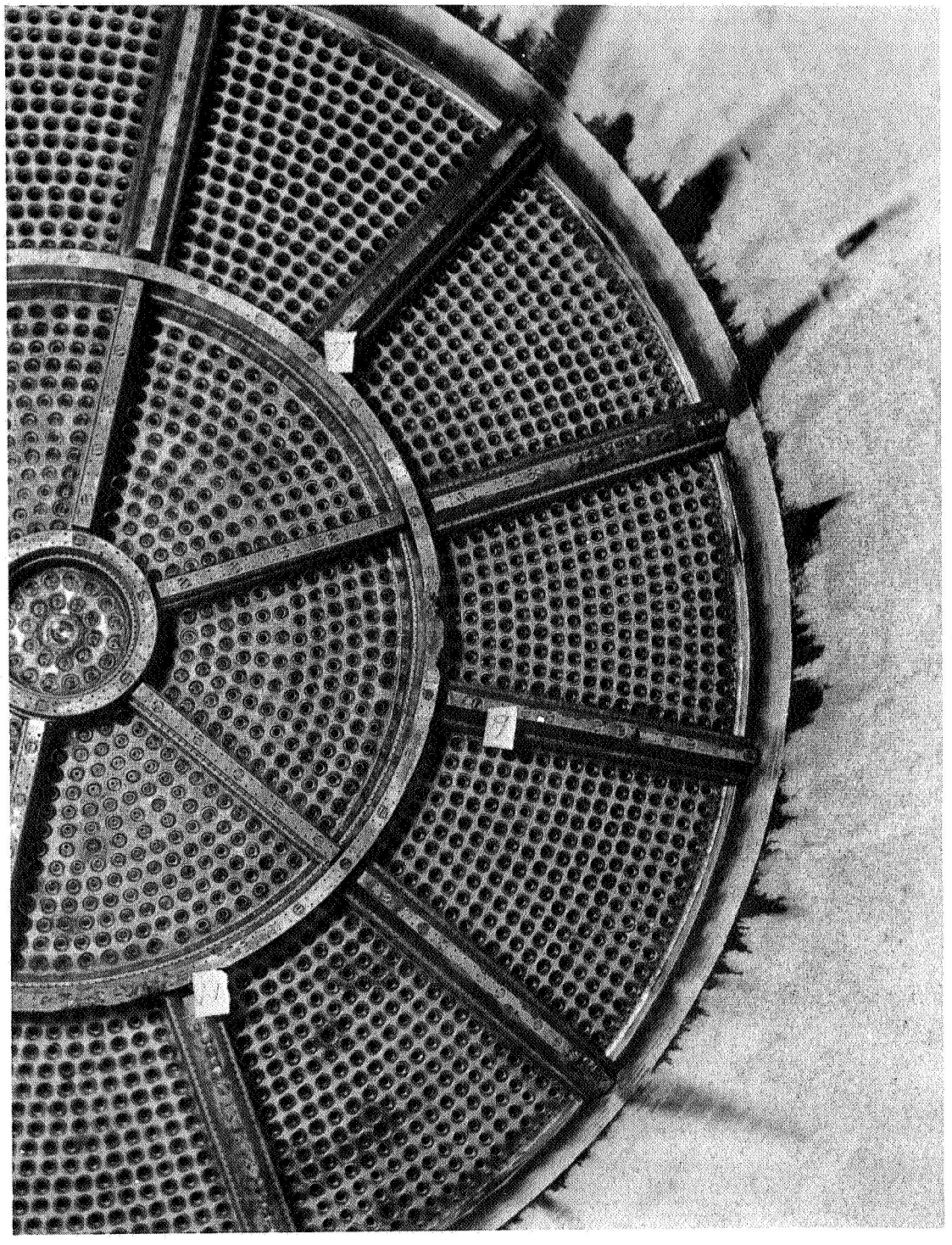

Figure 63. S/N 020 Injector Baffles after Test No. 1.2-05-EHM-008

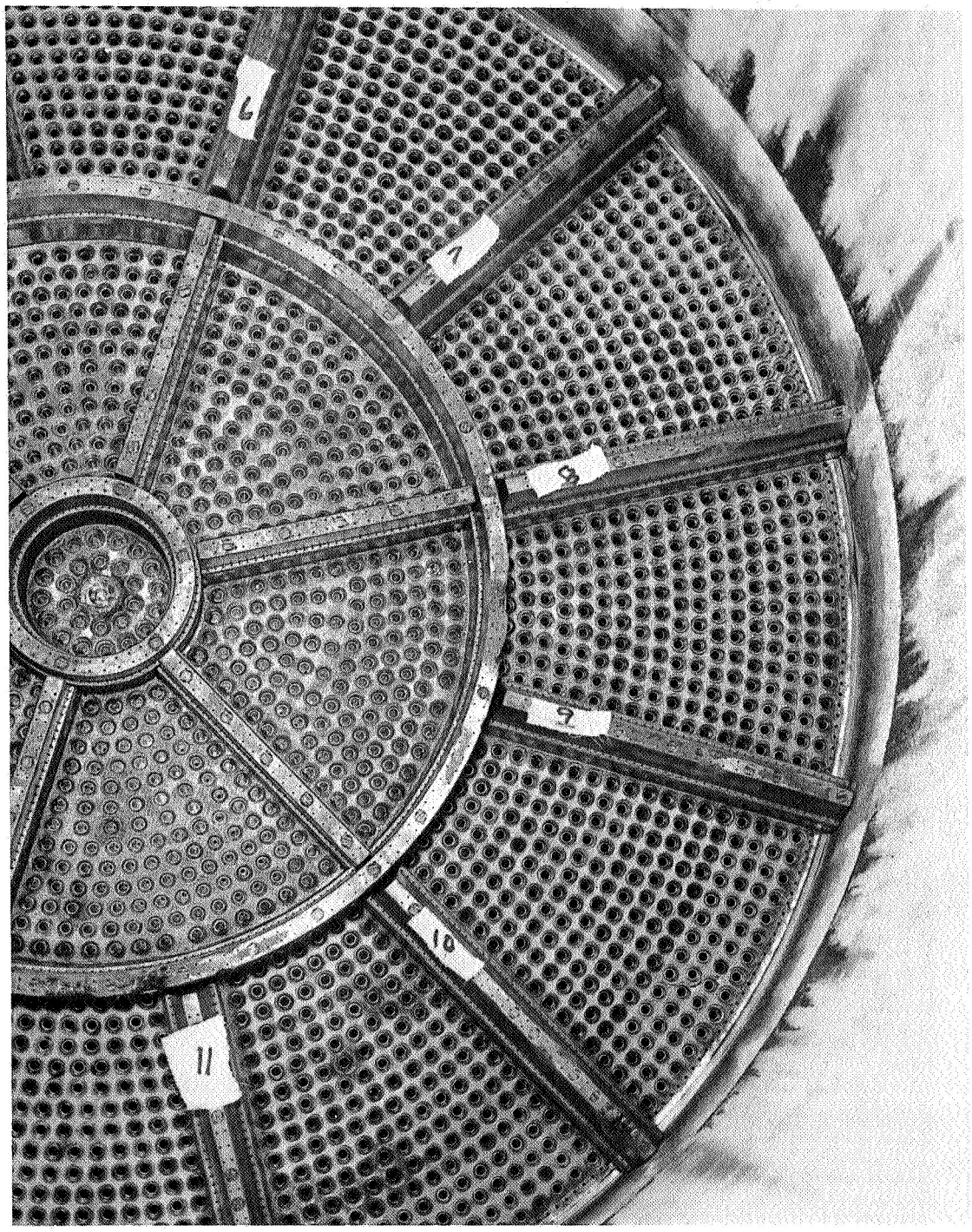


Figure 64. S/N 020 TCA Injector after Testing

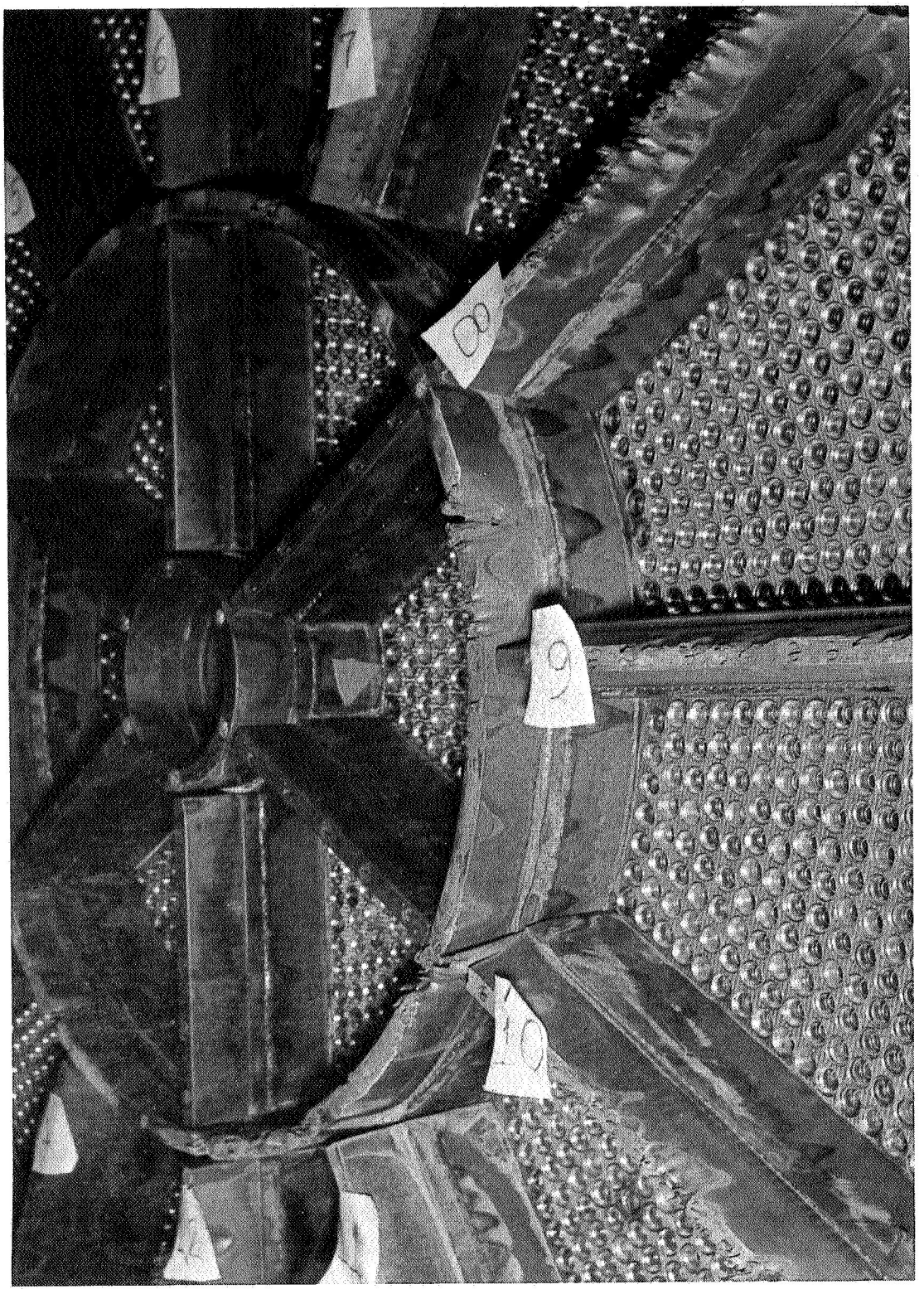

Figure 65. S/N 020 TCA Injector after Five Additional Tests

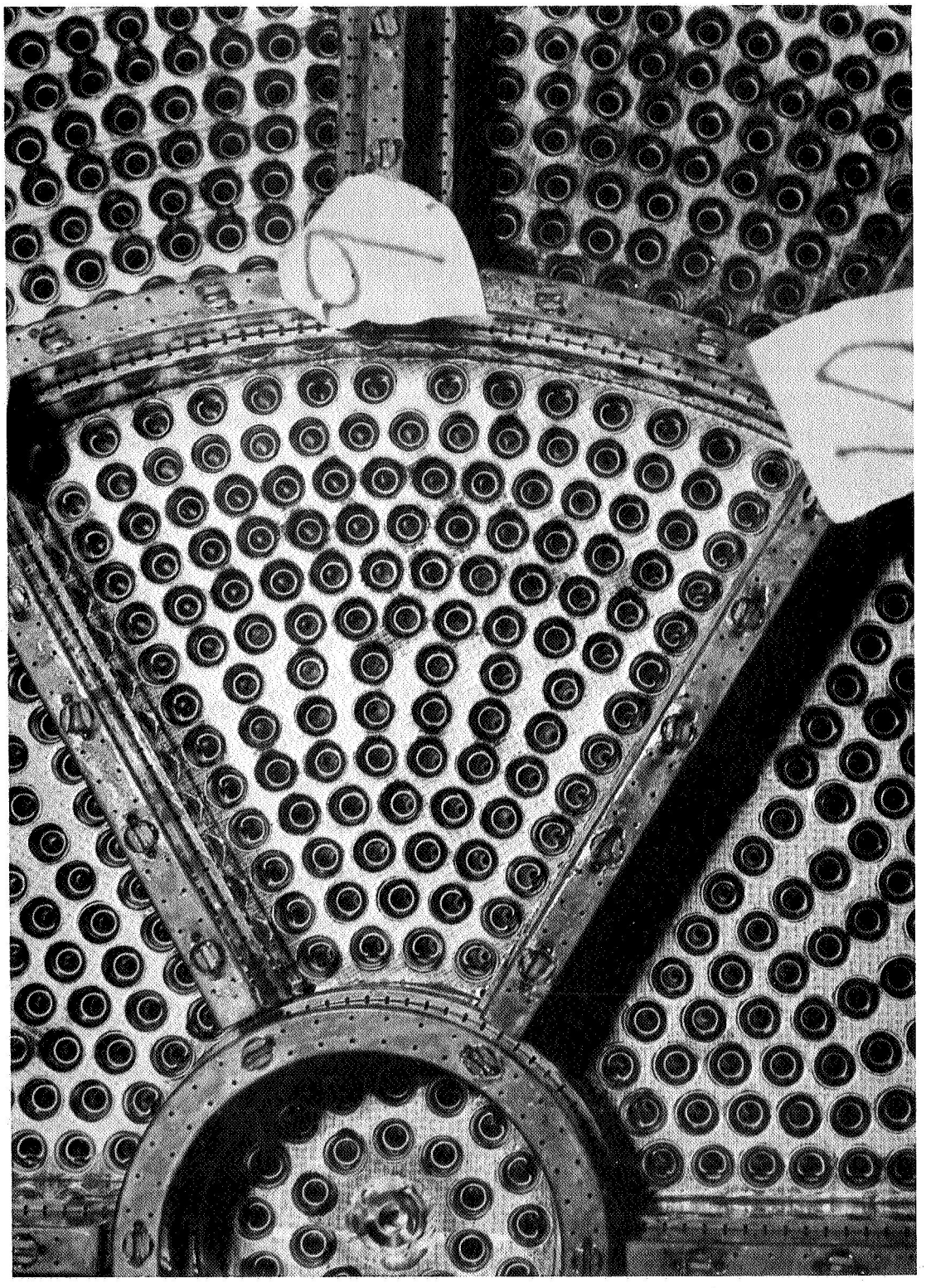

Figure 66. S/N 012 TCA Injector after Testing

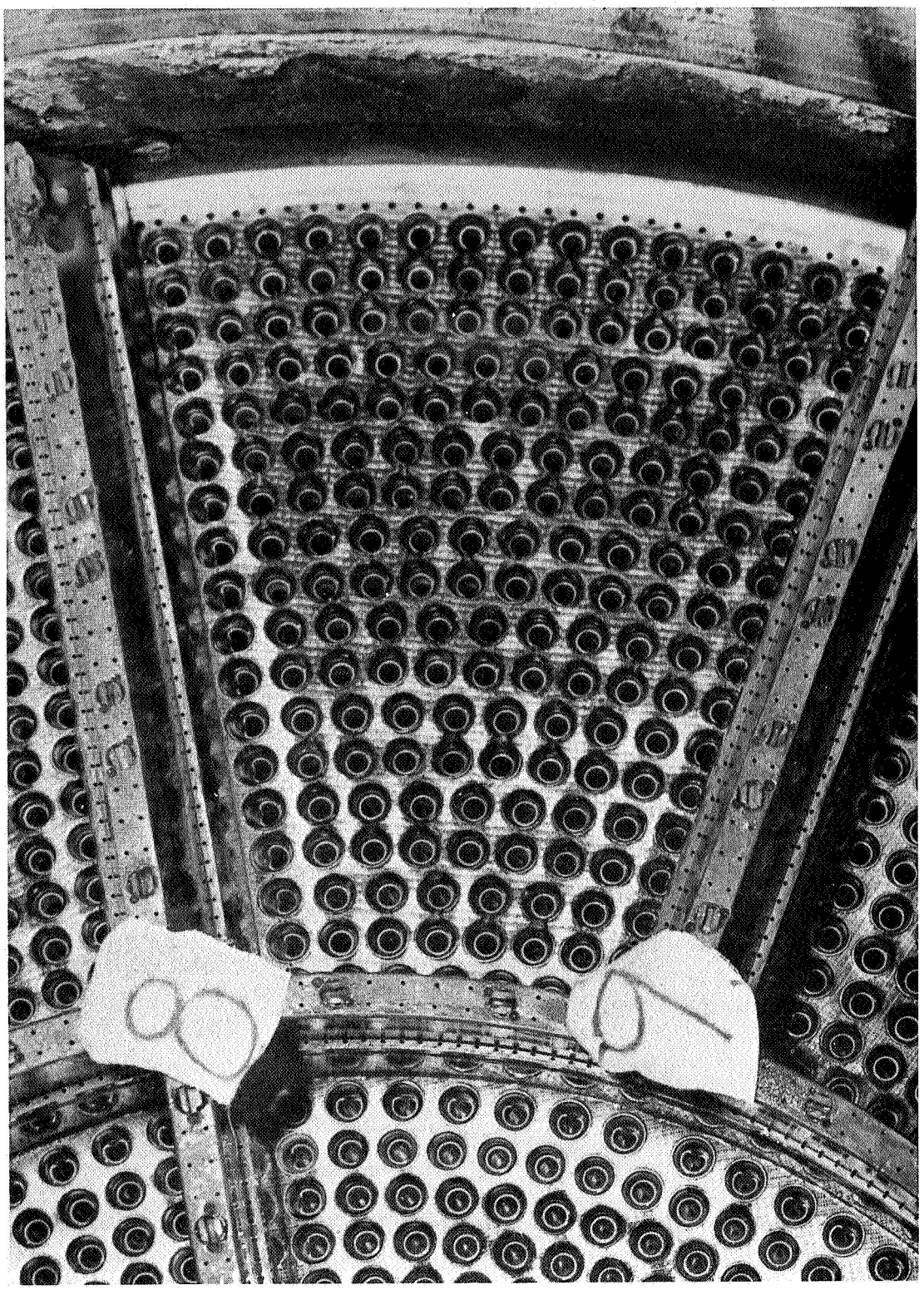

Figure 67. S/N 012 TCA Injector after Testing

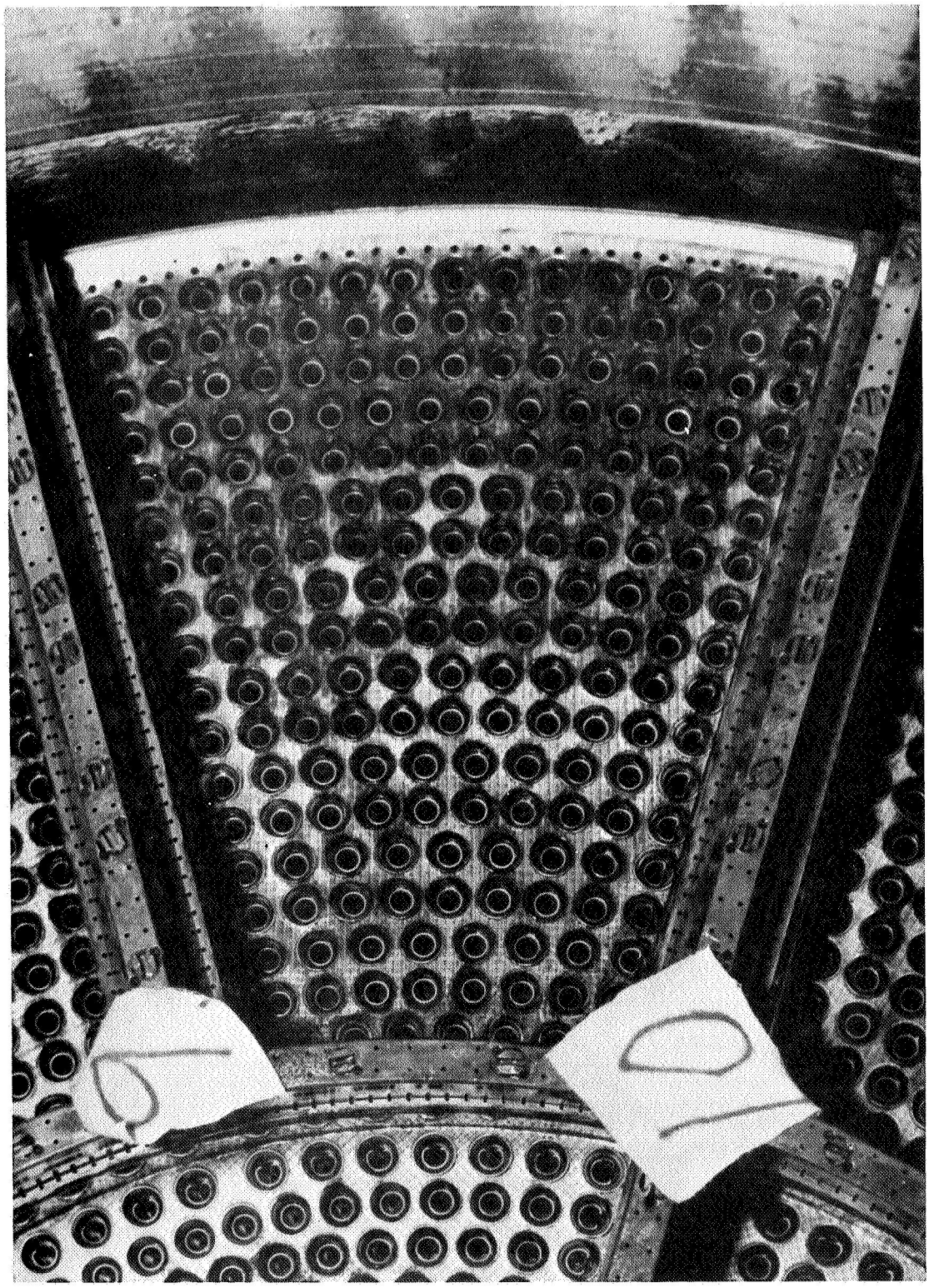

Figure 68. S/N 012 TCA Injector after Testing

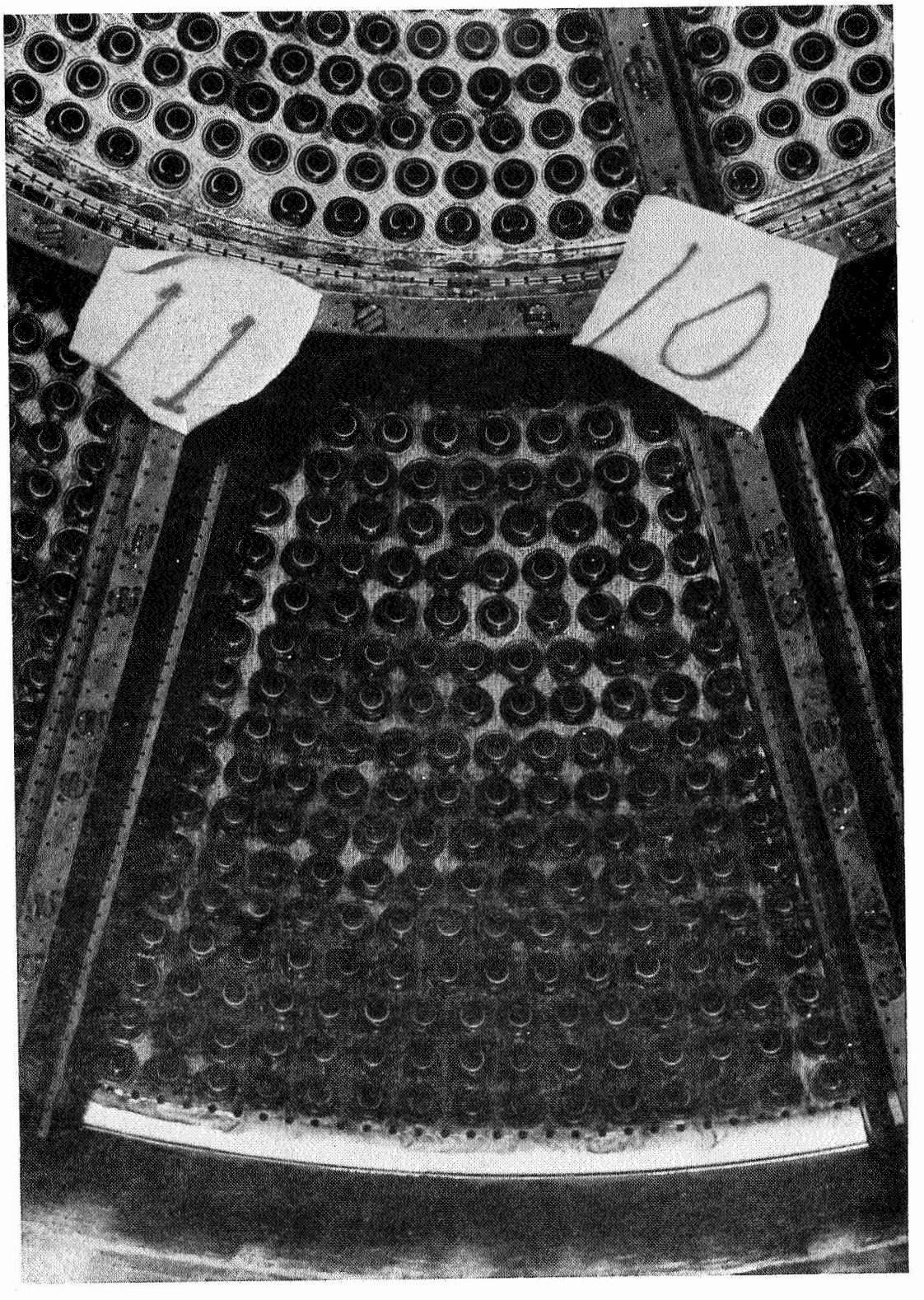

Figure 69. S/N 012 TCA Injector after Testing

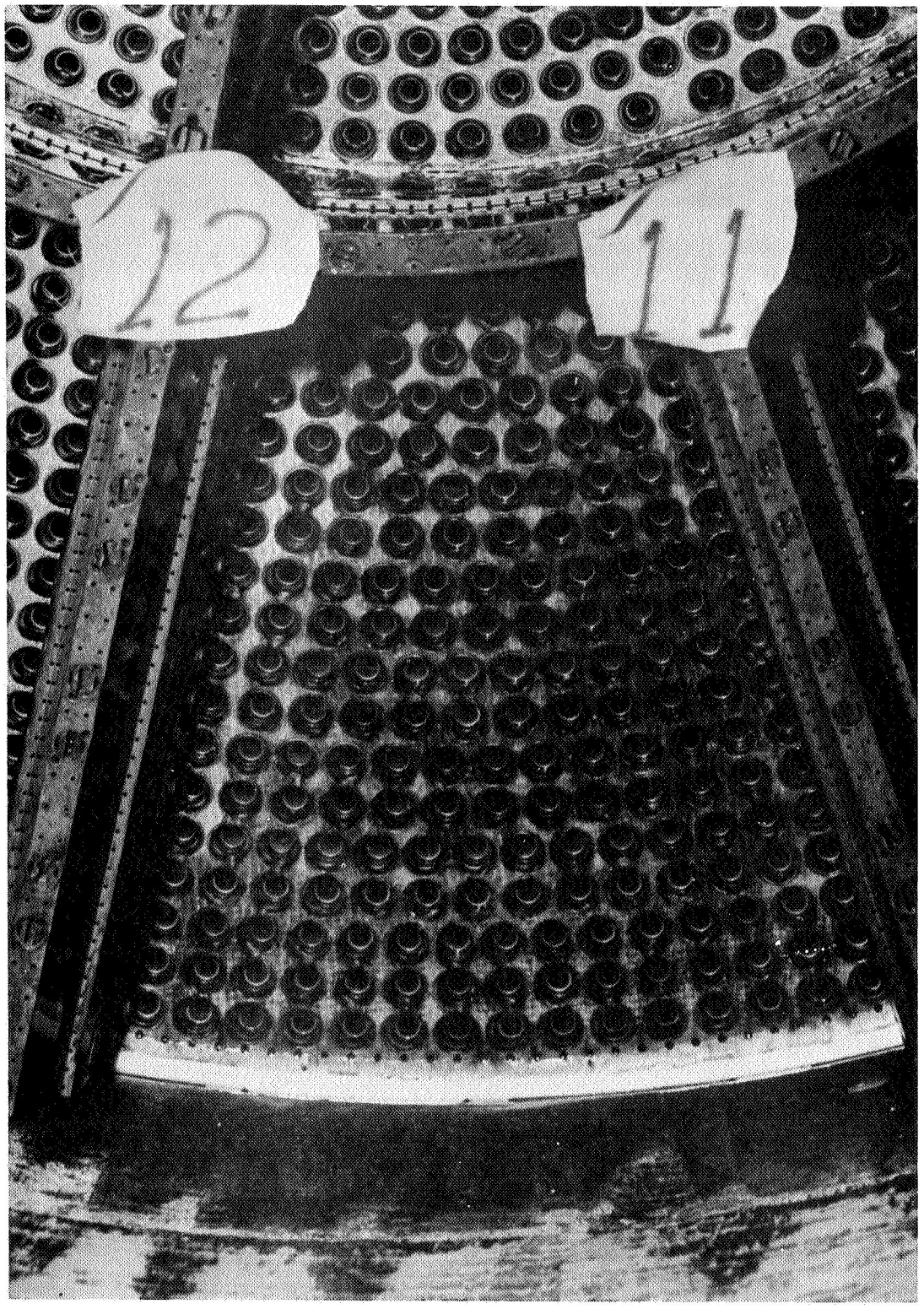


Figure 70. S/N 012 TCA Injector after Testing

erosion on the inner legs and ring while there is erosion on baffle 8, even in those areas with increased cooling. In subsequent tests, S/N 012 injector was used. This injector had baffle film cooling hole diameters that were approximately 7% larger than those on S/N 020. The film cooling holes on the outer legs also were 7% greater in diameter except for the last 2 in. where they were approximately 15% larger in diameter. Figures No. 66 through No. 70 show the condition of some of these baffles after test No. 1.2-07-EHM-010, which was the sixth test using this hardware. The worst erosion experienced is shown at the periphery of baffle 8 (see Figure No. 67). The only other significant area of erosion is shown on baffle 1 (see Figure No. 65). Again, the absence of erosion on the inner ring and legs can be noted. Also, the lack of erosion on any baffles upstream of the film coolant injection ledge.

It is obvious, particularly on injector S/N 020, that either coolant flows or combustion-side heat transfer coefficients are not uniform. The possible causes of non-uniformity of the baffle coolant flows are:

- Local clogging of coolant passages by particles already within the injector chamber or baffles, or dislodged from the tank or lines.

- Non-uniformity of the propellant flow passages within the baffles.

Possible causes of non-uniformity of the gas-side heat transfer coefficient are:

- Local clogging of either the fuel or oxidizer passages of the injection elements by particles.

- Non-uniformity in alignment of injection elements during installation.

- Non-uniformity of the injection element flow passages.

Reasons for accepting or rejecting these possible causes are presented in the ensuing discussion. However, the evidence is not adequate for total acceptance or rejection of any cause.

Local and possibly intermittent clogging of baffle coolant passages by particles is possible even though quite extensive cleaning and flushing procedures are used on the hardware in the test facilities. The cleaning of the oxidizer circuit was as extensive as that accomplished for the fuel circuit. After test No. 1.2-07-EHM-004, the oxidizer dome was removed from the injector plate and foreign particles were found. Similar particles in the fuel circuit would have been sufficient to clog the baffles. The absence of clogging with the inner baffles is possibly the result of the tortuous flow path through the oxidizer "posts" that a particle would have to follow to reach these portions of the injector. The relative lack of baffle

erosion in S/N 012 injector can probably be accounted for by the addition of cooling or by assuming that most of the particulate matter in the fuel circuit was removed during the tests with S/N 020 injector. Other arguments such as the recurrence of erosion on baffles 8 and 11 and minor increases in erosion from test to test also tend to reject this mechanism as the only cause.

Non-uniformity of the coolant passages within the baffles appears to be the least likely cause of the erosion. Extensive flow tests and considerable rework of the individual baffle system components were accomplished to assure that relatively uniform flow and heat transfer were attained. Final acceptance was based upon qualitative tests wherein the gas-side surface was coated with a thermally-sensitive medium, after which, water at a temperature different from that of the baffle was flowed through the passages. By observing the relative rate of change in color of the thermally-sensitive medium, it was possible to detect areas wherein the heat transfer from the fluid to the gas-side was being inhibited. The passages were reworked until these tests showed relatively uniform response of the medium over the entire surface. In addition to these controls during fabrication, the test results tend to negate the non-uniformity of coolant passages as a cause. It is unlikely that the inner baffles and those in S/N 012 injector would consistently be more uniform than the outer baffles of S/N 020 injector. The possibility that the replacement baffles 8 and 11 would have the same relative resistance to coolant flow as the original legs also is remote.

The erosion experienced could have resulted from local plugging of the oxidizer and/or fuel injection passages, which created zones of excess flame temperatures or gas velocities within the baffle compartments. The precautions taken to avoid extraneous particles and evidence that these were still present were previously discussed. Clogging in the oxidizer system is given further credence by two subsequent observations. Upon disassembly of S/N 020 injector plate and dome, it was found that portions of the oxidizer dome baffles had broken loose and were blocking the entrances to some of the oxidizer injection elements. These same baffles in S/N 012 injector, which exhibited insignificant baffle erosion, were held in place by additional bolts. The second observation was that, after the initial tests of the second injector, the oxidizer thrust chamber valve was disassembled and the non-metallic seat was missing. It is possible that portions of this seat passed through injector S/N 020 during its tests or that these pieces will be found in S/N 012 injector when it is disassembled. Neither the amount of material found nor its location after removal of the injector dome could account for either the extent or location of the baffle erosion.

Although non-uniform alignment of the injection elements at installation is possible, it appears unlikely. The close fits between element and injector body at the braze joint as well as the necessity for the element to pass through pre-drilled Rigimesh precludes significant misalignments. The lack of erosion nearer the center of the injector S/N 020 as well as on S/N 012 also indicates the improbability of non-uniform alignment.

A design/fabrication tolerance effect could have resulted in the differences in erosion characteristics of the two injectors. Inspection and flow tests of the initial elements obtained showed considerable differences in the propellant flow passages within the oxidizer element. This resulted in extensive work with the vendor to assure elements of better quality. Although the worst elements were eliminated by inspection and flow tests, considerable differences still existed in the elements installed in the S/N 020 injector whereas the elements used in the second injector, S/N 012, were of a much more uniform quality.

The major problem with the initial set of elements was a lack of concentricity between the small diameter pressure drop controlling hole and the larger diameter counterbore downstream of this hole. Investigation of vendor processing revealed that this was more likely to occur on the outer elements with the longer counterbores. The fabrication process was corrected to assure better alignment of these bores. In addition, other discrepancies, such as surface roughness and actual hole diameter variations, were corrected prior to fabrication of the second set of elements. As a result of these problems, each element for S/N 020 injector was flowed with water to assure adequate flow at anticipated available pressure drops. Elements showing abnormal resistances were either discarded or corrected by minor rework of the entrance surfaces. Although this assured reasonably constant flow rates, it did not guarantee proper stream directions. After injector S/N 020 was removed from the test stand, elements in the erosion-free areas were flowed individually with water. Visual observation of the flow patterns failed to show substantial differences in stream directions in the eroded and erosion-free areas.

None of the potential causes for the erosion of S/N 020 baffles is conclusive. Possibly, the relative lack of erosion on S/N 012 baffles resulted from the increase in the film coolant orifices openings.

3. Chambers

a. Ablative Chamber

The ablative chamber experienced a streaking erosion which was similar to that found on the baffles of injectors S/N 020 and S/N 012. Ablative liner No. 1 (S/N 002) was tested with S/N 020 injector and this streaking erosion can be seen on Figures No. 71, No. 72, and No. 73 after 2.7, 6.8, and 26.8 sec of steady-state operation.

After the first test, it was found that a gouge in the chamber downstream of baffle 3 had started (see Figure No. 71). As testing continued, this gouge became larger and additional gouges appeared near baffles 2 and 12 (see Figures No. 72 and No. 73). A cross-section of liner No. 1 (S/N 002) at approximately 4-in. upstream of the throat after test No. 1.2-07-EHM-006 (41.6 sec of steady-state exposure) is shown on Figure No. 74. Again, the gouging is apparent. Upon inspection, this throat area, which

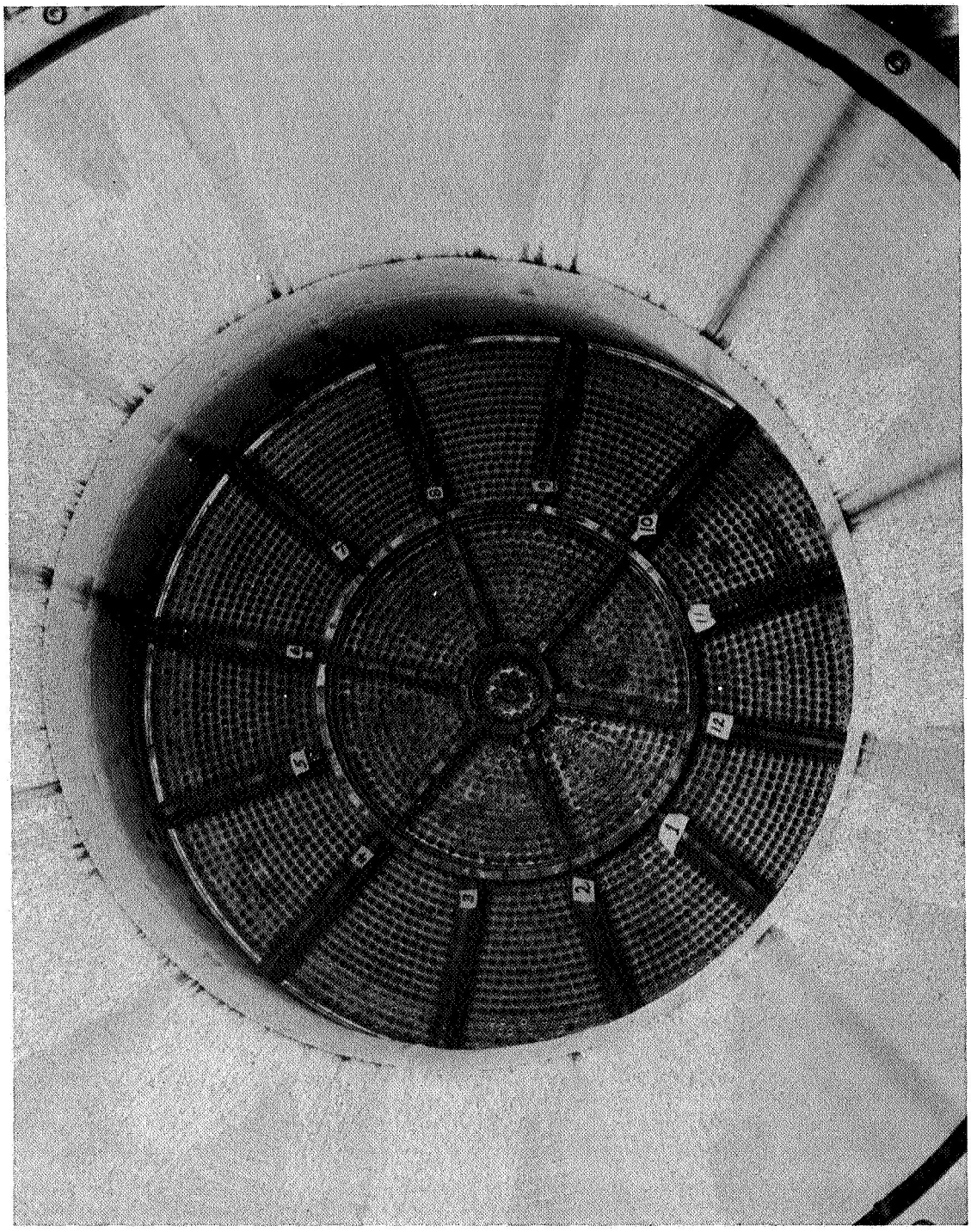

Figure 71. TCA Injector and S/N 002 Ablative Liner after Test

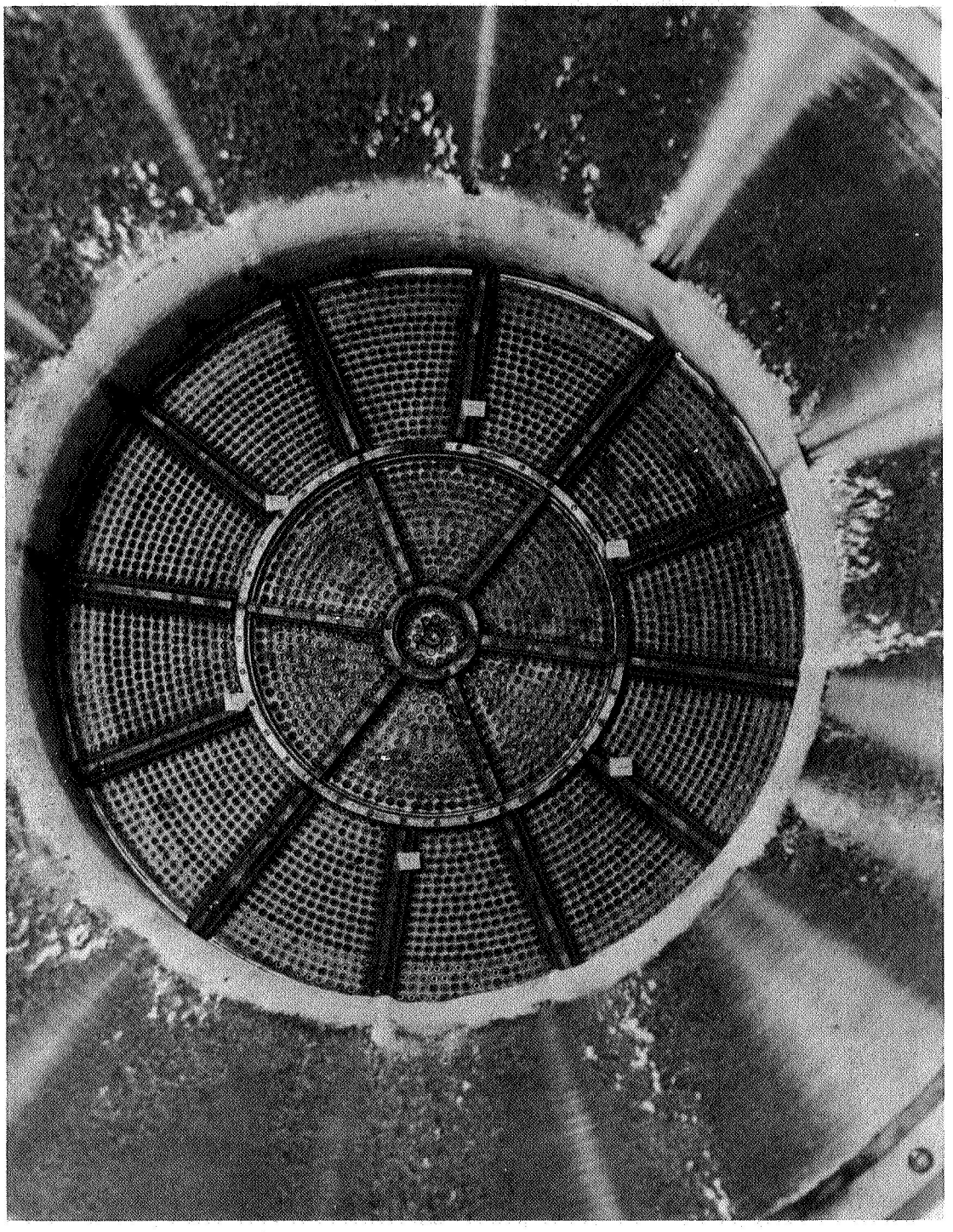

Figure 72. TCA Injector and S/N 002 Ablative Liner after Test

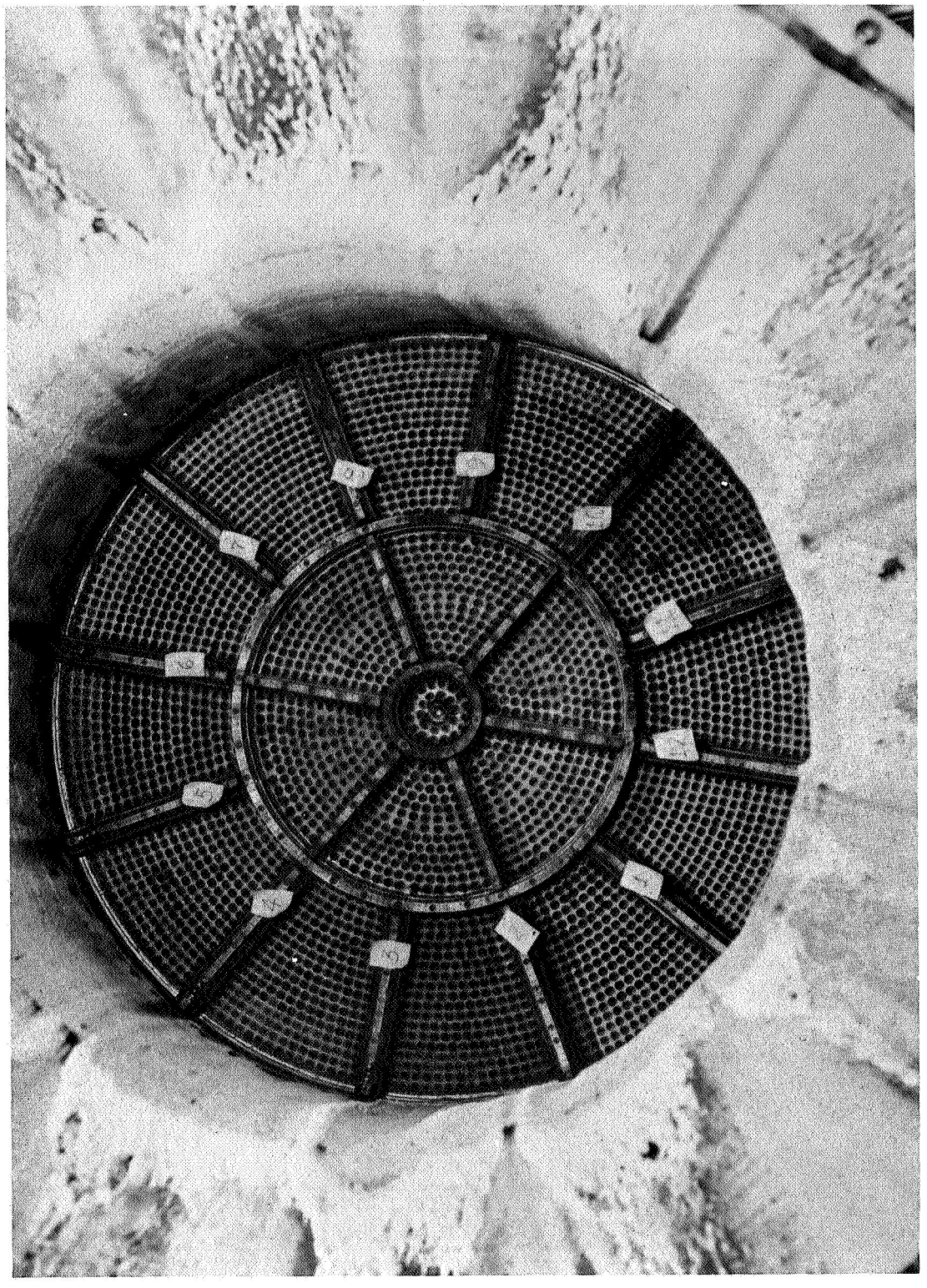

Figure 73. TCA Injector and S/N 002 Ablative Liner after Test

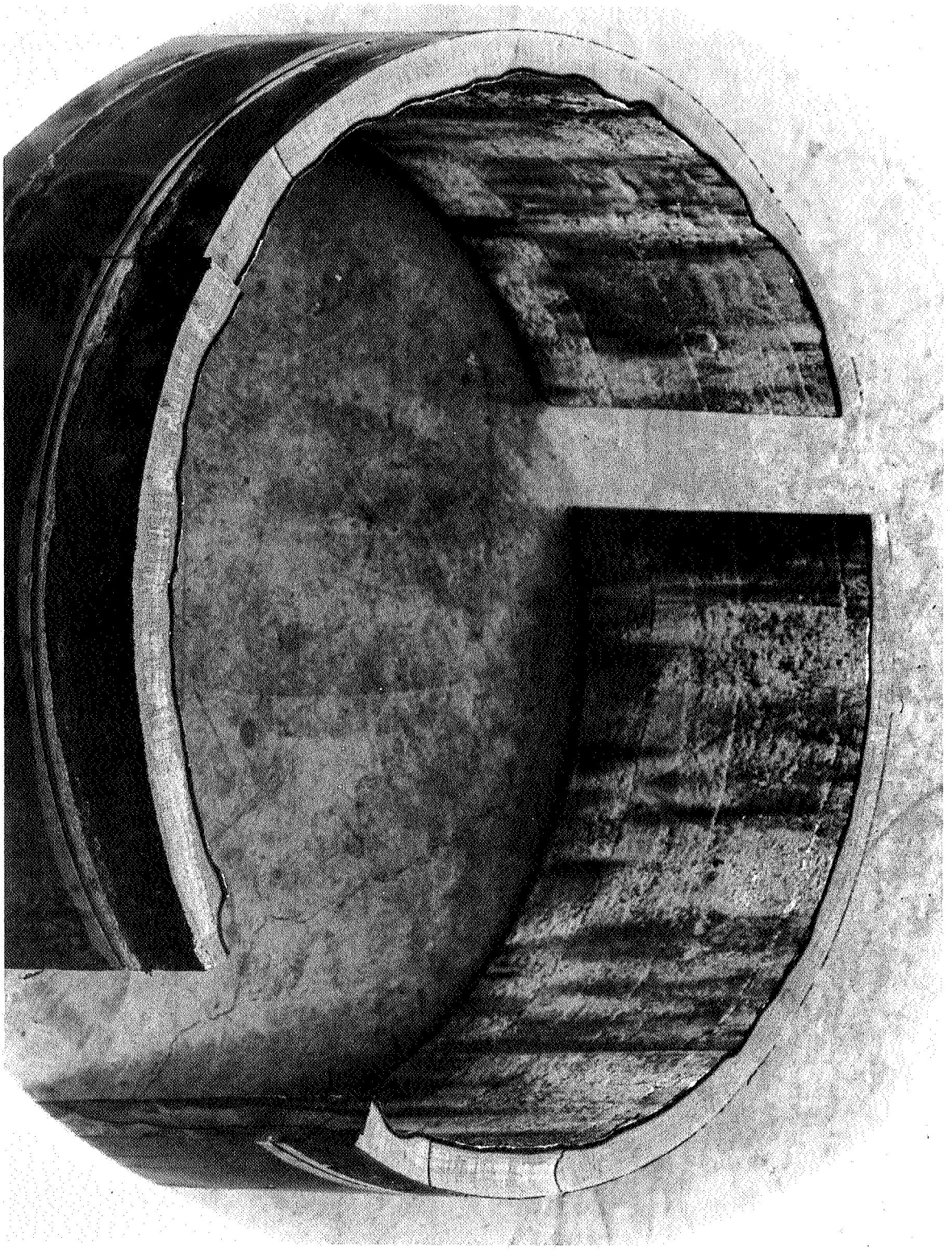

Figure 74. Cross-Section of S/N 002 Ablative Liner after Test

showed maximum erosion, revealed a combined erosion and char depth of 0.93 in. This was a decrease in the original liner thickness from approximately 1.48 in. to approximately 0.55 in.

Ablative liner No. 2 (S/N 001) is shown on Figure No. 75 after 30.8 sec of steady-state exposure with injector S/N 012. The relative absence of streaking here is apparent.

Available evidence indicates that the potential causes of streaking are similar to those for the baffles because the chamber film coolant holes can be considered similar to the baffle coolant passages.

Table XII provides a degradation evaluation for the liners tested while Figure No. 76 provides a comparison between the throat area increase in relationship to test duration for these same liners.

Ablative liner No. 1 was fabricated using compression-molded billets while liners No. 2 and No. 3 were tape-wrapped. It was found that the rate of degradation at the throat was significantly higher for liner No. 1 even when the erosion attributable to injector streaking was discounted. This erosion was generally located between baffles and ran the full length of the chamber.

Liner No. 2 experienced a pitting that was not present on liner No. 1. Also, liner 2 showed uniform erosion from the chamber/fuel torus interface to approximately 4 in. upstream of the throat. The throat itself was almost erosion-free.

Liner No. 3 (S/N 002A) was subjected to only one test. It was found that there was a build-up of ablated material over most of the convergent section. This is similar to what was found with liner No. 2 after one test and with liner No. 1 after six tests.

The results from the ablative chamber testing indicate that the easier, faster fabricated tape-wrapped liner offers greater performance capabilities than the liner made using compression-molded billets.

As a result of the limited testing with liner No. 3, no performance comparison can be made between it and liner No. 2. However, Table XIII is a listing of the differences between the two liners with respect to wrapping techniques as well as physical and mechanical properties. The cure cycles used to fabricate the billets for liner No. 1 are displayed on Figure No. 77.

It has been found from ablative study programs that a relationship can be established between physical and mechanical properties with respect to ablative performance. A laminate produced using the raw materials and fabrication processes applied to liner No. 2 will have greater

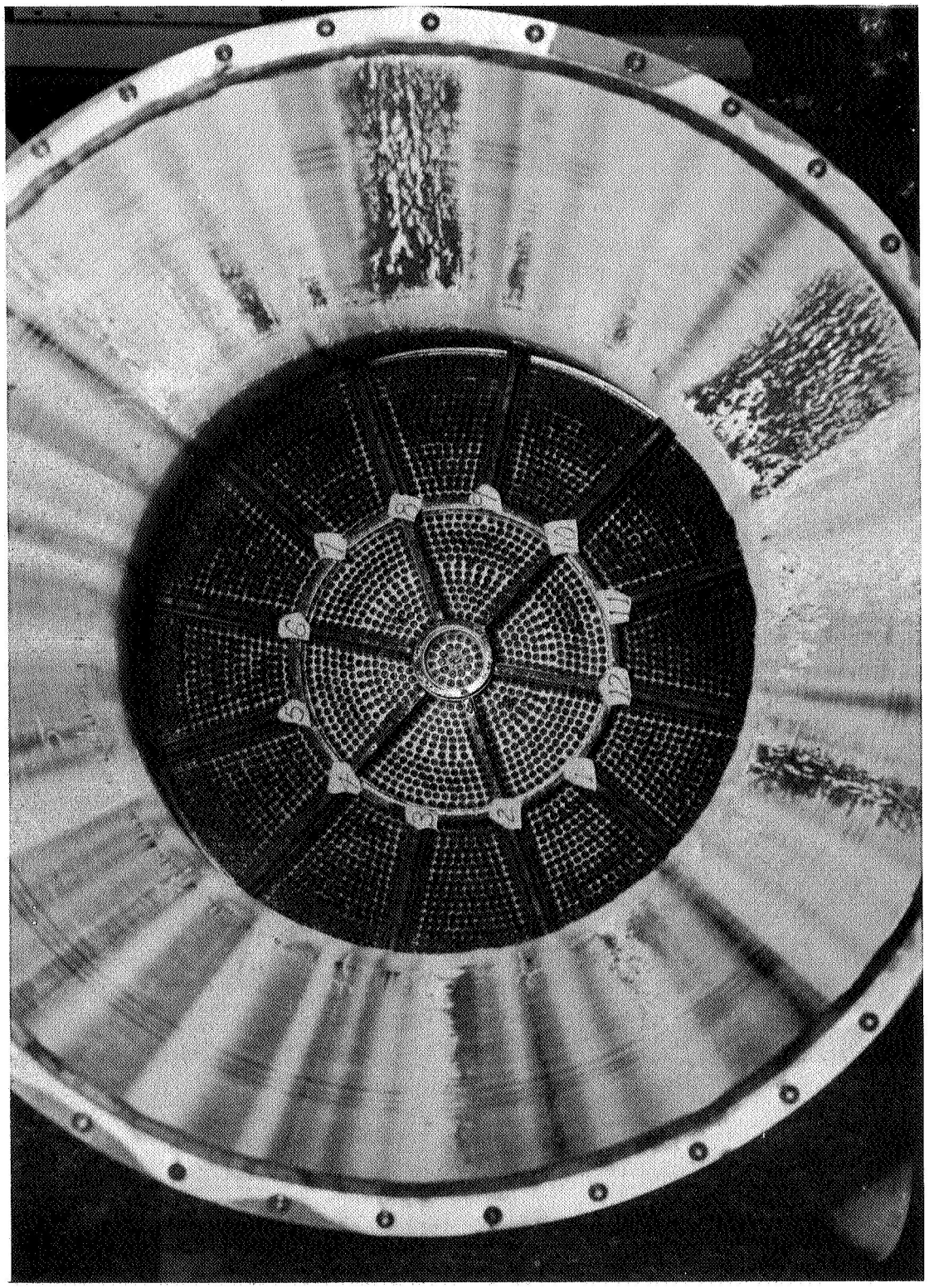

Figure 75. TCA Injector and S/N 001 Ablative Liner after Test

TABLE XII

ABLATIVE LINER DEGRADATION EVALUATION

| CHAMBER LINER NO. | 1 | | | | | 1 | 2 | | | | | | | | | 2 | 3 |
|---|---|---|---|---|---|---|---|---|---|---|---|---|---|---|---|---|---|
| CHAMBER S/N | 002 | | | | | 002 | 001 | | | | | | | | | 001 | 002A |
| FUEL TORUS LINER # | 1 | | | | | | | | | | | | | | | 1 | 2 |
| INJECTOR S/N | 020 | | | | | 020 | 012 | | | | | | | | | 012 | |
| TEST NO. | 1.2-05-EHM-006 | 007 | 008 | 009 | 010 | 1.2-07-EHM-001 | 002 | 003 | 004 | 005* | 006** | 007 | 008 | 009 | 010 | 011 | 014 | 015 | 016*** |
| TEST DURATION ($FS_1$ to $FS_2$)-SEC | 6.56 | 4.28 | 7.63 | 7.49 | 7.01 | 7.48 | 7.49 | 10.04 | 7.60 | 8.71 | 10.25 | 9.36 | 10.87 | 10.90 | 15.27 | 8.51 | 12.04 | 13.97 | 13.60 |
| TEST DURATION >90% Pc-SEC | 2.66 | 0.38 | 3.73 | 3.59 | 3.11 | 3.58 | 3.59 | 6.14 | 3.70 | 4.81 | 6.35 | 5.46 | 6.97 | 7.00 | 11.37 | 4.61 | 8.14 | 10.07 | 9.70 |
| AVERAGE $d_t$ (PRE-TEST)-in. | 29.95 | 29.99 | 29.99 | 30.80 | 30.00 | 30.08 | 30.05 | 30.11 | 30.18 | 30.23 | 30.36 | 30.00 | 29.97 | 30.01 | 30.02 | 30.02 | 30.03 | 30.05 | 30.00 |
| AVERAGE $d_t$ (POST-TEST)-in. | 29.99 | 29.99 | 30.00 | 30.00 | 30.08 | 30.05 | 30.11 | 30.18 | 30.23 | 30.36 | 30.48 | 29.97 | 30.01 | 30.02 | 30.02 | 30.03 | 30.05 | 30.07 | 29.97 |
| ACCUM. TIME (>90%Pc) ON CHAMB. LINER-SEC | 2.66 | 3.04 | 6.77 | 10.36 | 13.47 | 17.05 | 20.64 | 26.78 | 30.48 | 35.29 | 41.64 | 5.46 | 12.43 | 19.43 | 30.08 | 35.41 | 43.55 | 53.62 | 9.70 |
| ACCUMULATED TIME (>90% Pc) ON FUEL TORUS LINER-SEC | 2.66 | 3.04 | 6.77 | 10.36 | 13.47 | 17.05 | 20.64 | 26.78 | 30.48 | 35.29 | 41.64 | 47.10 | 54.07 | 61.07 | 72.44 | 77.05 | 85.19 | 95.26 | 9.70 |
| CHAR DEPTH (IN)/ EROSION (IN) | | | | | | | | | | | | | | | | | | | |
| IN-LINE WITH BAFFLE #11 | | | | | | | | | | | | | | | | | | | |
| 14-in FROM FACE | - | - | - | - | - | - | - | - | - | - | - | - | - | - | - | - | - | .03/ | .05/**** |
| 19-in FROM FACE | - | - | - | - | .07/0 | - | - | - | .10/0 | - | - | - | - | - | - | - | - | .06/ | .06/**** |
| 25-in FROM FACE | - | - | - | - | - | - | - | - | - | - | - | - | - | - | - | - | - | .14/ | .06/**** |
| 29-in FROM FACE | | | | | .09/0 | | | | .15/0 | | .12/.11 | | | | | | | .08/ | .18/**** |
| 2-IN CW OF BAFFLE #3 (LOOKING AFT) | | | | | | | | | | | | | | | | | | | |
| 14-in FROM FACE | - | - | - | - | - | - | - | - | - | - | - | - | - | - | - | - | - | .04/ | .03/**** |
| 19-in FROM FACE | - | - | - | - | .075/230 | - | - | - | .04/.715 | - | - | - | - | - | - | - | - | .04/ | .05/**** |
| 25-in FROM FACE | - | - | - | - | - | - | - | - | - | - | - | - | - | - | - | - | - | .05/ | .06/**** |
| 29-in FROM FACE | - | - | - | - | .075/350 | - | - | - | .04/.747 | - | .09/84 | - | - | - | - | - | - | .06/ | 16/**** |

* Rotated Chamber 10°

** Discharged Aft Chamber Liner @ $FS_1$ + 7.95 sec

*** Discharged Fuel Torus Liner @ Instability

**** Erosion Unobtainable Due to Surface Build-Up

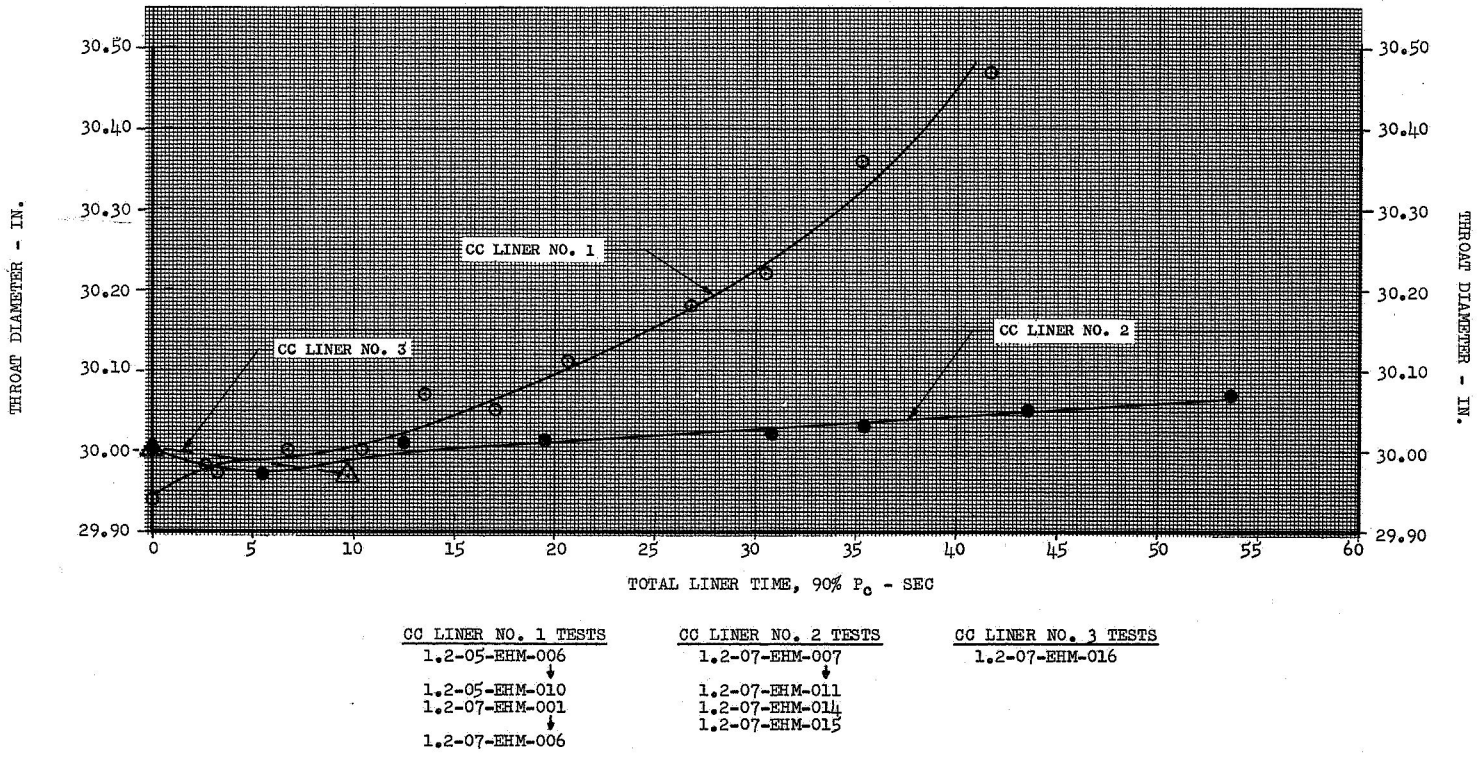


Figure 76. Ablative Liner Throat Diameter vs. Total Liner Time (90% $P_c$)

TABLE XIII

FABRICATION COMPARISON OF TAPE-WRAPPED LINERS

WRAPPING PROCESS

| | Liner No. 3 | Liner No. 2 |
|---|---|---|
| Tape Wrapping Temperature, °F | 165 to 184 | 230 to 240 |
| Tape Wrapping Pressure, psig | 270 to 283 | 230 to 240 |
| Tape Wrapping Speed, rpm | 1.0 to 1.5 | 0.5 |
| Tape Wrapping Span Time, hours | 12 | 36 |

UNCURED MATERIAL PROPERTIES

| Property | Requirement | Actual Test Liner No. 3 | Actual Test Liner No. 2 |
|---|---|---|---|
| Resin Solids, % | 24 to 28 | 25.5 | 27.5 |
| Resin Flow, % | 6 to 10 | 9.3 | 6.8 |
| Volatiles, % | | 3.6 | 3.8 |

CURED LAMINATE PROPERTIES

| Property | Requirement | Actual Test Liner No. 3 | Actual Test Liner No. 2 |
|---|---|---|---|
| Interlaminar Shear | 1000 psi Minimum | 1302 | 2539 |
| Acetone Extraction | 1% Maximum | 0.15 | 0.21 |
| Specific Gravity | 1.72 | 1.77 | 1.73 |
| Volatile Content | 3% Maximum | 1.9 | 2.3 |
| Tensile Strength | psi | 11,844 | 12,808 |

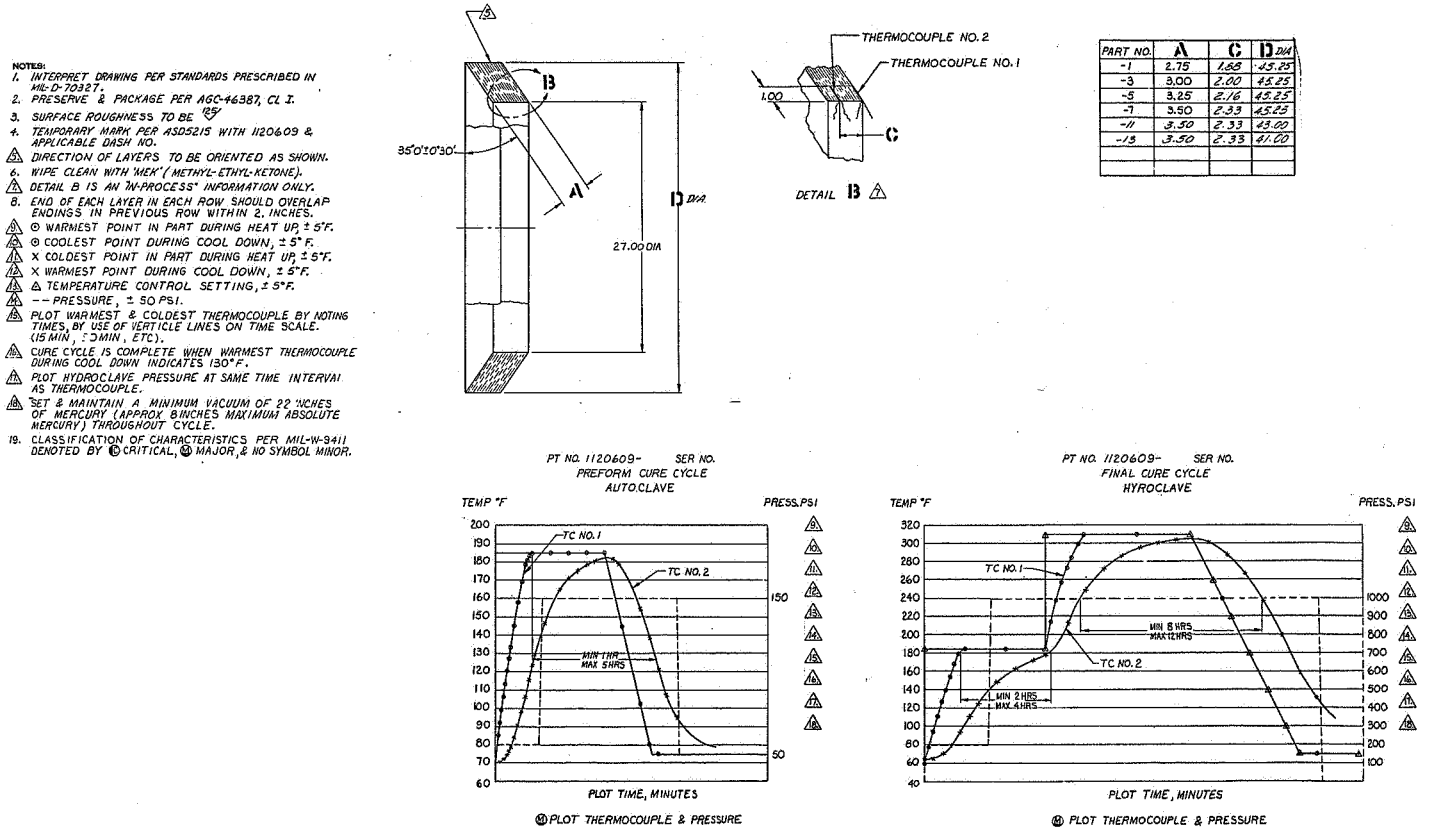


Figure 77. Cure Cycles Used to Fabricate Billets for S/N 001 Ablative Liner

susceptibility to surface regression than one produced similarly to liner No. 3. A more advanced tape, with a higher resin and volatile content, was used for liner No. 2. This tape was applied at a higher wrapping tape temperature with less application pressure. The resultant laminate with this "B" tape is more susceptible to mechanical removal as a result of shear because the oxidation resistance of the resin residue is less than that of the reinforcement. However, it has been established that a lower resin content material would provide a lower and more uniform surface regression.

b. Stainless Steel Chamber

The effectiveness of gaseous hydrogen film coolant at an appreciable distance, 15 in., downstream from its injection point was analyzed using the data from test No. 1.2-07-EHM-021. This test provided nearly constant wall temperature measurements in the throat region for a duration of 2.1 sec at a steady-state chamber pressure of 946 psia. These temperature data, which approximate the adiabatic wall temperature, are shown on Figure No. 78.

Data from the indicated test were compared using three empirical correlating relationships; Hatch and Papell[13], which was used in the original chamber design, Stollery and El-Ehwany's[14] boundary-layer mixing model, and a new approach suggested by Haering[15].

Experimental wall temperatures were best predicted using the boundary-layer mixing model. The values predicted using the Hatch and Papell correlation differed significantly from the observed values. Particularly, the calculated mixing or start length ($x_o$) was not borne out by the data. Haering's method offered no advantage for data correlation.

Film coolant injected midway down the combustion chamber significantly reduced the wall temperature at the throat and demonstrated that gaseous hydrogen is useful as a film coolant. The injection of 7.8% of the fuel as film cooling at the second injection point resulted in a steady-state, adiabatic wall temperature of 1600°R at the throat, which is 15.3-in. downstream. This suggests that an all film-cooled, unlimited duration, low cost combustion chamber is feasible, but at a sacrifice in performance, which was not detrimental during this testing.

(13) Hatch, J. E. and Papell, S. S., Use of a Theoretical Flow Model to Correlate Data for Film Cooling or Heating an Adiabatic Wall by Tangential Injection of Gases of Different Fluid Properties, NASA TN D-130, November 1959

(14) Stollery, J. L. and El-Ehwany, A. A. M., "A Note on the Use of a Boundary-Layer Model for Correlating Film Cooling Data," International Journal of Heat Mass Transfer, Vol. 8, 1965, pp. 55-65

(15) Haering, G. W., A Proposed Correlation Scheme for Gas-Film Cooling Data, AFRPL-TR-66-56, August 1966

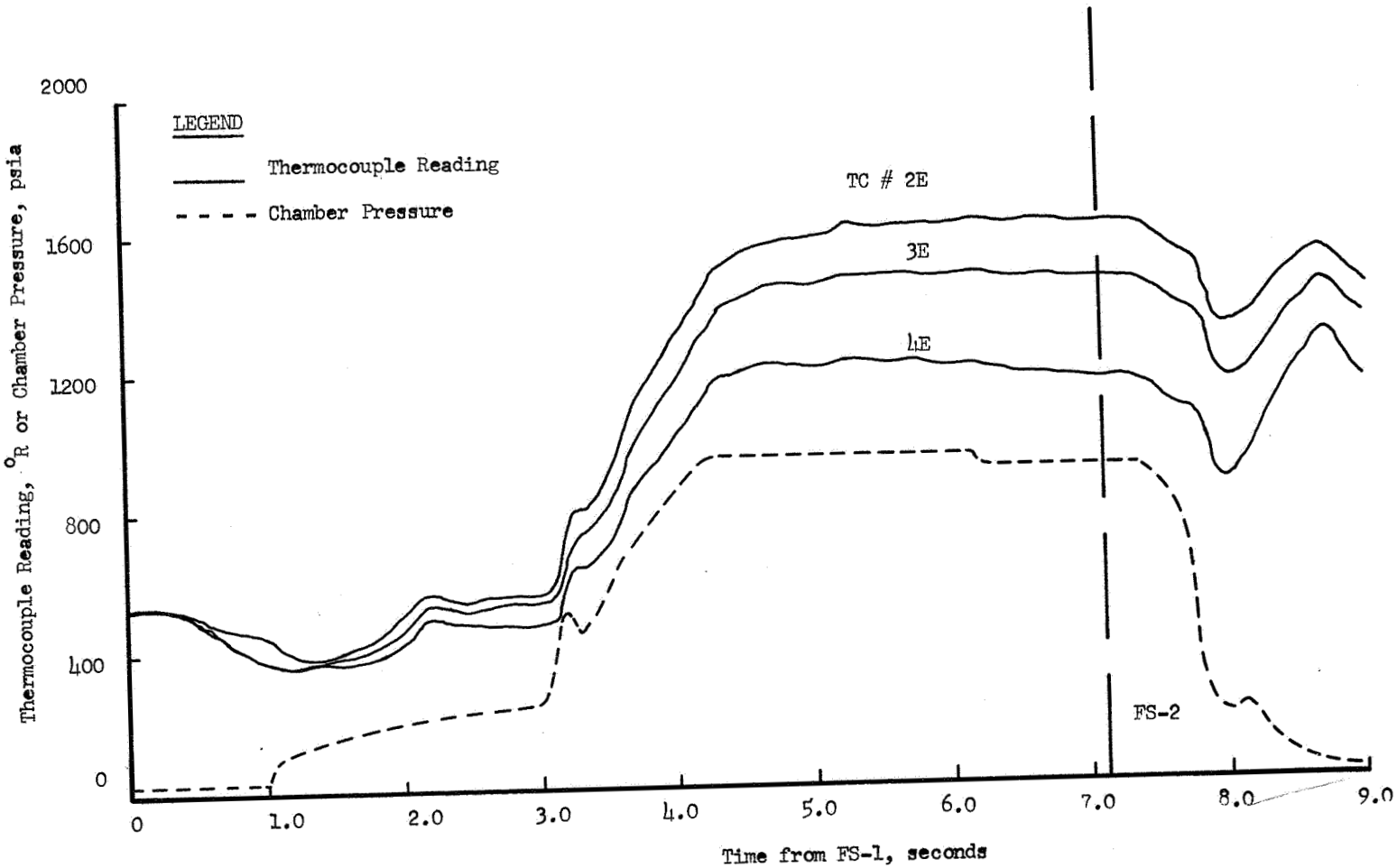


Figure 78. Chamber Pressure and Throat Region Thermocouple Response (Test No. 1.2-07-EHM-021)

Twelve thermocouple plugs were installed into the chamber wall to monitor wall temperatures and provide thermal data. These data were used to evaluate existing film cooling models for predicting film cooling effectiveness. A 0.040-in. to 0.050-in. zirconium oxide coating was sprayed onto the inner chamber wall for additional thermal protection of the steel chamber. The 12 thermocouples, also coated, were installed at the interface between the steel wall and the coating in six axial locations (designated Tc 1, 2, etc.) and six peripheral locations (designated A, B, etc.) as shown schematically on Figure No. 79.

The data from seven test firings showed that the coating failed locally at the thermocouples located in the high heat flux chamber and throat areas during the early tests. Subsequently, failure of the coating occurred in the region extending 8-in. to 10-in. upstream and 2-in. to 3-in. downstream. The exposed bare metal in this region provided an improved condition for thermal data analysis. No overheating occurred during the tests that followed. This indicates that the film cooling alone was sufficient to maintain reasonable wall temperatures in this portion of the chamber. The three throat region thermocouples read gas-side wall temperature during the remaining tests instead of the coating interface temperature. These thermocouples (2E, 3E, and 4E) reached steady-state (see Figure No. 78) during the longer duration firings and provided significant data. The six thermocouples which suffered local coating failures were located in two rows immediately downstream of the injector. After this, they were recessed 0.040 in. to 0.050 in. (the coating thickness). Subsequent readings from these thermocouples were suspect because of possible boundary-layer turbulence and mixing which resulted from this coating failure. They behaved erratically and provided inordinately high readings that were atypical of smooth wall values. The coating on the three thermocouples located in the expansion region remained intact during the testing as did the entire coating in the divergent nozzle. These thermocouple readings were transient throughout the tests as a result of the additional resistance and capacitance that the coating interposed between the film-cooled boundary-layer and the thermocouple junction. An unsuccessful attempt was made to establish the presence of film cooling effect downstream of the throat from these thermocouple readings. The long chamber start transients and the inadequate data regarding the coating thickness introduced uncertainties that could not be resolved during the analysis.

The equilibrium readings attained by the throat region thermocouples were reproducible for the longer duration tests. This also was true for the temperature response curves of the coated thermocouples in the expansion region. Although the thermocouples in the chamber region were erratic, they followed the same general trends from test to test. The data from test No. 1.2-07-EHM-021 were selected as being typical for the test series and were reduced for comparison with the film cooling models. There are two correlations generally used for thermodynamic analysis at Aerojet-General; a modified Hatch and Papell[16] and Stollery and El-Ehwany's boundary-layer model[17].

(16) Hatch, J. E. and Papell, S. S., op. cit.
(17) Stollery, S. L. and El-Ehwany, A. A. M., op. cit.

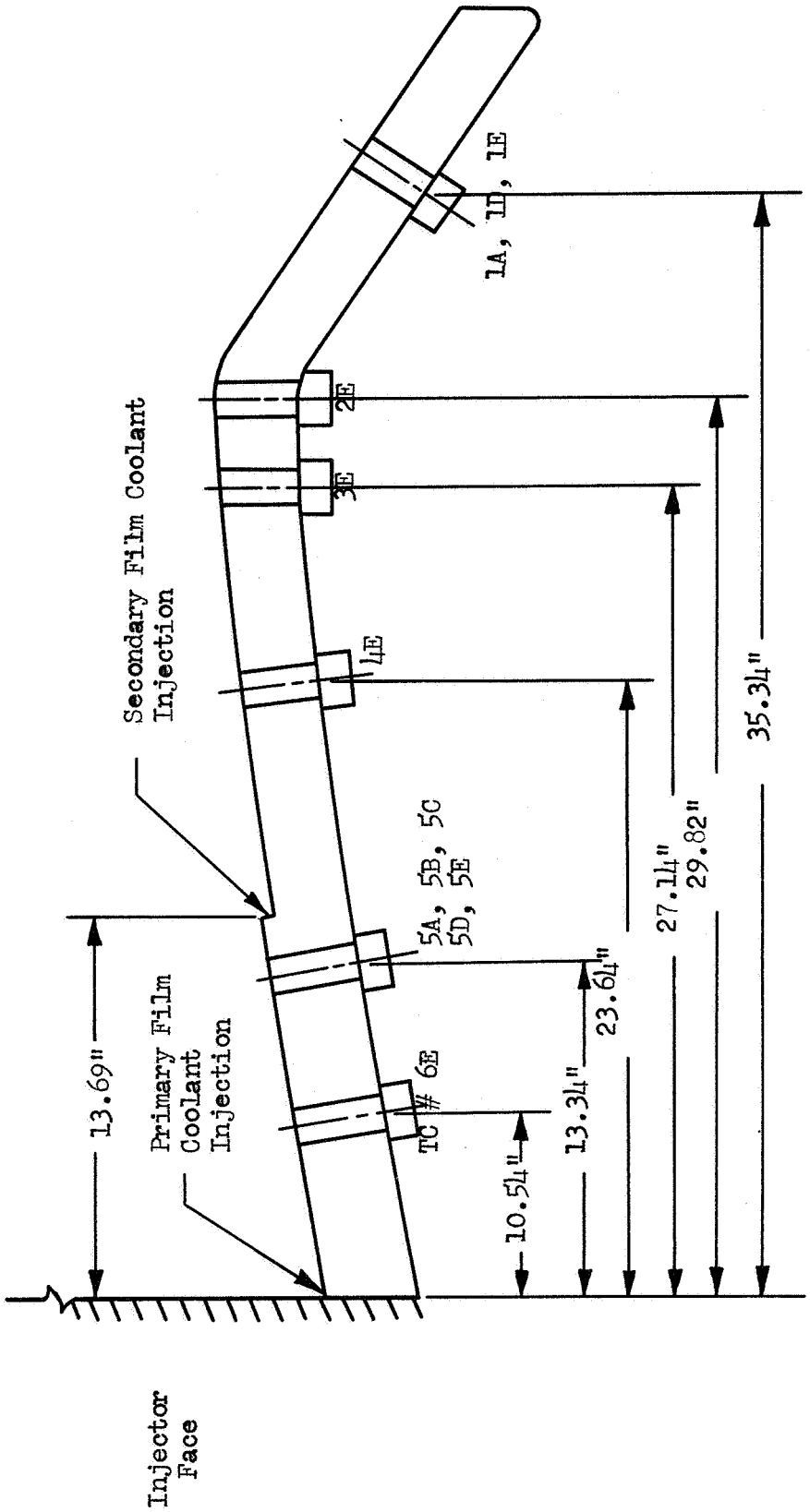


Figure 79. M-1 Workhorse Chamber Thermocouple Locations

The modified Hatch and Papell correlation is Aerojet-General Computer Program 8070, wherein the equation is solved in differential form. Table XIV defines the nomenclature used in the following analyses.

$$\frac{dT_F}{dx} = \frac{AB\ (T_r - T_F)}{W_F^{0.875}} \qquad \text{Equation (13)}$$

where,

$$A = \frac{h_g\ \eta D_c}{C_p}$$

$$B = 1.628 \left[ \left( \frac{V_g}{V_F} \right) \left( \frac{C_p}{K} \right) \left( \frac{1}{\eta D_c} \right) \right]^{0.125}$$

Also of interest in this investigation is the lower limit of integration, $x_o$, or start length, which is given by:

$$x_o = \frac{0.04\ W_F\ C_p}{h_g\ \eta D_c} \qquad \text{Equation (14)}$$

The second correlation is the boundary-layer model of Stollery and El-Ehwany. This boundary-layer model has three correlation forms depending upon whether the film and main gas streams are the same fluids, Equation (15); different fluids, Equation (16); or the boundary-layer thickness is non-zero at the point of injection, Equation (17)

$$\eta' = \frac{h_F - h_r}{h_{Fi} - h_r} = \frac{C}{(\bar{X})}\ 0.8 \qquad \text{Equation (15)}$$

where,

$$\bar{X} = \frac{x}{ms} \left( Re_c\ \frac{\mu_c}{\mu_r} \right)^{-0.25}$$

$$\eta'' = \frac{T_F - T_r}{T_{Fi} - T_r} = \frac{C_{pc}/C_{pg}\ \eta'}{1 + (C_{pc}/C_{pg} - 1)\ \eta'} \qquad \text{Equation (16)}$$

$$\eta' = \frac{C}{(\bar{X} + 4.1)^{0.8}} \qquad \text{Equation (17)}$$

TABLE XIV

CORRELATION NOMENCLATURE

| | |
|---|---|
| A | Hatch and Papell correlation parameter |
| B | Hatch and Papell correlation parameter |
| C | Boundary-layer model correlation constant |
| $C_p$ | Specific heat |
| $D_c$ | Thrust chamber diameter |
| h | Enthalpy |
| $h_g$ | Gas-side convection coefficient |
| K | Thermal conductivity |
| m | Mass velocity, $_cV_c/\ _gV_g$ |
| Re | Reynolds number |
| s | Slot height |
| V | Velocity |
| W | Flow rate |
| x | Distance |
| $\bar{X}$ | Boundary-layer model parameter |
| $\eta'$ or $\eta''$ | Film cooling effectiveness |
| $\rho$ | Density |
| $\gamma$ | Viscosity |

SUBSCRIPTS

| | |
|---|---|
| F | Film coolant |
| g | Mainstream gas |
| i | Initial |
| r | Recovery |

The value of the correlation constant C has been determined theoretically as 3.09; however, experimentally, it was found by others to be as high as 5.44. The data of Wieghardt and Seban also indicate that the constant varies with mass velocity ratio for values greater than 1.0 as shown on Figure No. 80.

A third correlation, which is recommended by Haering[18], also was compared with the data. Haering's correlation is given by:

$$\eta'' = \left\{ 1 + 3.6 \left( \frac{St_g}{m} \right) \left( \frac{x}{s} \right) \left( \frac{t_g}{t_c} \right)^{2/3} \left[ 1 + 0.4 \tan^{-1} \left( \frac{V_g}{V_c} - 1 \right) \right] \right\}^{-1} \quad \text{Equation (18)}$$

where,

$$St_g = \frac{h_g}{\rho_g V_g C_{pg}}$$

The throat region temperature data (thermocouples 2E, 3E, and 4E) were found to closely approximate the adiabatic wall temperature. These data are compared with the boundary-layer model predictions (Equations 15, 16, and 17) on Figure No. 81, using the theoretical value of C = 3.09, and also an empirical value in Equation (16) which best fits the data. The experimental value of C for throat region data is 1.22. This point, plotted as the shaded square on Figure No. 80, is in good agreement with existing experimental data. A similar empirical value for C was obtained in the chamber region (thermocouples 5 and 6) where the residual coating significantly influenced the results. Here, the empirical value of C ranges between 1.3 and 3.0 as shown on Figures No. 80 and No. 81.

Computer Program 8070 predictions (the prediction of the boundary-layer model using a C value of 1.22) and the data from test No. 1.2-07-EHM-021 are shown on Figure No. 82 as $T_F$ versus axial distance from the injector. The boundary-layer model is in excellent agreement with the three throat measurements. However, this is not true for the Computer Program 8070 version of the Hatch and Papell correlation. The predicted start length (Equation 14) of the Hatch and Papell correlation, which is the horizontal portion of the curve (see Figure No. 82), is notably greater than the data indicate.

The throat region data also are compared to Haering's correlation on Figure No. 83. This correlation gives conservatively low predictions for the effectiveness, except close to the injection location.

(18) Haering, G. W., op. cit.

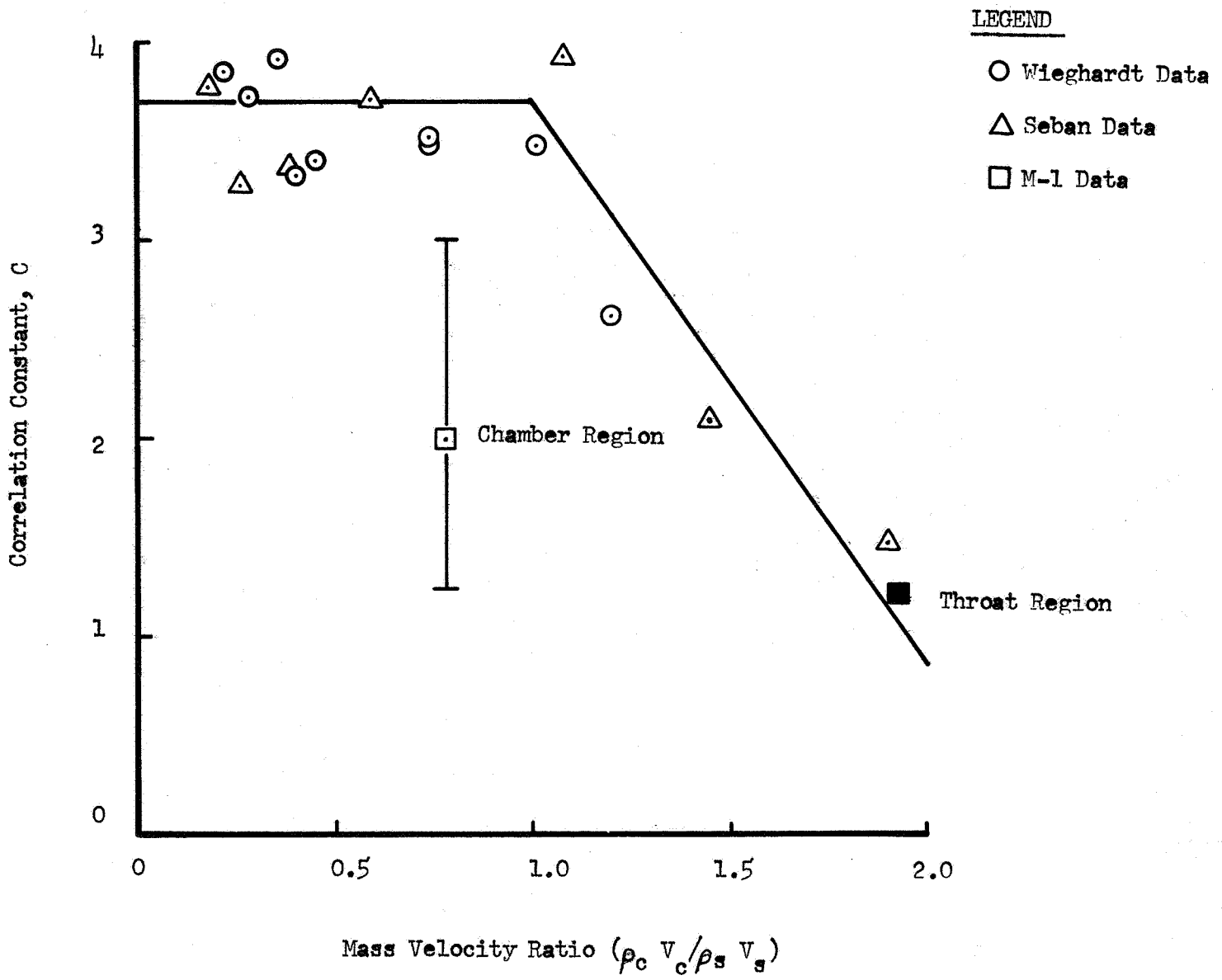


Figure 80. Experimental Boundary-Layer Film Cooling Model Correlation Constants

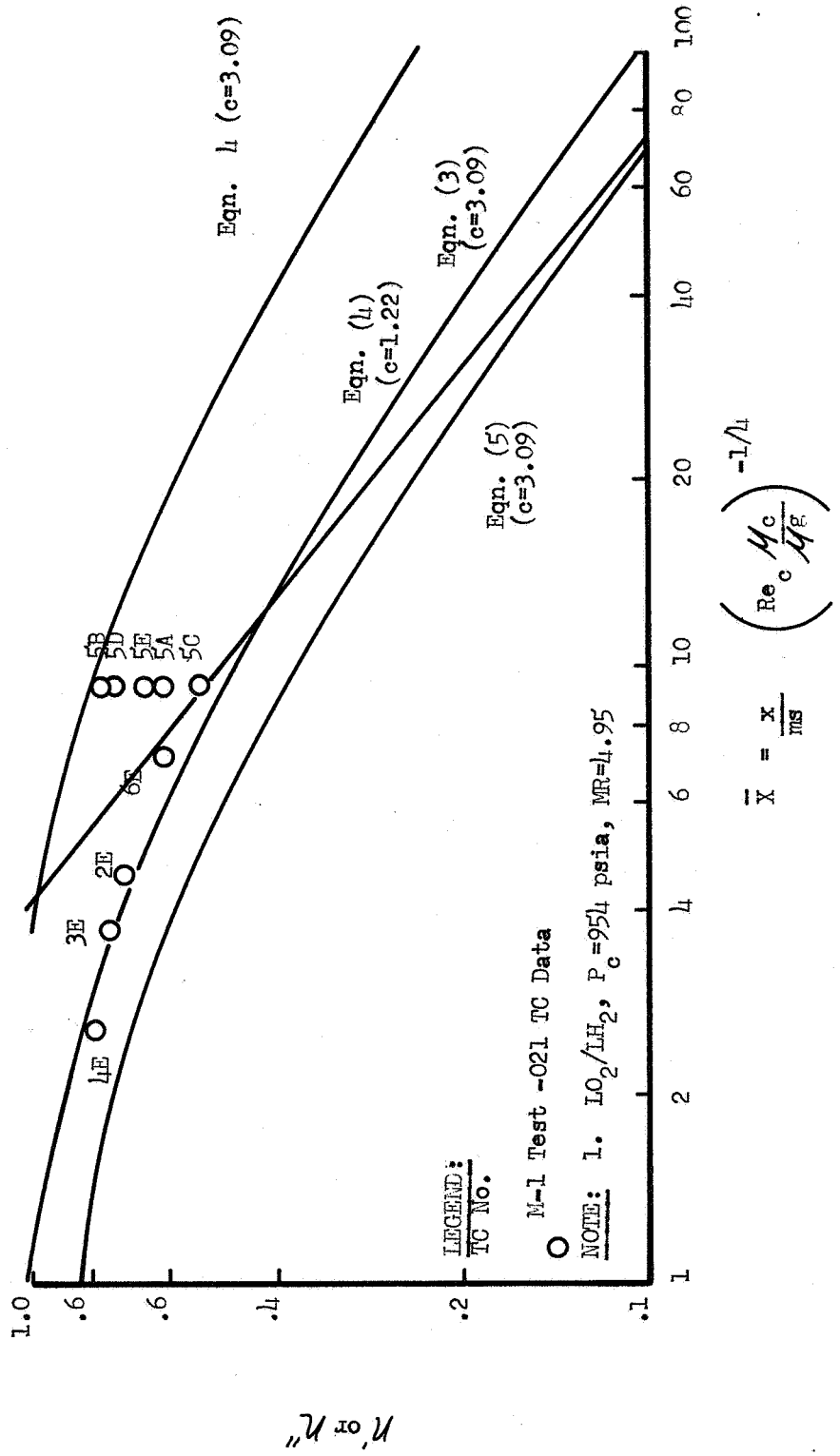


Figure 81. Comparison of M-1 Test Data to Boundary-Layer Film Cooling Model (Test No. 1.2-07-EHM-021)

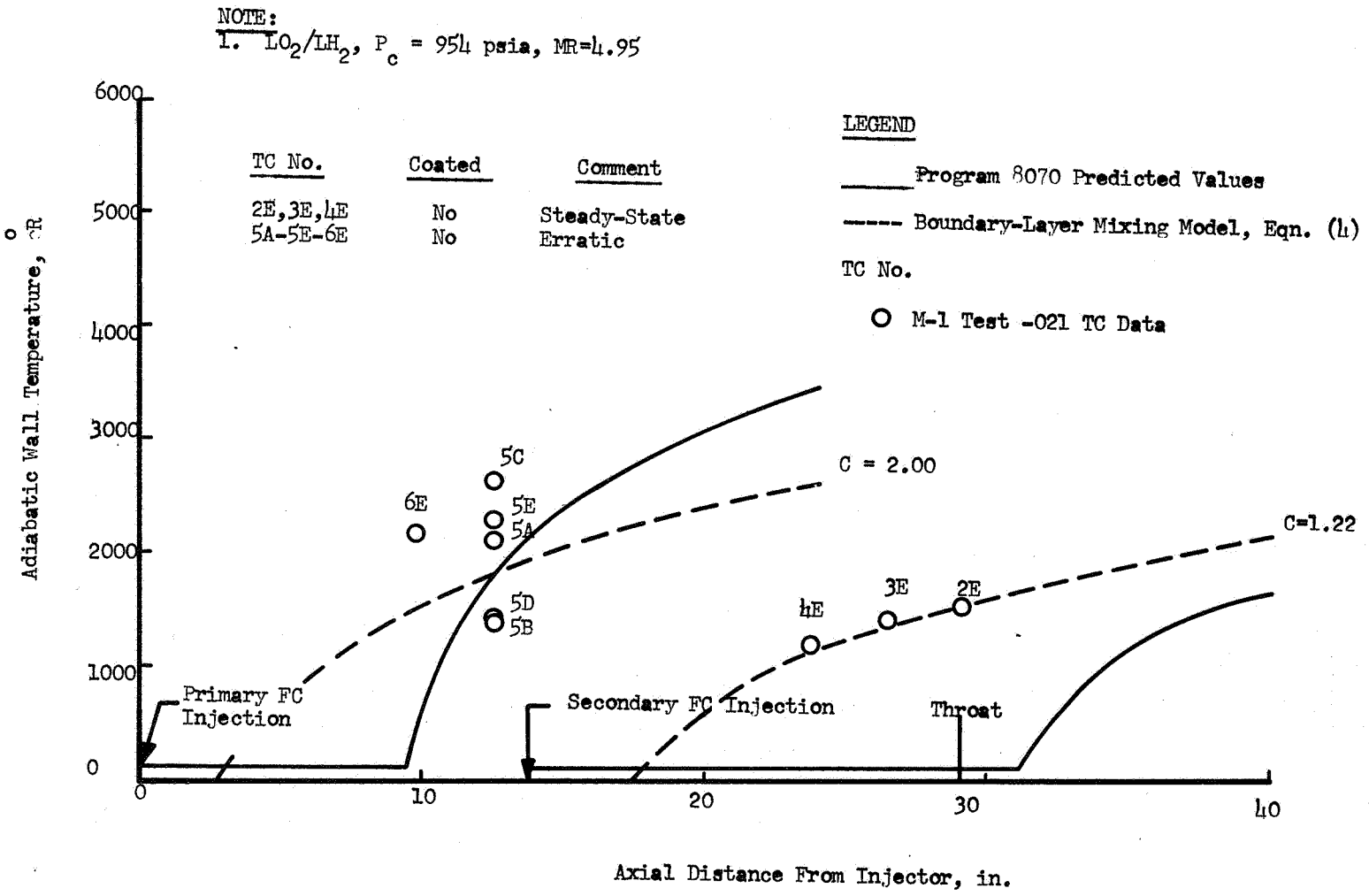


Figure 82. Predicted and Experimental Film-Cooled Adiabatic Wall Temperature

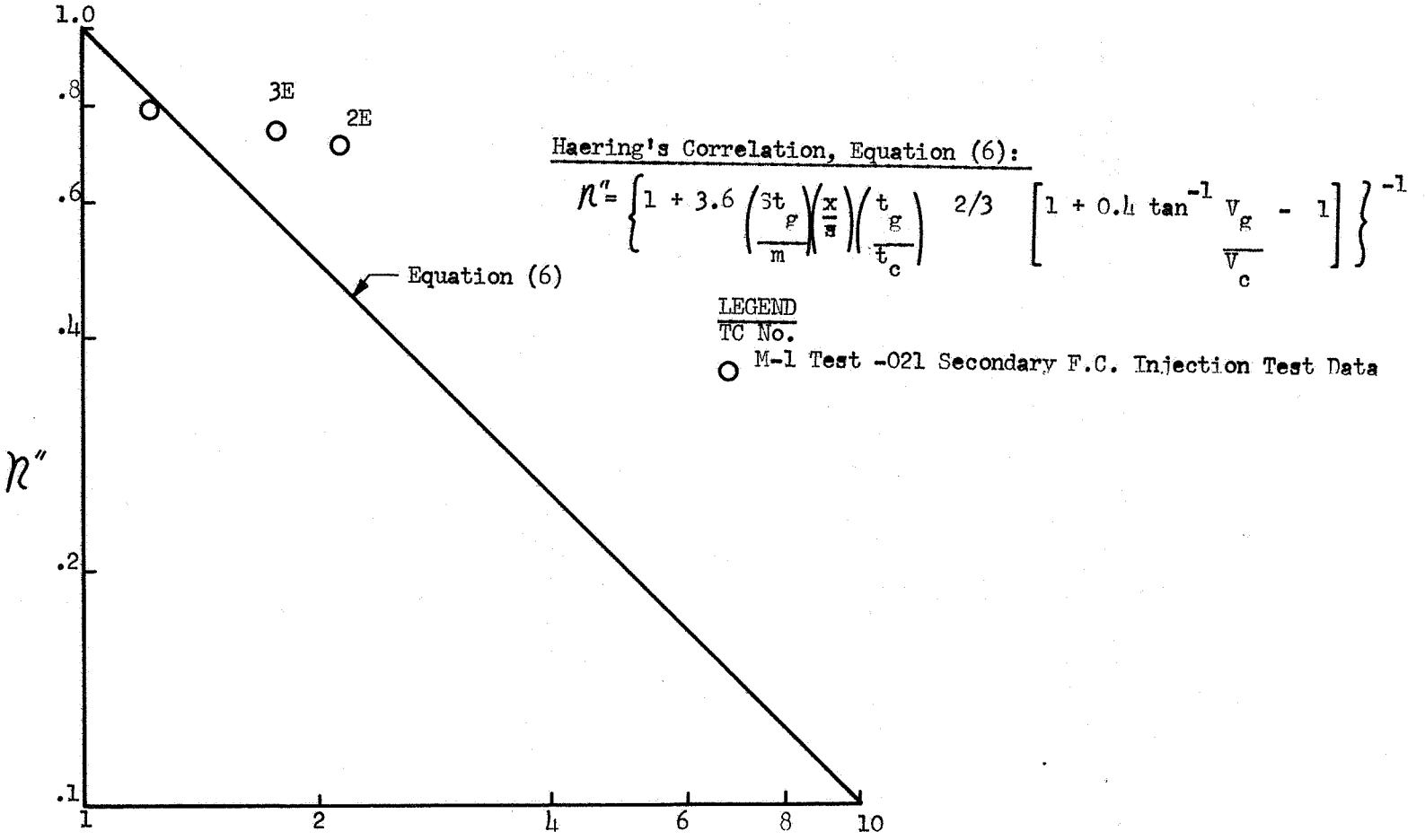


Figure 83. Comparison of M-1 Test Data to Haering's Correlation

D. STRUCTURE

1. Oxidizer Torus Calibration Testing

The original oxidizer torus, S/N 001, was designed without doublers. It was developed in anticipation of a negligible line load (see Figure No. 84). However, a re-evaluation of the line loading was conducted subsequent to the first Test Stand C-9 test firing. The original design was found to be inadequate for the increased loading. The above oxidizer torus S/N 001 was proof pressure tested to 2100 psi on 11 December 1964. Strains were monitored by means of 85 strain gages as well as stresscoat instrumentation at several locations on the torus. It was found that a 30-degree section of the torus in the inlet area was severely strained to a maximum of 3740 microinches-per-inch at 2100 psi proof pressure. The corresponding maximum stress level of 38,000 psi was judged to be only marginal because of the number of pressure loading cycles required in the M-1 Program. It was concluded that the torus would be inadequate for the design pressure plus line loads condition. Therefore, the inlet sections of both the proof-tested torus (S/N 001) and an untested one (S/N 002) were reinforced in the inlet area with welded plate doublers as shown on Figure No. 85.

The two strengthened torus assemblies were proof pressure tested (2100 psi) and then calibration load tested to determine their deflection response to line loads. The calibration testing was accomplished to provide more accurate torus spring rates, upon which a more accurate estimate of the design line loads could be based. In the third and final phase of the test, the design maximum effective operating pressure (1770 psi) was applied in combination with the currently estimated design line loads. Cracks in the original weld joint of the S/N 002 torus were found after the test. Additional repair welding would most likely have been detrimental; therefore, the entire 30-degree critical section at the inlet area was removed and replaced with a 0.687-in. thick reinforced plate welded in place. No cracks were found in the successfully proof tested S/N 001 torus and it was approved for engine service.

The final proof test of the S/N 002 torus was successfully conducted on 18 December 1965. Posttest inspection confirmed its structural soundness.

The line load deflection calibration testing was repeated to measure the increased stiffness of the strengthened torus. The S/N 002 torus was found to be approximately twice as stiff in the inlet area as it was prior to the addition of the reinforcement plate. The torus was strain gage calibrated during pressure and line loading so that the oxidizer inlet line loading during the TCA firing could be monitored.

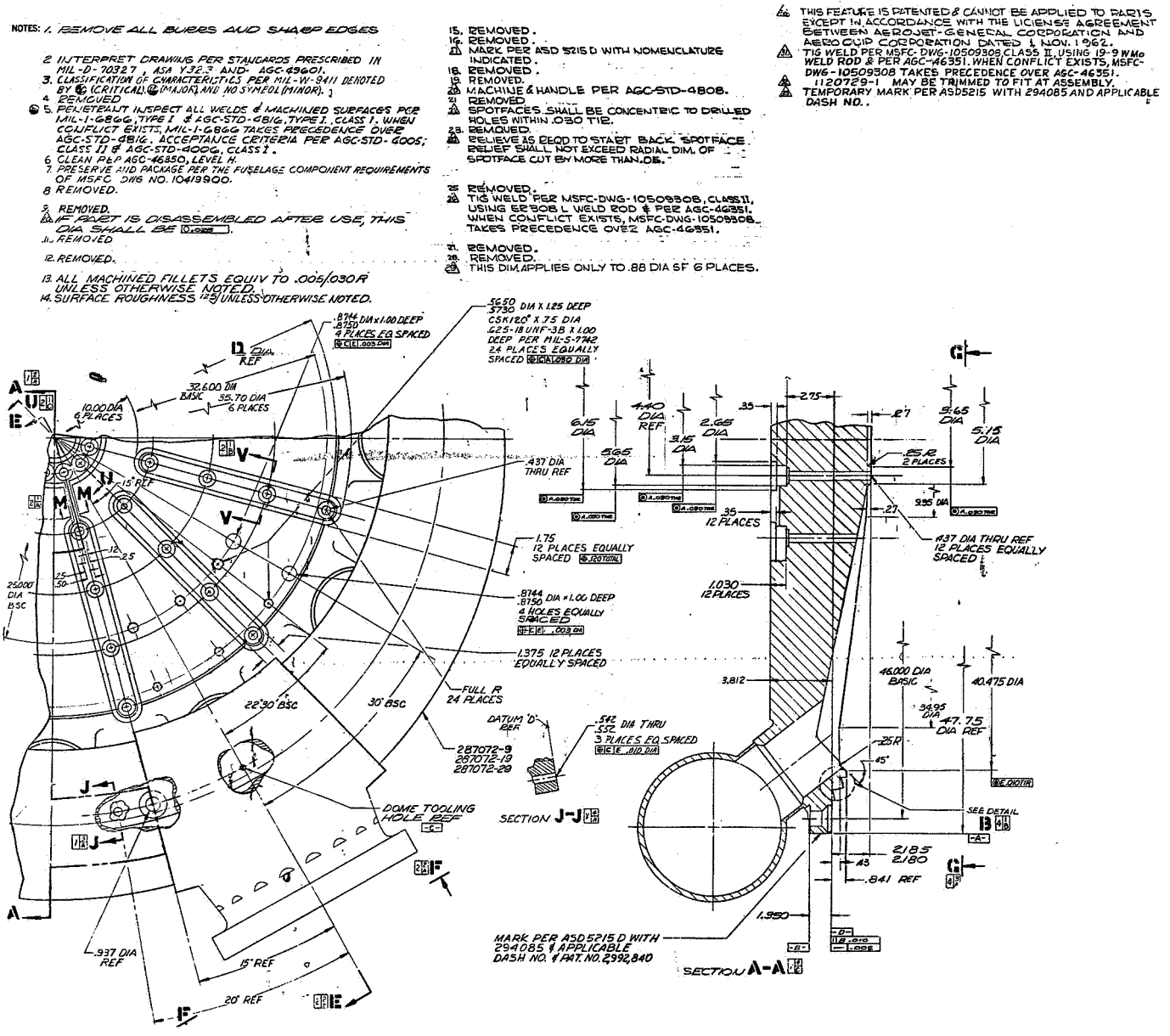


Figure 84. Oxidizer Torus and Dome Assembly (without Doublers)

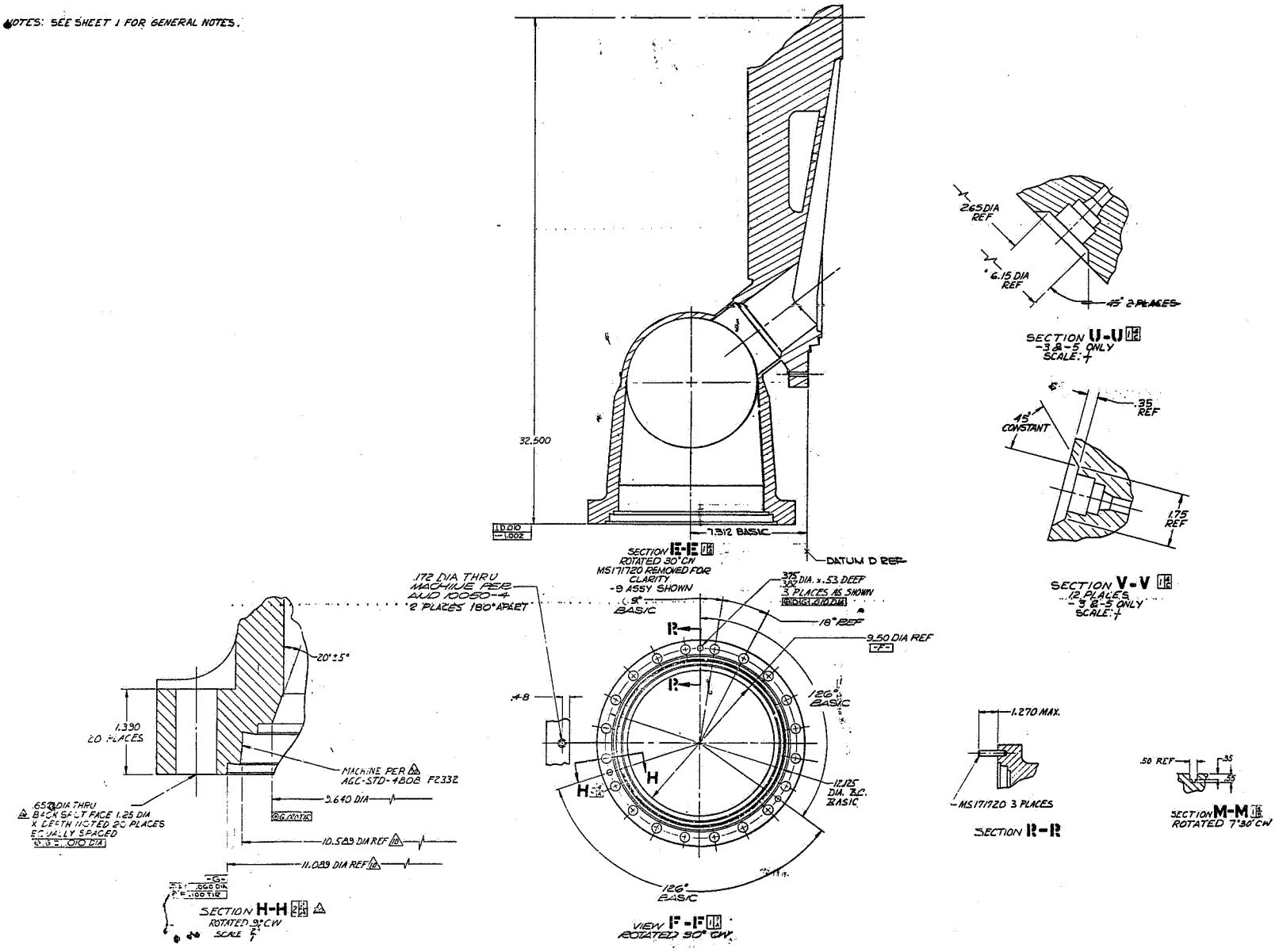


Figure 84. Oxidizer Torus and Dome Assembly (without Doublers)

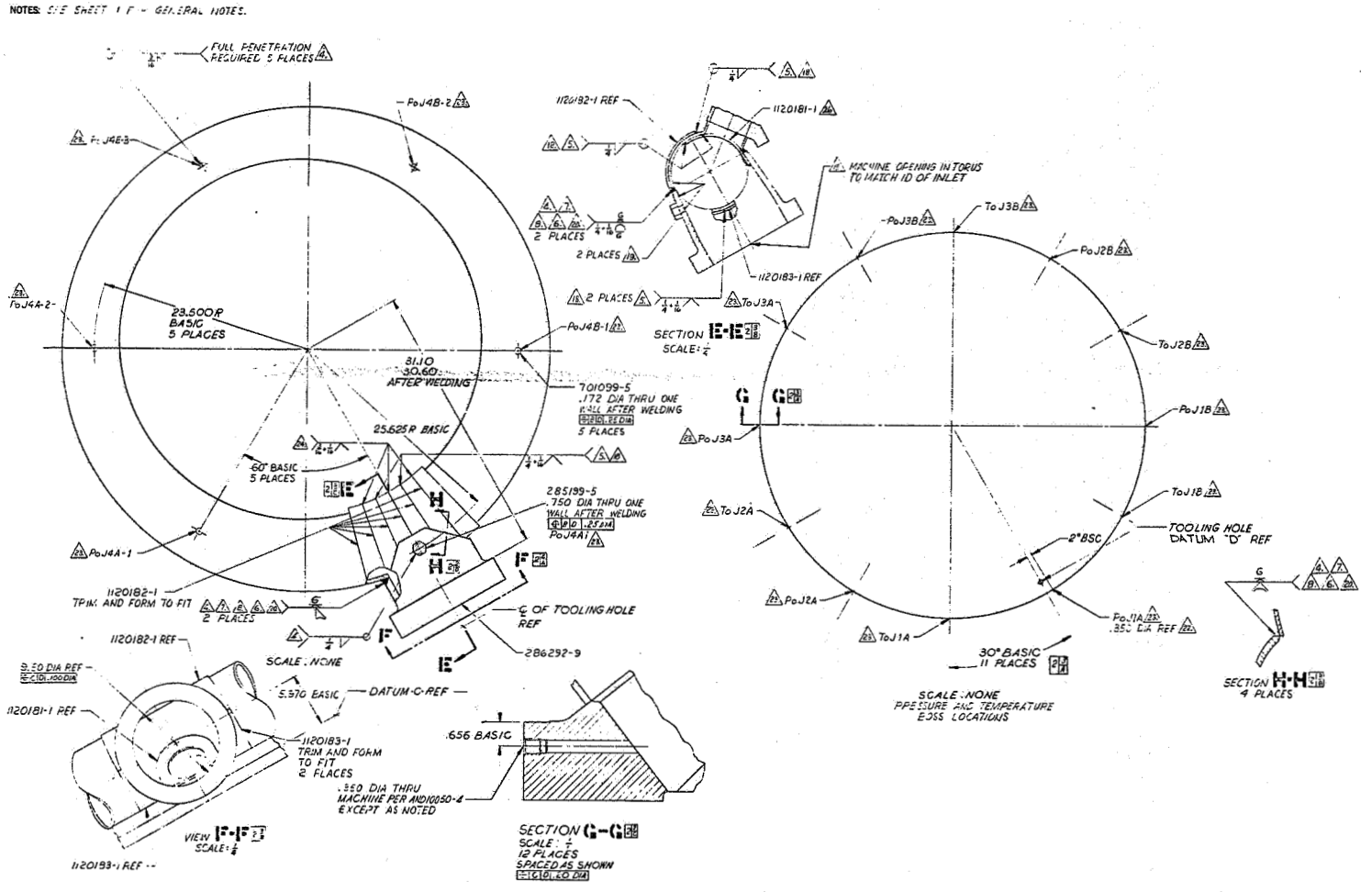


Figure 85. Oxidizer Torus with Doublers

2. Oxidizer Torus Dynamic Load Analysis

The maximum line loads at the torus inlet are shown on Table XV. These are based upon a direct comparison of the oxidizer torus strain gage readings obtained during the firings conducted with S/N 002 torus and S/N 020 injector. Note that these maximum line loads occurred after $FS_2$ and not during the start transient as was assumed for the design stress analysis. It is the shutdown transient condition that more closely simulates the originally anticipated start transient condition. The actual start transient was slowed considerably. The dynamic bending moment design value was 200,000 in.-lb.

The extremely low magnitude of all strains measured when combined with the complex load-strain relationship made it difficult to ascertain the accuracy of the loads listed in Table XV. A conservative data reduction was accomplished to assure that the actual values would not exceed the maximums shown.

After test No. 1.2-07-EHM-006, an investigation revealed that hot exhaust gas had gained access between the ablative liner and the chamber aft of the throat. This caused ejection of the liner and the resulting high line loads were indicated in the strain gage readings. These are tabulated on Table XV. The loads shown for the malfunction condition are in excess of the design loads; however, only 32 gages were used for S/N 001 torus with injector S/N 012. None of these gages were sensitive to the resultant line moment and only one gage was sensitive to the line torsion. Therefore, it is recommended that results be evaluated qualitatively rather than quantitatively.

3. System Response Analysis

The H-8 test stand natural frequency is 20 cps, with an equivalent viscous damping ratio of 0.02 to 0.03.

The maximum steady-state test stand response observed was approximately 0.3 g RMS, which implies that the dynamic loads in the oxidizer torus inlet are less than 10% of the design value.

The onset of combustion instability resulted in impulses estimated to range from 205 lb-sec to 720 lb-sec.

A load summary for some of the tests is presented on Table XVI. The values shown are zero-to-peak amplitudes of the 20 cps test stand frequency observed in the load cell output. The design moment for the torus inlet is 200,000 in.-lb, which roughly corresponds to a load cell oscillation amplitude of 375,000 lb, assuming no load reduction caused by the line dampers. Thus, an observed thrust oscillation of 40,000 lb 0-p would be interpreted as a torus inlet load of (40,000 ÷ 375,000) 100 = 10.7% maximum. This reflects the effectiveness of line dampers in reducing imposed loads (the equivalency between

TABLE XV

OXIDIZER INLET LINE LOADS AND TCA SUPPORT STRUT TRUSS LOADS

| Test 1.2-05-EHM | % Nominal Chamber Pressure | Peak Loads Before $FS_2$ | | | Peak Loads After $FS_2$ | | |
|---|---|---|---|---|---|---|---|
| | | Resultant Line Moment, in.-lb | Line Torsion, in.-lb | Support Strut Load, lb | Resultant Line Moment, in.-lb | Line Torsion, in.-lb | Support Strut Load, lb |
| 1 | 25 | 80,000 | 40,000 | 2,000 | 50,000 | 4,000 | 700 |
| 5 | 50 | 50,000 | 50,000 | 3,000 | 50,000 | 50,000 | 1,000 |
| 6 | 100 | 50,000 | 50,000 | 1,500 | 130,000 | 160,000 | 10,000 |
| 7 | 100 | 50,000 | 20,000 | 1,500 | 170,000 | 120,000 | 1,500 |
| 8 | 100 | 50,000 | 20,000 | 3,000 | 170,000 | 120,000 | 6,000 |
| 9 | 100 | 50,000 | 20,000 | 3,000 | 120,000 | 80,000 | 7,500 |
| 10 | 100 | 70,000 | 20,000 | 3,000 | 130,000 | 80,000 | 10,000 |
| 1.2-07-EHM | | | | | | | |
| 6 | 100 | 210,000 | 272,000 | | | | |

NOTE: Indicated loads are maximums and offer order of magnitude only.

TABLE XVI

AMPLITUDES OF LOAD CELL 20 cps OSCILLATIONS

(lb zero-to-peak)

| Firing No. | Ignition | Steady State | Liner Failure | Onset of Instability | Shutdown |
|---|---|---|---|---|---|
| 1.2-05-EHM-006 | 43,000 | 31,000 | N/A | N/A | 208,500 |
| 1.2-07-EHM-006 | 39,500 | 26,500 | 113,000 | 41,000 | 170,000 |
| 1.2-07-EHM-007 | 39,000 | 20,500 | N/A | 55,500 | 114,000 |
| 1.2-07-EHM-008 | 40,000 | 40,000 | N/A | 47,000 | 62,000 |
| 1.2-07-EHM-009 | 45,000 | 29,500 | N/A | SMALL | 56,000 |
| 1.2-07-EHM-010 | 38,500 | 30,000 | N/A | 67,500 | 55,500 |

thrust oscillation and torus inlet moment is 835,000 lb = = 200,000 in.-lb, respectively, with the dampers assumed to be effective). An approximate relationship between stand axial acceleration and torus inlet moment amplitude (assuming zero damper effectiveness) is 5 g = = 200,000 in.-lb.

Typical responses during ignition, steady-state, onset of instability, and shutdown are presented on Figure No. 86 for firing 1.2-07-EHM-006. Also shown is the effect of the liner failure during the test.

4. Seal Leakage

A significant problem during the tests was leakage of the large diameter flanges. Two of the large diameter joints had double Conoseals installed while a third utilized a Flexatallic® gasket. The leakage could have been caused by a combination of pressure loading and a thermal cycle which compressed the seal causing yielding followed by relief of the compression loading. Failure of a large diameter RACO® hydrogen seal also occurred because the Teflon coating shattered. This appears to be a basic problem with the non-metallics when subject to considerable flexing at liquid hydrogen temperatures. These leakages did not cause an excessively hazardous condition nor did they prevent the obtaining of required data; therefore, only expedient corrective action (i.e., purging between the two Conoseals and retorquing of the bolts) was undertaken to stop the leakage. The best long-term solution for large cryogenic joints appears to be the use of a seal weld.

E. OPERATIONAL EXPERIENCE

1. Test Set-Up and Propellant Feed System

All tests, except the initial unsuccessful attempt, were conducted with the thrust chamber assembly in a horizontal position on Test Stand H-8. Figure No. 87, whereon significant hardware items are labeled, shows the thrust chamber assembly installed in the test stand. Figure No. 88 is a schematic diagram of the test system showing propellant lines, valves and flowmeters, purge connections, and the fluorine supply system for ignition. As can be seen from this schematic, liquid hydrogen from the fuel tank (FT) is pressurized by gaseous hydrogen and flows through the fuel safety valve (FSV), the volumetric flowmeter (FMF), the mixer, the thrust chamber fuel valve (TCFV), and into the thrust chamber assembly. At the mixer, gaseous hydrogen is added to the liquid hydrogen to control the hydrogen temperature at the injector inlet. Liquid oxygen from the oxidizer tank (OT) is pressurized with gaseous nitrogen and flows through the oxidizer safety valve (OSV), the oxidizer volumetric flowmeter (FMO), the main thrust chamber oxidizer valve (TCOV), and/or by-pass (TCOV-BP) oxidizer thrust chamber valves into the thrust chamber assembly.

---

® Flexitallic Gasket Co.

® RACO Seal Engineering Division of R. E. Kreith Co.

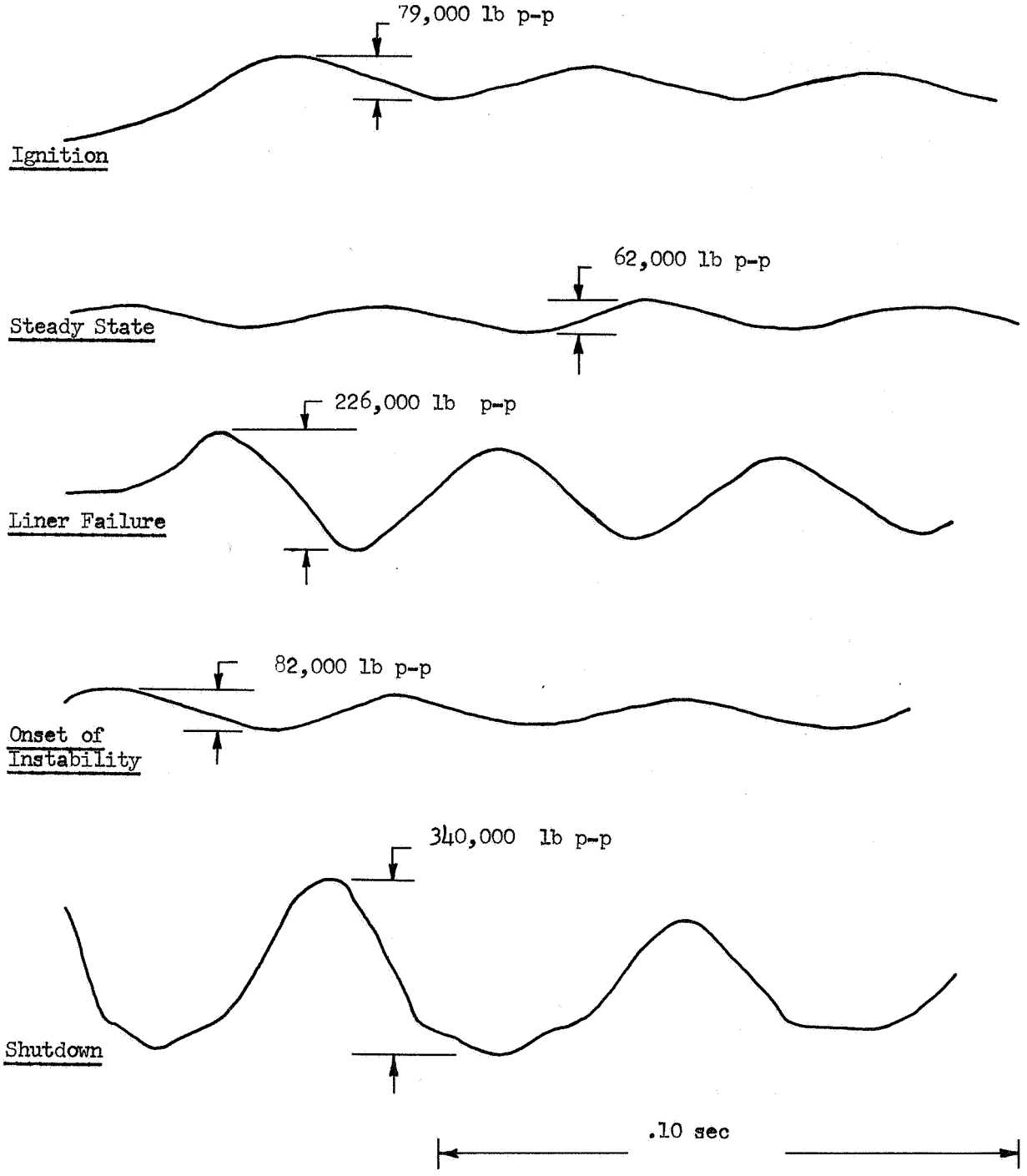


Figure 86. Typical Responses during M-1 TCA Firing, Test No. 1.2-07-EHM-006

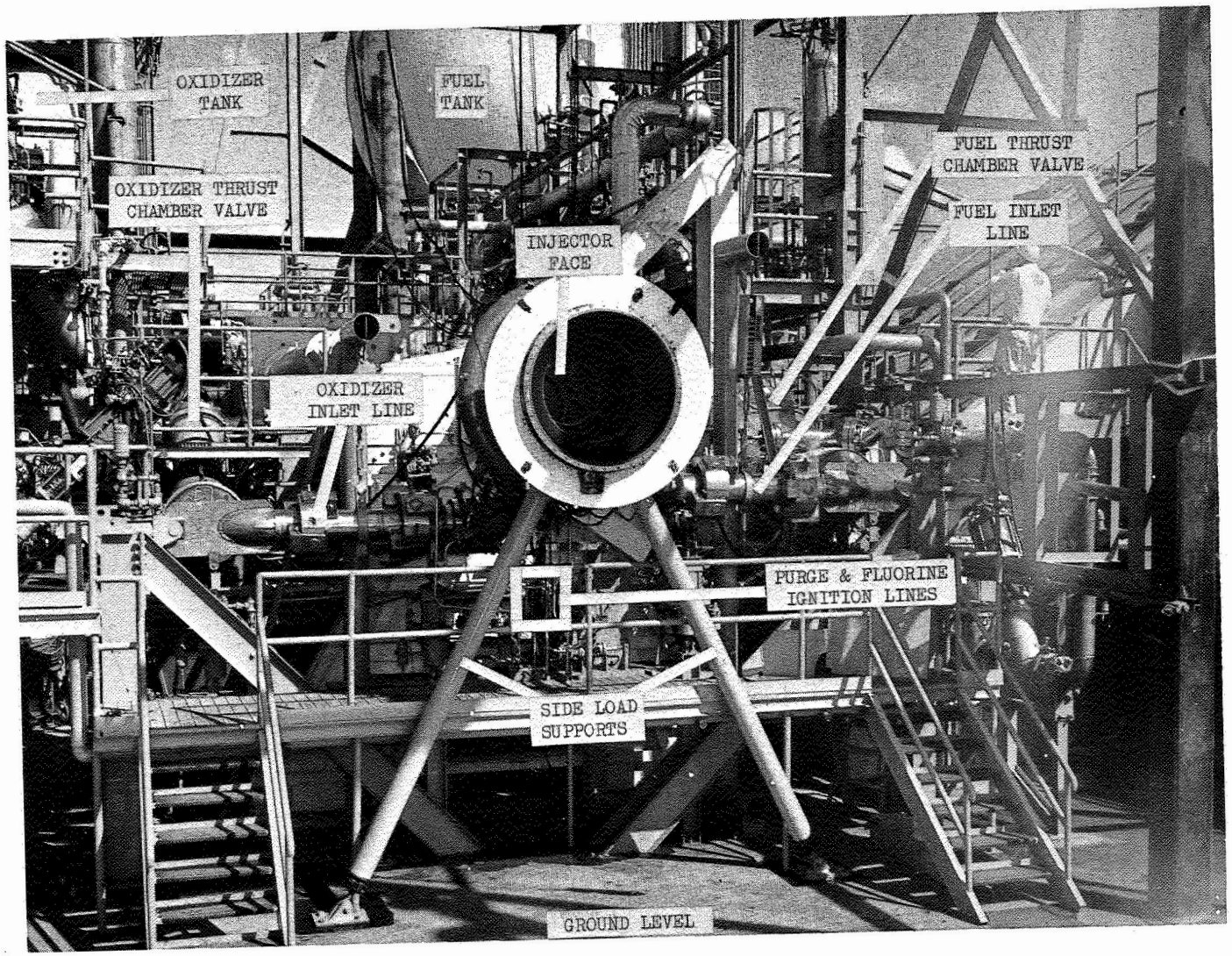


Figure 87. Thrust Chamber Assembly Installed in Test Stand H-8

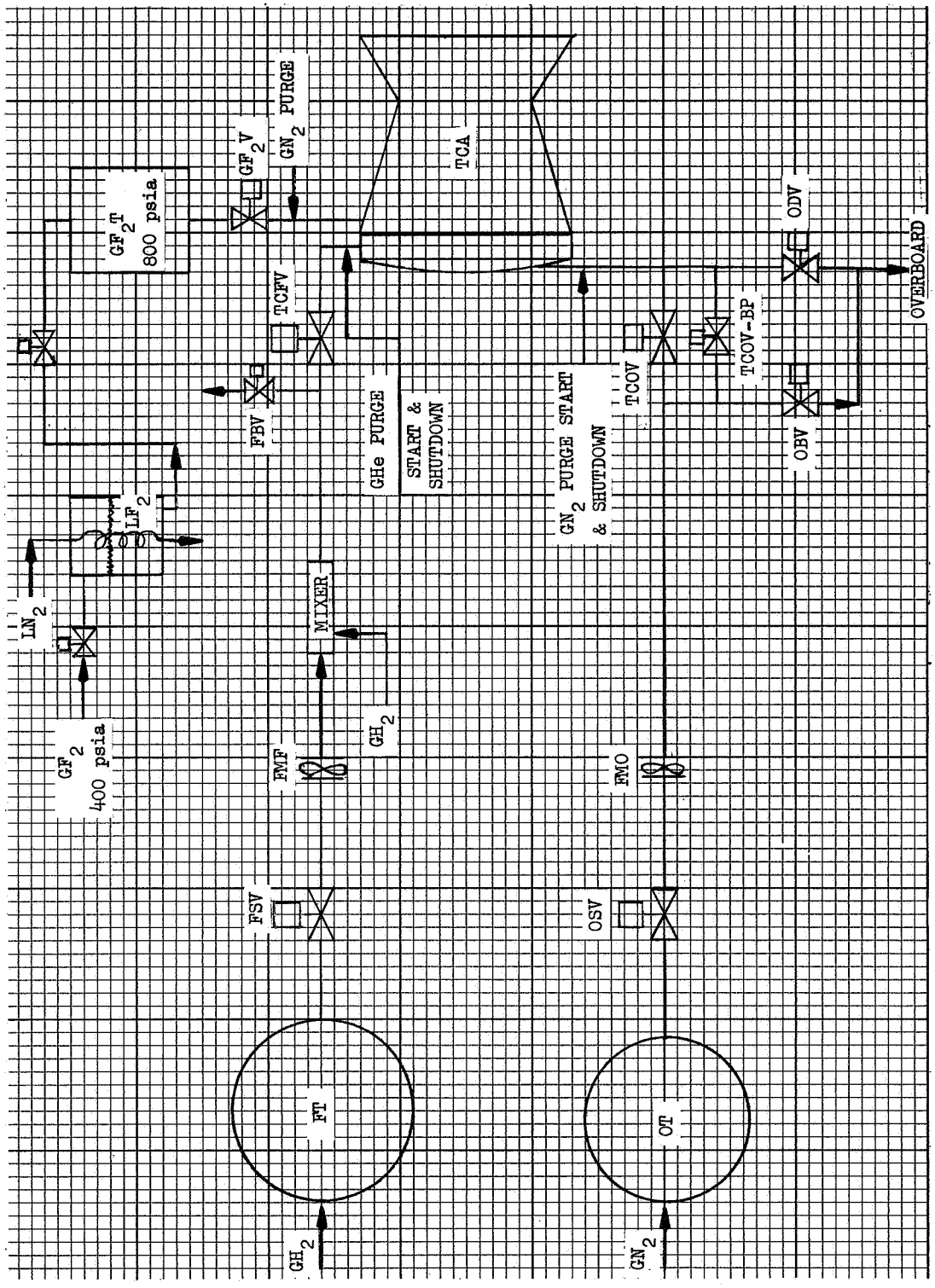


Figure 88. Test System Schematic

The system was instrumented to measure thrust, propellant flows, pressures, temperatures, line motions, thrust chamber and line accelerations as well as local strains at key locations. Appendix E is a typical instrumentation list. A motion picture coverage plot plan, which shows camera locations relative to the thrust chamber also is included in this appendix.

2. Start Sequence, Ignition System, and Start Transient

a. Start Sequence

The propellant tanks and the gaseous fluorine run tank are filled while low volume purges are provided to the thrust chamber propellant manifolds. The lines upstream of the thrust chamber valves are bled-in through the fuel bleed valve (FBV) and the oxidizer bleed valve (OBV) until filled with liquid (see Figure No. 88). Then, the purge to the oxidizer manifold is increased to provide a pressure of 10 psig to 20 psig in the manifold. The propellant tanks are pressurized to predetermined initial settings and pressure control is established. If the temperature downstream of the propellant valves indicate insignificant or no through leakage, fire switch is initiated.

The fire switch activates the fuel thrust chamber valve pilot valve to the open position and starts the shutdown timers. If the following have not occurred prior to pre-selected times, shutdown is signalled:

(1) Oxidizer by-pass valve full opening.
(2) Attainment of a chamber pressure of 200 psia or greater.
(3) Initiation of shutdown.

When the fuel valve reaches a 10% open position, it activates the circuits to open the fluorine ignition valve as well as the valve controlling the flow of gaseous hydrogen to the mixer. Burnout of the fluorine ignition line or an excess temperature at the hydrogen injector inlet at any time will cause a shutdown. A position switch on the fluorine valve, which is set at 50% open, creates a signal to open the by-pass oxidizer thrust chamber valve. If this sequence is completed, the fluorine ignition valve remains open and the oxidizer by-pass valve is opened prior to a pre-selected time. The fuel valve continues to open and the thrust chamber inlet lines and manifolds begin to fill. Fuel reaches the chamber first, followed rapidly by the fluorine. The entrance of fluorine provides an ignition source. Oxidizer reaches the combustion zone and ignition occurs. Shortly after ignition, the oxidizer manifold fills and chamber pressure rises rapidly to above 200 psia. This pressure is controlled by the oxidizer flow rate. If these events have been completed before a predetermined time and the oxidizer by-pass valve has remained open, the sequence continues. Also during this period, the valve admitting gaseous hydrogen to the mixer opens at a pre-set rate.

A chamber pressure switch set at 200 psia is used to signal ramping of the fuel tank from its initial setting to an intermediate value and signals closure of the oxidizer manifold purge valve. Attainment of a pressure in the fuel tank of approximately 10% above the initial setting, full opening of the fuel valve, full open position of the oxidizer by-pass valve, and 50% open position of the fluorine valve permit the main oxidizer thrust chamber valve to be signalled open and the continuation of the addition of gaseous hydrogen to the mixer. A position switch on the main oxidizer thrust chamber valve is set at approximately 50% open. It creates the signal to permit ramping of the hydrogen and oxygen tank pressure to the pre-selected steady-state values, closure of the fluorine ignition valve, and opening of a fluorine system purge valve.

The system proceeds to and remains at steady-state until shutdown is signalled by a pre-set timer circuit unless a safety shutdown occurs first. This sequence is illustrated graphically on Figure No. 89.

The following are the safety shutdown criteria:

- PaTCFV is greater than 1200 psia by $FS_1$ + 1.350 sec and is maintained until $FS_2$.
- Fuel safety open (from initial valve opening to $FS_2$).
- Loss of gaseous hydrogen pressurization to the mixer.
- Combustion Stability Monitor.
- Gaseous fluorine manifold burn-through.
- Fuel temperature at injector inlet too high.
- Loss of TCV actuation tank fluid level.
- Oxidizer tank overpressurization.
- Fuel tank overpressurization.

The sequence and shutdown devices were established as a result of the malfunction analysis presented on Table XVII. Protection against delayed ignition explosions, severe burning caused by high mixture ratios, and damage resulting from instability were deemed essential.

This sequence was used in all of the successful tests. Typical actual pressure, flow, and temperature histories are shown on Figures No. 90 through No. 95.

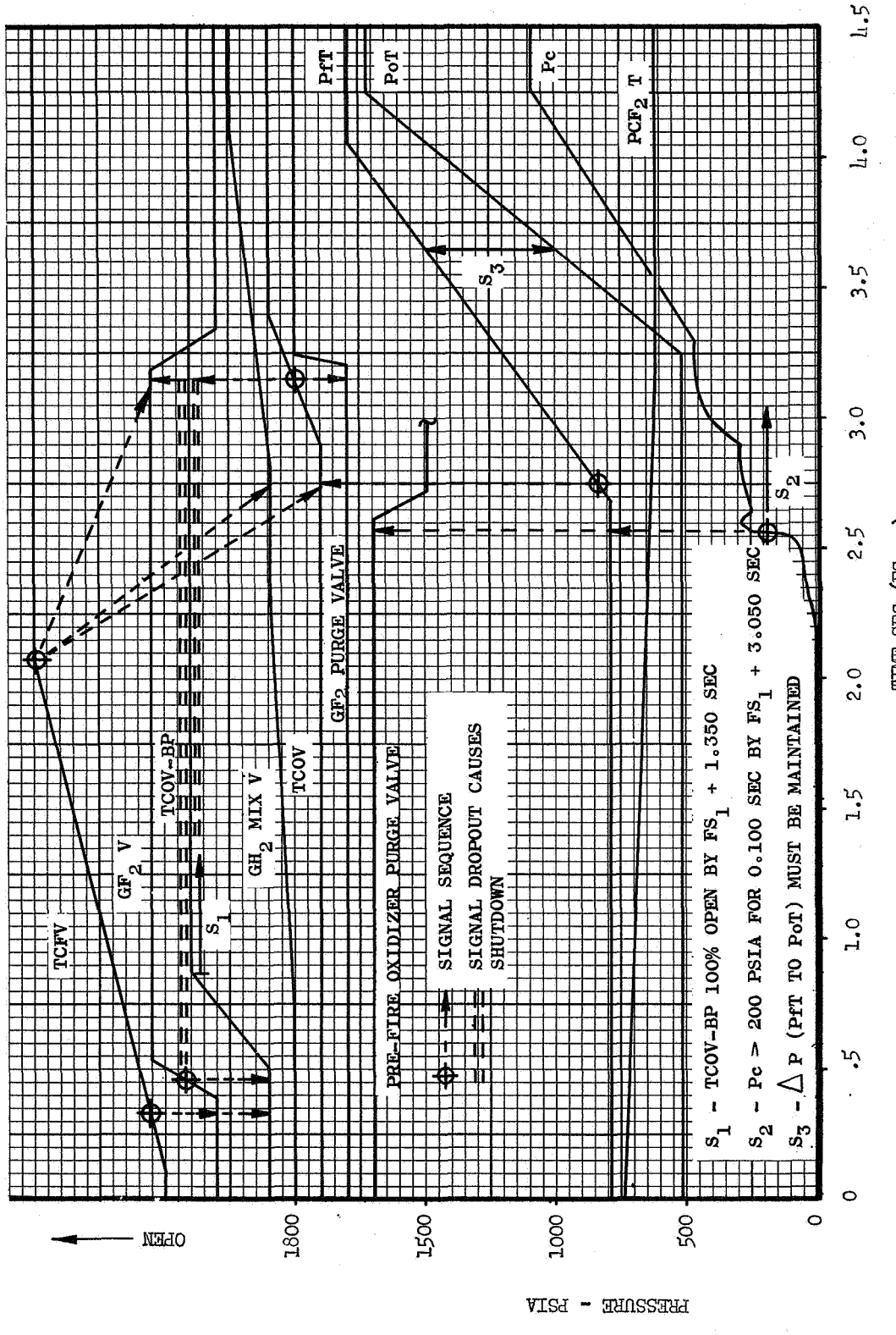


Figure 89. Start Sequence

TABLE XVII

MALFUNCTION ANALYSIS OF M-1 TRANSIENT CONTROLS

| Potential Control System Malfunction | Safety Feature | Predicted Test Result |
|---|---|---|
| 1. Delayed motion of $LH_2$ TCV at opening. | 1. All subsequent events dependent upon attaining $LH_2$ TCV 10% switch. | 1. Test conditions will be normal but delayed timewise after $FS_1$ to extent of $LH_2$ TCV initial delay. If delay sufficient to extend opening of oxidizer by-pass valve past 1.35 sec, shutdown is signalled. |
| 2. Fuel TCV does not open sufficiently to close 10% open switch. | 2. Fluorine gaseous hydrogen valve and oxidizer by-pass valve will not open. Timer shuts test down at 1.35 sec. | 2. Flow of hydrogen will not exceed normal hydrogen lead before ignition. |
| 3. Fluorine valve fails to open. | 3. Oxidizer by-pass valve will not open. Timer shuts test down at 1.35 sec. | 3. Hydrogen flow will not exceed normal hydrogen lead before oxidizer ignition. |
| 4. Gaseous hydrogen valve fails to open. | 4. CSM will shut down system if instability results from cold hydrogen. | 4. Baffles should prevent instability even with cold hydrogen. |
| 5. Gaseous hydrogen valve opens too rapidly. | 5. Temperature increase at thrust chamber valve will cause shutdown. | 5. Mixture ratio will be acceptable for low pressure operation. |
| 6. Fluorine supply line burns out. | 6. Continuity of burn wire on fluorine line will be interrupted and test will shut down. | 6. Same as items 2 and 3. |
| 7. $LO_2$ by-pass valve fails to open. | 7. Timer shuts test down if $LO_2$ by-pass valve not full-open by $FS_1$ + 1.35 sec. | 7. Flow of hydrogen prior to shutdown not in excess of normal hydrogen lead before ignition. |

TABLE XVII (cont.)

| Potential Control System Malfunction | Safety Features | Predicted Test Result |
|---|---|---|
| 8. Delayed motion of $LO_2$ by-pass valve at opening. | 8. Timer shuts test down if $LO_2$ by-pass valve is not full open in specified interval to obtain proper ignition. | 8. Hydrogen flow will be less than that as a result of normal fuel lead. |
| 9. $LO_2$ by-pass valve closure results from loss of electrical signal or hydraulic actuation after completion of full-open-timer circuit. | 9. $LO_2$ TCV will not open unless near-normal ignition is obtained. Propellant flow pressure on $LO_2$ by-pass valve gate forces valve closure at slower than normal closure rate. If $LO_2$ by-pass open signal is lost before oxidizer valve is 50% open, test is shut down. | 9. If failure is late enough so that normal ignition is obtained, normal test will result. If sub-normal ignition occurs, such that test could not proceed normally, $LO_2$ TCV will not open, combustion will terminate (fuel-rich) open oxidizer by-pass valve closure. |
| 10. Fluorine ignition valve closure results from loss of signal or actuation pressure after reaching 50% open position. | 10. If 50% open, signal of fluorine ignition valve is lost before oxidizer valve is 50% open, test will be shut down. | 10. Safe fuel-rich shutdown from any point of signal loss. |
| 11. $LH_2$ TCV opens to greater than the 10% position but less than the 100% position. Loss of electrical signal or hydraulic actuation occurs. | 11. $LO_2$ TCV will not open. In event of loss of current to pilot valve solenoid or loss of hydraulic actuation pressure. Shutdown will be signalled by decaying hydraulic pressure to opening side of the actuator. | 11. Based upon a predicted maximum $P_c$ of 480 on by-pass flow only, then shutdown purges of approximately 500 psi would be adequate to override any $P_c$ experienced and result in a near-normal shutdown. |
| 12. Less than specified rate of opening of $LH_2$ TCV. | 12. Test will be shut down by 1.35 sec timer if $LH_2$ TCV rate of opening precludes opening of $LO_2$ by-pass. | 12. Satisfactory shutdown would occur. |

TABLE XVII (cont.)

| Potential Control System Malfunction | Safety Features | Predicted Test Result |
|---|---|---|
| 13. $LH_2$ TCV sticks after reaching the 10% position but prior to reaching the 100% position. (Caused by mechanical interference.) | 13. The $LO_2$ TCV will not open if the $LH_2$ TCV does not reach the 100% position. Test will continue at low MR and $P_c$. | 13. Ignition would occur and attain a $P_c$ between 270 and 350 psi dependent upon $LH_2$ TCV position. In all cases, the MR will be 5.0 or less. Test would continue at this condition until shutdown. |
| 14. Fuel tank pressurization system fails to ramp. | 14. $LO_2$ TCV will not open until fuel tank pressure ramp is indicated. | 14. Test will continue at low $P_c$ and MR. |
| 15. 200 psi chamber pressure detection system fails to operate. | 15. $LO_2$ TCV will not open until detection system senses prescribed pressure. Test will shut down. | 15. Test will shut down at low MR. |
| 16. 200 psi chamber pressure detection system operates prematurely. | 16. $LO_2$ TCV will not open until after fuel tank pressure ramp is obtained. | 16. Computer model predicts $P_c$ surge of 825 psi at a MR of 4.6. Maximum system pressure surge occurs at the $LO_2$ TCV inlet at 1400 psi. Test will continue to schedule shutdown. |
| 17. $LO_2$ TCV fails to open. | 17. Oxidizer by-pass valve remains open until $FS_2$. | 17. Combustion will reach a $P_c$ of 555 and a MR of 1.63. Test will terminate on timed $FS_2$. |
| 18. Delayed motion of $LO_2$ TCV at opening. | 18. Oxidizer by-pass valve remains open until 50% $LO_2$ TCV opening. | 18. Delayed attainment of steady-state proportional to delay of valve motion. |

TABLE XVII (cont.)

| Potential Control System Malfunction | Safety Features | Predicted Test Result |
|---|---|---|
| 19. $LO_2$ TCV partially or fully opens and loss of electrical signal or hydraulic pressure occurs. | 19. $LO_2$ TCV will close at rate slightly less than normal because of propellant flow pressure on valve gate and loss of hydraulic pressure to the opening side of the actuator. | 19. $LO_2$ TCV closure will reduce $P_c$ level and MR to anywhere from 0 to that of item 17 (dependent upon position of by-pass valve), if full closure is attained prior to timed $FS_2$. If full closure is not attained by $FS_2$, $P_c$ and MR will be between 0 and steady-state value (dependent upon by-pass valve position). Stand safety valve or oxidizer by-pass will control shutdown. |
| 20. $LO_2$ TCV sticks (caused by mechanical interference) after partially opening. | 20. If $P_c$ level and MR results in in unstable operation (chugging most probable) low-frequency CSM device will signal shutdown. | 20. Mixture ratio and $P_c$ will be governed by degree of $LO_2$ TCV opening. MR cannot exceed 5.5. Test will continue for scheduled duration unless excessive chugging results causing initiation of shutdown. |
| 21. Less than specified rate of $LO_2$ TCV opening. | 21. $LO_2$ by-pass valve remains open until 50% $LO_2$ TCV opening. | 21. Test will continue with MR and $P_c$ at less than predicted values as a function of $LO_2$ TCV open position. Attainment of steady-state dependent upon degree of reduced rate of opening. |
| 22. $LO_2$ pressurization system fails to ramp. | 22. Low-frequency CSM shutdown may occur. | 22. Test will continue for scheduled duration at a MR of approximately 2.1 and a $P_c$ of approximately 660 psi unless excessive chugging results. |

TABLE XVII (cont.)

| Potential Control System Malfunction | Safety Features | Predicted Test Result |
|---|---|---|
| 23. Delayed motion or failure to close of $LO_2$ by-pass valve at 50% $LO_2$ TCV position. | 23. Sequenced closure of oxidizer stand safety valve at shutdown. | 23. Test will continue at a MR up to approximately 7% higher. Normal shutdown. |
| 24. Either main thrust chamber valve fails to close at shutdown or slow rate of closure. | 24. Stand safety valve closure sequence. | 24. Normal shutdown. |
| 25. Delayed motion of $LH_2$ TCV at closing. | 25. Sequenced closure of $LH_2$ stand safety valve. | 25. Normal shutdown controlled by stand fuel safety valve closure. |
| 26. Delayed motion of $LO_2$ TCV at closing. | 26. Sequenced closure of $LO_2$ stand safety valve, shutdown purges and dumps. | 26. Test would be terminated normally by closure of stand $LO_2$ safety valve. |
| 27. Failure of fuel manifold high pressure shutdown purge. | 27. Shutdown valve sequence, safeties and TCV's, provide intended fuel-rich condition at shutdown. | 27. Normal fuel override at shutdown would preclude excessive MR. Time to eliminate fuel downstream of $LH_2$ TCV would be extended. |
| 28. Failure of oxidizer manifold high pressure shutdown purge. | 28. Normal fuel-rich condition at shutdown plugs oxidizer dump valve sequence. | 28. Oxidizer dump system will minimize pressurized period after $FS_2$ of oxidizer circuit downstream of $LO_2$ TCV. If MR is high, it will be at a very low level of $P_c$. |
| 29. Actuator tank pressure regulator fails, overpressurizing system. | 29. Burst disc ruptures, preventing overpressurization of actuator tanks. | 29. Normal test will result because check valves maintain actuator tank pressures. Slight effect upon valve rate of motion caused by bleed-down of tank from any subsequent actuation. |

TABLE XVII (cont.)

| Potential Control System Malfunction | Safety Features | Predicted Test Result |
|---|---|---|
| 30. Actuator tank pressure regulator fails, providing less than required pressurization. | 30. Check valves prevent actuator tank pressure loss. | 30. Valve opening and closing rate reduced as a function of tank pressure at time of failure and loss resulting from actuation thereafter. Could result in lengthened transient, both start and shutdown. |
| 31. Loss of hydraulic fluid as a result of leakage. | 31. Liquid low level sensors set to provide a minimum of 3 full valve cycles under normal static conditions. Sensor circuit precludes test initiation if fluid level below sensor and will signal shutdown if test has progressed past $FS_1$. | 31. Normal shutdown will result. Leakage at such a rate as to reduce or exhaust 3 cycle capability during subsequent duration impossible without significant structural failure. |
| 32. Rupture of actuator tank pressurization line upstream of individual actuator tank check valves. | 32. Check valve precludes loss of actuator tank pressure. Actuator tank, even at low level sensor, provides 3 plus valve cycles. | 32. Test conditions will be normal. |
| 33. Loss of actuation pressure or signal to stand fuel safety valve. | 33. Shutdown signalled by movement of valve from 100% open position. | 33. Normal shutdown will result because of valve sequencing. |
| 34. Loss of actuation pressure or signal to stand oxidizer safety valve. | 34. Manual shutdown as TCA parameters decay. | 34. Fuel-rich shutdown. |

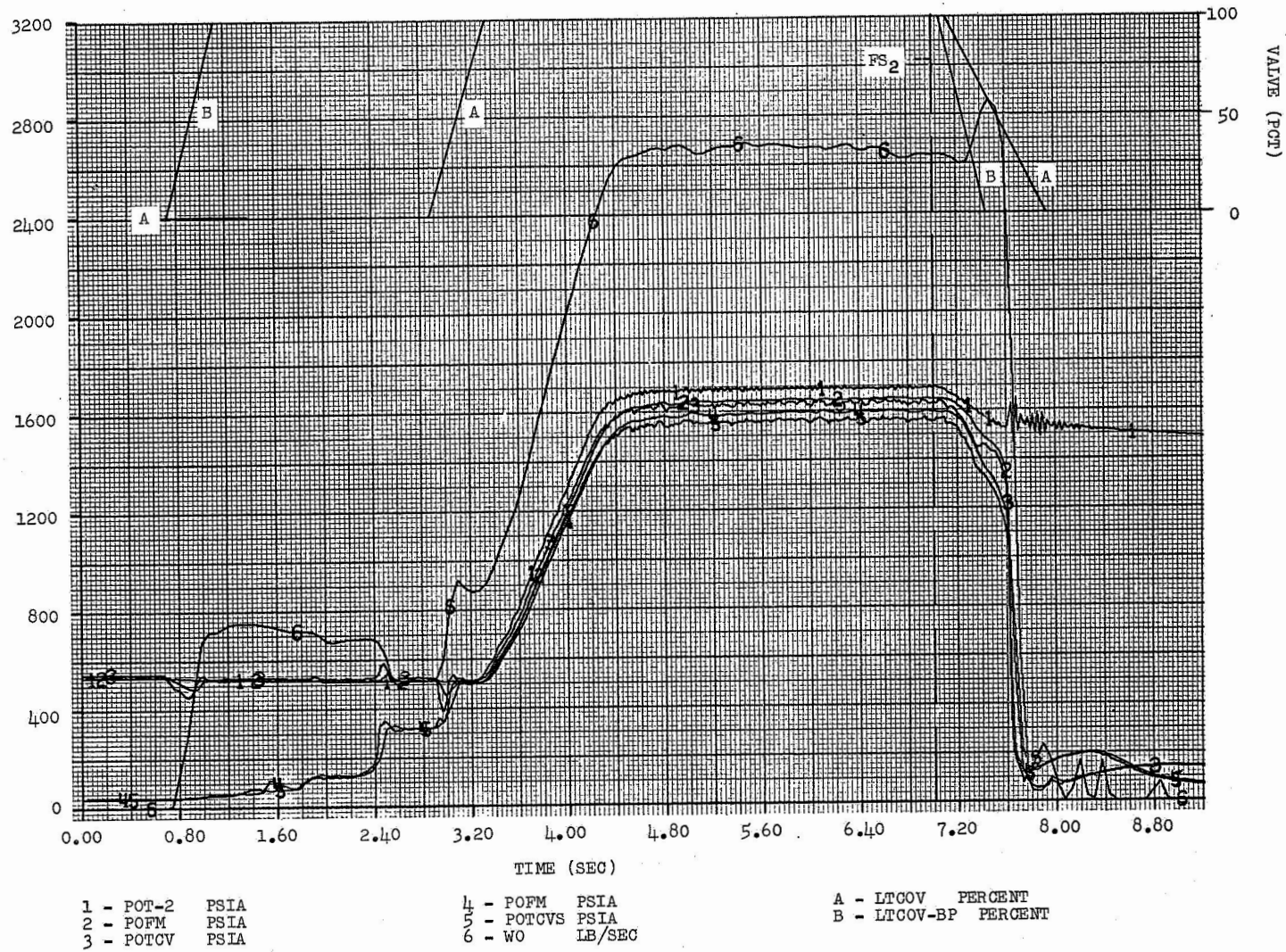


Figure 90. Typical Actual Pressure, Flow, and Temperature Histories (Test No. 1.2-05-EHM-010) - Oxidizer Pressures

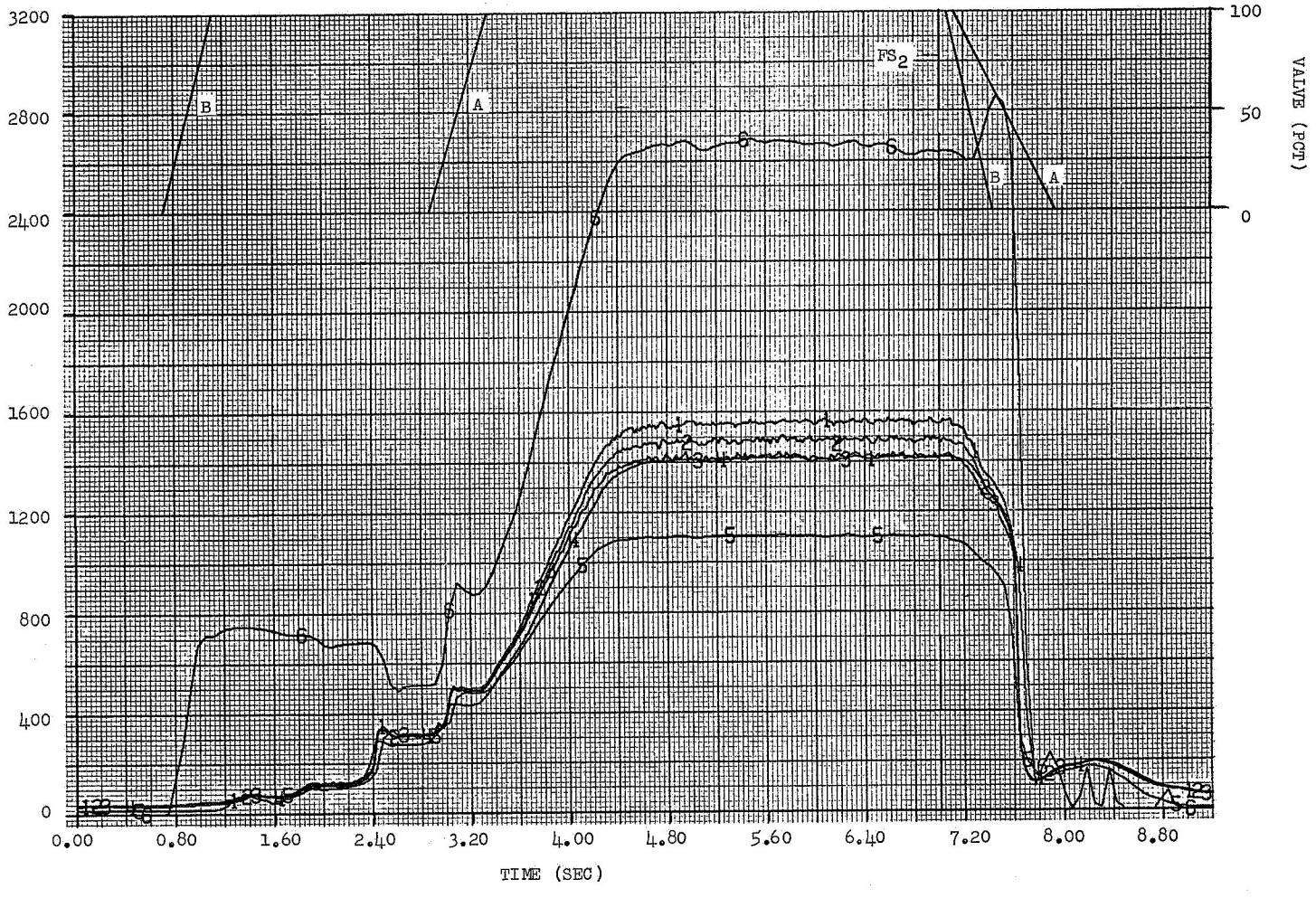


Figure 91. Typical Actual Pressure, Flow, and Temperature Histories (Test No. 1.2-05-EHM-010) - Oxidizer Pressures

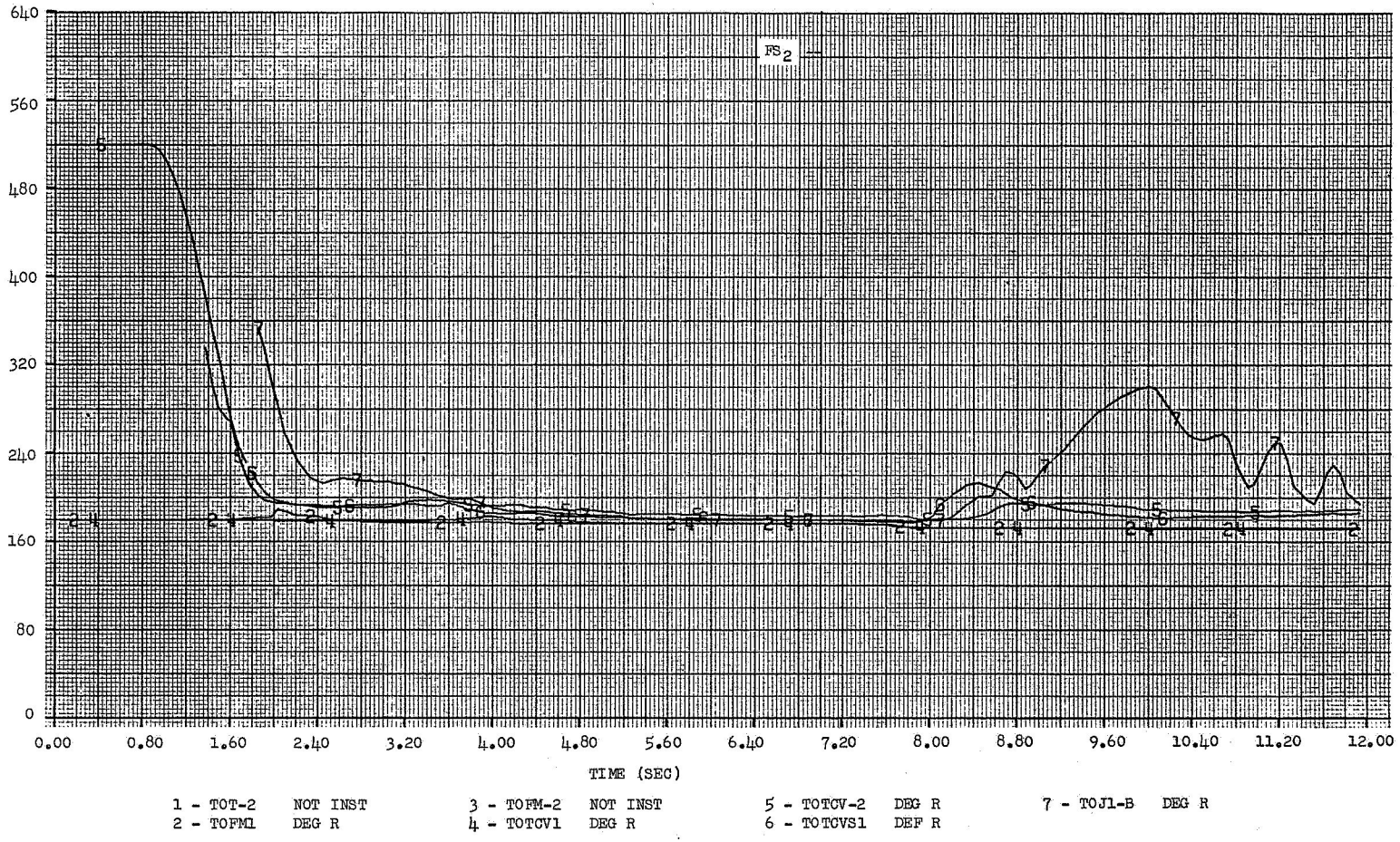


Figure 92. Typical Actual Pressure, Flow, and Temperature Histories (Test No. 1.2-05-EHM-010) - Oxidizer Temperatures

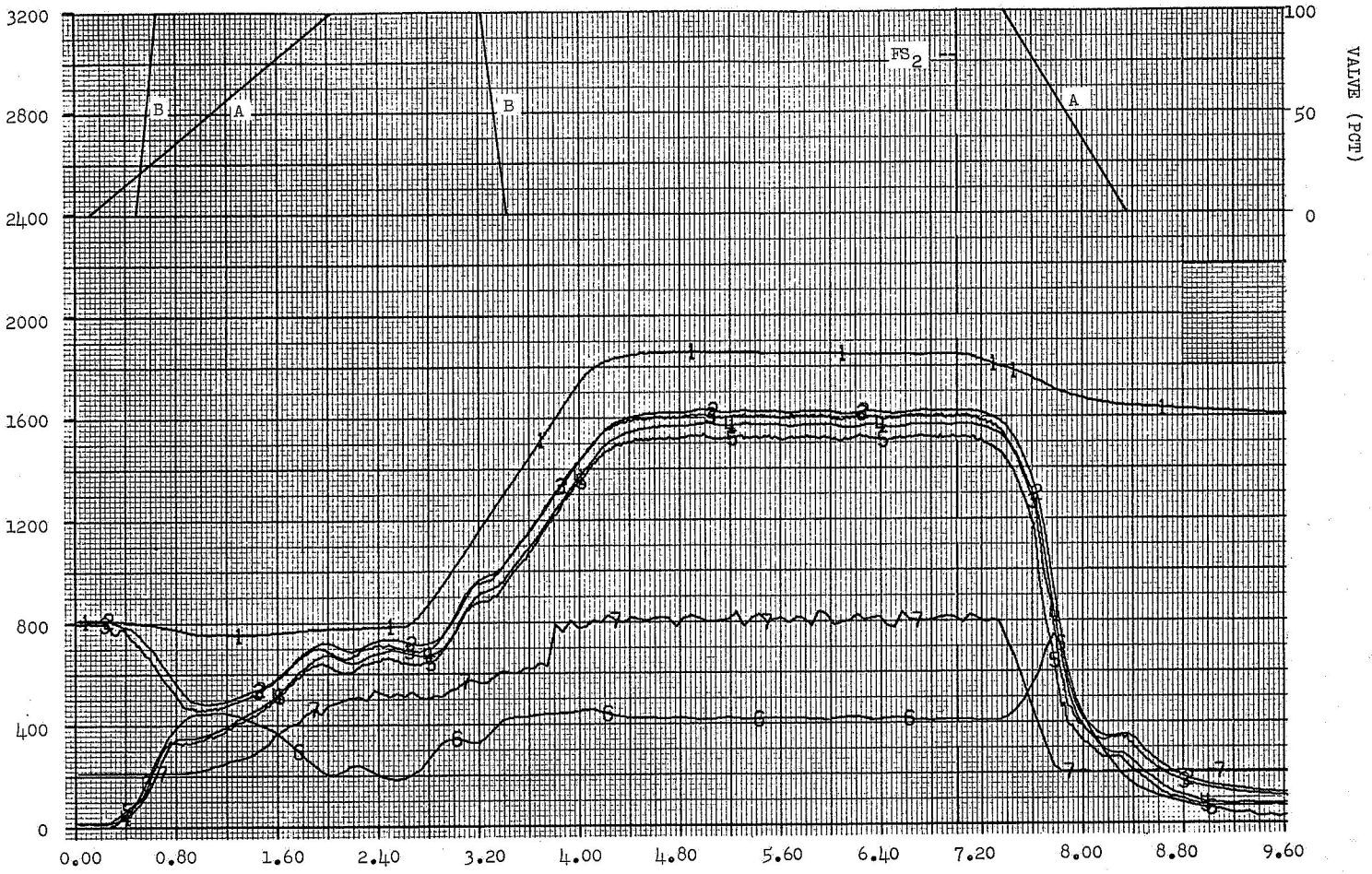


Figure 93. Typical Actual Pressure, Flow, and Temperature Histories (Test No. 1.2-05-EHM-010) - Fuel Pressures

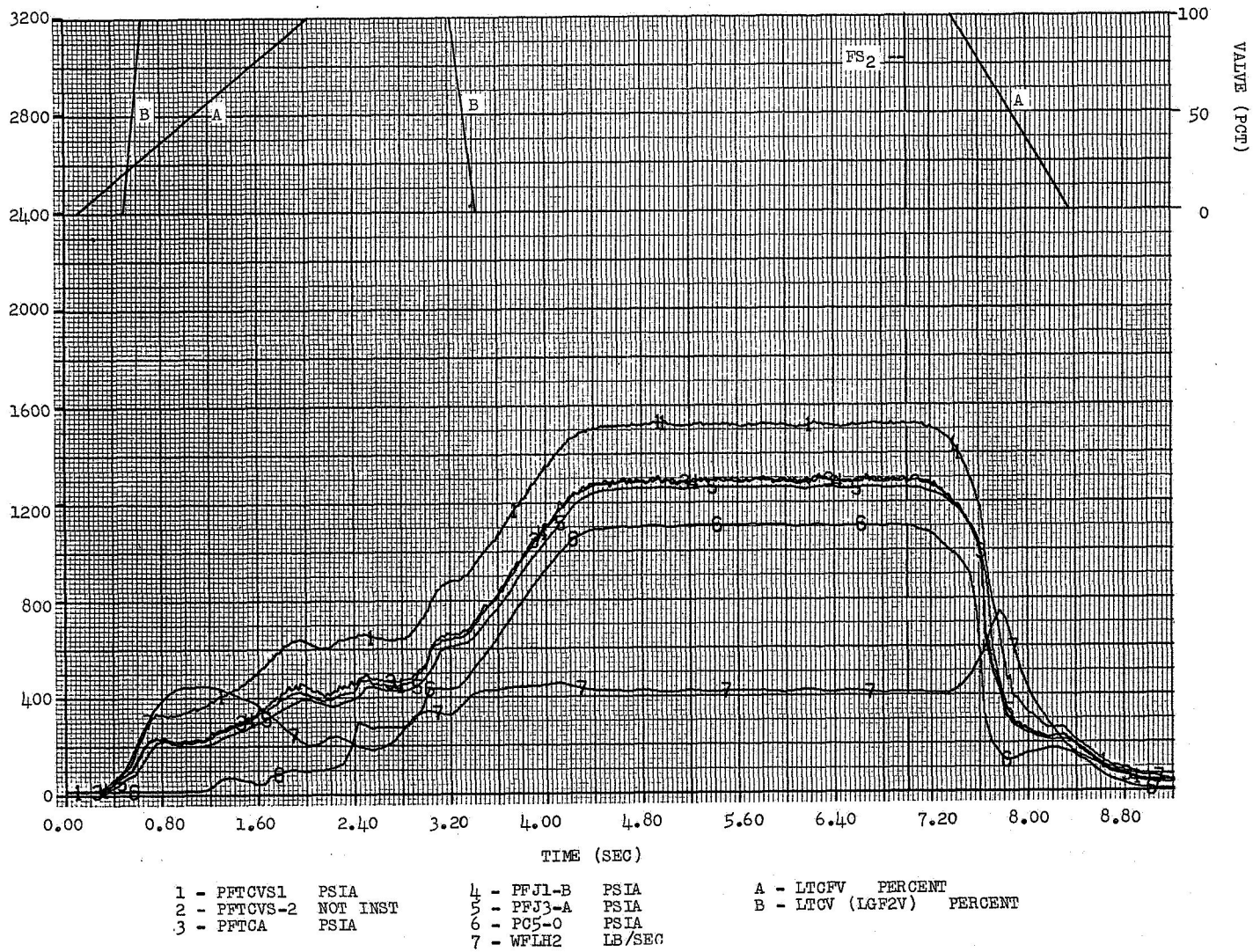


Figure 94. Typical Actual Pressure, Flow, and Temperature Histories (Test No. 1.2-05-EHM-010) - Fuel Pressures

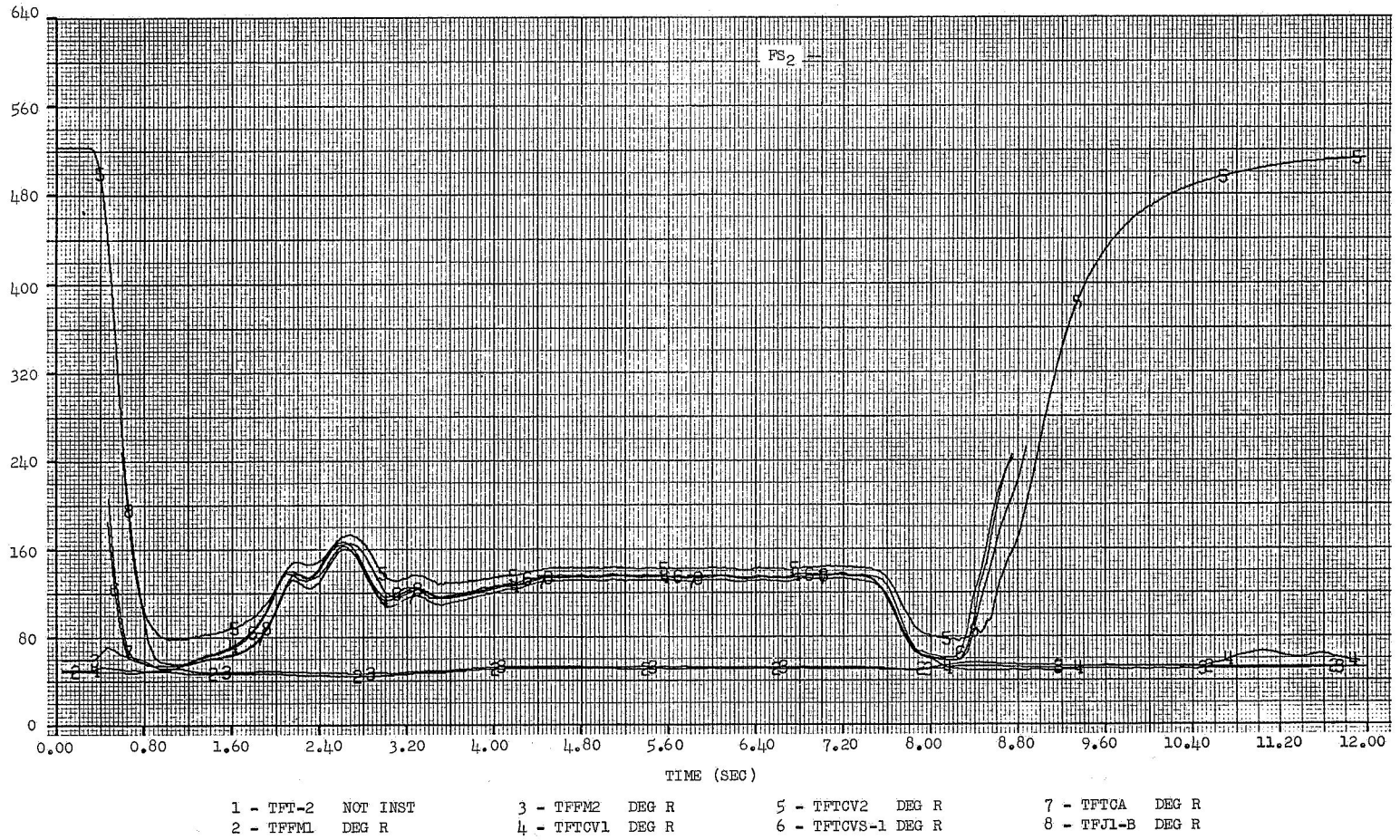


Figure 95. Typical Actual Pressure, Flow, and Temperature Histories (Test No. 1.2-05-EHM-010) - Fuel Temperatures

In the initial test attempt at Test Stand H-8, a closed-loop system was used for control of the gaseous hydrogen to the mixer. A signal from the liquid fuel flowmeter was used to fix the position of the gaseous hydrogen control valve. This setting was to be such that the hydrogen temperature at the thrust chamber assembly inlet would be constant throughout the start transient and steady-state. In the attempted test with this system, the liquid flow ceased and only gaseous hydrogen was admitted to the injector. In addition, gaseous hydrogen flowed from the mixer back to the fuel tank, reversing the flowmeter direction of rotation. Analysis showed that the initial gaseous hydrogen demand was so great that the mixture could not be forced through the downstream system without a pressure build-up at the mixer. As the pressure at the mixer built up, it reduced the liquid hydrogen flow and, consequently, the gaseous hydrogen demand. Before the control system could react to this decreased demand, the pressure in the mixer exceeded that in the fuel tank and gaseous hydrogen began to flow into the tank. With gaseous hydrogen flowing through the volumetric flowmeter, the rate of rotation increased rapidly, which resulted in a demand for even greater flow of gaseous hydrogen. Thus, the liquid flow ceased and only gaseous hydrogen flowed into the injector until shutdown.

These effects resulted in several changes to the system. A safety shutdown was added for excessive temperature at the thrust chamber assembly fuel inlet. Also, the mixer was modified to allow a major portion of the gaseous hydrogen to be directed axially downstream, which decreases the mixer pressure drop by a factor of 10. An open-loop control system was used to position the gaseous hydrogen control valve until the gaseous hydrogen flow reached approximately 50% of its final value. The hydrogen safety valve actuator was mechanically blocked to open to only 25% of its full stroke, which increases the liquid system resistance. Finally, pre-set hydrogen tank pressure was raised approximately 50%. These changes resulted in successful transients after an initial balance attempt wherein the rate of opening of the gaseous hydrogen valve was excessive.

The decrease to flow resistance in the mixer along with the increase of resistance in the fuel safety valve and greater pressure in the fuel tank permitted the pressure in the mixer to become larger when gaseous hydrogen was added to the flowing liquid hydrogen without exceeding tank pressure. Use of open-loop control of the gaseous hydrogen valve position until the gas flow was relatively high eliminated inaccuracies in the flow measuring system to react to the rapidly changing flow rates occurring early in the transient.

With the use of an open-loop control system it was necessary to assure that the gaseous hydrogen valve did not open prior to the main thrust chamber fuel valve as well as to pre-program the opening rate or position (LMix-PRV) in relationship to time. The former was accomplished by obtaining the signal to initiate opening of the gaseous hydrogen valve from a 10% open switch on the main fuel thrust chamber valve. The opening rate of the gaseous hydrogen valve was then set to provide relatively warm hydrogen to

the injector during the transient while assuring that the pressure at the gas/liquid mixer did not exceed that of the liquid hydrogen tank. A sample calculation for gaseous hydrogen valve position versus time is shown in Appendix F.

b. Ignition System

In the first test attempt conducted at Test Stand C-9, ignition was accomplished by eight electrically-initiated pyrotechnic igniter cartridges mounted at the center of the injector. These cartridges emitted 7000°F exhaust products axially toward the injector periphery. The propellant tanks were pressurized to steady-state values at the time that the main propellant valves were opened and no oxidizer by-pass valve was used. Shortly after ignition, the chamber pressure increased rapidly from approximately 100 psia to approximately 1200 psia in less than 50 millisec. This rapid rise in chamber pressure and thrust resulted in relatively high shock loading on the thrust take out system and propellant lines.

A slower chamber pressure rise was required to avoid the shock loading. This was accomplished by reducing pre-set oxidizer tank pressure, improving the diffuser for the oxidizer pressurant gas, and installing the smaller oxidizer by-pass thrust chamber valve. The decrease in the instantaneous oxidizer flow rate at ignition reduced the chamber pressure achieved shortly afterwards. This decrease in oxidizer flow rate resulted in a longer required time to fill the propellant system downstream of the thrust chamber valves. The increase in time requires that the pyrotechnic igniters (2.0 sec burning duration) be initiated after the initial opening of the propellant valves instead of at fire switch. To avoid potential delayed ignition explosions in the event that these igniters failed, a gaseous fluorine ignition system was incorporated into the hardware and test facility.

Approximately 1.5 lb/sec of gaseous fluorine was injected directly into the chamber through four copper fittings installed in the chamber flange (see Figure No. 96). The sequence of injection was previously discussed. To supply this gaseous fluorine, a fixed volume run tank (see Figure No. 88) was pressurized from 700 psia to 800 psia prior to fire-switch. Gaseous fluorine is commercially-available in bottles of approximately 4 lb capacity at 400 psia. Approximately 10 bottles were condensed in a container encased with liquid nitrogen to provide fluorine for one test. Then, the liquid fluorine was allowed to vaporize into the run tank until the desired pre-run pressure was reached.

Two gaseous nitrogen purges enter the gaseous fluorine system immediately downstream from the fluorine ignition valve. A low volume purge was provided prior to the fire-switch to prevent hydrogen from entering into the fluorine manifold prior to fluorine flow. At 50% opening of the main oxidizer thrust chamber valve, the fluorine ignition valve is signalled closed and a high volume purge initiated as previously discussed. This purge is at a pressure which is higher than the chamber pressure to prevent hot gas from entering the fluorine manifold.

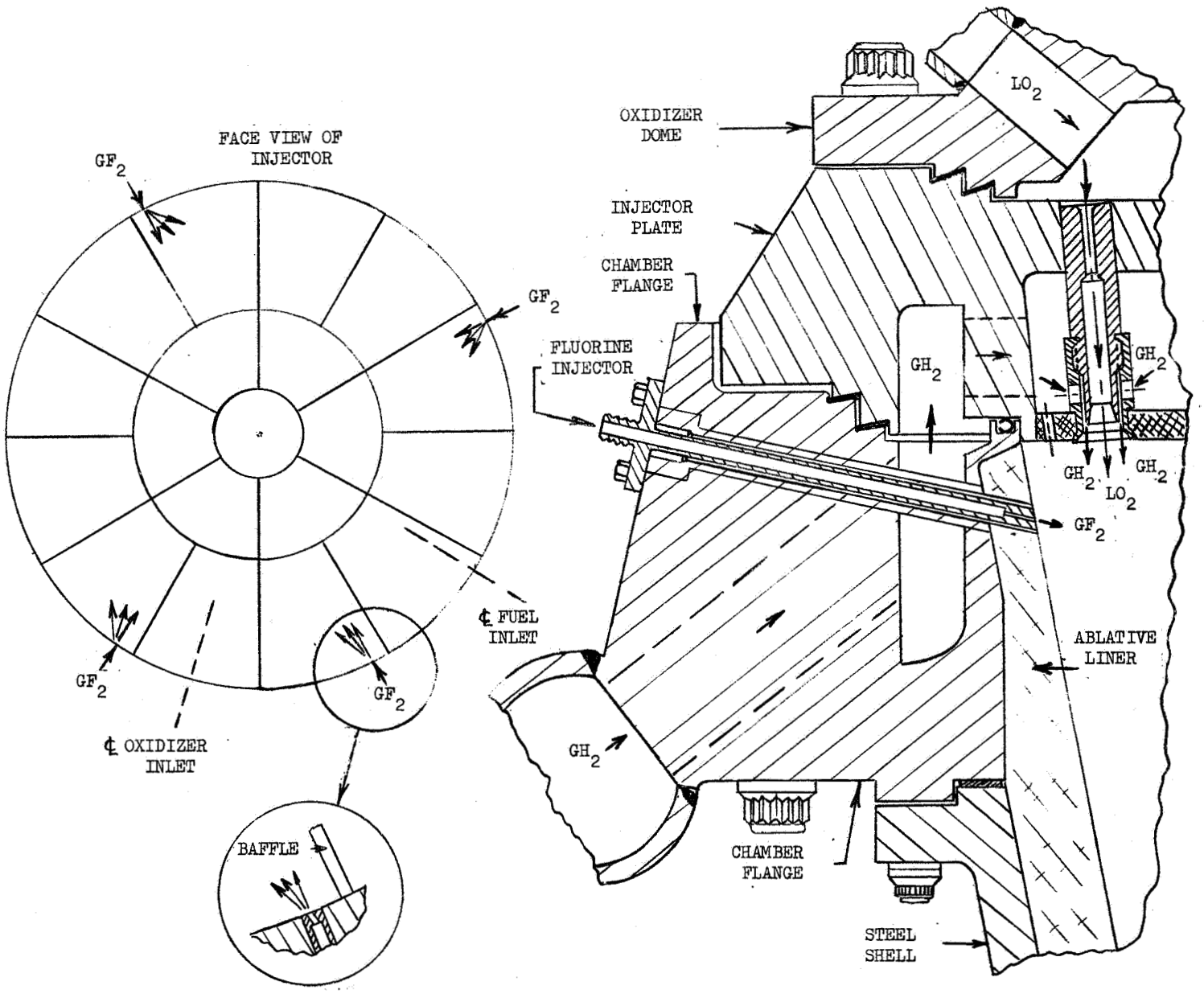


Figure 96. Fluorine Ignition Injection System

c. Shutdown Transient

It was deemed desirable to shut down the systems as rapidly as possible while remaining consistent with allowable water-hammer in the oxidizer system to avoid high mixture ratio excursions. The operation of valves during the shutdown sequence is as follows:

(1) Signals to Valves at $FS_2$

| Valve | Motion | Delay Time | Duration of Motion |
|---|---|---|---|
| LoTCV-BP | Closed | 0.085 | 0.375 ± 0.025 |
| LTCOV | Closed | 0.175 | 0.650 ± 0.050 |
| LTCfV | Closed | 0.425 ± 0.050 | 0.975 ± 0.050 |
| Mixer $GH_2$ PRV | Closed | ** | 0.600 ± 0.050 (Regardless of % open) (and biased closed at TCFVS-1) |
| Ign Cont. Valve | Closed | 0.090 | 0.20 ± 0.020 |
| $LO_2$ Tank Safety* | Closed | 0.250 | 0.450 |
| $LH_2$ Tank Safety | Closed | 0.70 ± 0.050 | 1.100 ± 0.050 |
| $GF_2$ Safety Valve | Closed | No time requirements | |
| $LH_2$ (Lo & Hi) Bleed | Open | 0.100 | 0.525 ± 0.025 |
| $LO_2$ (Lo & Hi) Bleed | Open | 0.100 | 0.425 ± 0.025 |
| $LO_2$ TCA Dump | Open | 0.100 | 0.475 ± 0.025 |

*$LO_2$ tank safety minimum closure at $FS_2$ + 0.400 sec.
**Signal closed at TCFV closing signal.

(2) High volume (50 lb/sec $GN_2$) oxidizer postfire injector manifold purge on $FS_2$. High volume (20 lb/sec GHe) fuel postfire injector manifold purge signalled on at TCFV closing signal. Purge valves signalled closed after 3 sec (minimum) flow.

(3) $GF_2$ system high pressure purge valve signalled closed at $FS_2$ + 3 sec minimum.

(4) $GF_2$ system trickle purge starts flowing when high pressure purge flow ceases. Trickle purge valve signalled to close at sequence "reset."

The high volume oxidizer postfire purge entered near the injector and was intended to cut-off the oxidizer stream at the purge location. Oxidizer downstream of the purge point was forced through the injector, while that upstream was forced out through the oxidizer dump valve, ODV (see Figure No. 88).

Review of the motion pictures and hardware after testing indicated that the mixture ratio did not become excessive during shutdown. Because bleed and dump valves downstream of the flowmeters were open during the transient, flow rates through the thrust chamber during this period cannot be readily established. Typical plots of thrust chamber parameters after the shutdown signal are included in Figures No. 90 through No. 95.

3. Sound Level Evaluation

The prediction of sound pressure levels was given considerable attention. This interest was based upon the concern over possible operational limitations which might be imposed on scheduling of test activities if sound pressure levels reached proportions which are objectionable to the surrounding community. In addition to scheduling limitations, it was considered that sound suppression systems might also be required, if sound levels were excessive.

Appendix G extends the past predictions to comparisons with actual sound measurement data taken during test firings of the M-1 uncooled thrust chamber assembly on Test Stand H-8 during the initial operational phase, July and August 1966.

F. MULTI-ORIFICE INJECTOR TEST RESULTS

A test was attempted in June 1964 with the S/N 004 injector and a film-cooled stainless steel chamber. It was scheduled for a duration of 3 sec, but was terminated prior to this by a malfunction failure in the liquid oxygen circuit.

Posttest inspection revealed considerable damage to the oxidizer feed system between the tank and the injector inlet. The oxidizer thrust chamber valve, the flowmeter, and several large flanges were severely burned. Sections of the oxidizer line were bent and displaced from their original position.

A M-1 Thrust Chamber Assembly Accident Special Investigation Team was assigned by NASA/LeRC to review all data and planning pertaining to this test. The findings of this team were published in a special report[19]. They narrowed the cause of the malfunction down to the following two possibilities:

(19) M-1 Thrust Chamber Assembly Accident (Test No. 1.1-02-EHM-003), M-1 Accident Special Investigation Team, Lt. Col. Joe E. Heatherly, Chairman, 28 August 1964

- Abnormal vibration and g-loading on the oxidizer thrust chamber valve resulting from the ignition in the thrust chamber assembly and which led to internal mechanical failure in the valve and the burning.

- Pressure surges in the liquid oxygen system which caused the contaminants in the system to be ignited.

Based upon the recommendations of this team, considerable changes were made in the system structure as well as the cleaning and operating procedures. A successful test program was then conducted with a coaxial injector.

## V. CONCLUSIONS

The following eight conclusions are the major ones resulting from the M-1 thrust chamber program.

A. The ablative liner appears to be a valuable injector test device which can be used to determine performance, stability, and if injectors are streaking before they are used with regeneratively-cooled hardware.

B. Chugging was experienced during the low chamber pressure phases of the start transient when injector pressure drops were low, but it disappeared completely as chamber pressure increased to steady-state.

C. Performance was achieved that is equal to the contract specification for PFRT (429.5 sec at a mixture ratio of 5.49) when it was extrapolated to vacuum conditions with a 40:1 expansion ratio nozzle.

D. The conditions that triggered instability were not significantly affected by baffle length, type of chamber wall (ablative or steel), distance of the chamber wall from the outer row of elements, or oxygen inlet temperature.

E. Increasing baffle length from 5/8 in. to 3-1/2 in. decreased amplitude and resultant hardware damage caused by instability.

F. The injector has an adequate stability margin at design operating conditions to permit satisfactory operation without baffles.

G. The reduction of baffle coolant from 4% with the long baffles to 2% with the short baffles had less than 1/2% affect upon performance.

H. Although operating conditions (i.e., hydrogen temperature, combustion efficiency, and injection velocity) were shown to have an affect upon the initiation of instability, no analytical method for correlating or extrapolating these effects was derived.

## VI. RECOMMENDATIONS

The following two recommendations are made because their accomplishment would provide additional technology, which would make the M-1 thrust chamber data even more meaningful.

A. Additional testing within the current test program to ascertain whether the film cooling now being utilized is adequate for a regeneratively-cooled combustion chamber.

B. In view of the satisfactory performance of the ablative liner, an additional test program would permit definition of its duration capability.

## BIBLIOGRAPHY


Haering, G. W., A Proposed Correlation Scheme for Gas-Film Cooling Data, AFRPL-TR-66-56, August 1966

Hatch J. E. and Papell, S. S., Use of a Theoretical Flow Model to Correlate Data for Film Cooling or Heating an Adiabatic Wall by Tangential Injection of Gases of Different Fluid Properties, NASA TN D-130, November 1959

Kreith, F., Principles of Heat Transfer, International Text Book Co., 1958

McAdams, W. H., Heat Transmission, McGraw-Hill, 1954

McFarland, B., Joerg, P., and Taft, M., Criteria for Plastic Ablation Materials as Functions of Environmental Parameters: Part 1 - Results of Analytical Studies, ASD-TR-61-439, Part 1, Contract AF 33(616)-7401, May 1962

Rannie, W. D., A Simplified Theory of Porous Cooling, Jet Propulsion Laboratory Report No. 4-50

Schneider, P. J., Conduction Heat Transfer, Addison-Wesley, 1957

Valentine, R. S., Dean, L., and Pieper, J. L., An Improved Method for Rocket Engine Performance Prediction, Aerojet-General Report PTDR 9642-034, 8 October 1965

An Experimental Investigation of Combustion Stability Characteristics of High Chamber Pressure, Final Report, Phase II, Aerojet-General Report No. 11741/SA6-F, Vol. 1, 25 August 1966

Analytical Study to Extend the Capabilities of the Aerojet-General Ablation Digital Computer Program, Aerojet-General Report No. 9140-64-1R, Contract NAS 9-2832, November 1964

M-1 Ambient Acoustic Tests, Aerojet-General Report No. TCER-019, 18 May 1966

M-1 Thrust Chamber Assembly Accident (Test No. 1.1-02-EHM-003), M-1 Accident Special Investigation Team, Lt. Col. Joe E. Heatherly, Chairman, 28 August 1964

M-1 Uni-Element Program, Aerojet-General Report No. 8800-57, 15 February 1966

Theoretical Performance of Hydrogen-Oxygen Rocket Thrust Chambers, NASA TR R-111, 1961

Bartz, D. R., "A Simple Equation for Rapid Estimation of Rocket Nozzle Heat Transfer Coefficients," Jet Propulsion, (1):49:51, 1957

Narkl, A. R. C., "Fatigue Tests for Piping Components," Trans. ASME, 1952

Stollery, J. L. and El-Ehwany, A. A. M., "A Note on the Use of a Boundary-Layer Model for Correlating Film Cooling Data," International Journal of Heat Mass Transfer, Vol. 8, 1965, pp. 55-65

# APPENDICES

# APPENDIX A

## M-1 THRUST CHAMBER TRANSVERSE MODE COMBUSTION STABILITY ANALYSIS*

* The information presented in this appendix was originally provided in response to LeRC Action Item No. 4 on 29 April 1963 as Aerojet-General Report No. TCR 9621-012.

# APPENDIX A

## TABLE OF CONTENTS



## LIST OF FIGURES

Appendix A

## I. INTRODUCTION

Combustion instability is one of the most critical problems in nearly every engine development program, which has been hindered by occurrences of oscillatory combustion. Usually, stability problems were solved by trial-and-error modifications of the injector pattern or starting procedure. However, more recently, baffles have been used to obtain stable operation.

The empirical development of an adequate baffle requires extensive hardware fabrication and testing. The purpose of this analysis was to predict, using available theoretical and experimental information, the stability behavior of the M-1 thrust chamber and the baffle configuration required to ensure stable operation.

The combustion process in any liquid propellant rocket thrust chamber is never entirely smooth. During the nominally steady-state period between starting and cutoff, fluctuations occur in all properties (pressure, temperature, velocity, etc.) around the desired operating values. The amplitude of these fluctuations can vary over a wide range from chamber to chamber and in one chamber, they can vary for different operating conditions. When the fluctuations are completely random, the operation is classified as "rough" combustion. A qualitative distinction can be made between "rough" and "smooth" combustion upon the basis of the root-mean-square amplitude of the fluctuations.

Combustion instability differs in that is consists of organized oscillations that are maintained and amplified by the combustion process itself. It is generally agreed that there are three kinds of instability, which are differentiated by the frequency of the resulting oscillations. These are known as low, intermediate, and high-frequency instability.

Low-frequency combustion instability has received much theoretical and experimental study. It involves the interaction of the propellant feed system with the combustion process. A theoretical analysis for the intermediate-frequency case exists although the phenomenon is rarely observed. This analysis is concerned with the high-frequency type of combustion instability, which is by far the most destructive type as well as the most difficult to control.

High-frequency instability is a forced oscillation of the combustion chamber gases, which is driven by the combustion process interacting with the resonance effects of the chamber geometry. The resulting oscillation patterns and frequencies are very similar to those of the acoustic modes of the chamber.

Most research has been concerned with circular cylindrical chambers, wherein longitudinal and transverse modes can be distinguished. In a longitudinal mode, the property variations occur in the axial direction while conditions are uniform on a section normal to the axis. In purely transverse modes, uniformity of the properties along the axis with variations in the radial and circumferential directions is involved. These transverse modes can be either radial or tangential. In radial modes, the pressure nodal surfaces

(i.e., surfaces upon which the pressure oscillation amplitude vanishes) are cylinders having an axis which coincides with the axis of the combustion chamber. The pressure nodes in tangential modes are diametral surfaces (i.e., planes passing through the chamber axis). In either case, the lowest mode has a single nodal surface, the second mode has two nodal surfaces, and so on.

Also, it is possible to have combined radial-tangential and longitudinal-transverse modes. Each tangential or combined mode with a tangential component can exist in two forms; the standing form, wherein the nodal surfaces are stationary; or the spinning form, wherein the nodal surfaces rotate at the angular frequency of the oscillation.

The amplitudes of transverse modes are usually very large. Peak-to-peak amplitudes of 300% of steady-state chamber pressure are not uncommon. One of the most detrimental consequences of such oscillations is the burnout of combustion chamber hardware because of the abnormally high heat transfer rates associated with instability. Measured heat flux increases of 400% to 500% have accompanied the onset of transverse mode oscillations.

## II. SUMMARY

Three of the most advanced methods for analyzing combustion stability were evaluated in connection with developing a method for eliminating combustion instability in the M-1 combustion chamber. Each method showed some desirable features.

The mechanistic approach developed at NASA Lewis Research Center and the Polytechnic Institute of Brooklyn was the most rigorous and quantitative; however, it was developed for a narrow range of chamber designs and operating conditions.

The available-energy concept developed at Aerojet-General was based upon a large quantity of empirical data, but it had not been developed into a quantitative theory.

The third approach proved to be the most logical selection for application in the M-1 chamber design. It is the Sensitive Time Lag Theory developed at Princeton University. This well-developed theory had been verified experimentally and appeared valid for application to a fairly wide range of chamber geometries.

In the Sensitive Time Lag Theory, two parameters are used to describe the dynamic combustion process. The interaction index, $n$, which is a measure of the sensitive time lag, $\tau$. The latter is a time characteristic of the combustion process and is controlled by injection pattern, propellant combustion, and operating conditions.

Probable values for the interaction index and the sensitive time lag can be determined upon the basis of hardware design and specified operating conditions. These values are then compared with data from similar chambers

and are used to predict the modes at which the chamber will most likely experience combustion instability. Applying this information permits the design of combustion zone baffles which will preclude oscillatory combustion in the frequencies peculiar to those modes.

Analysis of the M-1 combustion chamber disclosed that the most likely modes of combustion instability were the third and fourth tangential with frequencies in the 2000 cps to 3000 cps range. Accordingly, the baffle configuration recommended for inclusion was designed to preclude spinning modes and standing tangential modes lower than the sixth tangential.

## III. CONCLUSIONS AND RECOMMENDATIONS

A baffle configuration having a 21-in. diameter circular hub with 12 radial blades outside the six blades within the hub was recommended for the M-1 thrust chamber. Both the conventional and large thrust coaxial injector designs should be stable with such a baffle, although the coaxial injector was expected to show a somewhat greater resistance to instability than the conventional design.

The theoretical analyses upon which this study was based included the assumption that the mean axial velocity in the combustion chamber was small enough so that the square of the Mach number could be neglected when compared to unity. However, with a contraction ratio of less than 2.0, such an assumption cannot produce accurate definition of the unstable operating zones. The uncertainties introduced by this assumption are probably not of greater magnitude than the uncertainties in the estimated values of the stability parameters. Therefore, the results of the study should be adequate to provide guidance for the development of an effective baffle configuration.

More precise information can be obtained from analytical studies only when nonlinear theories applicable to high-velocity combustion chamber flow conditions are developed. With the accumulation of more experimental information, an understanding of the physical nature of the stability parameters can be gained. Only through parallel analytical and experimental effort can a complete and quantitative understanding of the combustion dynamic behavior of liquid propellant rocket engines be achieved.

## IV. BACKGROUND

### A. THEORETICAL APPROACHES

Examination of the published theoretical studies of high-frequency combustion instability showed the following three main avenues of approach:

Appendix A

- The Sensitive Time Lag Theory of Crocco and his co-workers at Princeton University[1][2][3][4][5]

- The Mechanistic Theories developed by Morrell, Priem, and Guentert at NASA Lewis Research Center[6][7] and by Torda and Burstein at the Polytechnic Institute of Brooklyn[8]

- The Available Energy Concept of Ellis, Pickford, and Peoples at the Aerojet-General Corporation[9][10][11][12]

The Princeton theoretical approach is that of the classical, linear, small perturbation stability theory, whereby, each of the quantities describing the flow in the combustion chamber is assumed to oscillate about its steady-state value. For certain unstable operating conditions, the

(1) Crocco, L. and Cheng, S. I., Theory of Combustion Instability in Liquid Propellant Rocket Motors, AGARDograph No. 8, Butterworths Scientific Publications, London, 1956

(2) Scala, S. M., Transverse Wave and Entropy Wave Combustion Instability in Liquid Propellant Rockets, Princeton University Aeronautical Engineering Report No. 380, 1 April 1967

(3) Crocco, L., Gray, J., and Harrje, D. T., "Theory of Liquid Propellant Combustion Instability and Its Experimental Verification," ARS Journal, Vol. 30, No. 2, February 1960

(4) Reardon, F. H., An Investigation of Transverse Mode Combustion Instability in Liquid Propellant Rocket Motors, Princeton University Aeronautical Engineering Report No. 550, 1 June 1961

(5) Crocco, L., Harrje, D. T., and Reardon, F. H., "Transverse Mode Combustion Instability in Liquid Propellant Rocket Motors," ARS Journal, Vol. 32, No. 3, March 1962

(6) Priem, R. J. and Morrell, G., "Application of Similarity Parameters for Correlating High-Frequency Instability Behavior of Liquid Propellant Combustors, American Rocket Society Paper No. 1721-61, Propellants, Combustion, and Liquid Rockets Conference, Palm Beach, Florida, April 26-28, 1961

(7) Priem, R. J. and Guentert, D. C., Combustion Instability Limits Determined by a Nonlinear Theory and a One-Dimensional Model, NASA TN D-1409, 1962

(8) Torda, T. P. and Burstein, S., Nonlinear Theory of Combustion Instability in Liquid Propellant Rocket Motors, Propellant Research Laboratory Report No. PRL-TN-58-1, December 1958 (AFOSR TN-59-60, ASTIA No. 209-491)

(9) Ellis, H. B. and Pickford, R. S., High-Frequency Instability, Aerojet-General TN-17, September 1956 (AFOSR TN-56-547)

(10) Pickford, R. S. and Peoples, R. G., Inherent Stability of the Combustion Process, Aerojet-General TN-36, November 1960 (AFOSR 676)

(11) Peoples, R. G. and Pickford, R. S., Analytical and Experimental Scaling of Thrust Chambers, Aerojet-General TN-40, November 1960 (AFOSR 677)

(12) Peoples, R. G., Baker, P. D., and Knowles, L. S., High-Frequency Combustion Instability, Aerojet-General Report No. 2126, November 1961 (AFOSR 1802)

oscillation amplitudes will increase with time, even for arbitrarily small initial amplitudes. Theoretical conditions can be established for the existence of neutral oscillations, the amplitudes of which neither increase or decrease with time. The assemblage of operating points of the thrust chamber which satisfy the conditions for neutral stability forms the "stability limits" that divide the unstable from the stable regions of operation. Thus, the complete stability behavior of the rocket engine is described by specifying the stability limits and indicating the unstable regions.

The unique feature of the Princeton theory is the use of the sensitive time lag concept. The idea of a combustion time lag as a coordinating influence to excite organized oscillations in a liquid propellant rocket combustion chamber originated with Von Karman at the Jet Propulsion Laboratory in 1941. Several analyses were made of low-frequency modes of instability, Crocco introduced the time-varying, or sensitive, combustion time lag.

In the time lag concept, the gradual evolution of combustion products from each portion of propellant mixture traveling through the combustion chamber after injection is approximated by a discontinuous conversion from reactants to products after a certain time (the total time lag) has elapsed. If the combustion chamber conditions fluctuate, the time lag also must vary. To simplify the description of the effect of the chamber conditions upon the time lag, the total time lag is taken as the sum of a "sensitive" part ($\tau$) and an "insensitive" part. The various physical conditions are assumed to affect the combustion process rates only during the sensitive portion of the total time lag. The magnitude of the response of the combustion process rate to changes in thermodynamic state is expressed by a "pressure interaction index" ($n$). Similarly, the effects of transport phenomena are measured by a velocity index ($\ell$) which is vectorial.

The synthetic representation of the combustion process by means of the time lag concept eliminates the need for information regarding any of the specific processes occurring in the chamber (i.e., atomization, vaporization, mixing, and chemical kinetics). This fact constitutes the primary advantage of the time lag analysis because very little quantitative information is available concerning the details of the various unsteady combustion processes.

For analytical simplicity, the Princeton theory assumes that the steady-state flow is one-dimensional with particle velocities being small in comparison with the sonic velocity and that the flow is inviscid within a rigid, adiabatic thrust chamber. Solutions of the conservation equations have been obtained in closed form as first-order corrections to the acoustic wave patterns.

The application of the Sensitive Time Lag Theory to the longitudinal modes was first made by Crocco in 1951. The expanded and generalized theory of longitudinal mode combustion instability was published in 1956 by Crocco and Cheng, but without experimental verification. Subsequently, the validity of the theory was shown in a series of experiments reported by Crocco, Gray,

and Harrje. In the latter paper, a simple means for measuring the combustion parameters $n$ and $\tau$ through stability limit tests was presented. The first application of the sensitive time lag concept to transverse modes was made by Scala, who considered only thermodynamic effects. The importance of velocity (or hydrodynamic) effects in transverse modes was shown by Reardon, who was able to present some experimental verification also. Subsequently, the crucial connection between longitudinal and transverse modes was established experimentally at Princeton.

The NASA Lewis Research Laboratory approached the problem of combustion instability from a more mechanistic viewpoint in that their theoretical formulations include rate expressions for assumed rate-controlling processes. They also have included nonlinear effects associated with both the combustion processes and with the fluid mechanical flow processes. Associated theoretical and experimental studies of vaporization and mixing under steady and unsteady conditions also are accomplished at NASA/LeRC.

A similitude study of the general conservation equations by Priem and Morrell disclosed two major similarity parameters. One parameter, a measure of viscous dissipation, is a Reynolds number based upon the average acoustic velocity in the combustor. The second parameter is a measure of the heat release rate. Values for these parameters were calculated for a series of hydrocarbon-liquid oxygen rocket engines using two assumptions as to the rate controlling process; steady-state spray vaporization and drop or jet shattering by a shock wave. Group separation of stable and unstable combustors was obtained with both rate expressions for the cases considered. This indicated the suitability of the parameters for first-order prediction of combustion stability.

A much more ambitious effort was started by Priem and Guentert for analysis of unstable combustion. The model used is that of an annular section of a combustor having very small thickness and length. The viscous dissipation and heat release rate similarity parameters discussed above are utilized in the analysis. The nonlinear equations of conservation of mass, momentum, and energy are solved numerically for an assumed initial disturbance. Two different rate-controlling processes are considered; vaporization and chemical reaction.

Calculations were performed only for the case of an initial disturbance having a first tangential mode amplitude distribution. The results obtained in this case showed that the vaporization model produces a rapid wave-steepening effect (such as has been observed experimentally) which is not shown by the chemical reaction model. Even with the latter model, effects of the reaction order and activation energy upon stability are small. For the annular combustor considered in this analysis, the viscous dissipation parameter was found to have a negligible influence because the model excluded a boundary layer or other wall effects. One of the most interesting results of the study is that the controlling mechanism for small laboratory combustors may be chemical in nature, while the corresponding mechanisms for larger

production engines may be related to vaporization. Thus, it is possible that research studies with small combustion chambers did not properly simulate the stability behavior of large engine systems.

The available energy concept developed at Aerojet-General is based, mostly inductively, upon the initial wave motion descriptions of Ellis and Pickford. The application of this approach to the tangential modes of high-frequency instability was discussed by Pickford and Peoples. Briefly, the conceptual basis of approach is that during steady-state, the injection of a given mass of propellants is followed by the processes of atomization, vaporization, and mixing, which require a certain time for completion. Thus, prepared, the reactants are then "available" for the final process of chemical reaction which results in the release of energy. The reaction proceeds over a time interval, $\tau$, during which the reactants are sensitive to a disturbance in pressure. The amount of pressure sensitive available energy per unit volume is found to be proportional to the time, $\tau$, and to the local intensity of combustion, measured by the gas velocity gradient, $\frac{dV}{d\tau}$.

The effect of the perturbation, which in the Aerojet-General approach is assumed to be of very short duration, is to increase the rate of reaction, thereby releasing excess energy and depleting the local available energy. The consequent expansion of the combustion products causes enhancement of the rates of the preparation processes so that the concentration of available energy may overshoot the steady-state value after a time, $\tau_a$, has elapsed. If no further disturbance occurs, the available energy will return to its steady-state value at a time, $\tau_b$, after the disturbance has passed.

In the case of periodic distrubance, amplification can result if the cycle period, $\tau_w$, is in the range $\tau_a<\tau_w<\tau_b$. Because of energy dissipation effects, there is probably a threshold perturbation value, below which the energy release by the perturbation is not sufficient to cause the available energy concentration to overshoot its steady-state value. This conclusion is based upon experimental observations of stability testing using the Aerojet-General pulse motor. In this device, a series of calibrated powder charges is fired tangentially into the combustion chamber to disturb the combustion and flow patterns. Each charge is stronger than the preceding one. The rocket motor is shut down automaticaly following the onset of instability. Thus, the number of charges fired in a measure of the relative stability of the thrust chamber at the particular operating conditions of the test.

Of the three theoretical approaches considered in this survey, only the Princeton was extensively developed. The Sensitive Time Lag concept had been applied to both longitudinal and transverse modes. Velocity, or transport, effects as well as thermodynamic effects were included analytically. Experimentally, the validity of the theory was demonstrated for several combinations of injector types and propellants, as well as for both longitudinal and tangential modes.

However, the very nature of the Sensitive Time Lag Approach makes it impossible to calculate the values of the stability parameters from basic principles. In addition, as then developed, the solutions were not valid for engines with nozzle contraction ratios of less than 2.0. The required extension, while complex, is straightforward. A more serious restriction is that of linearity. The effect of large amplitude, shock-type pulses can be considered qualitatively only. In spite of these limitations, the sensitive time lag approach had in its favor the facts that the theory was well developed, was verified experimentally, and could be used to correlate test data in a general and systematic fashion, permitting prediction of stability behavior of related but geometrically dissimilar thrust chambers.

The ultimate goal of the other two approaches is the analytical prediction of stability behavior. Of the two, the mechanistic approach is more rigorous and quantitative. However, it was only possible to obtain solutions for a single transverse mode for an annular section of a combustor. The extension to the full three-dimensional case was undertaken but it presented extreme difficulties. Therefore, no assistance was available for evaluating the stability of the entire combustion chamber.

The available energy approach had not been developed into a quantitative theory. The concepts involved were formulated upon the basis of a large number of experimental observations. Therefore, when properly expanded, it should be quite useful to liquid rocket researchers and designers. Although the available energy concentration can be derived experimentally, this process involves two successive differentiations. Thus, extremely accurate and precise measurements are required, which may not be possible in all cases. In addition, it was not clear how the concept is to be extended beyond local considerations to include the combustion and flow in the thrust chamber as a whole.

## B. USE OF THE SENSITIVE TIME LAG THEORY

According to the Sensitive Time Lag Theory, the stability of an injector-propellant combination can be described by two parameters: the interaction index, $n$, which measures the sensitivity of the combustion process to fluctuating chamber conditions, and the sensitive combustion time lag, $\tau$, which is a characteristic time of the combustion process. A given mode of high-frequency instability can occur only if the sensitive time lag is in proper relationship to the period of the corresponding acoustic oscillation and if the interaction index is sufficiently large, so that the exciting forces can overcome the damping forces. The stability parameters $n$ and $\tau$ are functions of the combustion process and hence, of the injection pattern, propellant combustion, and operating conditions. Although it was not possible to calculate $n$ and $\tau$ directly from physical and chemical property data, values could be inferred from appropriate experiments.

The investigation of the high-frequency combustion stability of a given thrust chamber assembly depends upon several considerations. Zones of instability can be drawn for each mode on the $n$, $\tau$ plane from information

regarding the size and shape of the combustion chamber and the general character of the combustion process and products.

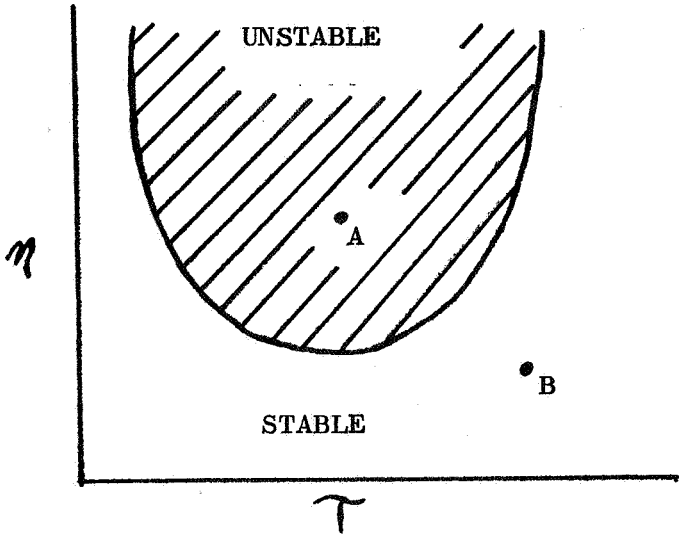


Typical Instability Zone for One Mode of High-Frequency Instability

FIGURE A-1

Then, if the $\eta$, $\tau$ point corresponding to the particular combustion process under consideration lies within the instability zone (point "A" on Figure No. A-1) spontaneously unstable combustion is to be expected. That is, small disturbances, always present in the combustion "noise," will amplify to levels that are likely to result in damaged hardware. For operating $\eta$, $\tau$ points outside, but sufficiently near a zone of instability (point "B"), a larger disturbance, such as that produced by the Aerojet-General pulse generator, will result in instability. Although there was no existing quantitative nonlinear theory, it could be reasoned intuitively that the nearer the $\eta$, $\tau$ point lies to an unstable zone, the smaller is the disturbance required to excite oscillatory combustion.

The influence of combustion chamber diameter upon the stability of transverse modes is shown by Figure No. A-2. For simplicity, only the instability zones for a single mode of oscillation have been shown. The zone of instability for each mode moves toward larger values for the sensitive time lag ($\tau$) as the chamber diameter (the characteristic length for transverse modes) is increased.

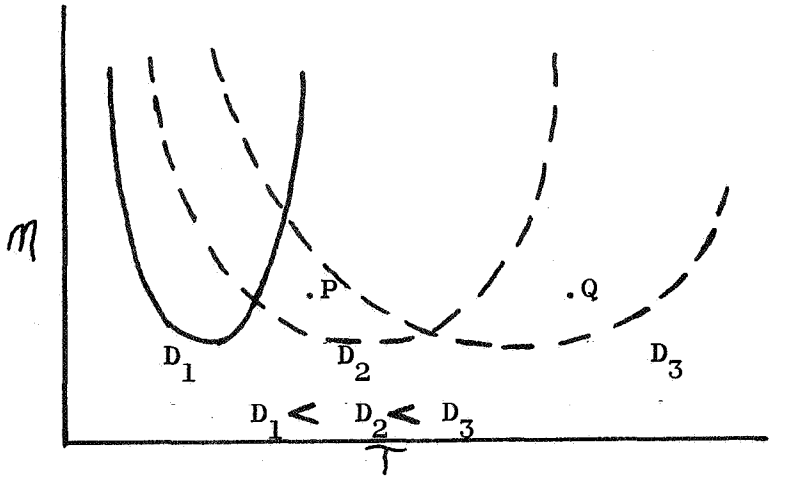


Effect of Chamber Diameter on the Instability Zone of One Mode

FIGURE A-2

For a combustion process (i.e., injector pattern and propellant combination at given operating conditions) with its $\eta$, $\tau$ point a ".P," the following stability picture is obtained. The mode of oscillation under consideration is unstable for diameter $D_2$, but stable for $D_1$ and $D_3$. However, instability in other modes is still possible in the latter cases. If the instability zones of Figure No. A-2 are drawn for the lowest transverse mode (first tangential), then diameter $D_1$ will be stable whereas $D_3$ may be unstable in one or more of the higher harmonics. For a system operating at point "Q," both diameters $D_1$ and $D_2$ will be stable. Thus, an increase in the sensitive time lag, $\tau$, permits an increase in chamber diameter with no adverse effect upon combustion stability.

C. STABILITY PARAMETERS

Although methods were developed for the experimental determination of the stability parameters, $\eta$ and $\tau$ of the Sensitive Time Lag Theory[13][14], the data available were not extensive. However, some work at both Princeton University and Aerojet-General yielded preliminary information regarding the effects of chamber pressure and injector element size. These results, shown on Figures No. A-3 and No. A-4, were originally presented in other published literature.[15][16][17]

(13) Crocco, L. Gray, J., and Harrje, D. T., op. cit.
(14) Crocco, L., Harrje, D. T., and Reardon, F. H., op. cit.
(15) Addoms, J. F., et al, Unique Injector Concepts Development (UNICODE), Aerojet-General Report No. 0518-00-5 (Quarterly), September 1962
(16) Reardon, F. H., Combustion Stability Behavior of the Nitrogen Tetroxide/AeroZINE-50 Propellant Combination with the 2 SIN Injector Pattern, Aerojet-General Report No. TM 9616/003, 13 March 1962
(17) Reardon, F. H., Combustion Stability Behavior of the Liquid/Oxygen/Liquid Hydrogen Propellant Combination, Aerojet-General Report No. TM 9616/002 March 1962

In general, the interaction index decreases with increasing element size (Figure No. A-3). This is a gross dependence; its physical basis had not yet been determined. The dependence of $\eta$ upon chamber pressure as inferred from these data is $\eta \sim P_c^{1/2}$. Tests conducted at Princeton University, using the propellant combination liquid oxygen/ethanol and a very-low-thrust-per-element injection pattern, indicated a similar pressure dependence of the interaction index.

The results from the high chamber pressure program did not show a clear trend as pertains to element size of the sensitive time lag. However, low pressure testing indicated that the time lag became greater with increasing thrust-per-element as shown on Figure No. A-4. For the low thrust, multiple-element injectors, the dependence of $\tau$ upon chamber pressure is approximately, $\tau \sim P_c^{1/2}$, and was in agreement with results obtained at Princeton.

It is interesting to note that the nature of the propellant combination appears to have very little influence upon the stability parameters. Of course, these conclusions are based upon very little data. Further work is needed to determine the processes that govern the stability parameter variations.

D. BAFFLES

In many research and development programs, stabilization of transverse modes has been effected by means of combustion chamber baffles[18][19]. The experimental results indicated that to prevent a spinning tangential mode, which is generally the most damaging, a single, diametral baffle (i.e., two radial blades) of sufficient length can be used. The necessary length is known to depend upon the propellant combination and injector pattern. In general, the available data indicated that the baffle need not extend axially through the entire region of most intense combustion. It was indicated that baffles control the mixing processes in the early combustion region. However, the data were too sparse to permit a priori estimation of minimum baffle length. The required baffle length also depends upon the spacing between blades. The wider the spacing (fewer blades) the greater must be the axial baffle length.

There is the possibility of a standing mode in the pockets between blades even if the baffle is sufficiently long. The available data pointed to a critical spacing. If the blade spacing is greater than critical, a standing mode can occur; if the spacing is smaller, no standing mode is possible. The effect of baffle configuration for a combustion chamber of fixed size is shown on Figure No. A-5. Points "X" and "Y" are unstable, but in different modes. Although it is possible that a disturbance will produce first tangential mode oscillations in the case of point "X," also. The use of a four-blade baffle

(18) Reardon, F. H., Princeton University Aeronautical Engineering Report No. 550, op. cit.
(19) Reardon, F. H., Aerojet-General Report No. TM 9616/003, op. cit.

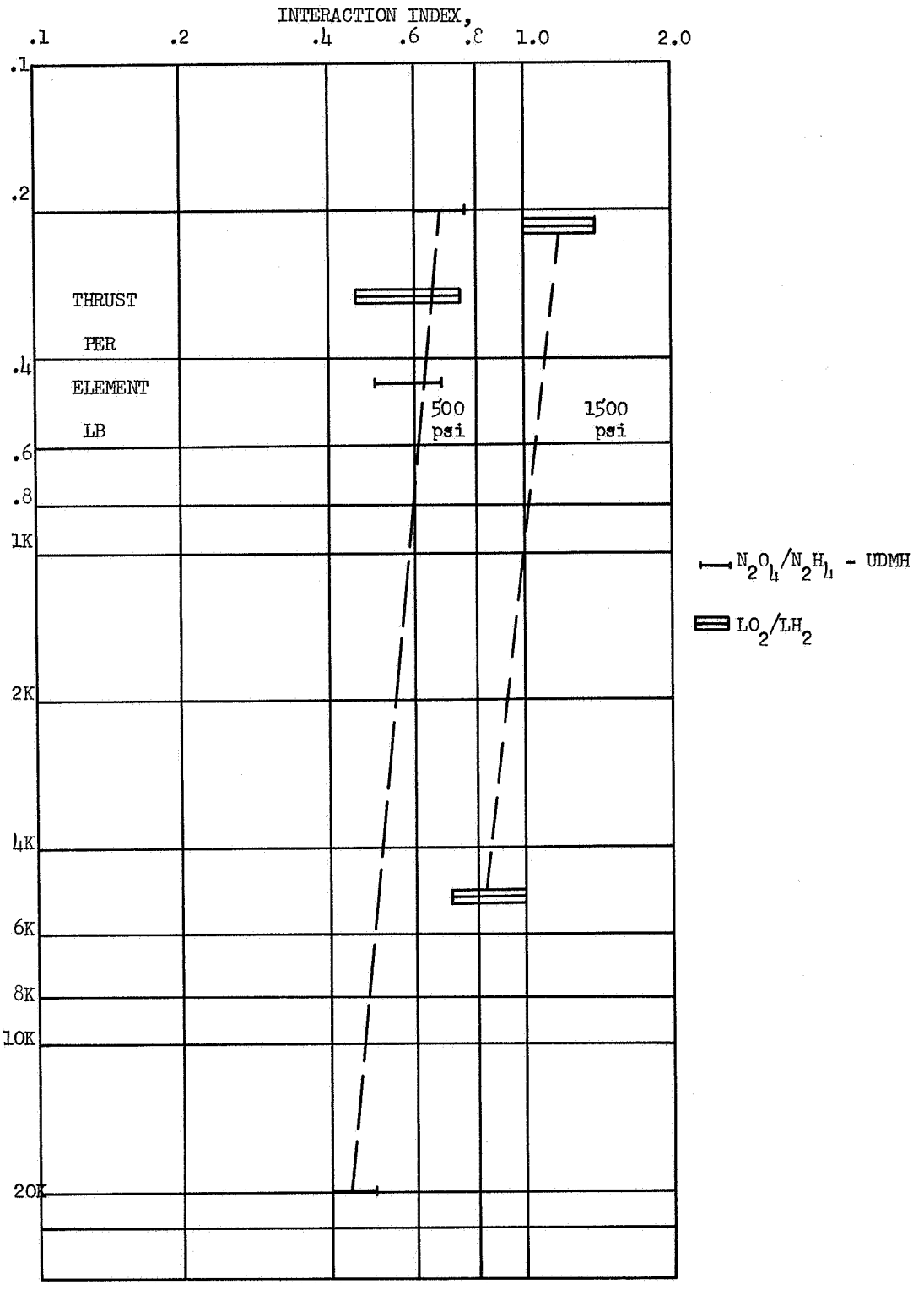


Figure A-3. Effect of Element Size Upon Interaction Index

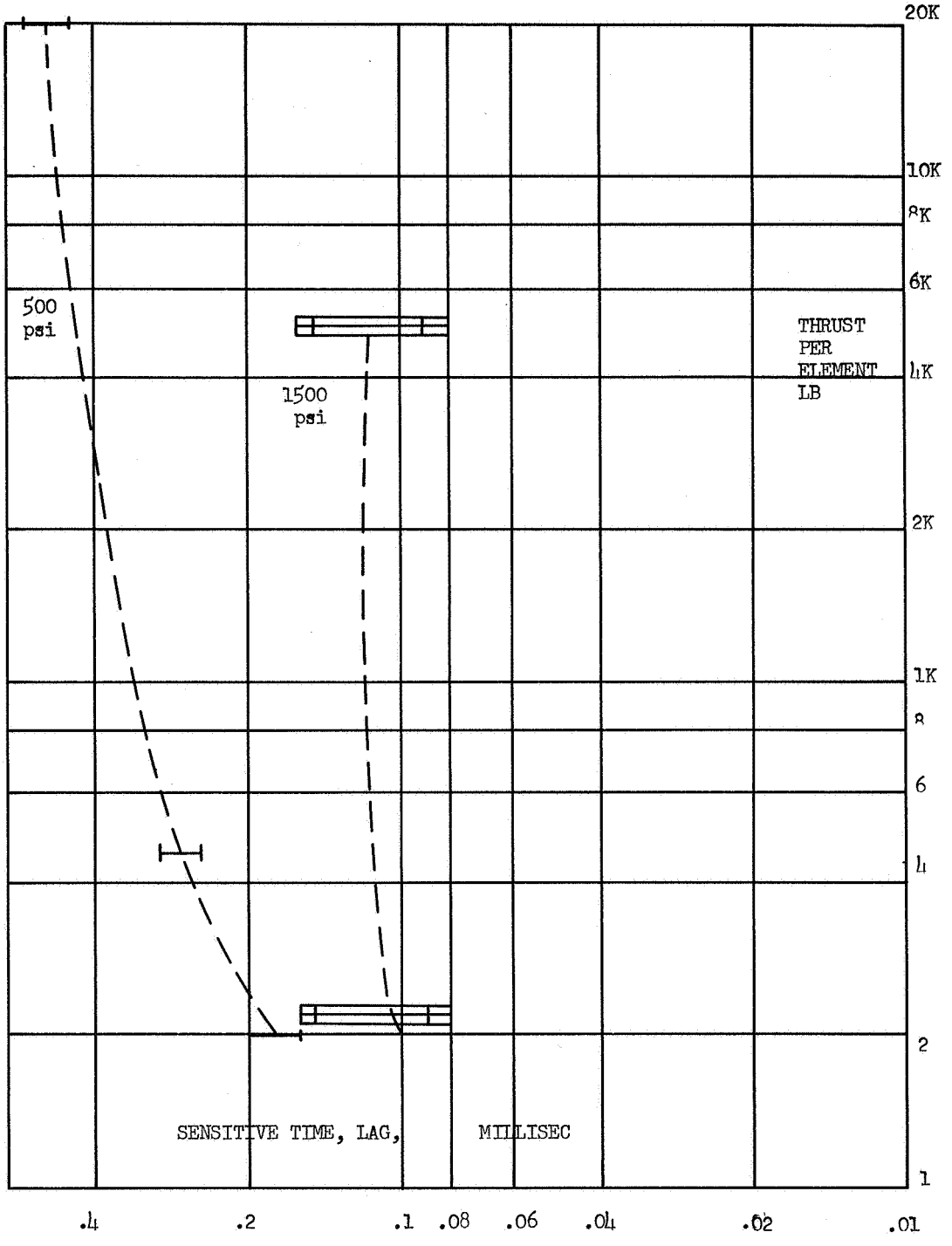


Figure A-4. Effect of Element Size Upon Sensitive Time Lag

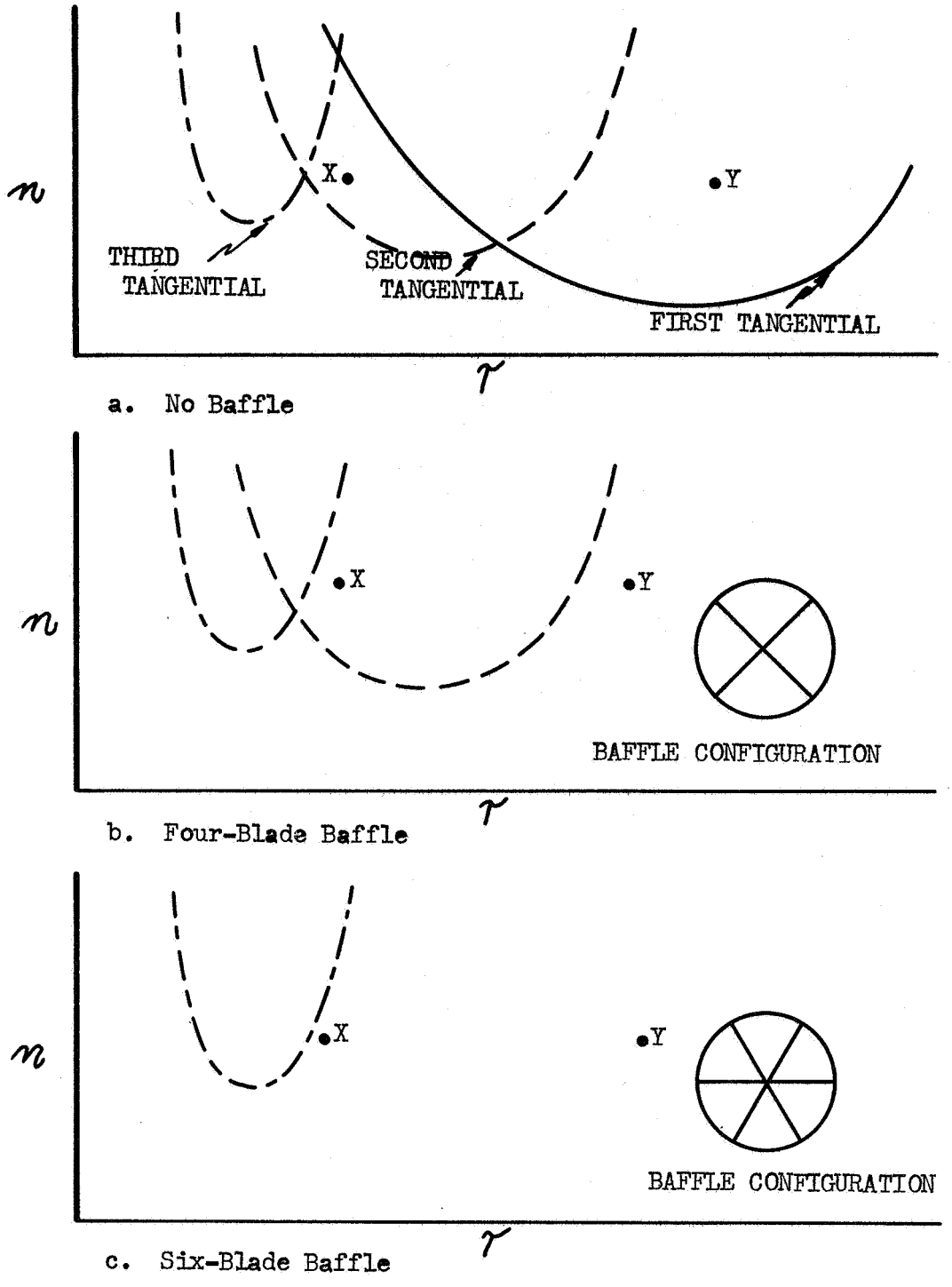


Figure A-5. Effect of Baffle Configuration Upon Stability

of sufficient length stabilizes injector "Y" but still allows a second tangential mode to occur for "X." With a six-blade baffle, both "X" and "Y" are stable, although a larger pulse may result in the third tangential mode instability with "X." Thus, an increase in $\tau$ allows a decrease in the number of baffle blades.

When the baffle blades do not extend to the sonic throat, the baffle pockets communicate in a region of subsonic flow. Then, for a circular chamber cross-section, any standing (or spinning) wave pattern must follow two conditions; the fluid properties must be continuous and they must be periodic with period $2\pi$ (360-degrees). That is, a pressure maximum and a pressure minimum cannot exist at the same point or immediately adjacent points. Because of these conditions, a steady, non-integral tangential mode cannot exist.

For a baffle with N radial blades, the lowest tangential mode which can exist is the N/2-th tangential if N is even, or the Nth tangential if N is odd. Thus, with respect to standing modes, a baffle with an odd number of blades is equivalent to a baffle with twice as many blades.

## V. STABILITY ANALYSIS

### A. THRUST CHAMBER CONFIGURATION

The internal configuration of the M-1 thrust chamber is shown on Figure No. A-6. The combustion chamber is conical, tapering from a diameter of 42-in. at the injector to a 32-in. throat diameter over a length of 20-in. The injector shown on Figure No. A-6 is flat-faced, which corresponds to the coaxial element pattern. An alternative injector design involves a dished face, with patterns composed of showerhead and like-impinging elements. The possible effects of injector face shape upon combustion instability could be handled analytically. Therefore, no distinction was made in this analysis between flat-faced and dish-faced injectors.

No theoretical analysis existed for high-frequency instability in conical combustion chambers. For the purposes of this stability analysis, the thrust chamber was divided into two parts as shown on Figure No. A-6. The "combustion chamber" was assumed to be a circular cylinder, approximately 6-in. long, wherein all of the combustion takes place at a relatively low flow velocity. In the "exhaust nozzle," the flow is accelerated without combustion. It reaches sonic velocity at the throat. Only transverse modes of high-frequency instability were considered. For these modes, the exact length of the combustion chamber and an accurate knowledge of the axial combustion distribution were not necessary.

### B. CHAMBER WITHOUT BAFFLES

Theoretical instability zones were calculated for several radial and tangential modes. These are shown on the $\eta$, $\tau$ plane of Figure No. A-7.

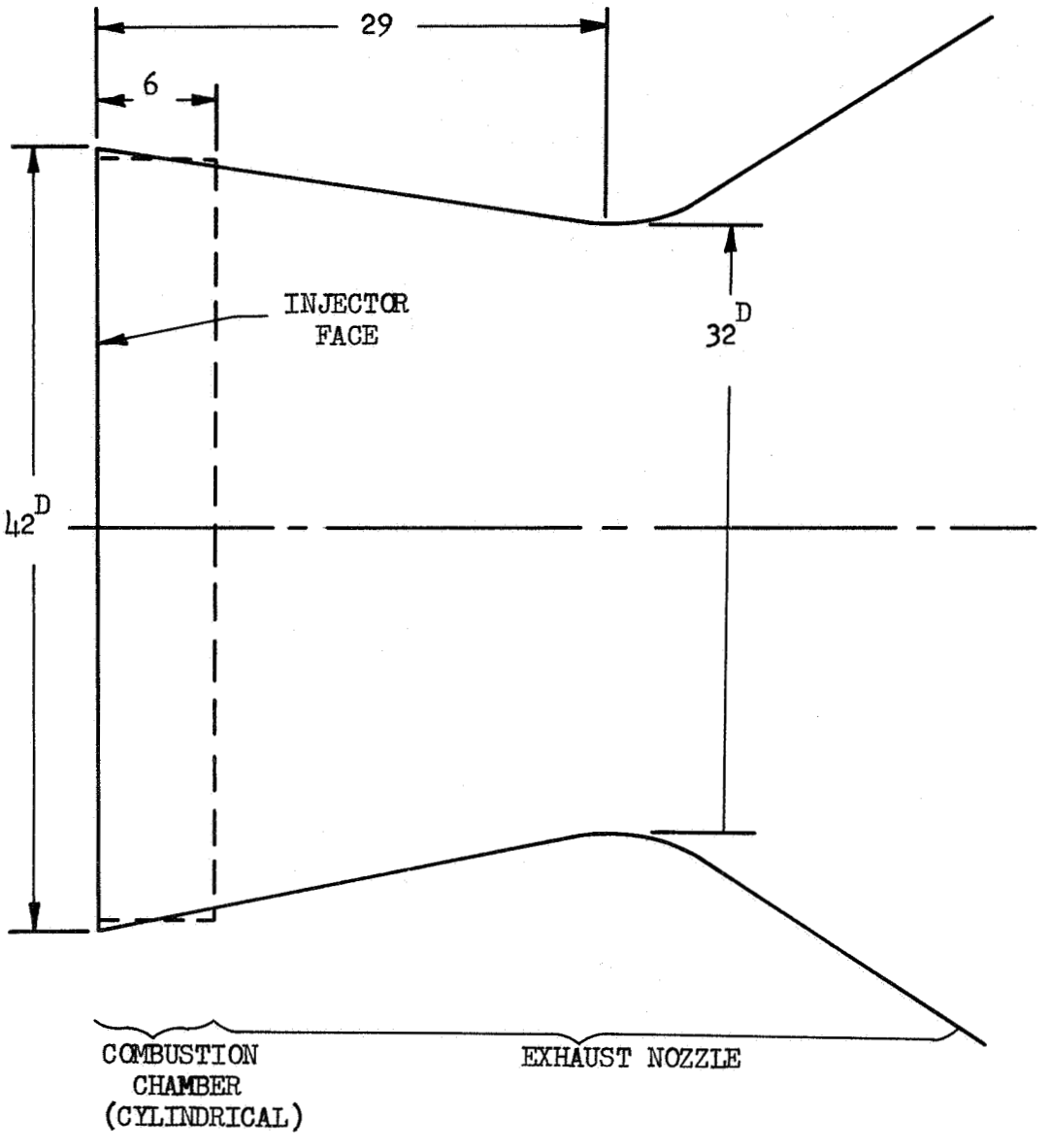


Figure A-6. M-1 Thrust Chamber Configuration

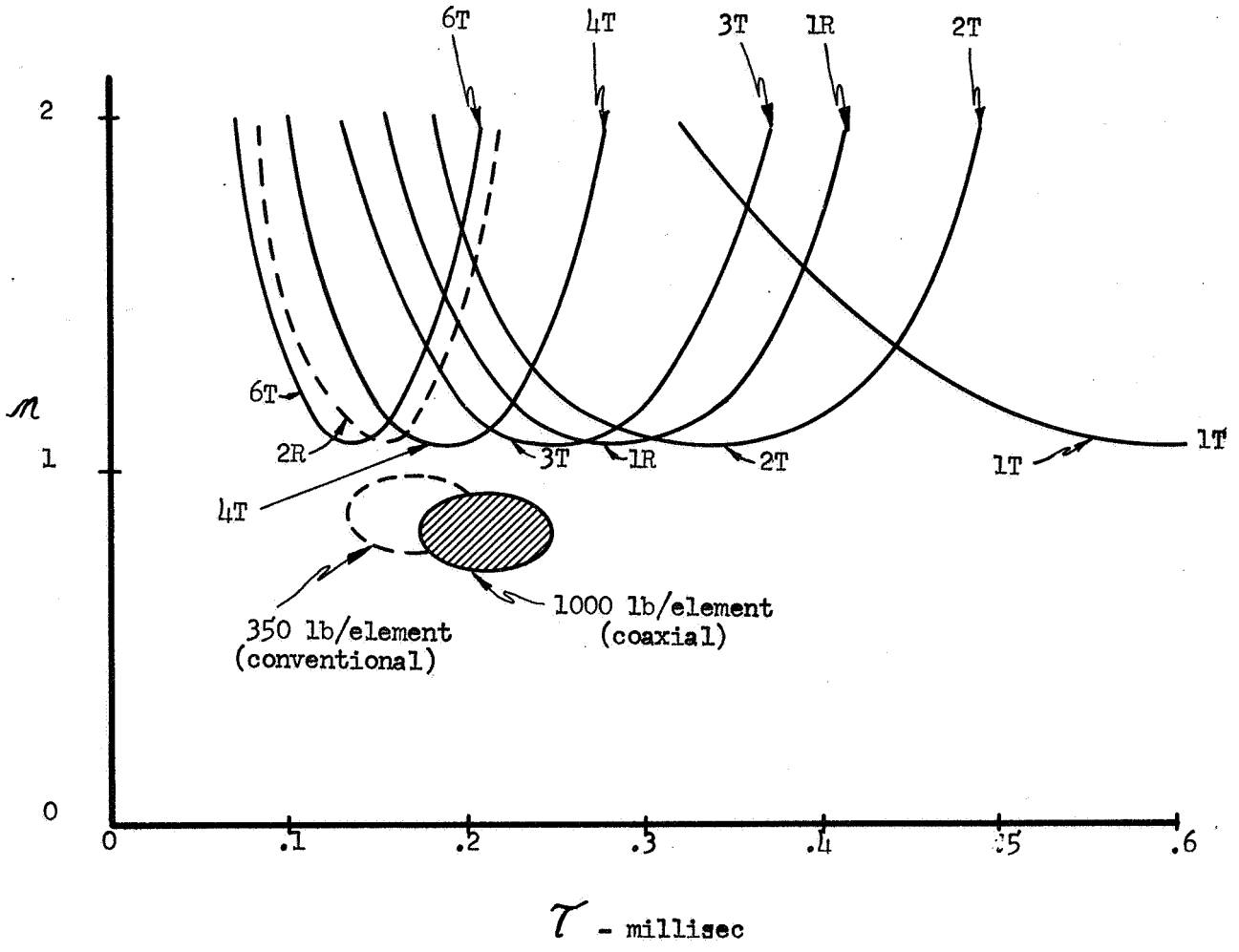


KEY:

| | | |
|---|---|---|
| 1T | = | first tangential mode |
| 2T | = | second tangential mode |
| 3T | = | third tangential mode |
| 4T | = | fourth tangential mode |
| 6T | = | sixth tangential mode |
| 1R | = | first radial mode |
| 2R | = | second radial mode |

Figure A-7. M-1 Thrust Chamber Instability Zones Without Baffles

The calculations were based upon previously derived equations[20][21]. Based upon a mean sound velocity of 5300 ft/sec, the following are the frequencies of the modes considered:

| | |
|---|---|
| First tangential, | 870 cps |
| Second tangential, | 1500 cps |
| First radial, | 1850 cps |
| Third tangential, | 2000 cps |
| Fourth tangential, | 2600 cps |
| Second radial, | 3400 cps |
| Sixth tangential, | 3600 cps |

To predict stability behavior, knowledge is required of the values of the stability parameters $\eta$ and $\tau$ which correspond to the propellant combination and injector pattern used. As previously discussed, $\eta$, $\tau$ data are limited and the effects of injector pattern variables and propellant properties were largely unknown. However, ranges of values could be obtained for classes of injector patterns by interpolation (see Figures No. A-3 and No. A-4). For the coaxial-spray-element injectors, which deliver 1000 lb thrust-per-element, the following ranges of $\eta$, $\tau$ values were obtained.

$$0.7 < \eta < 0.9$$

$$0.18 < \tau < 0.25 \text{ millisec}$$

Then, for a conventional showerhead or like-impinging pattern with 350 lb thrust-per-element,

$$0.75 < \eta < 0.95$$

$$0.15 < \tau < 0.22 \text{ millisec}$$

Both sets of values assume a chamber pressure of 1000 psia.

From Figure No. A-7, it can be seen that the most likely modes of high-frequency instability are the third and four tangential, with frequencies in the range of 2000 cps to 3000 cps. Both injector types were expected to be linearly stable; that is, stable with respect to the low-level disturbances associated with combustion noise. However, the effects of disturbances of relatively large amplitude could be estimated from available theories. In addition, if mixture ratio gradients are significant in the tangential direction, there can be strong velocity (mixing) effects leading to spinning tangential mode instability[22]. Because of the lack of data regarding velocity effects and nonlinear disturbances, these factors were not considered quantitatively in the analysis.

(20) Reardon, F. H., Princeton University Aeronautical Engineering Report No. 550, op. cit.
(21) Crocco, L., Harrje, D. T., and Reardon, F. H., op. cit.
(22) Reardon, loc. cit.

## C. BAFFLE CONFIGURATION

It is clear from the preceding discussion that protection had to be provided against spinning tangential modes and against standing modes lower than the sixth tangential. The selection of a baffle configuration involved a compromise between performance and stability, with various practical hardware limitations offering additional constraints. Interbaffle spacing had to be minimized to prevent standing transverse modes. This objective is realized by increasing the number of blades and hubs. However, by so doing, the injector area available is reduced and the baffle cooling requirements are increased. Fabrication problems also are likely to grow with increasing baffle complexity. Conversely, a thrust chamber with an inadequate baffle may never satisfy program requirements because of recurrent combustion instability.

The baffle configuration shown on Figure No. A-8 is not presented as an optimum design. However, it is believed that this configuration represents a reasonable compromise, based upon available information, among the various constraining factors.

The use of 12 radial blades of sufficient length protects against standing and spinning tangential modes lower than the sixth. With a purely radial blade baffle, the first radial mode could still exist. Therefore, a cylindrical hub with a diameter approximately one-half that of the chamber should be used. Within the hub, only six radial blades are required to provide stability which is equivalent to that of the 12 outside of the hub. The zone of instability shown on Figure No. A-9 is a composite of zones for the lowest radial and tangential modes that can occur within the interbaffle spaces.

It is not possible to analytically predict the baffle length required to effect stabilization of spinning tangential modes. The necessary baffle length is a function of the propellant preparation accomplished by the injection pattern and of the propellant characteristic reflected in the axial combustion distribution. Measurements of the combustion distribution for each injector pattern in suitable model chambers would be helpful in estimating the necessary baffle axial length.

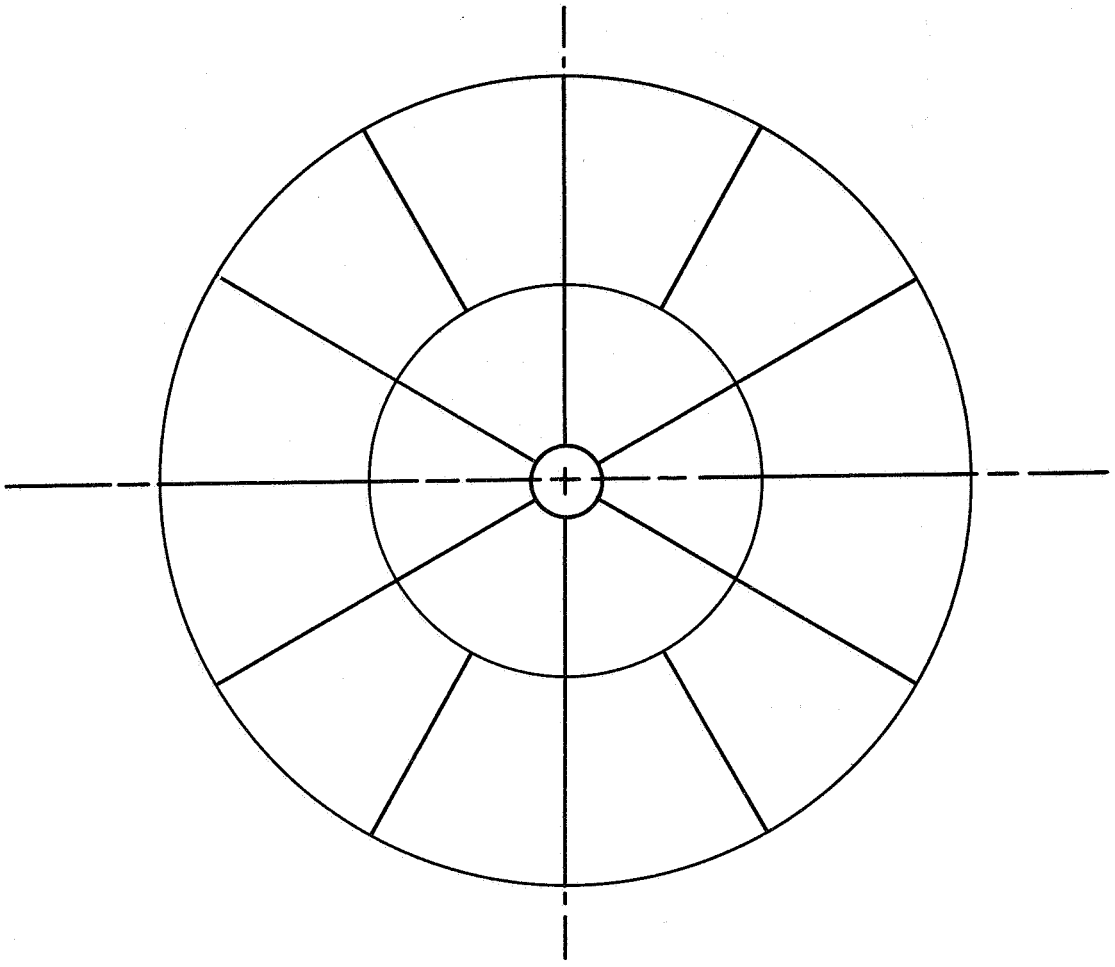

Figure A-8. Recommended Baffle Configuration

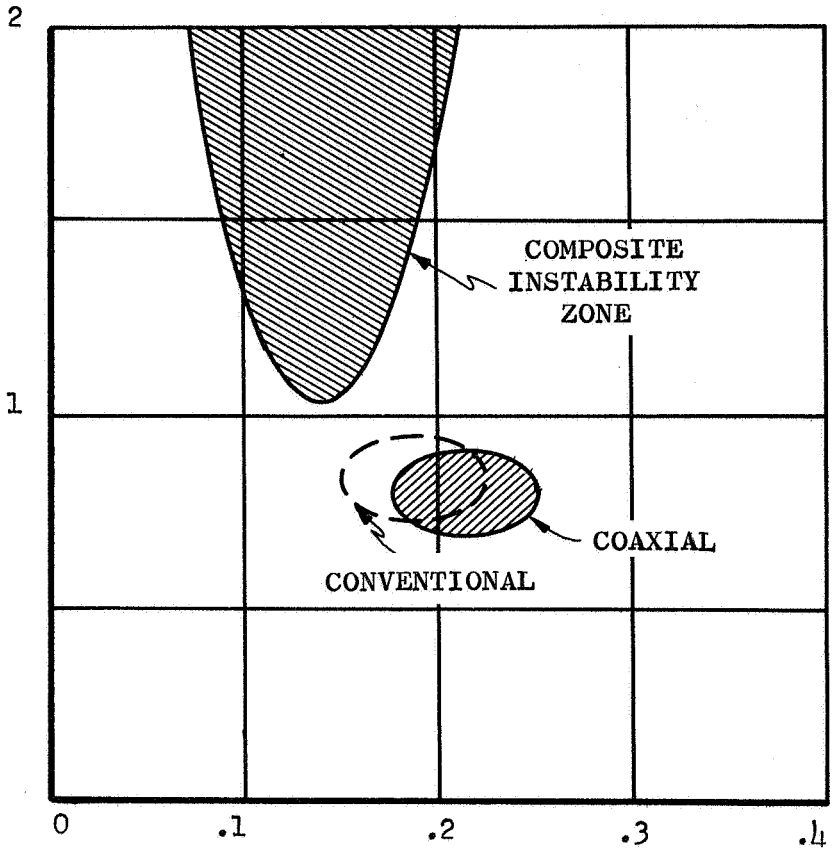


Figure A-9. Instability Zone of Chamber with Baffles

Appendix A

## BIBLIOGRAPHY


1. Addoms, J. F., et al, Unique Injector Concepts Development (UNICODE), Aerojet-General Report No. 0518-00-5 (Quarterly), September 1962

2. Crocco, L. and Cheng, S. I., Theory of Combustion Instability in Liquid Propellant Rocket Motors, AGARDograph No. 8, Butterworths Scientific Publications, London, 1956

3. Ellis, H. B. and Pickford, R. S., High-Frequency Instability, Aerojet-General TN-17, September 1956 (AFOSR TN-56-547)

4. Pickford, R. S. and Peoples, R. G., Inherent Stability of the Combustion Process, Aerojet-General TN-36, November 1960, (AFOSR 676)

5. Peoples, R. G. and Pickford, R. S., Analytical and Experimental Scaling of Thrust Chambers, Aerojet-General TN-40, November, 160 (AFOSR 677)

6. Peoples, R. G., Baker, P. D., and Knowles, L. S., High-Frequency Combustion Instability, Aerojet-General Report No. 2126, November, 1961 (AFOSR 1802)

7. Priem, R. J. and Guentert, D. C., Combustion Instability Limits Determined by a Nonlinear Theory and a One-Dimensional Model, NASA TN D-1409, 1962

8. Reardon, F. H., An Investigation of Transverse Mode Combustion Instability in Liquid Propellant Rocket Motors, Princeton University Aeronautical Engineering Report No. 550, 1 June 1961

9. Reardon, F. H., Combustion Stability Behavior of the Liquid Oxygen/Liquid Hydrogen Propellant Combination, Aerojet-General Report No. TM 9616/002, March 1962

10. Reardon, F. H., Combustion Stability Behavior of the Nitrogen Tetroxide/AeroZINE-50 Propellant Combination with the 2 SIN Injector Pattern, Aerojet-General Report No. TM 9616/003, 13 March 1962

11. Scala, S. M., Transverse Wave and Entropy Wave Combustion Instability in Liquid Propellant Rocket Motors, Princeton University Aeronautical Engineering Report No. 380, 1 April 1957

12. Torda, T. P. and Burstein, S., Nonlinear Theory of Combustion Instability in Liquid Propellant Rocket Motors, Propellant Research Laboratory Report No. PRL-TN-58-1, December 1958 (AFOSR TN-59-60, ASTIA No. 209-491)

13. Crocco, L., Gray, J., and Harrje, D. T., "Theory of Liquid Propellant Combustion Instability and Its Experimental Verification," ARS Journal, Vol. 30, No. 2, February 1960

BIBLIOGRAPHY (cont.)

14. Crocco, L., Harrje, D. T., and Reardon, F. H., "Transverse Mode Combustion Instability in Liquid Propellant Rocket Motors," ARS Journal, Vol. 32, No. 3, March 1962

15. Priem, R. J., and Morrell, G., "Application of Similarity Parameters for Correlating High-Frequency Instability Behavior of Liquid Propellant Combustors," American Rocket Society Paper No. 1721-61, Propellants, Combustion, and Liquid Rockets Conference, Palm Beach, Florida, April 26-28, 1961

16. High Chamber Pressure Operation for Launch Vehicle Engines, Aerojet-General Corporation, Final Report, Contract NAS 8-4008, 15 April 1963

# APPENDIX B

## SAMPLE CALCULATIONS

## FOR

## STEADY-STATE DATA

Appendix B

## DEFINITION OF SYMBOLS

| | |
|---|---|
| $A_t$ | chamber throat area ($in.^2$) |
| $P_{fJ}$ | pressure fuel injector (psia) |
| $P_{oJ}$ | pressure oxidizer injector (psia) |
| Pc5D | chamber pressure 1.43 in. from injector face (psia) |
| Pc4D | chamber pressure 10.67 in. from injector face (psia) |
| $T_{fJ}$ | temperature fuel injector (°R) |
| $T_{oJ}$ | temperature oxidizer injector (°R) |
| $\Delta P_f$ | pressure drop across fuel injector (psi) |
| $\rho_f$ | density fuel injector ($lbm/ft^3$) |
| $\Delta P_o$ | pressure drop across oxidizer injector (psi) |
| $\rho_o$ | density oxidizer injector ($lbm/ft^3$) |
| $P_{plenum}$ | nozzle stagnation pressure (psia) |
| $\dot{w}_{LH_2}$ | liquid hydrogen weight flow (lbm/sec) |
| $\dot{w}_{GH_2}$ | gaseous hydrogen weight flow (lbm/sec) |
| $\dot{w}_f$ | summation of liquid and gaseous hydrogen weight flows (lbm/sec) |
| $\dot{w}_o$ | oxygen weight flow (lbm/sec) |
| M.R. | mixture ratio (oxygen to hydrogen) |
| c* | characteristic exhuast velocity (ft/sec) |
| $N_2$ | nitrogen |
| h | enthalpy (B/lb) |
| $\eta$ | efficiency (%) |
| F | thrust ($lb_f$) |
| $I_{sp}$ | specific impulse ($\frac{lb_f\text{-sec}}{lbm}$) |
| $C_F$ | nozzle thrust coefficient |

The items listed in this appendix correspond with those shown on Table VII in the main text.

1. Serial No. of injector tested - 020

2. Test Series - 1.2-05-EHM

3. Test Number - 1.2-05-EHM-006

4. Test Date - 20 July 1966

5. Test Duration - from Fire Switch One ($FS_1$) to Fire Switch Two ($FS_2$):

   $FS_1$ to $FS_2$ = 6.56 sec

6. Data Summary Period - The period of time from $FS_1$ during which all data is averaged:

   (from $FS_1$ + 6.0 sec to $FS_1$ + 6.6 sec)

7. $A_t$ (Pre-Test) - The average combustion chamber throat area based upon 12 throat diameter measurements taken prior to the test (704.04-in.$^2$)

8. $A_t$ (Post-Test) - The average combustion chamber throat area based upon 12 throat diameter measurements taken after the test (705.99-in.$^2$)

9. $A_t$ (Data Summary Period) - The throat area during the middle of the data summary period assuming that the pre-test $A_t$ is representative of the throat area at $FS_1$ + 4.0 sec and the post-test $A_t$ is representative of the throat area at $FS_2$*.

   $A_t$ (Data Summary Period) =

$$704.04 + (705.99 - 704.04)\left[\frac{\frac{6.0 + 6.6}{2} - 4.0}{6.6 - 4.0}\right] = 705.75\text{-in.}^2$$

10. $P_{fJ}$ - Average pressure of two measurements in the inlet to the fuel injector manifold ($P_{fJ}$ = 1274 psia)

11. $P_{oJ}$ - Average pressure of two measurements in the periphery of the oxidizer injector manifold ($P_{oJ}$ = 1432 psia)

12. Pc5D - Injector face pressure located 1.43-in. from the injector face (Pc5D = 1106 psia)

---

* Assuming that the erosion rate is linear

13. Pc4D - Chamber pressure located 10.67-in. from the injector face.

    NOTE: This pressure measurement was not recorded until Test No. 1.2-07-EHM-007 when Pc5D was substituted with a high frequency pressure transducer.

14. $T_{fJ}$ - Average of two temperature measurements in the fuel injector manifold ($T_{fJ}$ = 154.3°R)

15. $T_{oJ}$ - Average of two temperature measurements in the oxidizer injector manifold ($T_{oJ}$ = 175.1°R)

16. $\Delta P_f$ (Injector) - Differential pressure from $P_{fJ}$ to Pc5D ($\Delta P_f$ = 168 psi)

17. $\rho_f$ (Injector) - Density of the fuel at $P_{fJ}$ and $T_{fJ}$ conditions ($\rho_f$ = 1.56 lb/ft$^3$)

18. $\rho_F \Delta P_f$ - The product of Item 16 and Item 17

    ($\rho F \Delta P_f$ = 262.1 lbm lb$_f$/in.$^2$ ft$^3$).

    Figure no. B-1 shows a plot of $\rho_f \Delta P_f$ versus $\dot{w}_f$ comparing injectors S/N 020 and 012.

    Note that S/N 012 calculated face pressure $\rho_f \Delta \rho_f$ data points are lower than S/N 020 and S/N 012 measured face pressure $\rho_f \Delta \rho_f$ data points. $P_{fJ}$, Pc5D, or both could be highly inaccurate. $P_{fJ}$ is an average of two measurements that were checked for accuracy and found to be valid. A simultaneous shift in the calibration of both transducers or a shift in the injector flow constant could have occurred. Also, the calculated face pressures could be highly inaccurate (a high reading), thereby lowering $\rho_f \Delta \rho_f$ and raising $\eta$ c*.

19. $\Delta P_o$ (Injector) - Differential pressure from $P_{oJ}$ to $P_c$5D ($\Delta P_o$ = 326 psi)

20. $\rho_o$ (Injector) - Density of the oxidizer at $P_{oJ}$ and $T_{oJ}$ conditions ($\rho_o$ = 70.32 lbm/ft$^3$)

21. $\rho_o \Delta P_o$ - The product of Item 19 and Item 20

    ($\rho_o \Delta P_o$ = 22,924 lbm lb$_f$/in.$^2$ ft$^3$).

    Figure No. B-2 shows a plot of $\rho_o \Delta P_o$ versus $\dot{w}_o$ comparing injectors S/N 020 and 012.

22. Contraction Ratio (C.R.) - The ratio of the chamber area at the trailing edge of the baffles to the throat area (Item 9).

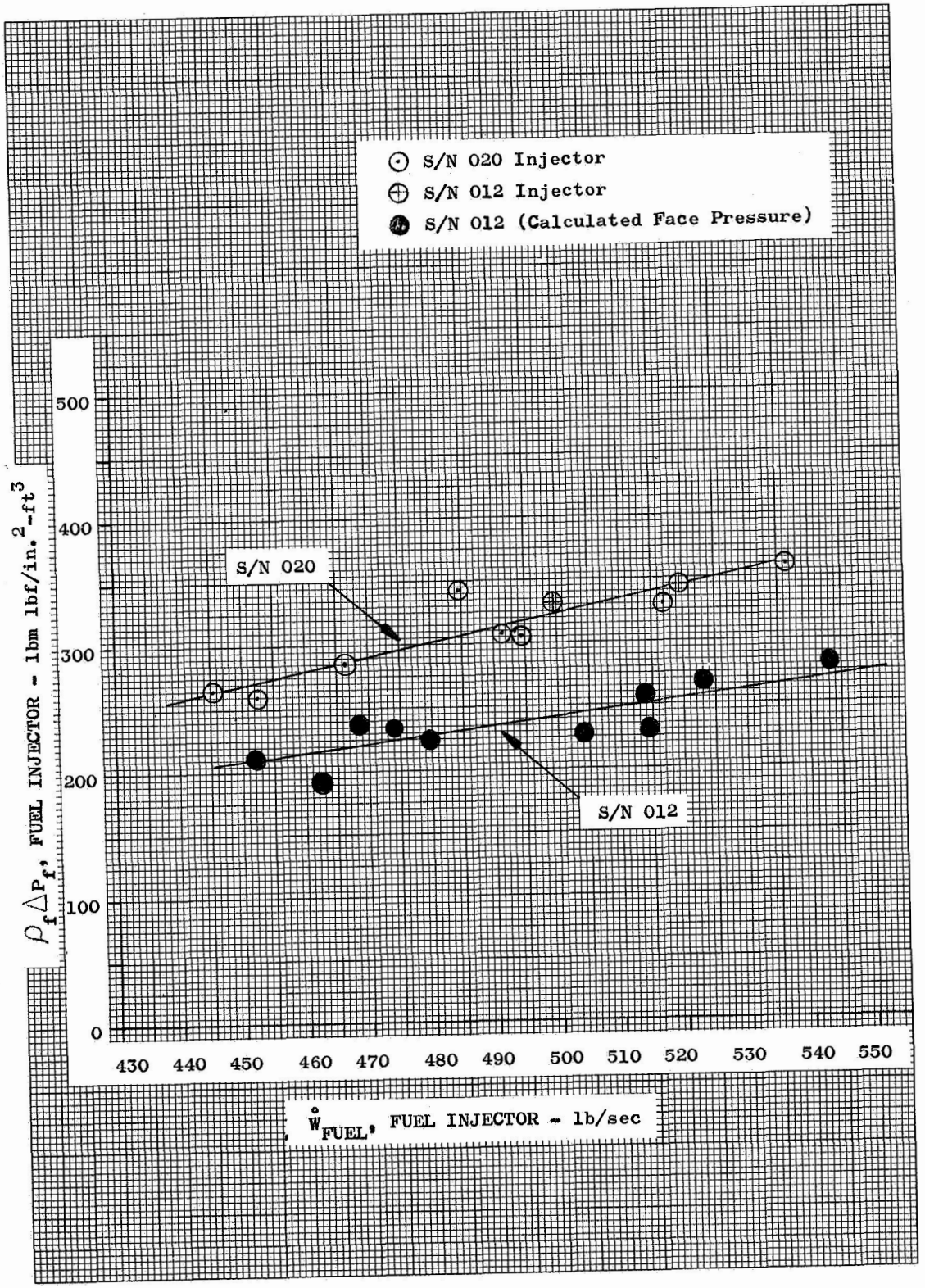


Figure B-1. $\rho_F \Delta P_F$ vs $\dot{W}_F$, Comparing Injectors S/N 020 and S/N 012

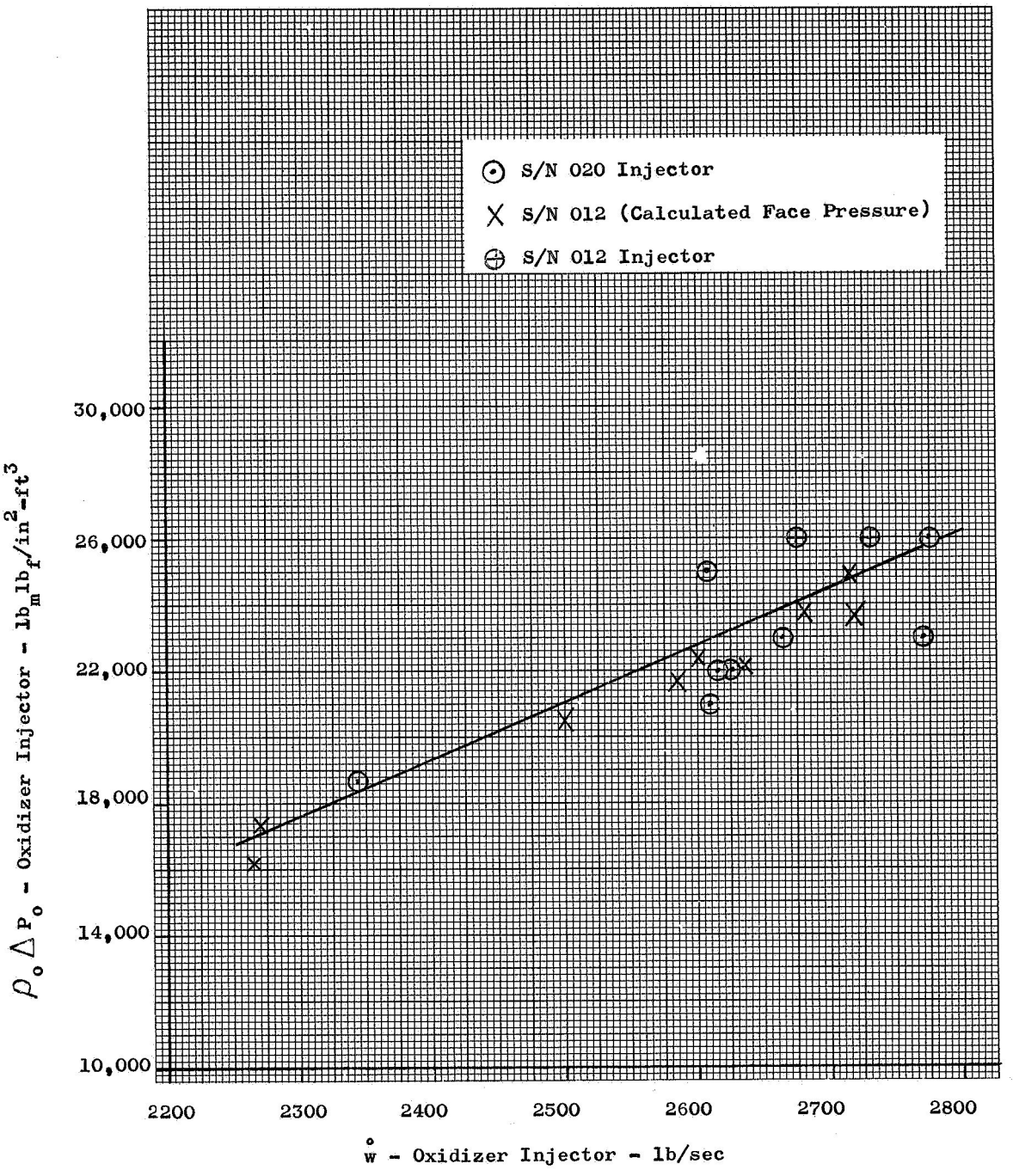


Figure B-2. $\rho_o \Delta P_o$ vs $\dot{W}_o$, Comparing Injectors S/N 020 and S/N 012

$$C.R. = \frac{\frac{\pi}{4}\ 39.24^2\text{-in.}^2}{705.74\text{-in.}^2} = \frac{1209.4}{705.74} = 1.714$$

23. $Pc5D/P_p$ - Ratio of injector face pressure to chamber plenum pressure obtained as follows:

$$\frac{Pc5D}{P_p} = \frac{P_s}{P_p} + \frac{V_S - V_{inj}}{C.R.\ c^*_{Theo.}\ \eta c^*} \qquad \text{Equation (1)}$$

where:

$$\frac{P_s}{P_c} = \left(1 - \frac{\gamma_s - 1}{2} M_s^2\right) - \frac{\gamma_s}{s-1}$$

$$\gamma_s = \frac{1}{1 - \frac{2 g \bar{R}_{Ts}}{M.S._s\ V_s^2}\left(\frac{T_c}{T_s} - 1\right)}$$

$$M_s^2 = \frac{V_s^2}{\gamma_s g}$$

$$V_{inj} = V_f \left(\frac{\dot{w}_f}{\dot{w}_t}\right) + V_o \left(\frac{\dot{w}_o}{\dot{w}_t}\right)$$

$$V_f = \frac{144\ \dot{w}_f}{\rho_f A_f} \qquad \text{and } V_o = \frac{144\ \dot{w}_o}{\rho_o A_o}$$

The subscript s refers to isentropic combustion conditions at the injector face where the $V_s$, $T_s$, $M.W._s$, and $T_c$ can be determined from chemical composition. $c^*_{theo}$ is corrected for enthalpy and nitrogen diluent.

$\frac{P_c 5D}{P_p}$ is iterated until $P_p$ is equal in Equation (1) and

$$c^* = \frac{P_p\ A_t g}{\dot{w}_t} \qquad \text{Equation (2)}$$

and

$$\eta c^* = \frac{c^*}{c^*_{corrected}} \qquad \text{Equation (3)}$$

$$\therefore \frac{P_c5D}{P_p} = 1.0662$$

However, in tests No. 1.2-07-EHM-007 through -025, injector face pressure ($P_c5$) was not measured. Instead, static pressure ($P_c4$) was measured at point approximately 11.7-in. downstream from the injector face. To obtain $P_p$ from $P_c4$, the following equations were used:

$$P_p = \frac{P_p}{P_c5D} \times \frac{P_c5D}{P_c4D} \times P_c4D \qquad \text{Equation (4)}$$

and

$$\frac{P_c5D}{P_c4D} = \left(\frac{P_c5D}{P_p}\right)\left(\frac{P_p}{P_c4D}\right) \qquad \text{Equation (5)}$$

where $\frac{P_p}{P_c4D}$ is available from the combustion tables for the appropriate conditions.(1)

Because:

$$C.R._4 = \frac{1023\text{-in.}^2}{705.74\text{-in.}^2} = 1.45$$

Then:

$$\left(\frac{P_p}{P_c4D}\right) = 1.128$$

Therefore:

$$\frac{P_c5D}{P_c4D} = \frac{P_c5D}{P_p} \quad (1.128)$$

24. $P_{Plenum}$ - Chamber Plenum Pressure = $\frac{\text{Item 12}}{\text{Item 23}} = \frac{1106}{1.0662} = 1037$ psia

(1) Gordon, S. and McBride, B. J., Theoretical Performance of Liquid Hydrogen with Liquid Oxygen as a Rocket Propellant, NASA TM 5-21-59E

25. $\dot{w}_{LH_2}$ - Liquid hydrogen weight flow to mixer (361.5 lb/sec)

26. $\dot{w}_{GH_2}$ - Gaseous hydrogen weight flow to mixer (91.0 lb/sec)

27. $\dot{w}_f$ - Fuel weight flow from mixer [Item 25 + Item 26 = 452.5 lb/sec]

28. $\dot{w}_o$ - Oxidizer weight flow (2767 lb/sec)

29. M.R. - Ratio of oxidizer weight flow (Item 28) to fuel weight flow (Item 27): $M.R. = \frac{2767}{452.5} = 6.12$

30. c* (measured) - Measured characteristic exhaust velocity calculated as follows:

$$c^* = \frac{P_p A_t g}{(\dot{w}_o + \dot{w}_f} = \frac{(\text{Item 24})\ (\text{Item 9})\ g}{\text{Item 28} + \text{Item 27}} = \frac{(1037)(705.74)(32.2)}{2767 + 452.5} = 7315 \text{ ft/sec}$$

31. $N_2$ diluent - That portion, by weight, of nitrogen in the oxidizer.

The percentage of nitrogen = 1.43%

32. $h_{I_{sp}}$ a. An enthalpy correction applied to the theoretical performance data to account for the difference between the fuel inlet test temperature and the temperature (36.5°R) of the theoretical data per the following equation(2)

$$h_{I_{sp}} = \frac{I_2}{I_o} = \frac{\sqrt{I_o^2 + 87\ (1 - T_e/T_c)\Delta_o h_c}}{I_o}$$

Figure No. B-3 is a plot of the enthalpy correction factor in relationship to fuel temperature. From this figure, it can be seen that at 154.3°R and 6.12 M.R., the enthalpy correction factor for specific impulse = 1.0037

b. Because $c^* C_F = I_{sp}$, the following is a good method for dividing the enthalpy correction between $I_{sp}$ and $h_I$ as well as between c* and $C_F$:

$$(h_{c^*}\ c^*)\ (h_{C_F}\ C_F) = (h_{I_{sp}}\ I_{sp})\ g$$

where $h_{c^*}\ h_{C_F} = h_{I_{sp}}$

(2) Theoretical Performance of Hydrogen-Oxygen Rocket Thrust Chambers, NASA TR- R-111, 1961

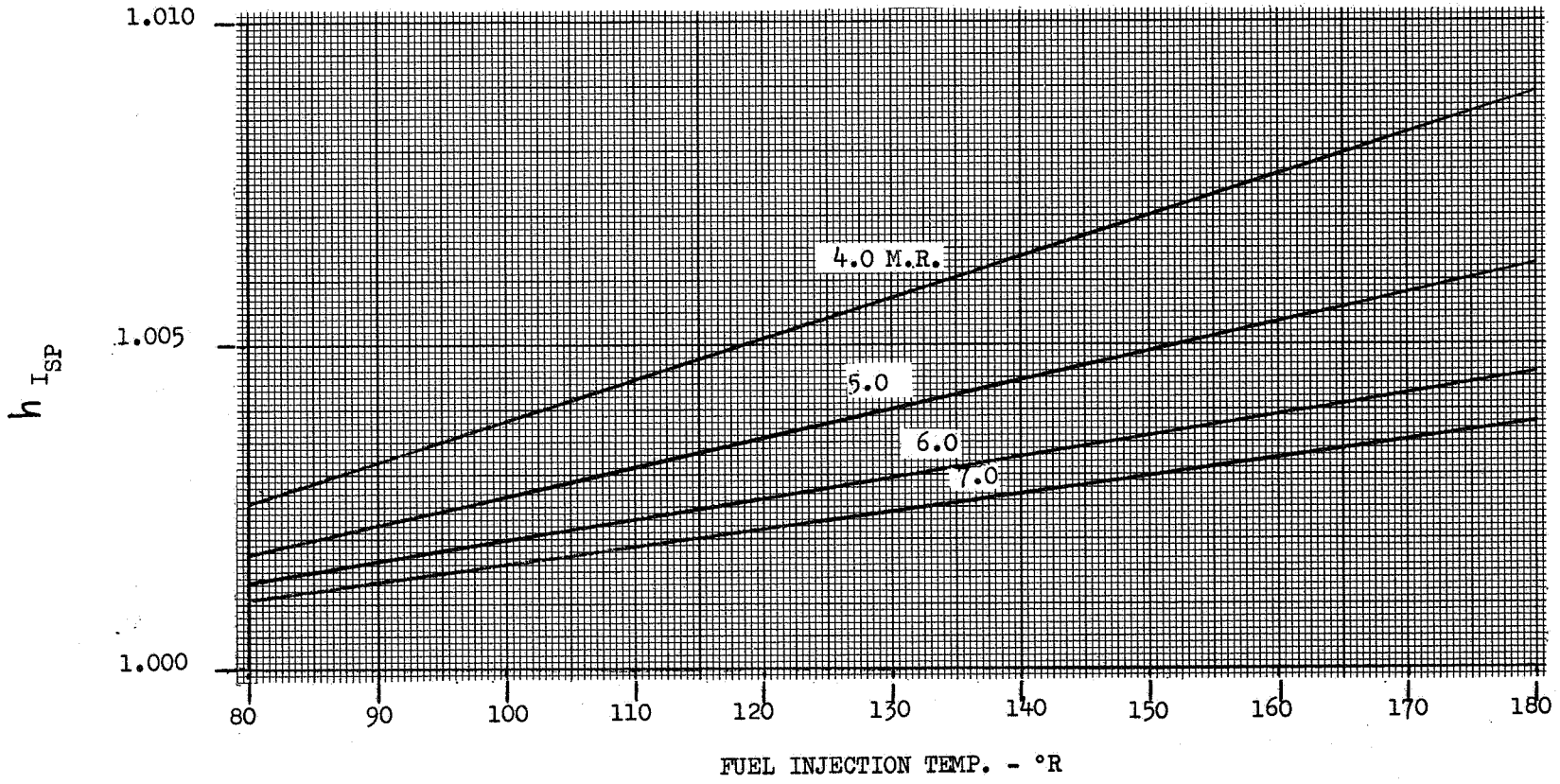


Figure B-3. Enthalpy Correction Factor in Relationship to Fuel Temperature

Let the nozzle/chamber interaction factor be "b"

$$b = \frac{\text{(Energy Release Loss @ E.R. = 2)}}{\text{(Energy Release Loss @ E.R. = 1)}} \text{ which is a function of O/F}$$

$$\therefore b = 1.43 - 0.052 \text{ (M.R. -4)}$$

Let: $h_{c^*} = (1 + k_{c^*})$, $h_{C_F} = (1 + k_{C_F})$, and $h_{I_{sp}} = (1 = k_I)$

$$\therefore (1 + k_{c^*})\ (1 + k_{C_F}) = (1 + k_{I_{sp}})$$

$$1 + k_{c^*} + k_{C_F} + k_{c^*}\ k_{C_F} = 1 + k_{I_{sp}}$$

If $k_{c^*}$ and $k_{C_F} \ll 1$, $k_{c^*}\ k_{C_F} \approx 0$

$$\therefore k_{c^*} + k_{C_F} \approx k_{I_{sp}}$$

Let $k_{C_F} = b\ k_{c^*}$

$$\therefore k_{c^*} + b\ k_{c^*} = k_{I_{sp}}$$

$$k_{c^*} = \frac{1}{1 + b}\ k_{I_{sp}} \text{ and } k_{C_F} = \frac{b}{1 + b}\ k_{I_{sp}}$$

The only aspect of interest to be plotted is the effect of $h_I$ upon c*, which is $k_{c^*}$

$$\therefore h_{c^*} = 1 + k_{c^*}$$

$$h_{c^*} = 1 + \frac{1}{1 + b}\ k_{I_{sp}}$$

$$h_{c^*} = 1 + \left( \frac{h_{I_{sp}} - 1}{1 + b} \right)$$

$$b = 1.43 - 0.052\ (6.12 - 4) = 1.22$$

$$h_{c^*} = 1 + \frac{1.0037 - 1}{1 + 1.22} = 1.0017$$

33. c* (theoretical - h, $N_2$) - Theoretical c* from Figure No. B-4 corrected for 1.43% (Item 31) $N_2$ dilution multiplied by the enthalpy correction factor for c* (Item 32b). At 6.12 M.R.:

$$7532 \text{ ft/sec} \times 1.0017 = 7544 \text{ ft/sec}$$

34. $\eta c^*$ (from $P_c$) - c* efficiency based upon $P_c$ is defined as

$$\frac{\text{(Item 30)}}{\text{(Item 33)}} \times 100$$

$$\eta c^* = \frac{7386}{7544} \times 100 = 97.9\%$$

35. c* (from nozzle losses) - c* efficiency based upon $C_F$ (thrust coefficient) is defined as follows:

$$\eta c^* \text{ (from nozzle losses)} = 100 + (\eta I_{sp} - \eta C_F)$$

where:

$$\eta I_{sp} = \left(100 - \frac{\Delta I_{sp\ Total}}{I_{sp_{Theo}}}\right) = \left(100 - \frac{\text{Item 69}}{\text{Item 42}}\right)$$

$$\eta C_F = \left(100 - \frac{\Delta I_{sp\ Nozzle}}{I_{sp_{Theo}}}\right) = \left(100 - \frac{\text{Item 63}}{\text{Item 42}}\right)$$

$$\eta I_{sp} = 88.1\% \text{ (Item 43)}$$

$$\eta C_F = 100 - \frac{28.3}{347.6} = 91.9\%$$

$$\therefore \eta c^* \text{ (from nozzle losses)} = 100 + 88.1 - 91.9 = 96.2\%$$

Figure No. B-5 presents a comparison of c* calculated by the nozzle losses and $P_p$ methods. Reducing the baffle coolant from 4% with the long baffles to 2% with the short baffles had less than an one-half percent affect upon the characteristic velocity. These data indicate that the hydrogen injected from the baffle tips was well-mixed with the main stream gases upstream of the throat. The c* at a nominal mixture ratio of 5.5 is 96.5%

The method of calculating $\eta c^*$ from $\eta I_{sp}$ and nozzle losses gives more precise results primarily because of the greater precision of the $I_{sp}$ measurement as compared with the c* measurement.

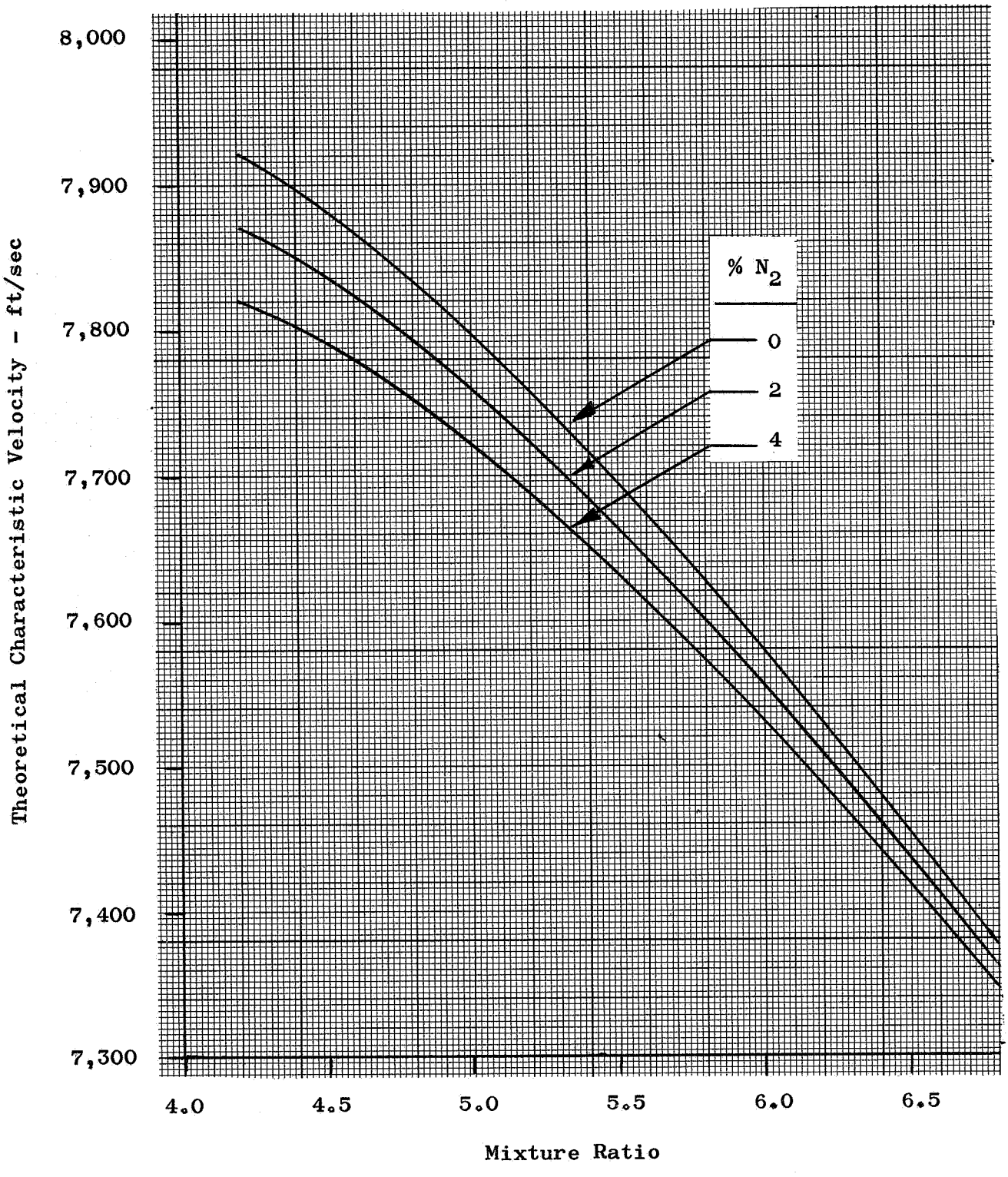


Figure B-4. Theoretical Characteristic Velocity vs Mixture Ratio

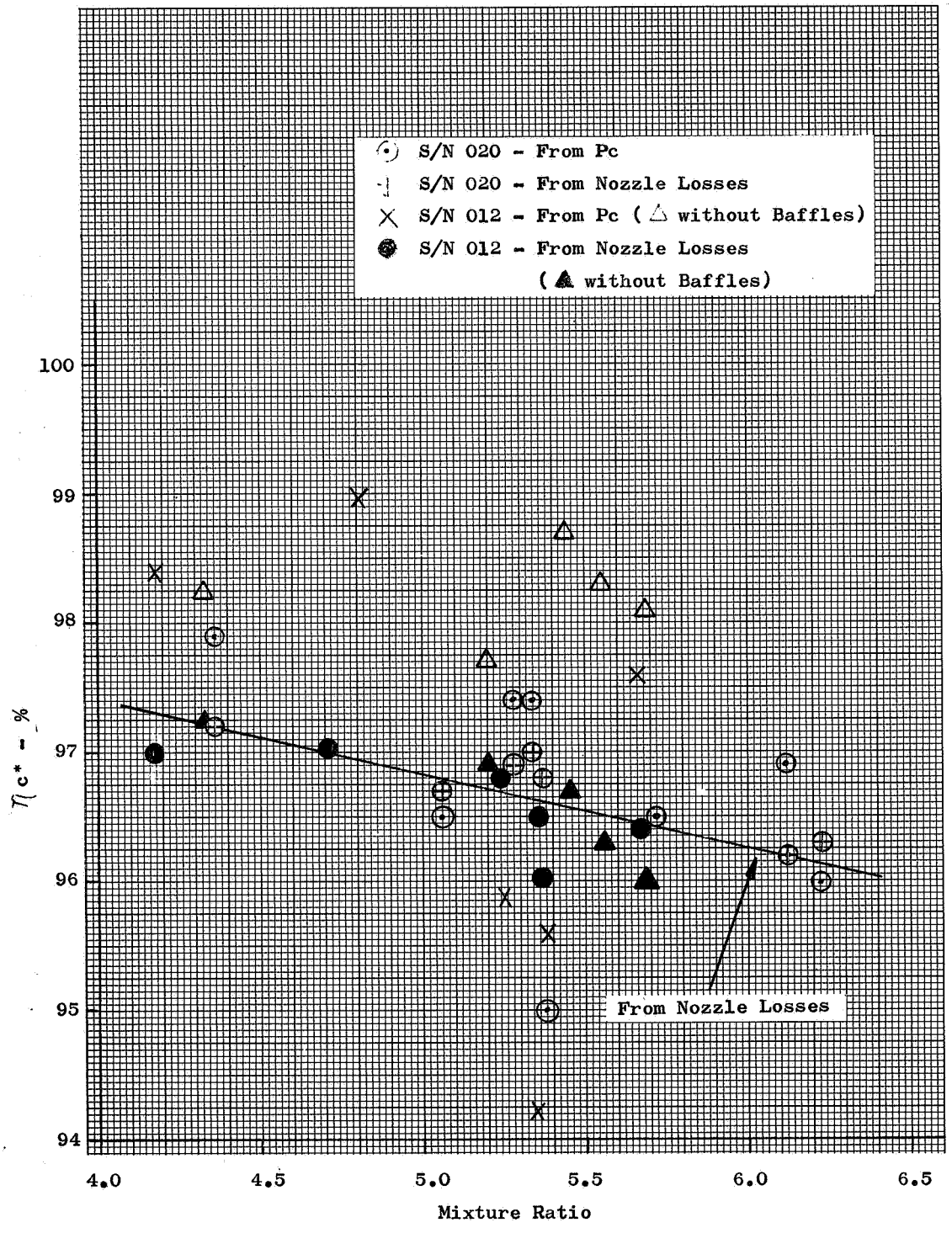


Figure B-5. $\eta$ C* vs Mixture Ratio

36. $F_{S.L.}$ (corrected) - Sea-level measured thrust corrected for 700 lb negative force effect upon the nozzle exit flange. No significant pressure difference is noted when comparing in-line with baffle nozzle exit pressure measurements and between baffle nozzle exit pressure measurements.

$F_{S.L.}$ (corrected) = $F_{S.L.}$ (measured) + 700 lb - 963486 + 700 = 964186 lb

37. $F_{VAC}$ - Measured sea-level thrust calculated at altitude

$F_{VAC} = F_{S.L.}$ (corrected) + $P_e A_e$ = 964189 + (1471 x 14.7) = 985814 lb

38. $I_{sp}$ (measured - S.L.) - Measured specific impulse at sea-level =

$$\frac{\text{(Item 36)}}{\text{(Item 27 + Item 28)}} = \frac{964186}{452.5 + 2767} = 299.5 \text{ sec}$$

39. $I_{sp}$ (measured - Vac) - Measured specific impulse corrected to altitude =

$$\frac{\text{(Item 37)}}{\text{(Item 27 + Item 28)}} = \frac{985814}{452.5 + 2767} = 306.2 \text{ sec}$$

40. Expansion Ratio (E.R.) - Ratio of nozzle exit area (1471-in.$^2$) to throat area = $\frac{1471}{705.74}$ = 2.085

41. $I_{spVAC_{2:1}}$ (Theoretical - E.R., h) - Theoretical vacuum specific impulse corrected for expansion ratio multiplied by the enthalpy correction factor. $I_{sp}$ from Figure No. B-6 at an E.R. of 2.085 and a M.R. of 6.12 multiplied by Item 32a = 348.4 sec.

42. $I_{spVAC_{2:1}}$ (Theoretical - E.E., h, $N_2$) - Theoretical vacuum specific impulse from Item 41 corrected for $N_2$ dilution. At 1.43% and a 6.12 M.R. (see Figure No. B-7), the net effect equals 0.8 sec. Therefore, the $I_{sp}$ = 347.6 sec.

43. $\eta I_{sp_{2:1}}$ - $I_{sp}$ efficiency with 2:1 area ratio nozzle is determined by dividing Item 39 by Item 42. Therefore:

$$\eta I_{sp_{2:1}} = \frac{306.2}{347.6} \times 100 = 88.1\%$$

Figure No. B-8 shows a plot of $\eta I_{sp_{2:1}}$ versus M.R.

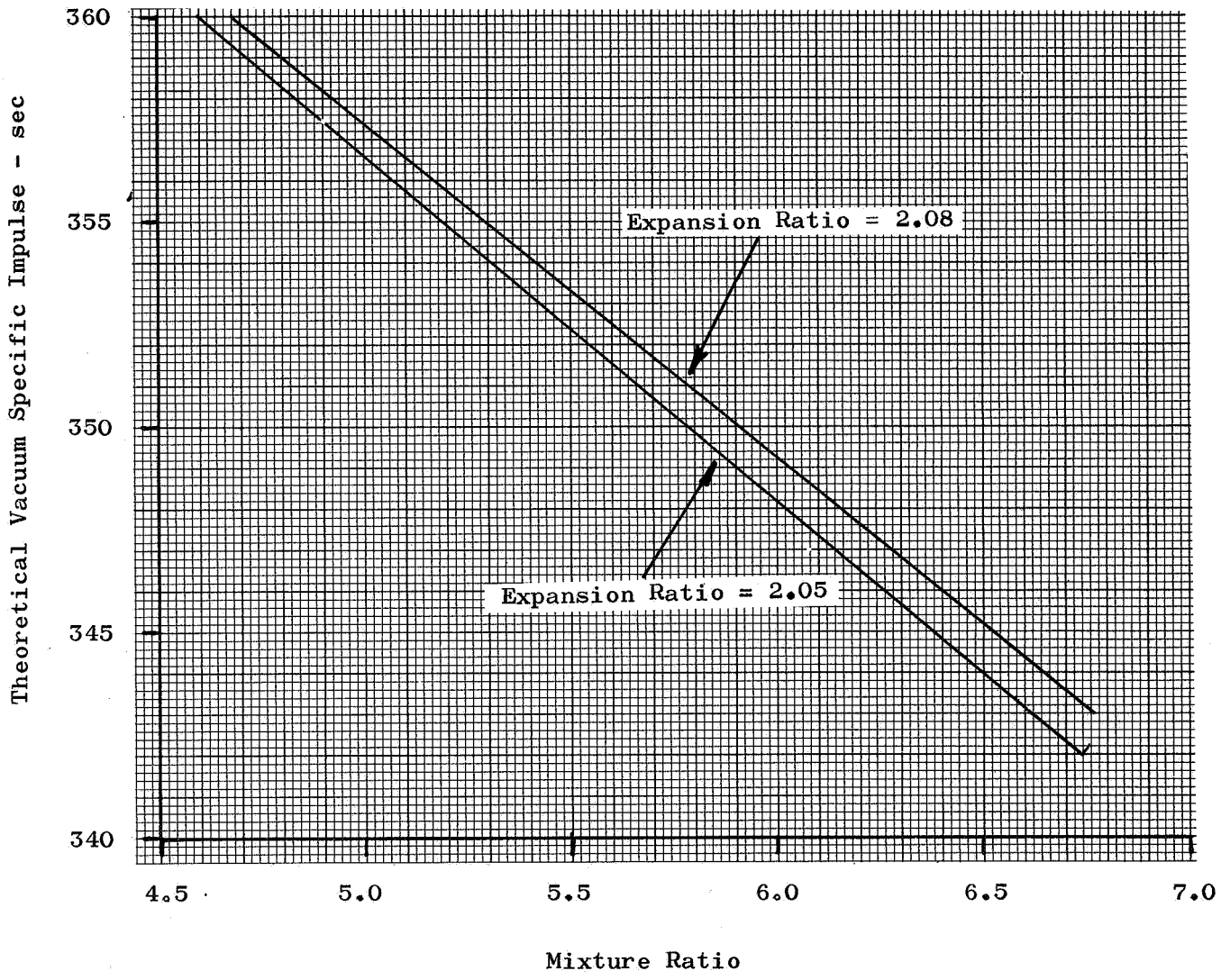


Figure B-6. Theoretical Vacuum Specific Impulse vs Mixture Ratio

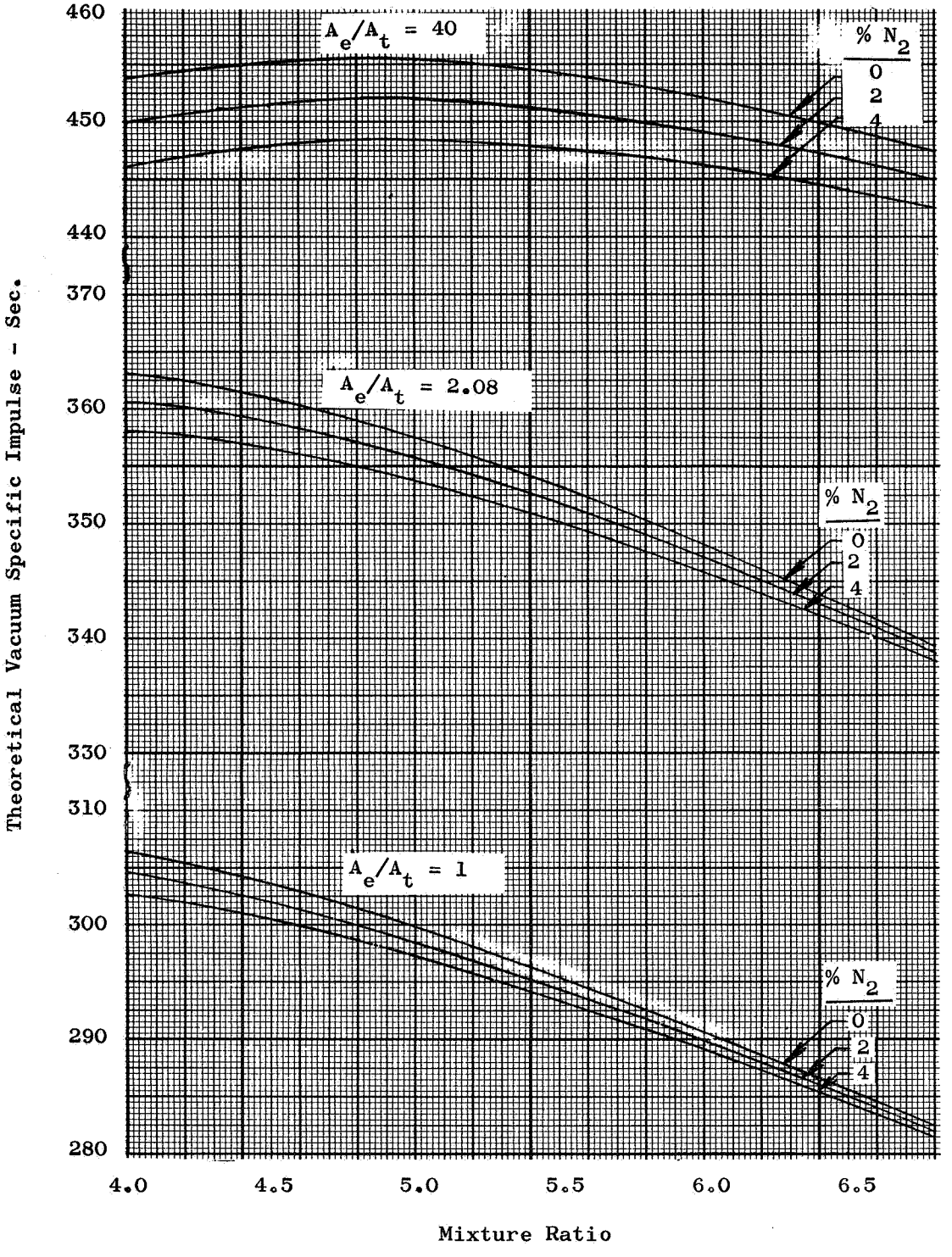


Figure B-7. Theoretical Vacuum Specific Impulse vs Mixture Ratio

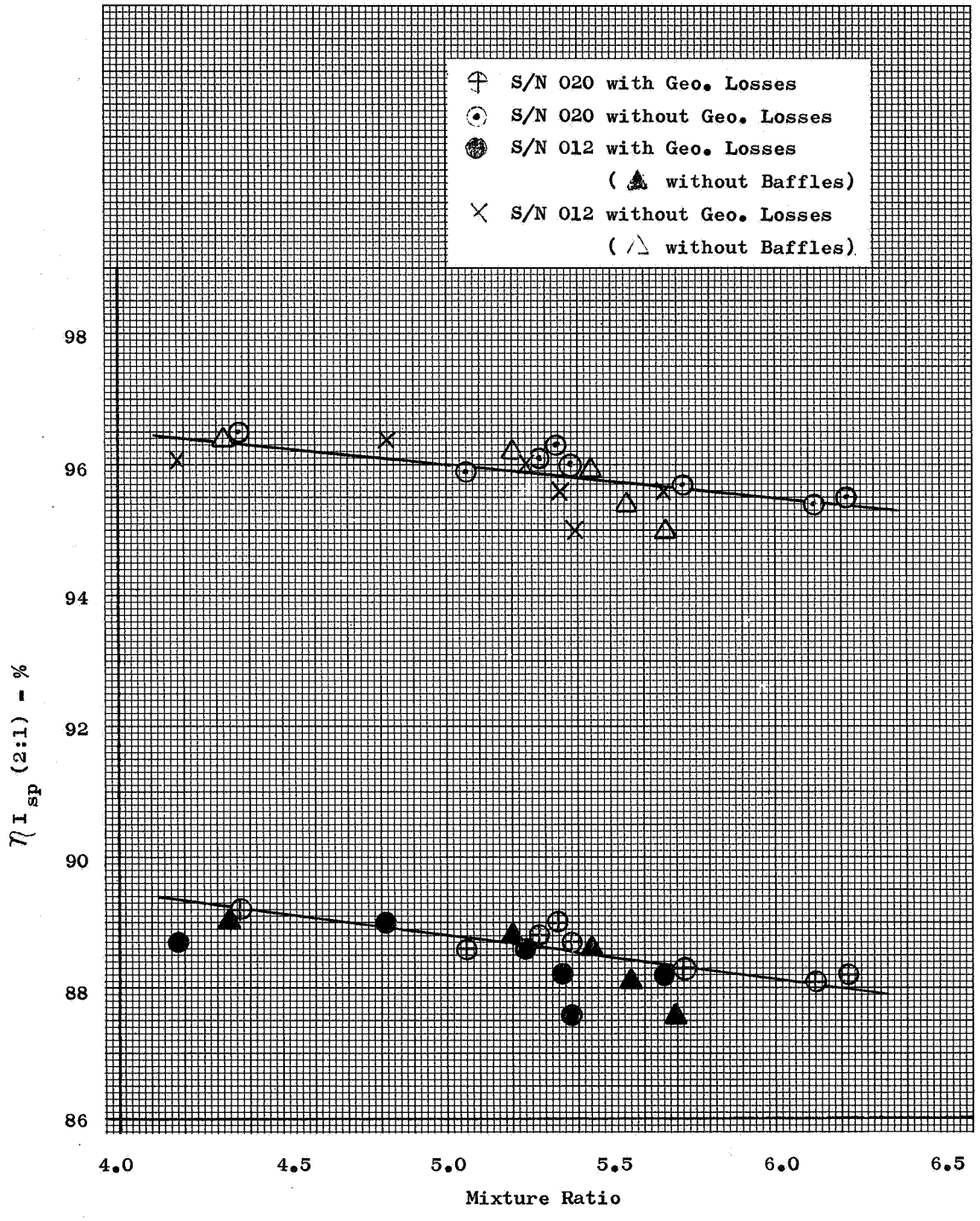


Figure B-8. $\eta I_{SP}$ (2:1) vs Mixture Ratio

44. $\eta C_{F_{2:1}}$ (from $P_c$) - Thrust coefficient efficiency at a 2:1 E.R. based upon $P_c$ is determined as follows:

$$\eta C_F \text{ (from } P_c) = 100 + \eta I_{sp} - \eta c^* \text{ (from } P_c) = 100 + \text{Item 43}$$

Item 34

$$\eta C_F \text{ (from } P_c) = 100 + 88.1 - 96.9 = 91.2\%$$

45. $\eta C_{F_{2:1}}$ (from nozzle losses) - Thrust coefficient efficiency at 2:1 expansion ratio based upon nozzle losses is determined as follows:

$$\eta C_F = \left(1 - \frac{\Delta I_{sp\ Nozzle}}{I_{sp\ Theo}}\right) = \left(100 - \frac{\text{Item 60}}{\text{Item 42}}\right)$$

$$\eta C_F = 1 - \frac{28.3}{347.6} = 91.9\%$$

46. $\eta C_{F_{2:1}}$ (from $P_c$ - w/o Geom) - Thrust coefficient efficiency based upon $P_c$ and without nozzle geometry loss is determined as follows:

$$\eta C_F = 100 + \eta I_{sp} \text{ (w/o Geom)} - \eta c^* \text{ (from } P_c)$$

$$\eta C_F = 100 + \text{Item 54} - \text{Item 34}$$

$$\eta C_F = 100 + 95.4 - 96.9 = 98.5\%$$

47. $\eta C_{F_{2:1}}$ (from nozzle losses - w/o Geom) - Thrust coefficient efficiency based upon nozzle losses and without nozzle geometry is determined as follows:

$$\eta C_F = 100 + \eta I_{sp} \text{ (w/o Geom)} - \eta c^* \text{ (from nozzle losses)}$$

$$\eta C_F = 100 + \text{Item 54} - \text{Item 35}$$

$$\eta C_F = 100 + 95.4 - 96.2 = 99.2\%$$

48. $I_{spVac}$ (Predicted 40:1) - Vacuum specific impulse at E.R. = 40 is predicted by extrapolating the energy release loss at E.R. = 2:1 to the throat and then scaling this loss up to E.R. = 40:1. The calculated geometry, friction, and mixture ratio distribution losses are added to the scaled-up energy release loss. This total loss is then subtracted from the theoretical, giving:

$$I_{sp_{VAC_{40:1}}} = 422.9 \text{ sec}$$

49. $I_{spVAC}$ (Theoretical, 40:1, h) - Theoretical vacuum specific impulse at E.R. = 40 and 6.12 M.R. From Figure No. B-7 and corrected for enthalpy:

$$I_{sp} = 451.5 \times 1.0037 = 453.2 \text{ sec}$$

50. $I_{spVAC}$ (Theoretical, 40:1, h, $N_2$) - Item 49 corrected for percentage of $N_2$ dilution. From Figure No. B-7, the net effect is 2.0 sec; therefore:

$$I_{sp} = 453.2 - 2.0 = 451.2 \text{ sec}$$

51. $\eta I_{sp_{40:1}}$ - Specific impulse efficiency at 40:1 E.R. defined as:

$$\frac{\text{Item 48}}{\text{Item 50}} = \frac{422.9}{451.2} \times 100 = 93.7\%$$

Figure No. B-9 is a plot of $\eta I_{sp_{40:1}}$ in relationship to mixture ratio.

52. $\eta C_{F_{40:1}}$ - Thrust coefficient efficiency at 40:1 E.R. determined as follows:

$$\eta C_F = 100 + \eta I_{sp_{40:1}} - \eta c^* \text{ (from nozzle losses)} =$$

$$100 + \text{Item 51} - \text{Item 35}$$

$$\eta C_F = 100 + 93.7 - 96.2 = 97.5\%$$

53. $I_{spVAC_{2:1}}$ (w/o Geom) - Item 39 plus the nozzle geometry loss (Item 60) at E.R. = 2:1

$$I_{sp} = 306.2 + 25.5 = 331.7 \text{ sec}$$

54. $\eta I_{spVAC_{2:1}}$ (w/o Geom) - $I_{sp}$ efficiency at 2:1 E.R. without nozzle geometry loss equals:

$$\frac{\text{Item 53}}{\text{Item 42}} = \frac{331.7}{347.6} \times 100 = 95.4\%$$

Figure No. B-8 shows a plot of $\eta I_{sp_{2:1}}$ (w/o Geom) in relationship to mixture ratio.

55, 59, and 64 Nozzle and Chamber Friction: This loss results from the viscous effects between the gaseous boundary layer and the nozzle or chamber wall.

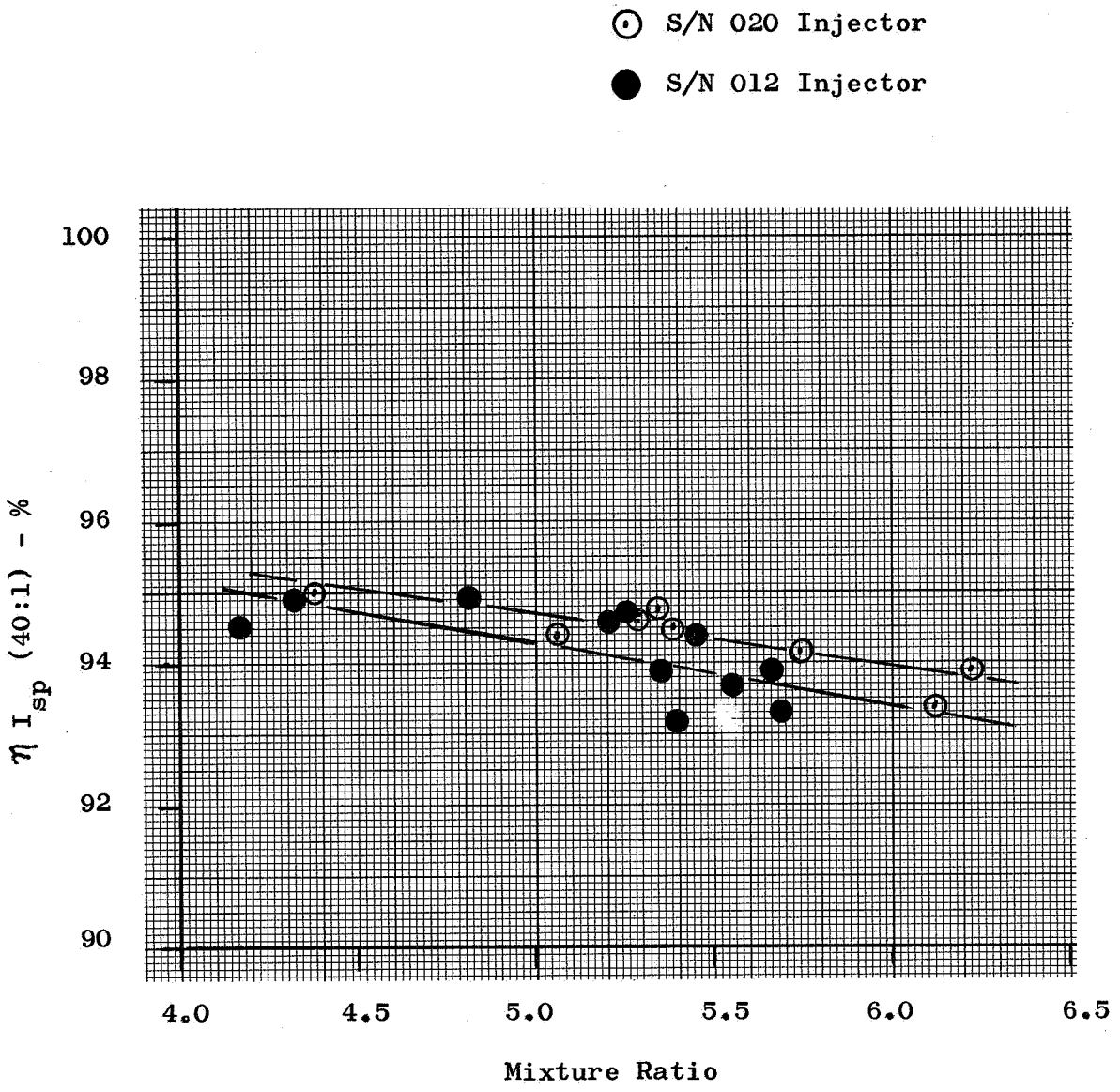


Figure B-9. $\eta I_{SP}$ (40:1) vs Mixture Ratio

56, 61, and 66. Mixture Ratio Distribution: This loss comprises both the performance loss resulting from irregular mixture ratio distribution across the injector face and the performance loss arising from heat transfer between the film coolant and the main stream propellants.

57, 62, and 67. Energy Release: This loss results because 100% combustion efficiency is not attained within fixed engine design limitations.

60 and 65. Nozzle Geometry: This loss can be attributed to the loss in thrust caused by the discharge coefficient of the throat and the loss in thrust resulting from non-axial exit momentum.

58. Subtotal chamber losses

63. Subtotal nozzle losses (E.R. = 2 to 1)

68. Subtotal nozzle losses (E.R. = 40 to 1)

69. Total losses (E.R. = 2) - Sum of chamber and nozzle losses at 2:1 E.R.

70. Total losses (E.R. = 40) - Sum of chamber and nozzle losses at 40:1 E.R.

# APPENDIX C

## SAMPLE CALCULATIONS

## FOR

## PERFORMANCE DURING TEMPERATURE DECREASE

6. TfJ Decrease Rate - Average slope of fuel injector temperature decrease between two data times.

7. TfJ - A plot of TfJ versus M.R. at instability is shown on Figure No. 43. Also shown is the TfJ at which stable operation reoccurs.

8. $\dot{W}_f$ Storage Factor - During a temperature decrease condition, the injector weight flow is less than the constant weight flow out of the mixer because of a decreasing volumetric flow rate from the mixer. Thus, a percentage of the fuel (this percentage is dependent upon the temperature ramp rate) is stored in the system during this temperature decrease condition. Figure No. C-1 was derived assuming a liquid fuel temperature of 50°R and a constant total fuel flow rate of 490 lb/sec from the mixer. This figure is a plot of % total fuel weight flow versus fuel injection temperature at varying temperature decrease rates. From Figure No. 41, at 120°R and 38.2°R/sec, the injector weight flow is .906 of the total measured weight flow.

10. $\dot{W}_f$ Injector - Fuel injector weight flow is equal to Item 8 multiplied by Item 9 which = .906 (544) = 495 lb/sec.

12. M.R. - Mixture Ratio

$$\text{Mixture Ratio} = \frac{\text{Item 11}}{\text{Item 10}} = \frac{2744}{495} = 5.55$$

22. A plot of $\eta I_{sp}$ versus TfJ is shown on Figure No. 41.

28. A plot $\eta C^*$ (from Pc) vs. fuel injection temperature is shown on Figure No. 42.

29. % $\dot{W}_f$ (element) - Portion of fuel weight flow flowing through fuel circuit of injection element (total fuel weight flow minus baffle, face and film coolant weight flows).

30. $V_f/V_o$ (element) - Injection element velocity ratio, fuel to oxidizer, determined as follows:

$$\frac{V_f}{V_o} = \frac{\dot{W}_f}{\dot{W}_o} \frac{\rho_o}{\rho_f} \frac{A_o}{A_f} = \frac{1}{\text{M.R.}} \times \frac{.04910 \text{ in.}^2}{.02125 \text{ in.}^2} \frac{\rho_o}{\rho_f} = \frac{2.31\ \rho_o}{\text{M.R.}\ \rho_f}$$

Where: $\text{M.R.} = \frac{\text{Item 12}}{\text{Item 29}}$

A plot of element $V_f/V_o$ versus fuel injection temperature at instability is shown on Figure No. 44. Table C-I shows $V_f/V_o$ vs. TfJ at instability for all stability tests.

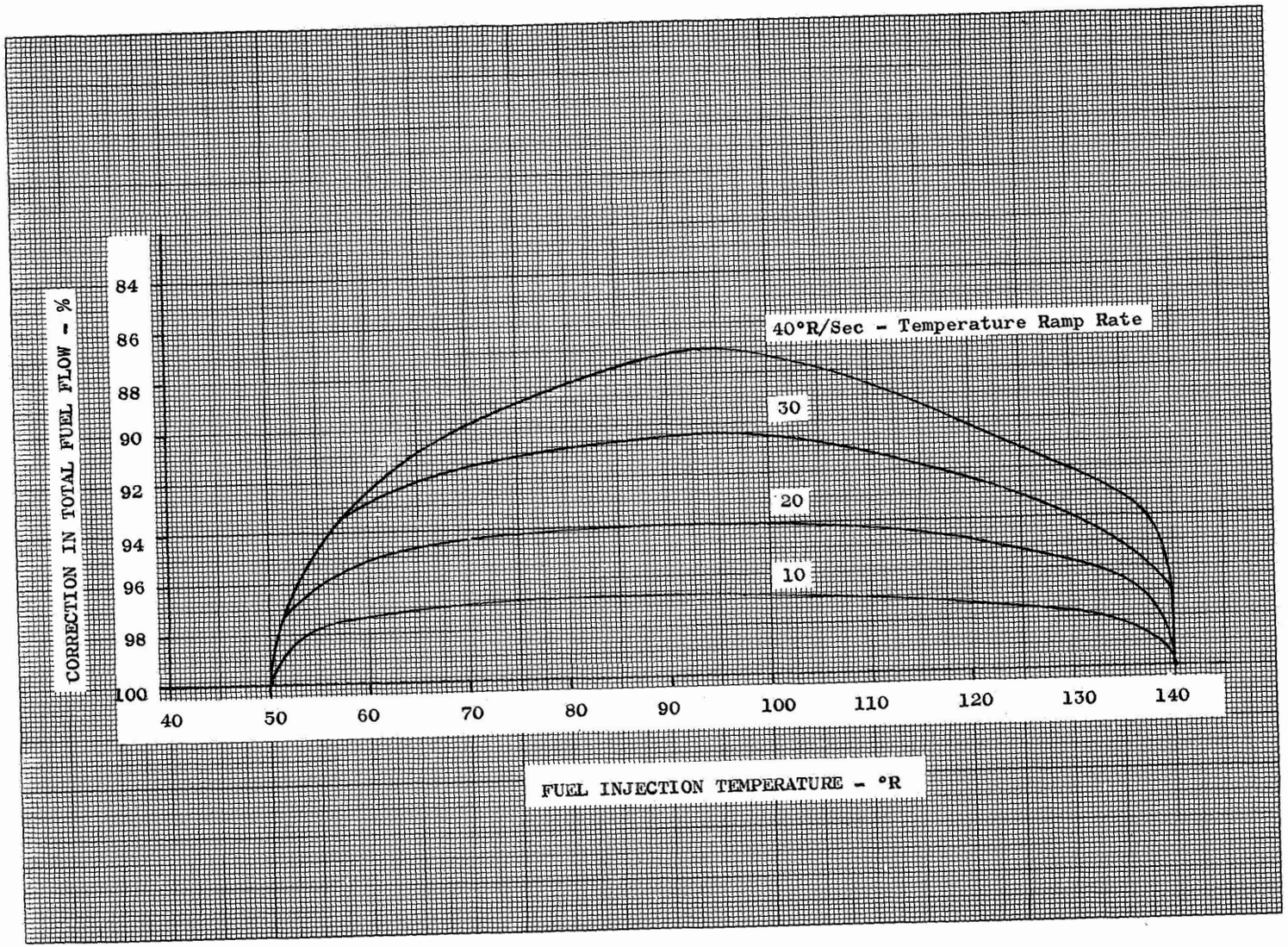


Figure C-1. Correction in Total Fuel Flow vs Fuel Injection Temperature

TABLE C-I

INJECTION ELEMENT VELOCITY RATIO AT INSTABILITY

| Test No. | % $W_f$ (element) | Temperature Decrease TFJ @ Instability °R | @ Instability Fuel | @ Instability Oxidizer | $V_f/V_o$ (element) | Remarks |
|---|---|---|---|---|---|---|
| 1.2-07-EHM 006 | 89.79 | 78.0 | 3.40 | 69.7 | 7.65 | Ablative Chamber - Long Baffles |
| -007 | 89.79 | 77.9 | 3.31 | 70.1 | 8.98 | " " |
| -008 | 89.79 | 77.8 | 3.38 | 70.4 | 7.14 | " " |
| -009 | 89.79 | 75.8 | 3.49 | 70.6 | 8.55 | " " |
| -010 | 89.79 | 81.8 | 3.25 | 70.3 | 8.15 | " " |
| -015B | 91.72 | 80.0 | 3.27 | 70.5 | 8.06 | Ablative Chamber - Short Baffles |
| -016 | 91.72 | 77.0 | 3.36 | 70.0 | 9.80 | " " |
| -019 | 81.79 | 85.0 | 3.02 | 68.4 | 8.13 | Steel Chamber - Long Baffles - Inserts |
| -020 | 81.79 | 77.3 | 3.42 | 69.1 | 7.41 | Inserts Chamber |
| -021 | 81.79 | 81.7 | 3.17 | 56.2 | 6.84 | Steel Chamber - Warm Oxygen |
| -022 | 81.79 | 85.4 | 2.98 | 61.8 | 7.27 | " " |
| -023 | 76.79 | 84.8 | 3.03 | 69.8 | 8.06 | Steel Chamber - No Inserts |
| -025 | 76.79 | 79.6 | 3.23 | 68.1 | 9.09 | " " |
| | | Temperature Increase | | | | |
| -009 | 89.79 | 102.7 | 2.15 | 70.4 | 15.87 | |
| -010 | 89.79 | 102.0 | 2.31 | 70.5 | 13.67 | |

# APPENDIX D

## HELIUM BLEED

## KISTLER TRANSDUCER SYSTEM

Calibration tests were made to reconstruct the true dynamic pressure seen by the 1.25-in. coupled transducers. These tests consisted of a shock tube perturbation of each transducer. A spectral analysis was then made of the frequency response of each transducer giving frequency and gain up to the resonant frequency. From this, it was possible to approximate the amplitude of the true chamber pressure signal. A gain curve for S/N 012 (used on Pc3A-M-(HK) in Test No. 008) is shown on Figure No. D-1. This gain curve could have changed slightly during the actual hot test firings. How much the transducer resonance frequency can change during a test is a function of the amount that the helium bleed tube is burned off (shortened), the area change of the tube opening, and the thermal shift of the transducer itself. The tube length change for the entire test series is given on Table D-I but it is never greater than a 20% reduction in length. The open end tube area was not measured, but its effect would drive the resonant frequency down in all cases. The resonance frequency, as calculated by the Helmholtz formula, is given below.

$$f_r = \frac{C}{2} \frac{A}{V e}$$

where:

$f_r$ = resonant frequency (cps)

C = speed sound (in./sec)

A = area of opening ($in.^2$)

V = volume of resonator ($in.^3$)

e = effective length (in.)

This indicates that the frequency of the transducer resonance can either increase a maximum of 20% (from tube length reduction) or decrease significantly (from open end area reduction), possibly to zero, if the tube closes entirely. Another source of variation is the conversion of nitrogen shock tube test data to hot helium of the actual transducer environment. The number used is 2.65 (the ratio of molecular weights), which assumes the gases to be at the same temperature. However, in actual hot tests, the helium will be at some elevated temperature which increases the $f_r$ slightly. The possible limits of the $f_r$ are considered because it adds credibility to estimating what frequency (sometimes, a drifting one) is the true resonance of the transducer system. Another factor in determining which resonant peak belongs to the transducer system is the consistency and continuity of the frequency throughout the run; that is, before the instabilities as well as during them. If one frequency occurs during the entire run, it is more likely the transducer resonance than a frequency that appears only with the increased combustion activity.

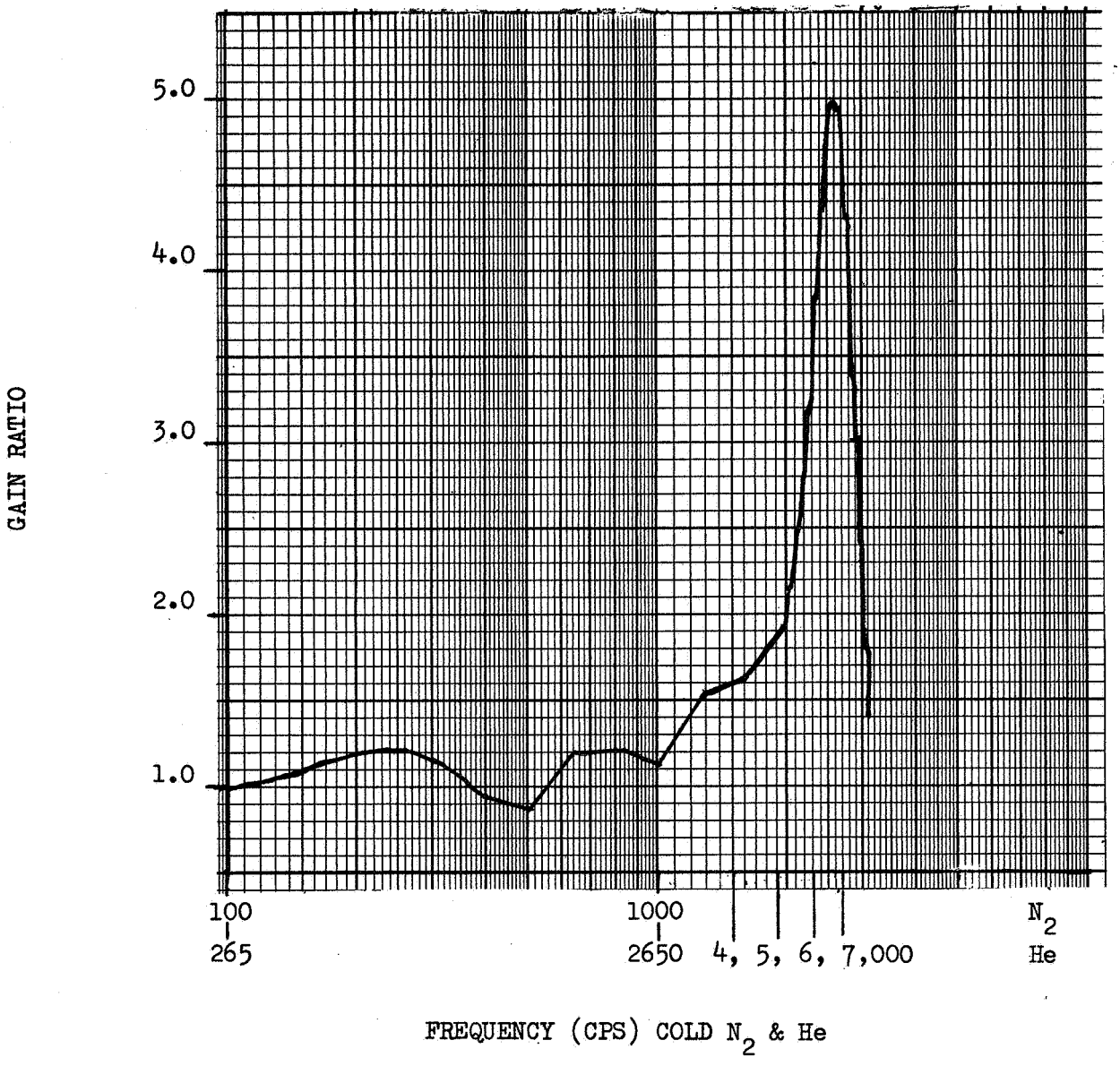


Figure D-1. Gain Ratio vs Frequency

TABLE D-I

M-1 HELIUM-BLEED TRANSDUCERS
(SHOCK TUBE CALIBRATIONS)

| Helium Bleed P/N | Helium Bleed S/N | KIB S/N | Calibr. Date | Calibr. Gas | $GN_2$-fr (1) (cps) | He-fr (2) (cps) | Calculated (3) fr-$GN_2$ (cps) | Tube Length (in.) | Tube Length After Test 1.2-07 EHM 050 |
|---|---|---|---|---|---|---|---|---|---|
| 1120921-9 | 001 | 16029 | 5-24-66 | $N_2$-$N_2$ | Calibr. | Invalid | - | 1.250 | - |
| " | 002 | 16227 | 3-3-66 | " | 2900 | 7675 | (2860) | 1.250 | 1.063 |
| " | 003 | 16210 | 3-3-66 | " | 2600 | 6880 | (2600) | " | - |
| " | 003 | 15033 | 5-24-66 | " | 1900 | 5030 | (1920) | " | - |
| " | 005 | 16124 | 5-24-66 | " | Bad Plot | 7550 | (2850) | " | - |
| " | 006 | 16197 | 3-3-66 | " | 2350 | 6220 | (2330) | " | 0.875 |
| " | 007 | 16194 | 5-24-66 | " | Bad Plot | 6700 | (2530) | " | 1.125 |
| " | 008 | 16218 | 5-24-66 | " | 3200 | 8470 | (2920) | " | 1.125 |
| " | 009 | 14313 | 5-24-66 | " | 2400 | 6350 | (2400) | " | 1.063 |
| " | 010 | 16202 | 3-3-66 | " | 2650 | 7020 | (2630) | " | 0.938 |
| " | 011 | 16230 | 3-3-66 | " | 2530 | 6700 | (2530) | " | 1.125 |
| " | 012 | 16589 | 3-3-66 | " | 2580 | 7420 | (2570) | " | - |
| " | 013 | 16206 | 3-3-66 | " | 2500 | 6620 | (2430) | " | 1.125 |
| " | 014 | 16213 | 5-24-66 | " | 2600 | 6880 | (2570) | " | - |

(1)Taken from computer plotted frequency response curve.
(2)He-fr = (2.65) ($GN_2$-fr) = He-He resonant frequency.
(3)Calculated from first 2 or 3 cycles of plotted transient response.

# APPENDIX E

## TYPICAL INSTRUMENTATION

## FOR INJECTOR TEST

Appendix E

TYPICAL INSTRUMENTATION-INJECTOR TEST

| FUNCTION | RANGE | AMPEX | ADC | VISUAL | STRIP CHART | BERKELEY | SANBORN | OSCILLOGRAPH R-1 | R-2 | R-3 | R-4 | R-5 | R-6 | REMARKS |
|---|---|---|---|---|---|---|---|---|---|---|---|---|---|---|
| | | | | | | | | TCA | Fuel | Seq | Oxid | SG | SG | |
| **1.0 $GN_2/LO_2$ SYSTEM** | | | | | | | | | | | | | | |
| **LOW FREQUENCY PRESSURES** | | | | | | | | | | | | | | |
| $P_gN_2B$ * | 0-5000 psig | | L | X | | | | | | | | | | |
| $P_gN_2PRVi$ * | 0-5000 psig | | L | X | | | | | | | X | | | |
| PoT-1 * | 0-2000 psig | | | | | | | | | | | | | Controls (tank top) |
| PoT-2 (M) * | 0-2000 psig | | M | | X | | | | | | X | | | Instr. (tank bottom) |
| PoFM (M) * | 0-2000 psig | | L | | | | | | | | | | | |
| PoTCV-1 (M) * | 0-2000 psig | | M | | X | | | X | | | | | | |
| PoTCV-2 (M) * | 0-2000 psig | | L | | | | | X | | | | | | |
| **DIFFERENTIAL PRESSURES** | | | | | | | | | | | | | | |
| $\Delta PgN_2F$ * | 0-5000 psid | | L | X | | | | | | | | | | Main $N_2$ filter |

| FUNCTION | RANGE | AMPEX | ADC | VISUAL | STRIP CHART | BERKELEY | SANBORN | OSCILLOGRAPH R-1 TCA | OSCILLOGRAPH R-2 Fuel | OSCILLOGRAPH R-3 Seq | OSCILLOGRAPH R-4 Oxid | OSCILLOGRAPH R-5 SG | OSCILLOGRAPH R-6 SG | REMARKS |
|---|---|---|---|---|---|---|---|---|---|---|---|---|---|---|
| **THERMOCOUPLES** | | | | | | | | | | | | | | |
| TgN2B * | ± 10 MV | | L | | | | | | | | | | | TCC |
| $TGN_2$PRVi * | ± 10 MV | | L | | | | | | | | | | | TCC |
| ToT-2 (M) * | ± 10 MV | | | | x | | | | | | | | | TCC (8 PT Brown) |
| ToTCV-2 (M) * | ± 10 MV | | L | | x | | | | | | | | | TCC, USH, 1/4" Immer |
| T LO2BD-2 * | ± 10 MV | | L | x | | | | | | | | | | TCC |
| T LO2BD-1 | ± 10 MV | | | | x | | | | | | | | | |
| T LO2-Dump | ± 10 MV | | | | x | | | | | | | | | |
| **RTT's** | | | | | | | | | | | | | | |
| ToFM-1 (M) * | -200 to -300°F | | L | | x | | | | | | | | | RTT, Code 1, Immer 1 to 1.5 |
| TOTCV-1 * | -200 to -300°F | | L | | x | | | | | | | | | Code "W" for cold flow |
| **FACILITY VALVES** | | | | | | | | | | | | | | |
| L-$LO_2$ Safety (M)* | Valve Trace | | | | | | | | | x | | | | |
| L-$LO_2$ TCA d (M)* | Valve Trace | | | | | | | | | x | | | | |
| L-$LO_2$ LPT b (M)* | Valve Trace | | | | | | | | | x | | | | |
| PwD | 0-500 psig | | | x | | | | | | | | | | $H_2O$ deluge press |
| $PLO_2$-BD-1 | 0-3000 | | | | | | | | | | x | | | Dump Valve upstream press |
| | | | | | | | | | | | | | | BD = Burst Disc |

| FUNCTION | RANGE | AMPEX | ADC | VISUAL | STRIP CHART | BERKELEY | SANBORN | OSCILLOGRAPH R-1 TCA | OSCILLOGRAPH R-2 Fuel | OSCILLOGRAPH R-3 Seq | OSCILLOGRAPH R-4 Oxid | OSCILLOGRAPH R-5 SG | OSCILLOGRAPH R-6 SG | REMARKS |
|---|---|---|---|---|---|---|---|---|---|---|---|---|---|---|
| **FLOWS** | | | | | | | | | | | | | | |
| FMO-1 (M)* | 0-4000 lb/sec $H_2O$ | | M | | x | x | | x | | | | | | |
| FMO-2 (M)* | 0-4000 lb/sec $H_2O$ | | M | | | x | | | | | | | | |
| $PLO_2$-Pitot | ± 50 psid | x | | | | | | | | | | | | |
| **LIQUID LEVEL** | | | | | | | | | | | | | | |
| $LO_2$ Cap Probe | continuous | | L | | | | | | | | | | | |
| **$LO_2$ SYSTEM MOVEMENT** | | | | | | | | | | | | | | |
| LNSS-Y | Position Tr | | | | | | x | | | | | | | $GN_2$ purge on ball joints Pots required |
| $LLO_2$LTS-X | Position Tr | | | | | x | | | | | | | | $GN_2$ purge on ball joints Pots required |
| **SOIL HEATERS** | | | | | | | | | | | | | | |
| ThFLPB | + 10 MV | | | | x | | | | | | | | | ) |
| ThFALPB | + 10 MV | | | | x | | | | | | | | | ) Temp of heater coils |
| ThOFV | + 10 MV | | | | x | | | | | | | | | )on various valves |
| ThFFV | + 10 MV | | | | x | | | | | | | | | ) |
| ThFHPB | + 10 MV | | | | | | | | | | | | | ) |

| FUNCTION | RANGE | AMPEX | ADC | VISUAL | STRIP CHART | BERKELEY | SANBORN | OSCILLOGRAPH R-1 TCA | OSCILLOGRAPH R-2 Fuel | OSCILLOGRAPH R-3 Seq | OSCILLOGRAPH R-4 Oxid | OSCILLOGRAPH R-5 | OSCILLOGRAPH R-6 | REMARKS |
|---|---|---|---|---|---|---|---|---|---|---|---|---|---|---|
| **2.0 $GH_2/LH_2$ SYSTEM** | | | | | | | | | | | | | | |
| **LOW FREQUENCY PRESSURES** | | | | | | | | | | | | | | |
| PgH2B * | 0-5000 psig | | L | x | | | | | | | | | | |
| $PGH_2$ PRVi * | 0-5000 psig | | L | x | | | | | x | | | | | |
| PfT-1A * | 0-2000 psig | | | | | | | | | | | | | Controls (tank top) |
| PfT-1B (M)* | 0-2000 psig | | M | | x | | | | x | | | | | Instr. (tank top) |
| PffM-2 (M)* | 0-2000 psig | | L | | | | | | x | | | | | Mixer inlet |
| PfMIX-0 (M)* | 0-2000 psig | | L | | | | | | x | | | | | |
| PfTCV-1 (M)* | 0-2000 psig | | M | | x | | | x | | | | | | |
| PfTCV-2 (M)* | 0-2000 psig | | L | | | | | x | | | | | | |
| PfT 850 psia | Switch Trace | | | | | | | x | | | | | | Computer Function |
| ΔPΔ | Switch Trace | | | | | | | x | | | | | | Computer Function (PoT > PfT) |
| PaTCFV | Switch Trace | | | | | | | x | | | | | | Computer Function |
| Pc200 psia | Switch Trace | | | | | | | x | | | | | | Computer Function |
| PfTS-1 | 0-2000 psig | | L | | | | | | | | | | | Upstream of safety valve |
| **HIGH FREQUENCY PRESSURES** | | | | | | | | | | | | | | |
| **DIFFERENTIAL PRESSURES** | | | | | | | | | | | | | | |
| ΔPgH2F * | 0-2000 psid | | L | x | | | | | | | | | | Main $GH_2$ Filter |
| ΔPLH2 (pitot) B (M) * | 0-20 psid | x | | | | | | | | | | | | |
| ΔPLH2 (pitot) -A | 0-20 psid | | | | | | | | | | | | | Controls |

| FUNCTION | RANGE | AMPEX | ADC | VISUAL | STRIP CHART | BERKELEY | SANBORN | OSCILLOGRAPH R-1 TCA | OSCILLOGRAPH R-2 Fuel | OSCILLOGRAPH R-3 Seq | OSCILLOGRAPH R-4 Oxid | OSCILLOGRAPH R-5 | OSCILLOGRAPH R-6 | REMARKS |
|---|---|---|---|---|---|---|---|---|---|---|---|---|---|---|
| **THERMOCOUPLES** | | | | | | | | | | | | | | |
| $TGH_2PRVi$ * | ± 10MV | | LL | | | | | | | | | | | TCC |
| TfT-2 (M)* | + 200°F to - 435°F | | | | x | | | | | | | | | TCC (1/4" Immer) (8 pt Brown) |
| TfTCV-2 (M)* | + 10MV | | M | | x | | | | | | | | | TCC |
| $T\text{-}LH_2\text{-}T$ | Direct Reading | | | | Spt | | | | | | | | | TCC skin temp. |
| **RTT's** | | | | | | | | | | | | | | |
| TffM-1 (M)* | -300 to -435 | | L | | x | | | | | | | | | RTT Code N |
| TfTCV-1 (M)* | +75 to -435 | | L | | x | | | | | | | | | RTT Code L PC12 Function (Range as necessary for cold flow) |
| TSDFTCV-1 | ST #31 | | | | | | | | x | | | | | Pc 12 temp. kills |
| **FACILITY VALVES** | | | | | | | | | | | | | | |
| L-LH2 Safety (M)* | Valve Trace | | | | | | | | | x | | | | |
| LICV | Valve Trace | | | | | | | | | x | | | | |
| FLPBVS-1 | Switch Trace | | | | | | | | | x | | | | |
| FLPBVS-2 | Switch Trace | | | | | | | | | x | | | | |
| **FLOWS** | | | | | | | | | | | | | | |
| FMF-1 (M)* | 10,000 lb/ sec $H_2O$ | | L | | x | x | | x | | | | | | |
| FMF-2 (M)* | 10,000 lb/ | | M | | | x | | | x | | | | | |

| FUNCTION | RANGE | AMPEX | ADC | VISUAL | STRIP CHART | BERKELEY | SANBORN | OSCILLOGRAPH R-1 TCA | OSCILLOGRAPH R-2 Fuel | OSCILLOGRAPH R-3 Seq | OSCILLOGRAPH R-4 Oxid | OSCILLOGRAPH R-5 | OSCILLOGRAPH R-6 | | REMARKS |
|---|---|---|---|---|---|---|---|---|---|---|---|---|---|---|---|
| **LIQUID LEVEL** | | | | | | | | | | | | | | | |
| $LH_2$ Cap Probe * | Continuous | | L | | | | | | | | | | | | |
| **3.0 MIXER SYSTEM LOW FREQUENCY PRESSURES** | | | | | | | | | | | | | | | |
| PgH2MixPRV-i * | 0-5000 psig | | L | x | | | | | x | | | | | | |
| PgH2Mix-i (M)* | 0-3000 psig | | L | | | | | | x | | | | | | |
| **HIGH FREQUENCY PRESSURES** | | | | | | | | | | | | | | | |
| **DIFFERENTIAL PRESSURES** | | | | | | | | | | | | | | | |
| PgH2Mix F | 0-4000 psid | | | x | | | | | x | | | | | | Mixer filter |
| PgH2Mix (Pitot) (M)* | 0-50 psid | | Hi | | | | | | x | | | | | | |
| **THERMOCOUPLES** | | | | | | | | | | | | | | | |
| TgH2MixPRV-i | ± 10 mv | | LL | | | | | | | | | | | | TCA |
| TgH2Mix(Pitot)(M)* | ± 10 mv | | LL | | | | | | | | | | | | TCA |

| FUNCTION | RANGE | AMPEX | ADC | VISUAL | STRIP CHART | BERKELEY | SANBORN | OSCILLOGRAPH R-1 TCA | OSCILLOGRAPH R-2 Fuel | OSCILLOGRAPH R-3 Seq | OSCILLOGRAPH R-4 Oxid | OSCILLOGRAPH R-5 | OSCILLOGRAPH R-6 | REMARKS |
|---|---|---|---|---|---|---|---|---|---|---|---|---|---|---|
| MIXER SYSTEM MOVEMENT | | | | | | | | | | | | | | |
| 4.0 TCV ACTUATION SYSTEM | | | | | | | | | | | | | | |
| PaTCOV-O (M)* | 0-4000 psig | | L | x | | | | | | x | | | | |
| PaTCOV-C (M)* | 0-4000 psig | | L | x | | | | | | x | | | | |
| PaTCFV-O (M)* | 0-4000 psig | | L | x | | | | | | x | | | | |
| PaTCFV-C (M)* | 0-4000 psig | | L | x | | | | | | x | | | | |
| PaTCOVBB-O (M)* | 0-4000 psig | | L | x | | | | | | x | | | | |
| PaTCOVBP-C (M)* | 0-4000 psig | | L | x | | | | | | x | | | | |
| 5.0 TCV SYSTEM | | | | | | | | | | | | | | |
| LTCOV (M)* | Valve Trace | | x | | | | x | x | | x | x | | | |
| LTCOV-BP (M)* | Valve Trace | | x | | | | x | x | | x | x | | | |
| TCOVS-2 (M)* | Switch Trace | | | | | | | | | x | x | | | |
| TCOVBPS-2 (M)* | Switch Trace | | | | | | | | | x | | | | |
| TCOVPV-1 (M)* | Current Trace | | | | | | | | | x | | | | |
| TCOVPV-2 (M)* | Current Trace | | | | | | | | | x | | | | |
| TCOVBPPV-1 (M)* | Current Trace | | | | | | | | | x | | | | |
| TCOVBPPV-2 (M)* | Current Trace | | | | | | | | | x | | | | |
| E-ALTCV-O | ST #40 | | | | | | | | | | x | | | |
| E-ALTCV-F | ST-#32 | | | | | | | | x | | | | | |
| LTCFV (M)* | Valve Trace | | x | | | | x | x | x | x | | | | |
| TCFVS-1 (M)* | Switch Trace | | | | | | x | | x | x | | | | |
| TCFVS-2 (M)* | Switch Trace | | | | | | | | | x | x | | | |
| TCFVPV-1 (M)* | Current Trace | | | | | | | | | x | | | | |
| TCFVPV-2 (M)* | Current Trace | | | | | | | | | x | | | | |
| LMPRVS | Switch Trace | | | | | | x | | | | | | | Controls switch trace |

| FUNCTION | RANGE | AMPEX | ADC | VISUAL | STRIP CHART | BERKELEY | SANBORN | OSCILLOGRAPH R-1 TCA | OSCILLOGRAPH R-2 Fuel | OSCILLOGRAPH R-3 Seq | OSCILLOGRAPH R-4 Oxid | OSCILLOGRAPH R-5 | OSCILLOGRAPH R-6 | REMARKS |
|---|---|---|---|---|---|---|---|---|---|---|---|---|---|---|
| **6.0 PURGES OXIDIZER** | | | | | | | | | | | | | | |
| PoTCAP-LP * | 0-50 psig | | | x | | | | | | | | | | Moisture Preventive purge |
| PoTCAPHP-1 (M)* | 0-4000 psig | | L | x | | | | | | | | | | Downstream of purge regulator |
| TCOPV-1 (M)* | Switch Trace | | | | | | | | | | x | | | |
| TCOPV-2 (M)* | Switch Trace | | | | | | | | | | x | | | |
| **FUEL** | | | | | | | | | | | | | | |
| PgHeB * | 0-5000 psig | | L | x | | | | | | | | | | |
| PfTCAP-LP * | 0-50 psig | | | x | | | | | | | | | | Moisture preventive purge |
| TCFPV (M)* | Switch Trace | | | | | | | | x | | | | | |
| **7.0 PRV FUNCTIONS** | | | | | | | | | | | | | | |
| **GN2** | | | | | | | | | | | | | | |
| LoPRV * | Valve Trace | | M | | | | x | | | | | | | |
| ERO * | Voltage Trace | | | | | | x | | | | x | | | Voltage, Tank Ramp Command |
| PgN2ACC * | 0-4000 psig | | | x | | | | | | | | | | |
| PhD * | 0-4000 psig | | L | x | | | | | | | | | | |
| **GH2** | | | | | | | | | | | | | | |
| LfPRV * | Valve Trace | | M | | | | x | | x | | | | | |
| ERF * | Voltage Trace | | | | | | x | | x | | | | | Voltage, Tank Ramp |

| FUNCTION | RANGE | AMPEX | ADC | VISUAL | STRIP CHART | BERKELEY | SANBORN | OSCILLOGRAPH R-1 TCA | OSCILLOGRAPH R-2 Fuel | OSCILLOGRAPH R-3 Seq | OSCILLOGRAPH R-4 Oxid | OSCILLOGRAPH R-5 | OSCILLOGRAPH R-6 | REMARKS |
|---|---|---|---|---|---|---|---|---|---|---|---|---|---|---|
| GH2 Mix | | | | | | | | | | | | | | |
| L Mix PRV | Valve Trace | | M | | | | x | | x | | | | | |
| EPM | Voltage Trace | | | | | | x | | x | | | | | Error signal, $GH_2$ mix PRV voltage, Mix PRV Ramp |
| EMC | Voltage Trace | | | | | | | | x | | | | | |
| EMFB | | | | | | | x | | x | | | | | Voltage, mix feedback |
| 8.0 THRUST MEASURING | | | | | | | | | | | | | | |
| FA (M)* | 0-2,000,000 lbs | x | M | | x | | | x | | | | | | Filter required 5 cps |
| FB (M)* | 0-2,000,000 | x | M | | | | | x | | | | | | Filter required 5 cps |
| LTMTO | ± 1-in. | | | | | | x | | | | | | | |
| FRFA (M)* | 0-2,000,000 lbs | | L | | | | | | | | | | | |
| FRFB (M) | 0-2,000,000 | | L | | | | | | | | | | | |
| 9.0 TCA LOW FREQUENCY PRESSURES | | | | | | | | | | | | | | |
| PoTCVS-1 * | 0-2000 psig | | M | | | | | x | | | | | | |
| PoJ-1A (M)* | 0-2000 psig | | M | | x | | | x | | | x | | | |
| PoJ-2A (M)* | 0-2000 psig | | L | | | | | x | | | | | | |
| PoJ-4Ai * | 0-2000 psig | | | | | | | x | | | | | | |
| PCVP-1 | 0-2000 psig | | L | | | | | | | | | | | |
| PCVP-2 | 0-2000 psig | | L | | | | | | | | | | | |
| PCVP-3 | 0-2000 psig | | L | x | | | | | | | | | | |
| PCV-4 | 0-2000 psig | | L | x | | | | | | | | | | |

| FUNCTION | RANGE | AMPEX | ADC | VISUAL | STRIP CHART | BERKELEY | SANBORN | OSCILLOGRAPH R-1 TCA | OSCILLOGRAPH R-2 Fuel | OSCILLOGRAPH R-3 Seq | OSCILLOGRAPH R-4 Oxid | OSCILLOGRAPH R-5 | OSCILLOGRAPH R-6 | REMARKS |
|---|---|---|---|---|---|---|---|---|---|---|---|---|---|---|
| PfTCVS-1 * | 0-2000 psig | | M | | | | | x | | | | | | |
| PfJ-1B (M)* | 0-2000 psig | | MZ | | x | | | x | | | | | | |
| PfJ-3A (M)* | 0-2000 psig | x | L | | | | | x | x | | | | | LF CSM |
| PfCO-1B | 0-2000 psig | | M | | | | | x | | | | | | Use TfOA boss |
| Pc5D-1 (M)* | 0-1500 psig | | M | | x | | | x | x | | x | | | |
| Pc5D-2 (M) | 0-1500 psig | | M | | x | | | x | x | | x | | | |
| **10.0 TCA HIGH FREQUENCY PRESSURES** | | | | | | | | | | | | | | |
| PoJ-2B M(K)(M)* | 0-3000 psig PK to PK | x | | | | | | | | | | | | Kistler |
| PfJ-2B M(K)(M)* | PK to PK | x | | | | | | | | | | | | Kistler |
| Pc4C M(K) (M)* | PK to PK | x | | | | | | | | | | | | Kistler (CSM HF) ** |
| Pc4A M(HK) (M)* | PK to PK | x | | | | | | | | | | | | Kistler ** |
| Pc-2A-M(HK) (M)* | PK to PK | x | | | | | | | | | | | | Kistler ** |
| Pc-3A M(HK) (M)* | PK to PK | x | | | | | | | | | | | | Kistler ** |
| Pc-4B M(HK) (M)* | PK to PK | x | | | | | | | | | | | | Kistler |
| Pfi-HDF(K) | PK to PK | x | | | | | | | | | | | | |
| ** USE HELIUM BLEND KISTLER INSTEAD OF PHOTOCON ON ABLATIVE LINED CHAMBER | | | | | | | | | | | | | | |
| Pc-4D M(HK) (M)* | 0-300 psig PK to PK | x | | | | | | | | | | | | Kistler |
| **11.0 TCA THERMOCOUPLES** | | | | | | | | | | | | | | |
| TSoT-i | ± 10 mv | | L | | | | | | | | | | | ) Skin temps on oxid |
| TSoT-90° | ± 10 mv | | L | | | | | | | | | | | ) torus both C. A. ) skin temps. |

| FUNCTION | | RANGE | AMPEX | ADC | VISUAL | STRIP CHART | BERKELEY | SANBORN | OSCILLOGRAPH R-1 TCA | OSCILLOGRAPH R-2 Fuel | OSCILLOGRAPH R-3 Seq | OSCILLOGRAPH R-4 Oxid | OSCILLOGRAPH R-5 | OSCILLOGRAPH R-6 | REMARKS |
|---|---|---|---|---|---|---|---|---|---|---|---|---|---|---|---|
| TFI-1 | (M)* | ± 10 mv | | LL | | | | | | | | | | | TCA ) |
| TFI-2 | | ± 10 mv | | LL | | | | | | | | | | | TCA ) |
| TFI-3 | (M)* | ± 10 mv | | LL | | | | | | | | | | | TCA ) |
| TFI-4 | | ± 10 mv | | LL | | | | | | | | | | | TCA ) Shielded |
| TFI-5 | | ± 10 mv | | LL | | | | | | | | | | | ) temperature |
| TFI-5 | (M)* | | | | | | | | | | | | | | TCA ) rake |
| TFI-6 | | ± 10 mv | | LL | | | | | | | | | | | TCA ) |
| TFI-7 | (M)* | ± 10 mv | | LL | | | | | | | | | | | TCA ) |
| TFI-8 | | ± 10 mv | | LL | | | | | | | | | | | TCA ) |
| TFI-9 | (M)* | ± 10 mv | | LL | | | | | | | | | | | TCA |
| 12.0 TCA RIT'S | | | | | | | | | | | | | | | |
| ToTCVS-1 | * | -200 to - 300°F | | L | | | | | | | | | | | RFF, Code 1 Immer 1-in to 1.5-in cold flow only code "W" for cold flow. |
| ToJ-1B | (M)* | - 200 to - 300°F | | L | | | | | | | | | | | RFF, Code 1 Immer 1-in. to 1.5-in. cold flow only code "W" for cold flow. |
| ToJ-2A | * | - 200 to - 300°F | | L | | | | | | | | | | | RFF, Code 1 Immer 1-in. to 1.5-in. cold flow only code "W" for cold flow. |
| TfTCVS-1 | * | - 200°F to - 435°F | | L | | | | | | | | | | | RTT, Code W, Immer 1-in. to 1.5-in. |
| TfJ-1A | (M)* | - 200°F to - 435°F | | L | | | | | | | | | | | RTT, Code W, Immer 1-in. to 1.5-in. |
| TfJ-1B | * | - 200°F to - 435°F | | L | | | | | | | | | | | RTT, Code W, Immer 1-in. to 1.5-in. |
| 13.0 | | | | | | | | | | | | | | | |
| CSM LF | (M) | Sw Tr | | | | | | | x | | x | | | | |
| CSM | (M) | Sw Tr | | | | | | | x | | x | | | | |
| RSD | (M)* | Sw Tr | | | | | | | | | x | | | | |
| FS1 - FS2 | (M)* | Sw Tr | x | | | | x | | x | x | x | x | x | x | x With 17 bit time code |
| ESS | * | Sw Tr | | | | | | | | | x | | | | |
| FOPS | * | Sw Tr | | | | | | | | x | | | | | |

| FUNCTION | RANGE | AMPEX | ADC | VISUAL | STRIP CHART | BERKELEY | SANBORN | OSCILLOGRAPH R-1 TCA | OSCILLOGRAPH R-2 Fuel | OSCILLOGRAPH R-3 Seq | OSCILLOGRAPH R-4 Oxid | OSCILLOGRAPH R-5 | OSCILLOGRAPH R-6 | REMARKS |
|---|---|---|---|---|---|---|---|---|---|---|---|---|---|---|
| OOPS * | Sw Tr | | | | | | | | | | x | | | |
| 14.0 TCA ACCELEROMETERS | | | | | | | | | | | | | | |
| GTCA-X (LF) (M) | ± 10 g's | | | | | | | x | | | | | | Strain gage type (0-100 cps) |
| GTCA-Y (LF) (M) | ± 10 g's | | | | | | | x | | | | | | Strain gage type (0-100 cps) |
| GTCA-Z (LF) (M) | ± 10 g's | | | | | | | x | | | | | | Strain gage type (0-100 cps) |
| GoTCVS-X ) * | ± 10 g's | | | | | | | | | | x | | | Strain gage type (0-100 cps) |
| GoTCVS-Y )2(M)* | ± 10 g's | | | | | | | | | | x | | | Strain gage type (0-100 cps) |
| GoTCVS-Z ) * | ± 10 g's | | | | | | | | | | x | | | Strain gage type (0-100 cps) |
| GfTCVS-X ) * | ± 10 g's | | | | | | | | x | | | | | Strain gage type (0-100 cps) |
| GfGTCV-Y ) 2(M)* | ± 10 g's | | | | | | | | x | | | | | Strain gage type (0-100 cps) |
| GfTCVS-Z ) * | ± 10 g's | | | | | | | | x | | | | | Strain gage type (0-100 cps) |
| GTCA-X (HF)(M) | ± 200 g's | x | | | | | | | | | | | | Piezo Electric type |
| GTCA-Y (HF)(M) | ± 200 g's | x | | | | | | | | | | | | Piezo electric type |
| GTCA-Z (HF)(M) | ± 200 g's | x | | | | | | | | | | | | Piezo electric type |
| *Refers to combined systems $LN_2$ flow. | | | | | | | | | | | | | | |
| (M) Indicates parameter is mandatory to go into test. All other parameters may be individually considered for omission. | | | | | | | | | | | | | | |
| 15.0 STRAIN GAGES | | | | | | | | | | | | | | |
| STS-1A 120 ohm single leg G.F.2.10 | ± 2000 $\mu$ in | | | | | | | | | | | x | | Strain gage axial, north TCA support |
| STS-1B 120 ohm single leg G.F.2.10 | ± 2000 $\mu$ in | | | | | | | | | | | x | | Strut (located at |
| STS-1C 120 ohm single leg G.F.2.10 | ± 2000 $\mu$ in | | | | | | | | | | | x | | Strut longitudinal center & 90° circumferentially apart) |
| STS-1D 120 ohm single leg G.F.2.10 | ± 2000 $\mu$ in | | | | | | | | | | | x | | |

| FUNCTION | RANGE | AMPEX | ADC | VISUAL | STRIP CHART | BERKELEY | SANBORN | | OSCILLOGRAPH R-1 | R-2 | R-3 | R-4 | R-5 | R-6 | | REMARKS |
|---|---|---|---|---|---|---|---|---|---|---|---|---|---|---|---|---|
| STS-2A 120 ohm single leg G.F.2.10 | ± 2000 μ in | | | | | | | | | | | | x | | | Strain gage axial, |
| STS-2B 120 ohm single leg G.F.2.10 | ± 2000 μ in | | | | | | | | | | | | x | | | South . . . . |
| STS-2B 120 ohm single leg G.F.2.10 | ± 2000 μ in | | | | | | | | | | | | x | | | South . . . . |
| STS-2C 120 ohm single leg G.F.2.10 | ± 2000 μ in | | | | | | | | | | | | x | | | South . . . . |
| STS-2D 120 ohm single leg G.F.2.10 | ± 2000 μ in | | | | | | | | | | | | x | | | South . . . . |
| STM-1A 120 ohm single leg G.F.2.13 | 0-1000 μ in | | | | | | | | | | | | x | | | Strain gage axial, (Thrust |
| STM-1B 120 ohm single leg G.F.2.13 | 0-1000 μin | | | | | | | | | | | | x | | | Mount adapter, equally Spaced near test stand attach point) |
| STM-1D 120 ohm single leg G.F.2.13 | 0-1000 μin | | | | | | | | | | | | x | | | Spaced near test stand attach point) |
| SOI-1H | 0-2000 μin | | | | | | | | | | | | | x | | Strain gage, oxidizer inlet, tension force |
| SOI-1M | 0-2000 μin | | | | | | | | | | | | | x | | Strain gage, oxidizer inlet, tension force |
| SOI-3 | 0-2000 μin | | | | | | | | | | | | | x | | Strain gage, oxidizer inlet, tension force |
| SOI-5 | 0-2000 μin | | | | | | | | | | | | | x | | Strain gage, oxidizer inlet, tension force |
| SOI-6 | 0-2000 μin | | | | | | | | | | | | | x | | Strain gage, oxidizer inlet, tension force |
| SOI-7 | 0-2000 μin | | | | | | | | | | | | | x | | Strain gage, oxidizer inlet, tension force |
| SOI-8 | 0-2000 μin | | | | | | | | | | | | | x | | Strain gage, oxidizer inlet, tension force |
| SOI-9 | 0-2000 μin | | | | | | | | | | | | x | | | Strain gage, oxidizer inlet, tension force |
| SOI-10 | 0-2000 μin | | | | | | | | | | | | x | | | Strain gage, oxidizer inlet, tension force |
| SOI-11 | 0-2000 μin | | | | | | | | | | | | x | | | Strain gage, oxidizer inlet, tension force |

| FUNCTION | RANGE | AMPEX | ADC | VISUAL | STRIP CHART | BERKELEY | SANBORN | OSCILLOGRAPH R-1 | R-2 | R-3 | R-4 | R-5 | R-6 | REMARKS |
|---|---|---|---|---|---|---|---|---|---|---|---|---|---|---|
| SOI-MT | 0-2000 µin. | | | | | | | | | | | x | | Gages 12, 14, 15, 17 in bridge |
| SOI-AXIAL | 0-2000 µin. | | | | | | | | | | | | x | Gages 13 & 16 in bridge |
| SOI-18 | 0-2000 µin. | | | | | | | | | | | x | | Gages 13 & 16 in bridge |
| SOI-19 | 0-2000 µin. | | | | | | | | | | | x | | Strain gage, oxidizer inlet, tension force |
| SOI-20 | 0-2000 µin. | | | | | | | | | | | x | | Strain gage, oxidizer inlet, tension force |
| SOI-21 | 0-2000 µin. | | | | | | | | | | | | x | Strain gage, oxidizer inlet, tension force |
| SOI-22 | 0-2000 µin. | | | | | | | | | | | | x | Strain gage, oxidizer inlet, tension force |
| SOI-23 | 0-2000 µin. | | | | | | | | | | | | x | Strain gage, oxidizer inlet, tension force |
| SOI-24 | 0-2000 µin. | | | | | | | | | | | x | | Strain gage, oxidizer inlet, tension force |
| SOI-25 | 0-2000 µin. | | | | | | | | | | | x | | Strain gage, oxidizer inlet, tension force |
| SOI-26 | 0-2000 µin | | | | | | | | | | | x | | Strain gage, oxidizer inlet, tension force |
| SOI-27 | 0-2000 µin. | | | | | | | | | | | | x | Strain gage, oxidizer inlet, tension force |
| SOI-28 | 0-2000 µin. | | | | | | | | | | | | x | Strain gage, oxidizer inlet, tension force |
| SOI-29 | 0-2000 µin. | | | | | | | | | | | | x | Strain gage, oxidizer inlet, tension force |
| SOI-MR | 0-2000 µin. | | | | | | | | | | | x | | Gages #31, 34, 37, 40 |
| SOI-MZ | 0-2000 µin. | | | | | | | | | | | x | | Gages #32, 35, 38, 41 |
| SOI-43 | 0-2000 µin. | | | | | | | | | | | | | Gages #32, 35, 38, 41 |
| SOI-44 | 0-2000 µin. | | | | | | | | | | | | | Gages #32, 35, 38, 41 |
| SOI-46 | 0-2000 µin. | | | | | | | | | | | | x | Gages #32, 35, 38, 41 |
| SOI-47 | 0-2000 µin. | | | | | | | | | | | | x | Gages #32, 35, 38, 41 |
| SOI-48A | 0-2000 µin. | | | | | | | | | | | | x | Gages #32, 35, 38, 41 |
| SOI-49A | 0-2000 µin. | | | | | | | | | | | | x | Gages #32, 35, 38, 41 |
| SOI-50 | 0-2000 µin. | | | | | | | | | | | | x | Gages #32, 35, 38, 41 |
| SOI-51 | 0-2000 µin. | | | | | | | | | | | | x | Gages #32, 35, 38, 41 |
| Make the R-5 a reproducible graph | | | | | | | | | | | | | | |

| FUNCTION | RANGE | AMPEX | ADC | VISUAL | STRIP CHART | BERKELEY | SANBORN | OSCILLOGRAPH R-1 | R-2 | R-3 | R-4 | R-5 | R-6 | REMARKS |
|---|---|---|---|---|---|---|---|---|---|---|---|---|---|---|
| 16.0 CHAMBER EXIT PRESSURES | | | | | | | | | | | | | | |
| Pe 1A | 0-100 psig | | L | | | | | | | | | | | (M) For rated Pc and $\dot{W}$ tests |
| Pe 1B | 0-100 psig | | L | | | | | | | | | | | PeB's not req'd for tests below 90% pc. |
| 17.0 FLUORINE SYSTEM | | | | | | | | | | | | | | |
| PgHeM | 100 psig | | | x | | | | | | | | | | Pressure gas helium manifold |
| $PLN_2ST$ | 100 | | | x | | | | | | | | | | Pressure $LN_2$ supply tank |
| PgF2M | 1500 | | | x | | | | | | | | | | Pressure gas fluorine manifold |
| $PGF_2CT$ | 1500 | | | x | | | | | | | | | | Pressure gas fluorine condenser tank |
| $PGF_2L$ | 1500 | | L | x | x | | | | | | | | | Pressure gas fluorine line |
| $PgF_2i$ | 1000 | | M | | x | | | x | | | | | | Pressure gas fluorine ignition |
| PgHe V/TP | 1000 | | | x | | | | | | | | | | Pressure gas helium vent/tank purge |
| $TGF_2$ Burner | 0-2500°F | | | x | Pyrometer | | | | | | | | | |
| $TGF_2M$ | ± 10 mv | | | x | | | | | | | | | | |
| $TGF_2L$ | ± 10 mv | | LL | | | | | | | | | | | |
| $TGF_2i$ | ± 10 mv | | LL | | | | | | | | | | | |
| $TKN_2CT1$ | | | | x | | | | | | | | | | ) Temperature $LN_2$ |
| $LLN_2CT_2$ | $LN_2$ detector | | | x | | | | | | | | | | ) Condenser Tank Jacket |
| ICVPV | Switch tr. | | | | | | | | | x | | | | $LF_2$ Switch Traces |
| ICVS-2 | Switch tr. | | | | | | | | | x | | | | $LF_2$ Switch Traces |
| IMPVS-2 | Switch tr. | | | | | | | | | x | | | | $LF_2$ Switch Traces |
| EBR-WIRE | Switch tr. | | | | | | | | | x | | | | $LF_2$ Switch Traces |
| $TSF_2$-MAN | ± 10 mv | | L | | | | | | | x | | | | Skin Temp TCC |
| GSL-X | ± 50 g's | | | | | | | | | | x | | | $GN_2$ Support Strut |
| GSL-Y | ± 50 g's | | | | | | | | | | x | | | $GN_2$ Support Strut |

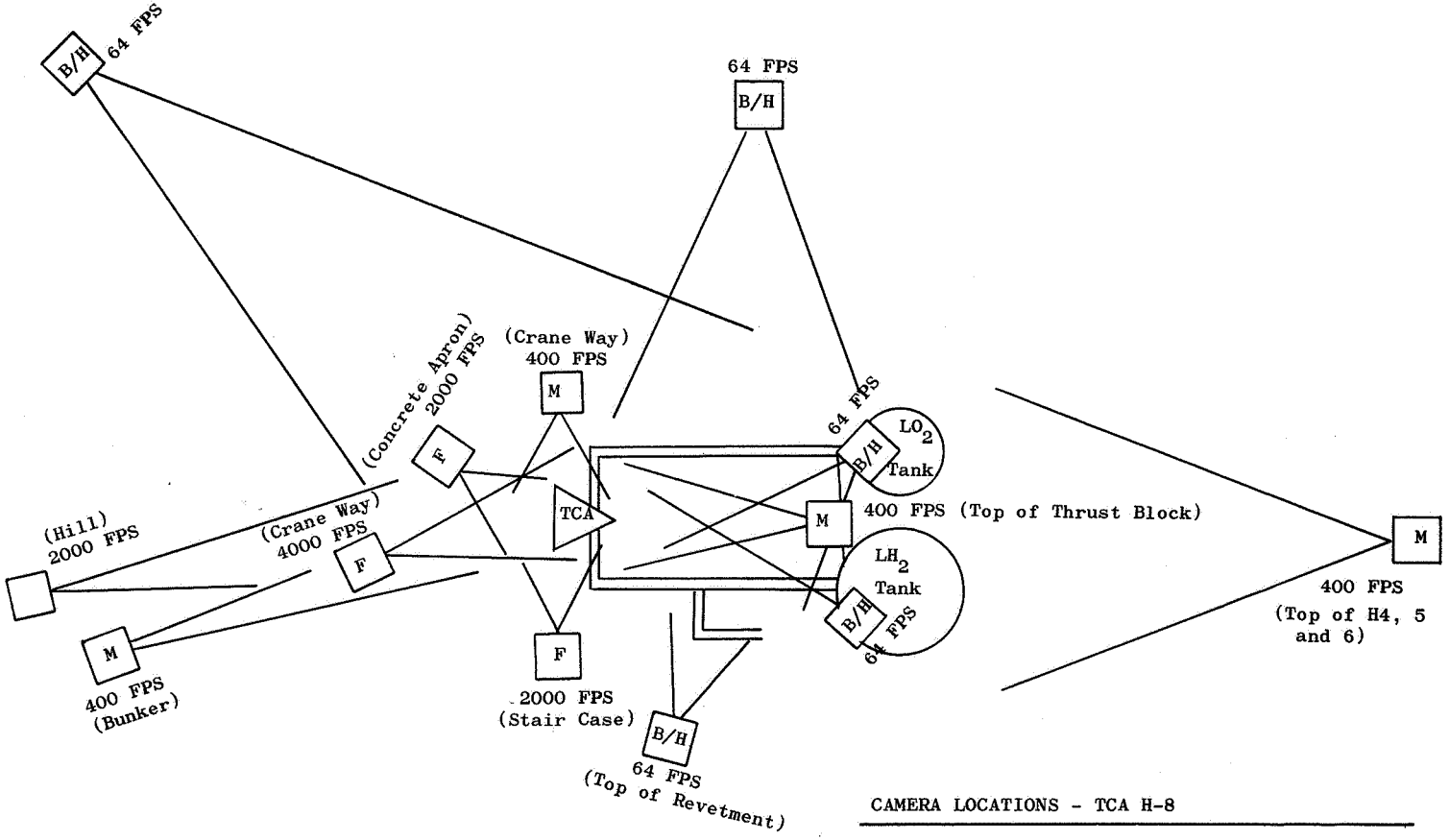


CAMERA LOCATIONS - TCA H-8

# APPENDIX F

## SAMPLE CALCULATION

## OF

## GASEOUS HYDROGEN VALVE POSITION VERSUS TIME

In this sample calculation, it was assumed:

- The hydrogen tank pressure would be pre-set at 600 psia.
- The motion of the hydrogen thrust chamber valve would be linear from initial travel to 100% in 2.0 sec.
- The gaseous hydrogen valve would be signalled from a 10% travel switch located on the fuel thrust chamber valve.
- The lines and injector manifolds would be filled and the thrust chamber valve approximately 20% open before the gaseous hydrogen flow is initiated (based upon the initial test attempt). This condition would be reached at 0.52 sec after fire-switch one ($FS_1$) (based upon valve reaction times and opening rates).

A gaseous hydrogen valve position versus time was selected as shown on Figure No. F-1. Flow will not be affected by downstream pressure because of the high pressure ($\cong$ 3400 psia) at the inlet of this valve as shown on Figure No. F-1. A time interval of 0.100 sec was selected for calculations because it appeared that flows could be averaged over this interval. Although a shorter interval would define the transient better, it would require increased calculation time.

While the average flow rate through the injector is assumed, the gaseous and liquid flows into the mixer are calculated. In addition, the flow through the injector is calculated, taking into account the propellant stored in the constant volume system between the mixer and the injector outlet. The calculation is reiterated until the calculated and assumed injector flows are equal. Then, the process is repeated for the next time interval.

An injector flow of 350 lb/sec is assumed for the first time interval between $FS_1$ + 0.52 sec and $FS_1$ + 0.62 sec. The average gaseous hydrogen flow, which was obtained from Figure No. F-1 by integrating the flow under the curve and dividing by the time interval, is approximately 6.6 lb/sec. To obtain the liquid flow into the mixer, it is necessary to calculate the pressure at the mixer.

The pressure at the mixer is obtained from the equation: P mix = $P_1$ inj. + $\Delta$P mixer to inj. ($P_1$ inj. = pressure at injector inlet).

It was apparent from the initial test attempt that the system was such that sonic flow was being experienced across the fuel injection annulus. To calculate the pressure at the injector inlet with sonic flow through the orifices, it is necessary to assume a value for the pressure at the inlet and the critical pressure ratio. Then, the resultant flow is computed. When the proper pressure is selected, the flow will be equal to the 350 lb/sec assumed initially. Because of the heat input by the surface downstream of the thrust chamber valve, it is assumed that the temperature at the injection orifice is 110°R.

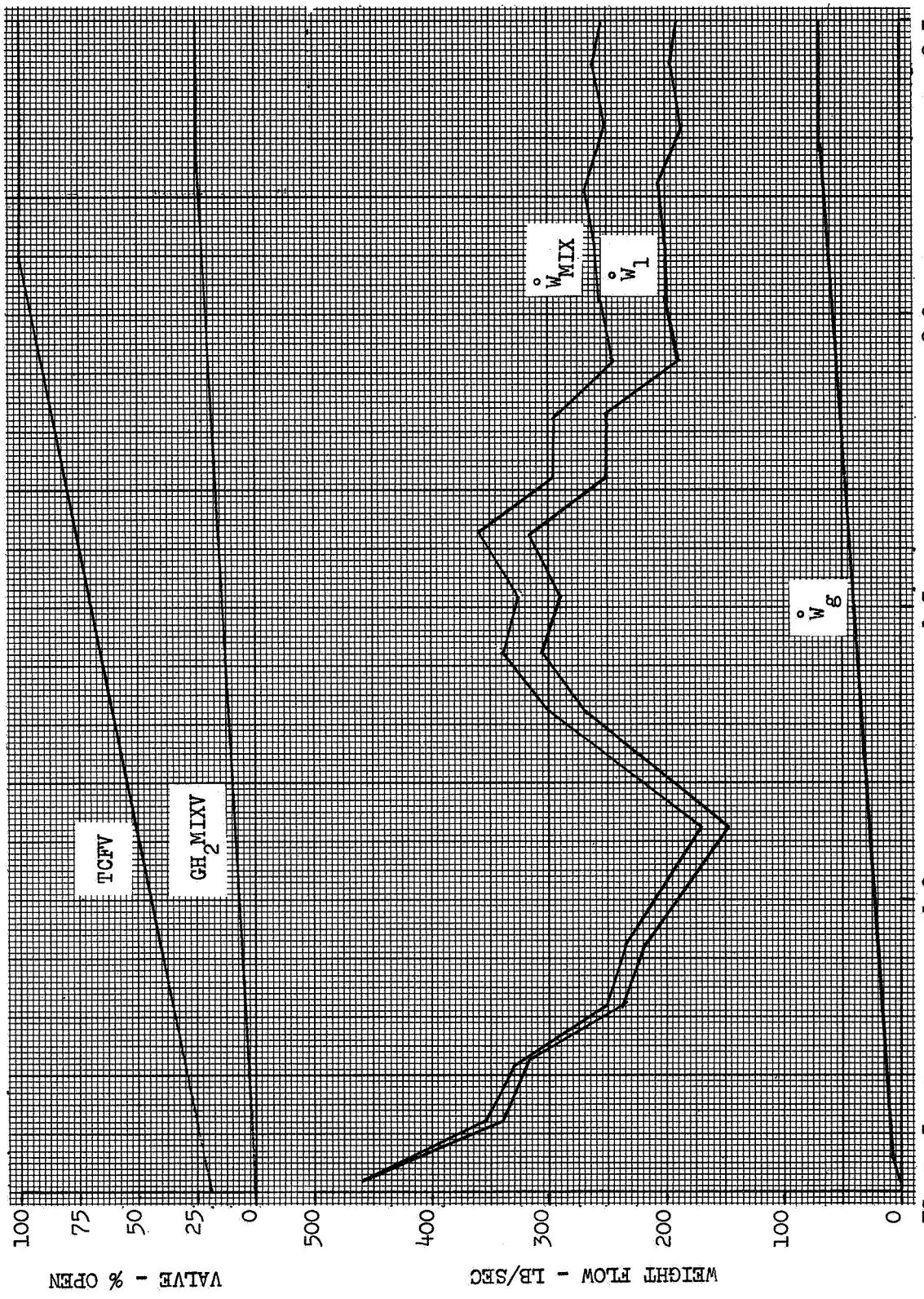


Figure F-1. Weight Flow and Valve Position vs Time

The pressure at the injector orifice inlet, $P_0$ inj., is assumed to be 350 psi and the pressure ratio $P_T$ inj/$P_0$ inj, where $P_T$ inj is the pressure at the orifice throat, is assumed to be 0.5. Thus, $P_T$ inj = 175 psig, and at 110°R the specific heat ratio, k, = 1.78. The pressure ratio is confirmed by

$$\frac{P_T \text{ inj}}{P_0 \text{ inj}}$$

$$\left(\frac{2}{k+1}\right)^{\frac{k}{k-1}} = 0.471 \tilde{=} 0.5.$$

The flow through the injector with sonic flow can be calculated from the equation:

$$\dot{W}_{inj} = \rho_s V_a A C$$

where:

$\rho_s$ = static density at throat

Va = acoustic velocity at throat

A = injector orifice throat area

C = flow coefficient = 0.8

$$\frac{\rho_s}{\rho_o \text{ inj}} = \left(\frac{2}{k+1}\right)^{\frac{1}{k-1}} = .656$$

and

$\rho_o$ inj @ 350 psia and 110°R = 0.66 lb/ft$^3$

therefore $\rho_s$ = 0.433 lb/ft$^3$

Va at 110°R and 175 psia = 2100 fps.

A = 77/144 feet$^2$

thus

$$\dot{W} \text{ inj} = (.433)\ (2100)\ (.535)\ (0.8) = 388 \text{ lb} \tilde{=} 350 \text{ lb/sec}$$

Some portion of the pressure drop through the injector is not in the orifice; therefore, it is reasonable to assume a pressure at the injector inlet of 350 psia.

The pressure drop from the mixer to the injector is calculated next. Water flow tests of the system had given values of Kw versus percent valve opening in the relationship $\dot{W}_{water} = K_w \sqrt{\Delta P \text{ water flow}}$. Thus, the pressure

drop from the mixer to the thrust chamber valve can be obtained from the equation:

$$\Delta P_{\text{mixer to inj.}} = \left( \frac{\dot{W}_{\text{fluid}}}{K_w} \right)^2 \frac{\rho_{\text{water}}}{\rho_{\text{fluid}}}$$

if the density of the fluid is obtained. To obtain the density of the fluid, 4.12 $lb/ft^3$, a pressure of 400 psia and temperature of 50°R, is assumed.

The pressure drop then becomes:

$$\Delta P_{\text{mixer to injector}} = \left( \frac{350}{132.7} \right)^2 \left( \frac{62.4}{4.12} \right) = 105 \text{ psia}$$

The pressure at the mixer, $P_{mix}$, $= P_{1\ inj} + \Delta P_{\text{mixer to injector}}$

$$= 350 + 105$$

$$= 455 \text{ psia.}$$

$$\text{with } \overline{P}_{\text{mixer to injector}} = \frac{455 + 350}{2} = 402 \overset{\sim}{=} 400 \text{ assumed.}$$

The weight flow of liquid from the tank similarly becomes:

$$\dot{W}_1 = K_{w\ \text{tank to mixer}} \sqrt{\left( P_{\text{tank}} - P_{\text{mixer}} \right) \frac{\rho_{\text{fluid}}}{\rho_{\text{water}}}}$$

$$= 110.4 \sqrt{(600 - 455) \left( \frac{4.2}{62.4} \right)}$$

$$= 347 \text{ lb/sec}$$

The next step is to calculate the change in weight of the fluid in the constant volume (44 $ft^3$) line between the mixer and the thrust chamber valve caused by changes in density. The weight of fluid$^{(W)}$ = volume of line$^{(V)}$ X density$^{(\rho)}$ of the fluid and the density is a function of pressure and temperature; therefore, an average pressure of the fluid between the mixer and the valve must be obtained. The injector is not included because the properties of the fluid in the injector will not change significantly during the interval.

The weight of liquid flow,

$$\dot{W}_1 \text{ @ } 0.520 \text{ sec} = K_{w_{\text{tank to } P_c}} \sqrt{\left(P_T - P_C\right)\left(\frac{\rho \text{ fluid}}{\rho \text{ water}}\right)}$$

$$= 74.4 \sqrt{(600-15)\quad \frac{4.09}{62.4}}$$

$$= 460 \text{ lb/sec}$$

where $\rho$ fluid is obtained at $\overline{P}_{\text{tank to } P_c} = \frac{600 + 15}{2} = 307$ psia

The pressure at the mixer can be calculated:

$$P_{mix} = P_T - \left(\frac{\dot{W}_1}{K_{w_{\text{tank to mixer}}}}\right)^2 \quad \left(\frac{\rho \text{ water}}{\rho \text{ fluid}}\right)$$

Assume average pressure between the tank and mixer is 170 psia and the temperature is 50°R, then $\rho$ fluid = 4.18 lb/ft$^3$, and

$$P_{mix} = 600 - \left(\frac{460}{110.4}\right)^2 \quad \left(\frac{62.4}{4.18}\right) \quad = 342 \text{ psia}$$

$$\overline{P}_{\text{tank to mixer}} = \frac{P_{\text{tank}} + P_{mix}}{2} = \frac{600 + 342}{2} = 471 \simeq 470$$

The weight of fluid contained between the mixer and the valve then equals:

W = Volume X $\rho$ 470 psia and 50°R = 44 x 4.05 = 178.2

The average pressure between the mixer and the valve is approximately equal to the pressure at the mixer because the line has very little pressure drop.

At $FS_1$ + 0.62 sec, the fluid stored in the line between the mixer and the valve is not homogeneous. That fluid just downstream of the mixer is warmer and thus, less dense than that at the valve because of the addition of the gaseous hydrogen. If complete mixing of the gas and liquid in the mixer is assumed, the temperature of this fluid can be obtained from an enthalphy chart if an enthalphy balance is made.

$\dot{W}_{mix} h_{mix} = \dot{W}_1 h_1 + \dot{W}_g$ hg where enthalphies are obtained at $P_{mix}$, Tg = 530°R, and $T_1$ = 50°R.

thus $353.6\ h_{mix} = (347)(-59) + 6.6\ (1812)$

and $h_{mix} = 24.1$

With the enthalpy and pressure of the mixture known, the temperature, $T_{mix}$, is obtained as 58°R. The density of this mixture is then, $\rho_{mix} = 3.73$ lb/ft$^3$. The volume occupied by this mixture which is formed in 0.1 sec is $V_{mix}$ =

$$\frac{.1\ (\dot{W}_l + \dot{W}_g)}{\rho_{mix}} = \frac{.1\ (347 + 6.6)}{3.73} = 9.48\ ft^3$$

Thus, the volume of the original propellant remaining in the line is equal (44 - 9.48) or 34.52 cu ft. As previously shown, the average pressure is 400 psia, the temperature is approximately 50°R, the density is 4.12 lb/ft$^3$, and the total weight of this fluid is 142 lb. Thus, the change in weight stored is 178.2 - (142 + 0.1 (347 + 6.6)) or 0.84 lb or 8.4 lb/sec equivalent flow rate. Because the weight stored at the end of the interval is less than that stored at the beginning, this weight has to pass through the injector. Thus, the weight flow rate through the injector becomes:

$$\dot{W}_{inj} = \dot{W}_l + \dot{W}_g + \Delta\dot{W}_{stored}$$

$$= 347 + 6.6 + 8.4$$

$$= 362 \text{ lb/sec}$$

As can be seen, this value is higher than the initially assumed weight flow of 350 lb/sec. Iteration is required until the assumed and calculated weight flows are equal.

These calculations are continued at 0.100 sec intervals until ignition occurs and chamber pressure begins to increase. In the subsequent calculations, the change in weight of hydrogen stored between the thrust chamber valve and injector caused by changes in pressure and temperature must be included. After ignition occurs, the flow of fuel and oxidizer must also be balanced to satisfy the relationship:

$$C^* = \frac{P_c\ A_{tg}\ \rho}{\dot{W}_{total}}$$

Figure No. F-1 and No. F-2 show flow rates and pressure in the hydrogen system for the sample problem case with a tank pressure of 600 psia. It can be noted on Figure No. F-2 that at approximately 1.9 sec, pressure in the mixer must equal tank pressure to achieve a system balance. If the mixer valve were to continue to open, flow reversal upstream of the mixer would result.

For the successful tests, a fuel tank pressure of 800 psia and a slower opening rate of the mixer valve were selected. Figures No. F-3 through No. F-5 show predicted versus actual values of hydrogen line parameters versus time. As can be seen, agreement is relatively good after $FS_1$ + 1.5 sec. Disagreements prior to this time are caused by a combination of differences in valve timings and initial conditions of the fluid in the line being other than assumed.

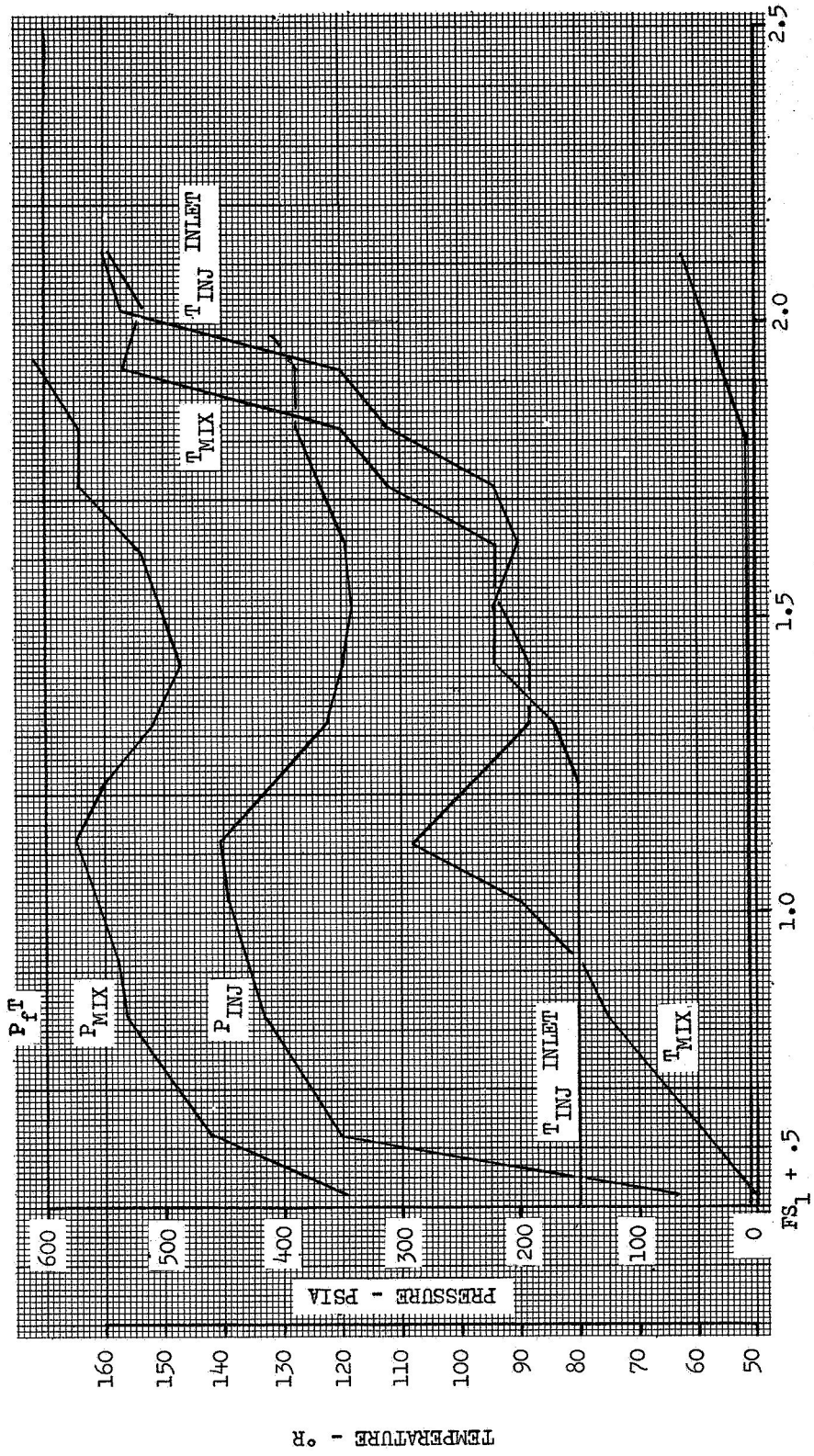


Figure F-2. Pressure and Temperature vs Time

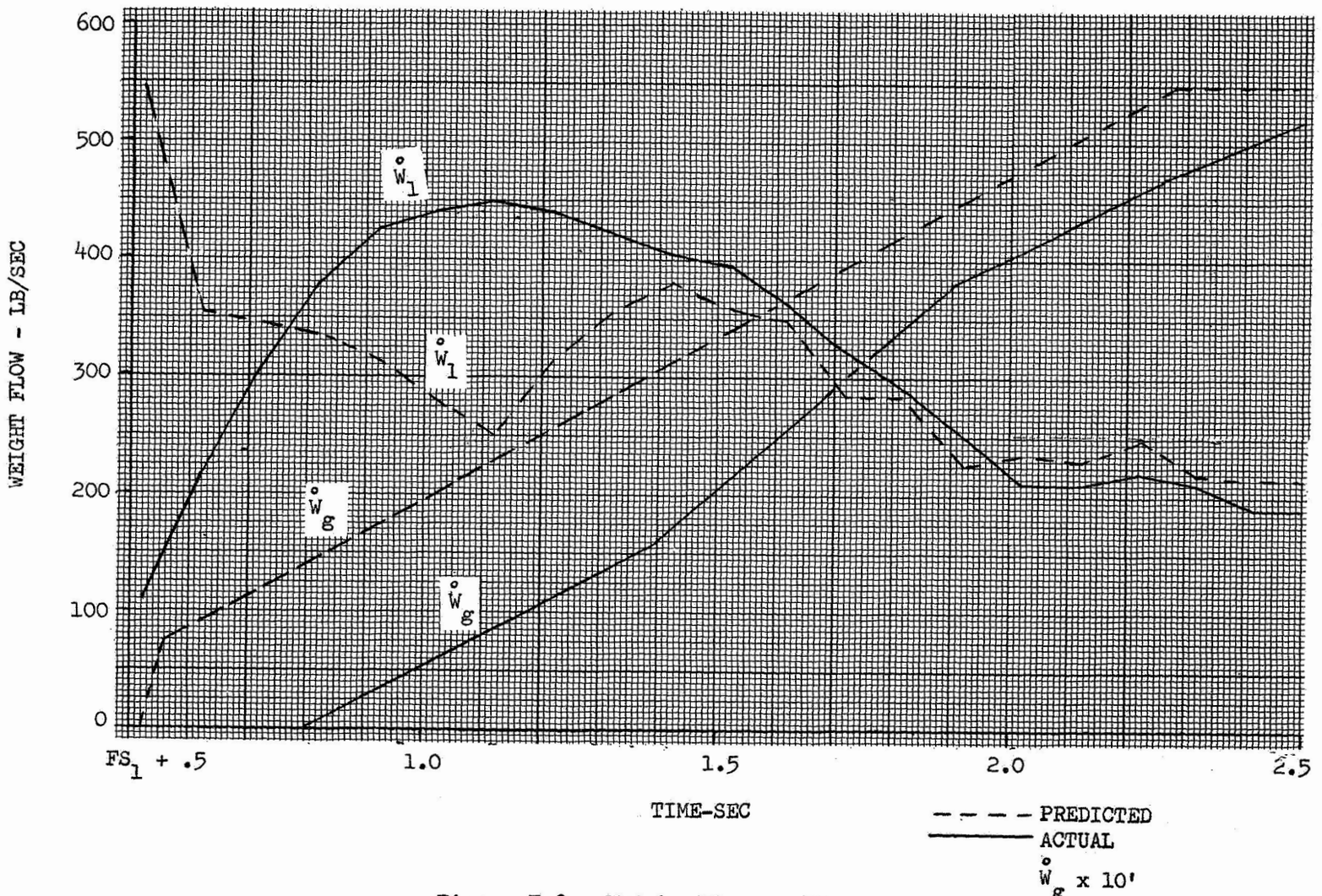


Figure F-3. Weight Flow vs Time

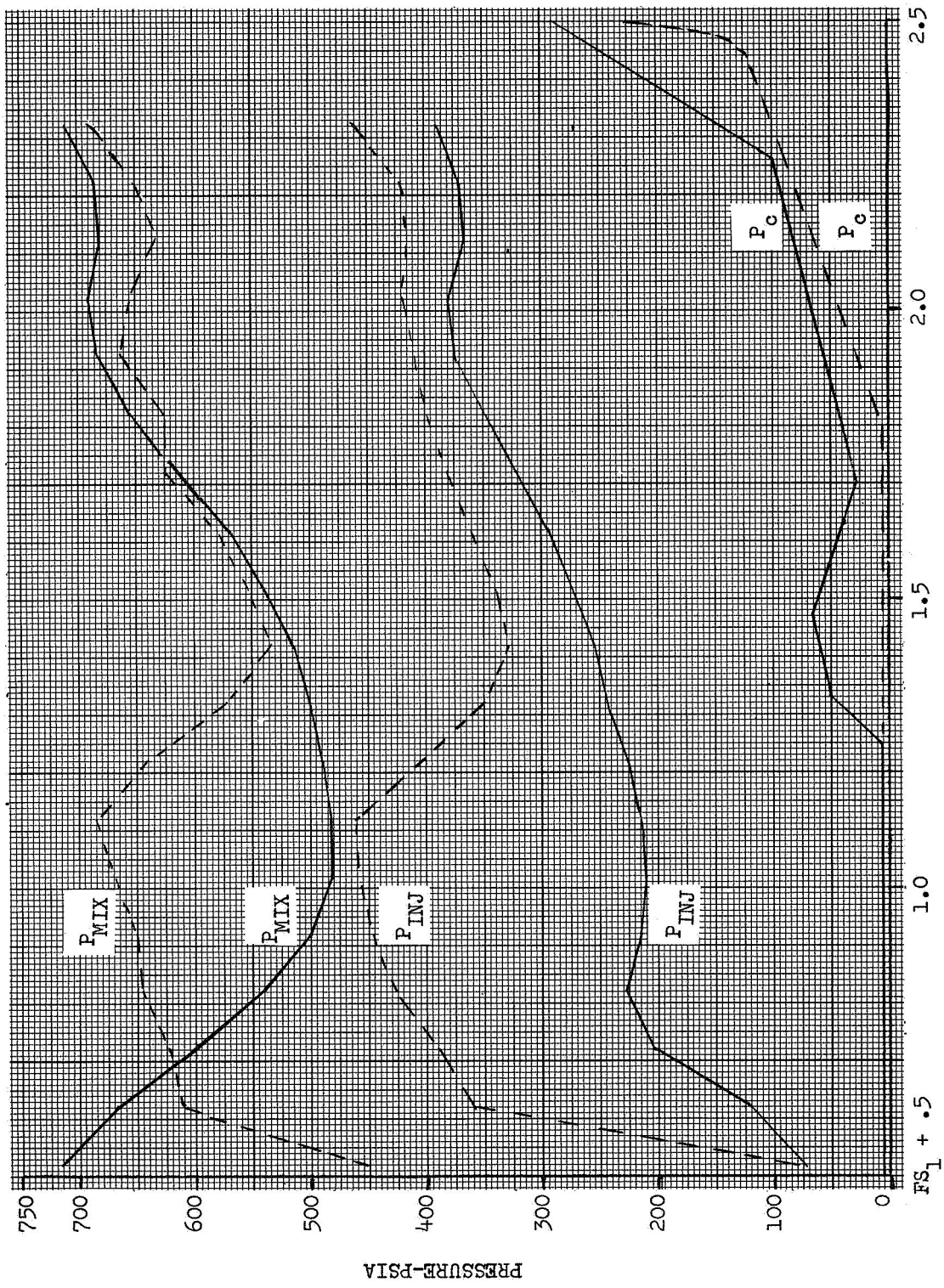


Figure F-4. Pressure vs Time

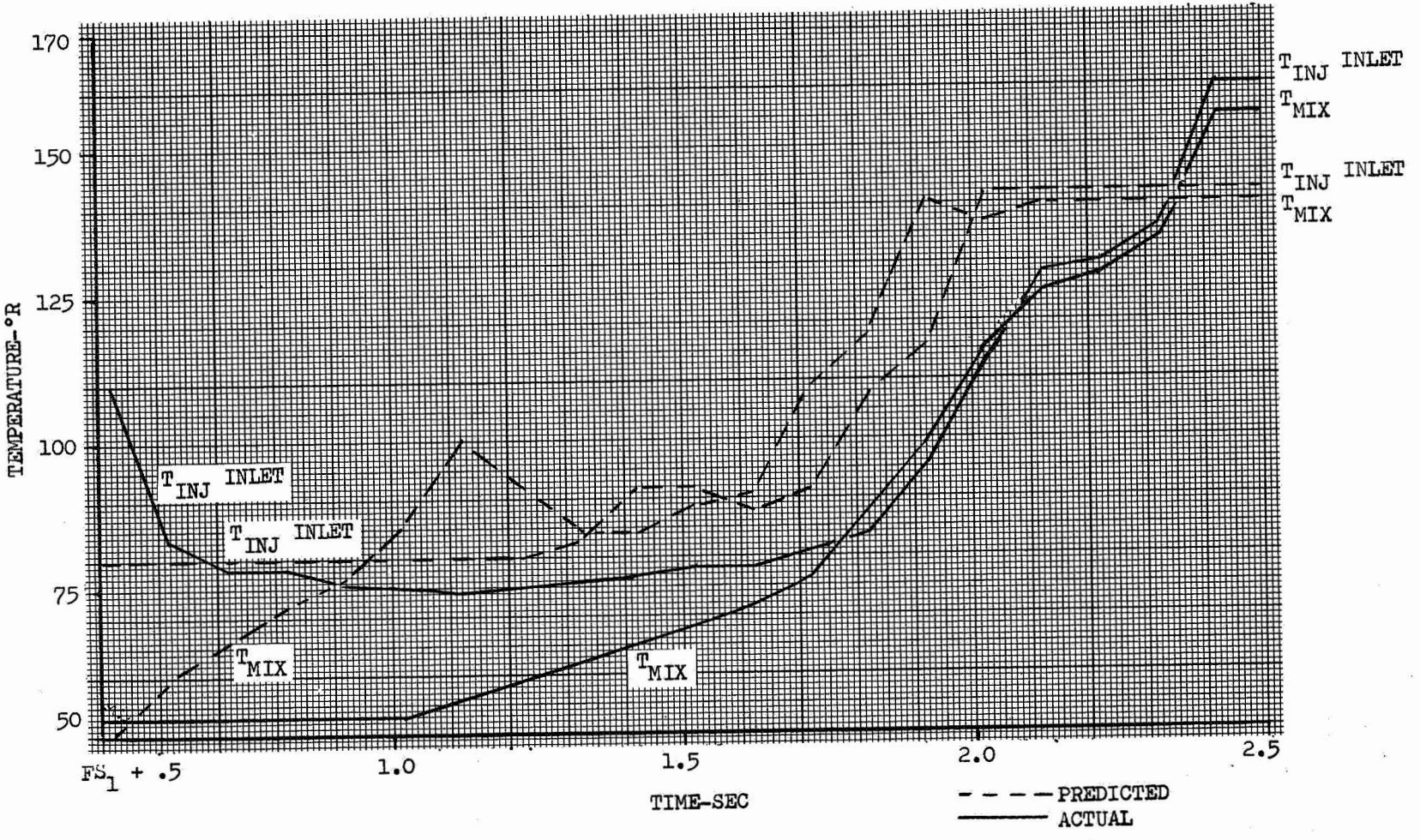


Figure F-5. Temperature vs Time

# APPENDIX G

## MEASUREMENT AND EVALUATION

## OF

## SOUND LEVELS FROM M-1 THRUST CHAMBER TESTS*

* The information presented in this appendix was originally issued as Aerojet-General Report No. 0830-99, 27 June 1967

## I. SUMMARY

This appendix describes the sound pressure level (SPL) measurements taken during the M-1 thrust chamber test firings 1.2-05-EHM-004 through 010, the latter part of the M-1 thrust chamber assembly phaseout program, and tests 1.2-07-EHM-001 through 004. Test Series 1.2-07 was a portion of the large $LO_2/LH_2$ injector test program. The measurements were taken from short duration tests (10 sec maximum) of the M-1 thrust chamber assembly mounted in a horizontal position on Test Stand H-8, which is located in Test Zone H of the Aerojet-General Corporation Sacramento Plant Test Operations facilities. The thrust chamber nozzle was a 2:1 uncooled ablative liner configuration. Thrust levels were approximately 1.0 million pounds, sea-level conditions, with chamber pressure in the 1050-1100 psi range. A total of 25 measurements were made at seven different locations. Magnetic tape recordings and visual observations via sound level meters were obtained. The overall sound level energy peaked between 63 and 80 Hertz (measured at 150 feet from the nozzle). The steady-state sound source for the M-1 thrust chamber assembly was calculated to be 204.5 db; it was measured at 202 db. The predicted acoustic efficiency was 0.5%; the actual efficiency was 0.4%. Fair agreement exists between measured and predicted sound levels. Precise atmospheric data were not available to permit estimates of sound reinforcement.

## II. INTRODUCTION

The prediction of sound pressure levels to be expected during static test firings of the 1.5 million lb thrust $LO_2/LH_2$ NASA M-1 Engine and Thrust Chamber Assembly (TCA) at the Aerojet-General Corporation Sacramento test facilities was given considerable attention. This interest was based upon concern over possible operational limitations which might be imposed upon scheduling of test activities if sound pressure levels reach proportions that are objectionable to the surrounding community. In addition to scheduling limitations, it has been considered that sound suppression systems also might be required if sound levels were excessive. The latter factor is estimated to have considerable influence upon facility construction costs.

These concerns were supported by test experience developed in the Saturn Test Program at Marshall Space Flight Center, Huntsville, Alabama, where both scheduling limitations and sound suppression systems were required.

This appendix extends the past predictions to comparisons with actual sound measurement data taken during test firings of the M-1 uncooled thrust chamber assembly at Test Stand H-8 during the initial operational phase, July and August 1966.

The measurements reported were largely taken in the near field; however, a few far field data points also are included. The primary purposes for the measurements were the determination of:

- The attenuation characteristics of the sound pressure waves for the Aerojet-General area and surrounding property.

- The amplitude and major frequency of the sound source.

- The off-plant sound level where surrounding community reaction to the firings could become significant relative to test scheduling.

Microphones were placed at strategic locations during the firings to accomplish these objectives. Figure No. G-1 is a plot plan showing the locations of all measurements and predicted decibel contours. Note that these contours are not spherical, but lobular. This lobular pattern was based upon sound data obtained at Marshall Space Flight Center, Huntsville, The distance between contours takes into account the normal 1/R attenuation plus excess attenuation of 8 db per mile. Recording ranges were selected based upon predicted sound levels. Data were recorded on magnetic tape and then analyzed in the Aerojet-General Plant Test Operations Data Processing Center. Figure No. G-2 is a block diagram of the acquisition and analysis system used. In addition to tape recordings, hand-held sound level meters were used for three measurements.

Of significant importance is the lack of ability to correlate far field measurements with data regarding atmospheric conditions because of funding limitations imposed by the reduction in program scope. As subsequently discussed, this factor is of considerable importance where winter weather and/or long duration testing is to be performed.

## III. MEASUREMENT LOCATIONS AND EQUIPMENT

The physical location of each of the measurement points is shown on Figure No. G-1. Because of the scale used, the off-plant measurement near Nimbus Dam (SPL-4) is shown out of scale in relationship to all of the other points. The information is summarized on Table G-I along with the equipment used. The location designator includes the measurement number (SPL-1, etc.), the straight line distance from the source, and the angle between that line and the line of firing from Test Stand H-8.

The Photocon microphone is a L-C tuned circuit. Diaphragm movements, which are caused by pressure fluctuations, result in a change in capacitance. This change is translated by the "Dynagage" signal conditioner to an analog voltage proportional to the pressure variations. The Shure Bros. microphone is a piezo-ceramic device, wherein movement of the diaphragm creates a charge across a ceramic crystal. This charge is equivalent to a voltage which is the analog of the pressure against the microphone.

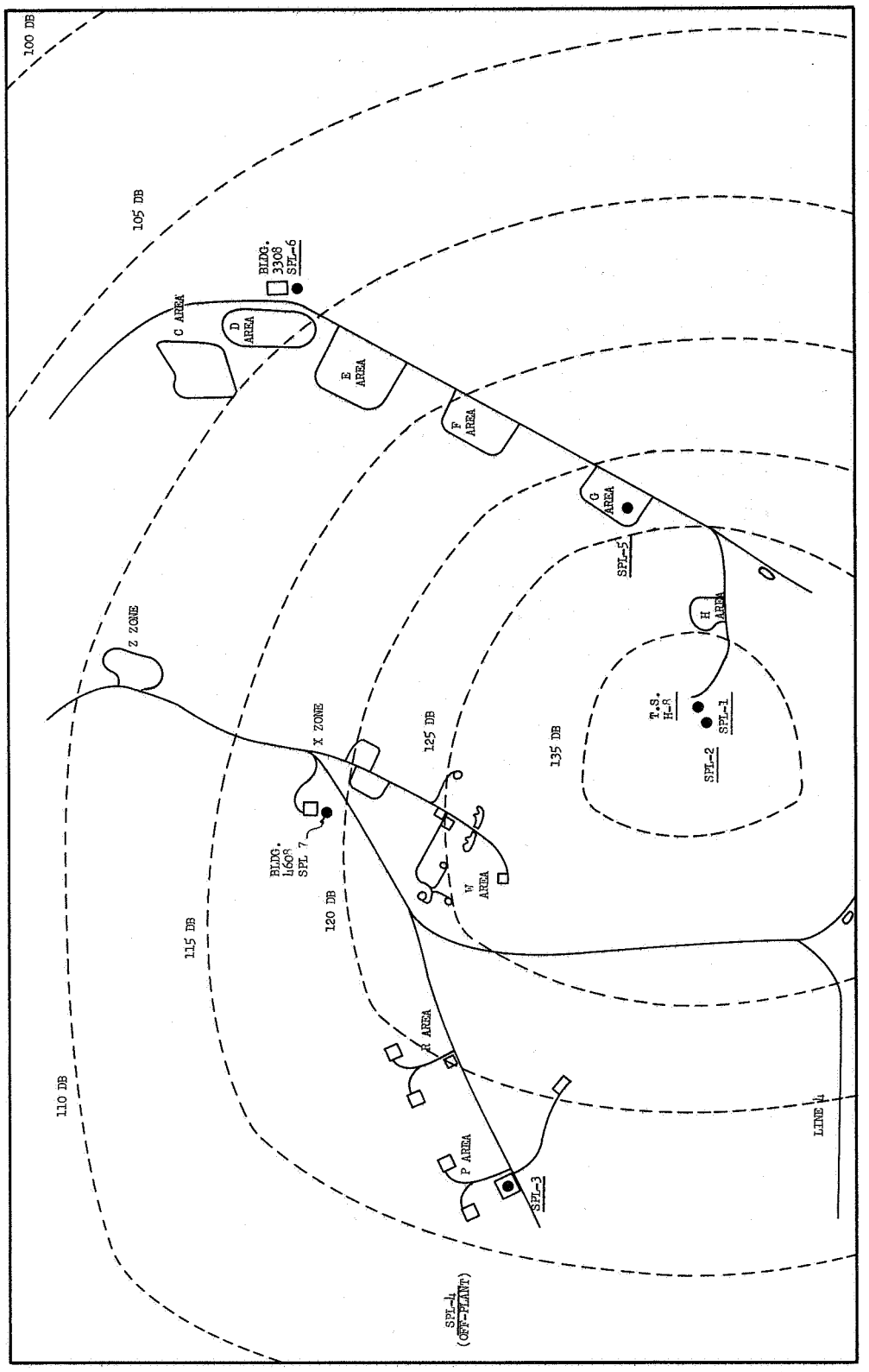


Figure G-1. Plan View of Microphone Array

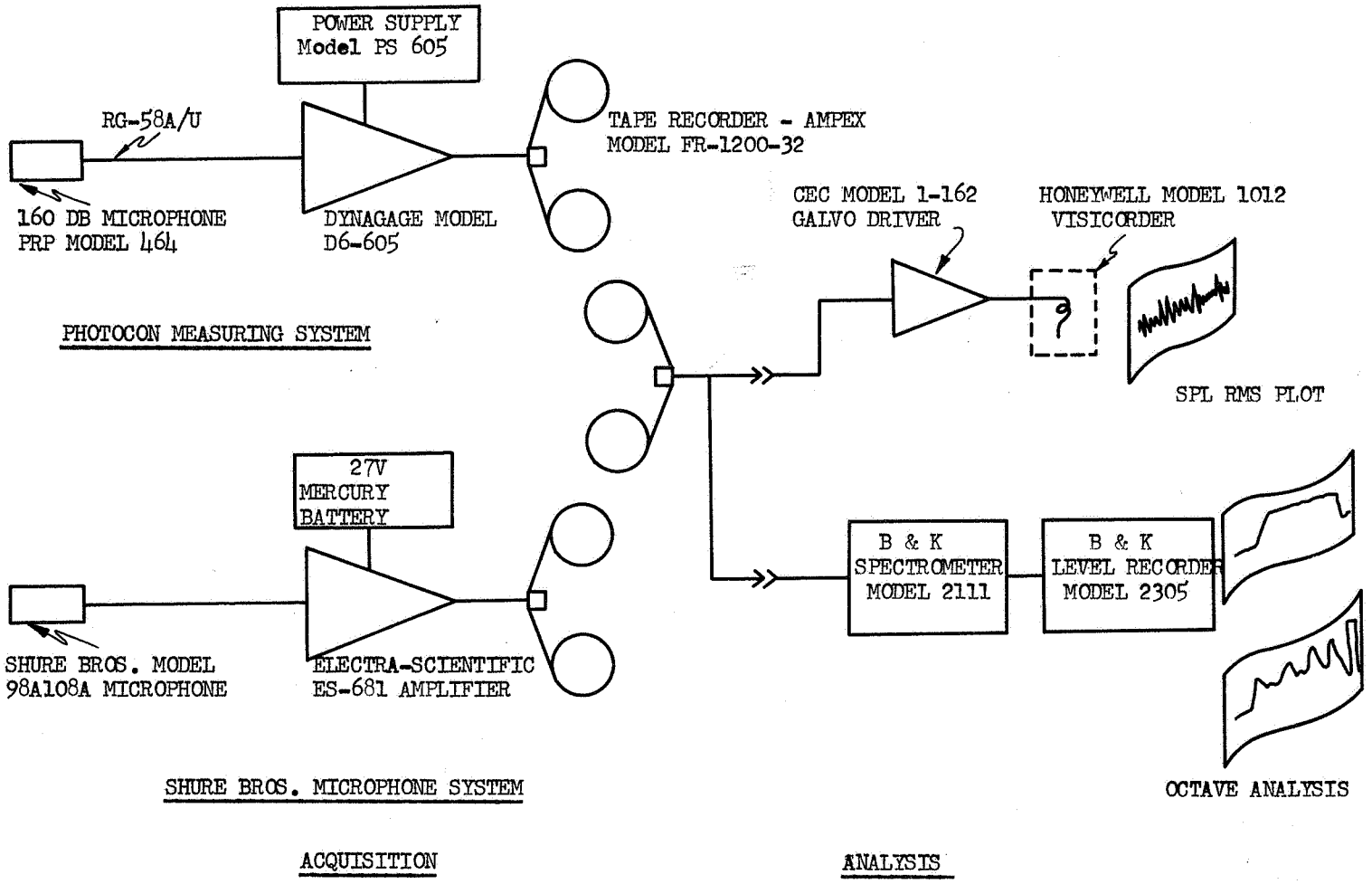


Figure G-2. Sound Level Data Acquisition and Analysis Block Diagrams

Appendix G

TABLE G-I

SOUND LEVEL MEASUREMENT LOCATIONS AND EQUIPMENT

| | DESIGNATOR | LOCATION | EQUIPMENT |
|---|---|---|---|
| A. | SPL-1, 150 feet, -20° | H-8 | Photocon Microphone, Dynagage Signal Conditioner |
| B. | SPL-2, 300 feet, -20° | H-8 | Same as above |
| C. | SPL-3, 5050 feet, +20° | Test Zone P | Shure 98A108A Microphone, Electra-Scientific Amplifier |
| D. | SPL-4, 16,600 feet, +20° | Bluff over Nimbus Dam | G.R. Sound Level Meter, Model 1551* |
| E. | SPL-5, 2000 feet, +160° | Test Zone G | Photocon Microphone, Dynagage Signal Conditioner |
| F. | SPL-6, 5400 feet, +150° | Outside Building 33008 | G.R. Sound Level Meter, Model 1551 |
| G. | SPL-7, 3850 feet, +80° | Outside Building 46008 | G.R. Sound Level Meter, Model 1551 |

* Plans included a CP-100 recorder; operational problems in the field prevented successful recording.

## IV. RESULTS

The following discussion describes the results by geographical location of the measurement points as shown on Figure No. G-1. These points are identified by a SPL number, which defines the distance from the source and the direction away from the nozzle. Table G-II summarizes predicted and measured values.

### A. SPL-1, 150 FEET, -20 DEGREES

This measurement was recorded during ten tests. The average SPL was 158 db; 2 db higher than predicted. A frequency analysis showed peak spectra at 63 to 80 $H_z$, and secondary energy at 205 $H_z$. The initial peak over-scaled in all tests, which indicated that the level was above 166 db at that location. This inital peak is a result of the ignition of the hydrogen "lead" gas, which is part of the normal start sequence for these tests.

### B. SPL-2, 300 FEET, -20 DEGREES

The average SPL for all tests was 153 db as compared with a predicted value of 150 db. The initial peak was measured at 164 db at this distance. The microphone revealed a 200 $H_z$ oscillation during Test -009 from FS-1 + 2.6 to FS-1 + 3.1 sec. This same 200 $H_z$ component reveals itself in several pressure measurements during this time, which is the period of ramp-up of the fuel tank pressure.

### C. SPL-3, 5050 FEET, +20 DEGREES (P-AREA CONTROL ROOM ROOF)

In this location, the SPL-3 measurement was made for two firings. It showed an average SPL of 113 db. The inital peak was measured at 127 db. This correlates with the 164 db transient measured at SPL-2. Extrapolating these measurements along with SPL-6 ignition data to the nozzle yields an ignition transient of 211 db.

### D. SPL-4, 16,600 FEET, +20 DEGREES (BLUFF OVERLOOKING NIMBUS DAM)

This was the only off-plant measurement. The sound level meter data indicated a steady-state level of 88.5 db (Test No. 1.2-05-EHM-007) as compared with a predicted 90 db. It is emphasized that no detailed information exists relative to upper air conditions which could contribute to reinforcement of sound at these distances. Therefore, it is not necessarily a conclusion that the assumptions behind the 90 db prediction are validated by these limited data. The 90 db value assumes no reinforcement and 8 db excess attenuation per mile.

## TABLE G-II

### SUMMARY OF PREDICTED AND MEASURED VALUES

| STATION | DISTANCE | PREDICTED DB | MEASURED DB |
|---|---|---|---|
| SPL-1 | 150 | 156 | 158 |
| SPL-2 | 300 | 150 | 153 |
| SPL-3 | 5050 | 117 | 113 |
| SPL-4 | 16,600 | 90 | 88.5 (1) |
| SPL-5 | 2000 | 124 | 116 (2) |
| SPL-6 | 5400 | 110 | 107 (1) |
| SPL-7 | 3850 | 120 | 108 (1)(3) |

(1) Measured with sound level meter

(2) Steady state 116 db, 200 $H_z$ data 122 db

(3) Questionable data

E. SPL-5, 2000 FEET, 160 DEGREES (ROOF OF G-1 CONTROL ROOM)

This measurement was extremely interesting in that it clearly showed the distinct 200 $H_z$ oscillation in tests -006, -007, and -008 during the start sequence. When the main oxidizer valve opened and tank pressure was at steady-state, the oscillations stopped. These oscillations were revealed in most of the pressure functions as well as in the high-speed movies of the jet stream. The sound level of the ignition transient over-scaled during all three tests, which showed that it was in excess of 128 db. The steady-state level was 116 db as compared with a predicted value of 124 db. No clear explanation exists for this discrepancy and more data would be needed to resolve it. The 200 $H_z$ data measured 122 db.

F. SPL-6 AND SPL-7

In addition to the five standard measurement locations, two additional measurements were made during Run 1.2-05-EHM-006. Sound level meters were monitored at the Building 33008 parking lot (SPL-6) and outside Building 46008 (SPL-7). The sound levels were 107 db and 108 db, respectively as compared with predicted values of 110 db and 119 db, respectively. The 108 db measurement is probably invalid, but further tests would be required to resolve the difference.

## V. CONCLUSIONS

The following conclusions are made based upon the results of this study:

A. Near-field and limited far-field data confirm that the steady-state source sound pressure level is 2.5 db lower than calculated.

B. The measured efficiency (acoustic coupling factor, N) was 0.4% as compared with the assumed 0.5%. An acoustic efficiency of 0.6% was previously reported(1).

C. At 150 ft from the nozzle, peak sound level energy was between 63 and 80 $H_z$. By comparison, at the same distance, the Titan I first-stage engine (300,000 lb thrust, $LO_2$, RP-1) peaked at 123 $H_z$, and a 100-in. Solid Propellant Motor (500,000 lb thrust) peaks around 70 $H_z$.

D. Near-field sound level data clearly reflects pressure oscillation frequencies associated with combustion processes, particularly during the start transient.

E. There is insufficient data to confirm or reject the assumption of 8 db excess attenuation per mile for this area.

(1) Sound Pressure Level Measurements for Large Solid Rocket Motors, Aerojet-General Technical Memorandum 202SR, 10 November 1962

F. If 90 db (or 88.5 db) is the correct non-reinforced sound level at the three-mile distance, SPL-4, then potential sound level problems in the communities of Orangevale and Folsom exist. This is based upon Marshall Space Flight Center reports which predict reinforcement as high as 40 db and adverse community reactions at approximately 115 db sound levels for sustained periods at very low frequencies (20 $H_z$ and below). Such reinforcement conditions can be circumvented through the use of detailed atmospheric data and selective test times.

G. The sound level associated with the start sequence is approximately 10 db higher than the steady-state level and would probably contribute to a majority of the community reactions to testing.

H. Any future extensive program involving engines of the M-1 size or larger should incorporate a thorough sound level and meteorological study as well as a measurement program, which was originally planned to support the M-1 so as to avoid speculation regarding reinforcement, excess attenuation, and sound level contour configurations.

## VI. CALCULATIONS

### A. CALCULATION OF SOURCE LEVEL

The following calculations were used in performing the sound level predictions. The parametric values in the equations were from engineering data.

The total acoustical output of the source, in watts, is:

$$W = 1/2\ \dot{M} V_e^{\,2}$$

where:

$W$ = acoustic power in watts
$\dot{M}$ = total mass flow
$V_e$ = expanded jet velocity
$\eta$ = acoustic efficiency, estimated at 0.5%

The jet velocity, $V_e$, is equal to $\frac{F.g}{\dot{W}}$

Therefore, $W = 1/2\ \frac{\dot{W}}{g} \cdot \frac{F^2 g^2}{\dot{W}^2} \cdot \eta = 1/2\ \frac{F^2 g\, \eta}{\dot{W}}$

Substituting the proper values for F and $\dot{W}$, yields

$$\frac{W = (1/2)\ (1.1 \times 10^6)^2\ (32)\ (5 \times 10^{-3})}{3.5 \times 10^3} = 2.8 \times 10^7 \text{ watts}$$

The sound power level (PWL) is defined as

$$PWL_{db} = 10 \log \frac{W}{W_{ref}} \quad \text{where } W_{ref} = 10^{-13} \text{ watts}$$

Therefore, $PWL = 10 \log \frac{2.8 \times 10^{7}}{10^{-13}} - 10 \log 2.8 \times 10^{20}$

$$PWL = 204.5 \text{ db}$$

B. SOUND PRESSURE LEVEL CALCULATIONS AT THE MICROPHONES

The Sound Pressure Level (SPL), assuming hemispherical radiation, is given as

$$SPL = PWL - 10 \log 2 - 20 \log R \pm D.I. - E.A.$$

where:

SPL = Sound Pressure Level (db)
PWL = Sound Power Level (db) Source
R = Distance from microphone to source (feet)
D.I. = Directivity Index (per MSFC Test, 19 March 1963)

20° = +2.5 db
160° = -4 db
70° = +1.5 db
135° = -4 db

EA = Excess Attenuation = $\frac{R}{5280} \times 8$ when R = 1000 ft (per TM 202, SRP)

Simplifying,

$$SPL = 204.5 - 8 - 20 \log R \pm D.I. - E.A. = 196.5 - 20 \log R \pm D.I. - E.A.$$

SPL-1 (150 ft - 20-degrees)

$$SPL = 196.5 - 20 \log (150) + 2.5$$
$$= 196.5 - 43.5 + 2.5$$
$$= 156 \text{ db}$$

SPL-2 (300 ft -20 degrees)

$$SPL = 196.5 - 20 \log (300) + 2.5$$
$$= 196.5 - 49.5 + 2.5$$
$$= 150 \text{ db}$$

SPL-3 (5050 ft - 20-degrees)

$$SPL = 196.5 - 20 \log (5050) + 2.5 - \frac{5050}{5280} \times 8$$
$$= 196.5 - 74 + 2.5 - 7.65$$
$$= 117 \text{ db}$$

SPL-4 (16,600 ft +20-degrees)

$$SPL = 196.5 - 20 \log (16{,}600) + 2.5 - \frac{16600}{5280} \times 8$$
$$= 196.5 - 84.4 + 2.5 - 25$$
$$= 90 \text{ db}$$

SPL-5 (2000 ft, 160-degrees)

$$SPL = 196.5 - 20 \log (2000) - 4 - \frac{2000}{5280} \times 8$$
$$= 196.5 - 66 - 4\text{-}3$$
$$= 124 \text{ db}$$

SPL-6 (5400 ft, 135-degrees)

$$SPL = 196.5 - 20 \log (5400) - 4 - \frac{5400}{5280} \times 8$$
$$= 196.5 - 74.6 - 4 - 8.2$$
$$= 110 \text{ db}$$

SPL-7 (3850 ft, 70-degrees)

$$SPL = 196.5 - 20 \log (3850) + 1.5 - \frac{3850}{5280} \times 8$$
$$= 196.5 - 71.7 + 1.5 - 5.8$$
$$= 120 \text{ db}$$

C. CALCULATION OF PWL FROM MEASURED SPL DATA

SPL-1; PWL = 204.5 + 2 = 206.5 db
SPL-2; PWL = 204.5 + 3 = 207.5 db
SPL-3; PWL = 204.5 - 4 = 200.5 db
SPL-4; PWL = 204.5 - 1.5 = 203.0 db
SPL-5; No Steady Measurement
SPL-6; PWL = 204.5 - 3 = 201.5 db
SPL-7; PWL = 204.5 - 12 = 192.5 db

Average PWL = 202 db

Calculated $\eta$ = 2.5 db down from 0.5% - 0.39%

D. CALCULATION OF IGNITION TRANSIENT FROM SPL DATA

The ignition spike at SPL-2 measured 164 db, which is 14 db above the predicted level. Assuming a source level of 202 db, the ignition transient at the source was 216 db.

The ignition transient from SPL-3 data was 127 db, which extrapolates to 212 db at the source.

SPL-6 data showed the ignition spike at 112 db, or 2 db over the PWL. This yields a source spike of 204.

The average of the three measurements yields an ignition transient of 211 db at the source.

Appendix G

## BIBLIOGRAPHY


1. Acoustic Focal Zones Around Saturn Static Tests, MSFC Report MTD-Test-MC-61-21, December 1961

2. "Sound Pressure Level Measurements for Large Solid Rocket Motors", Aerojet-General Technical Memorandum 202SRP, 10 November 1962

3. Memorandum to J. S. Laws from G. R. Deppe, dated 24 August 1966, Subject: "Preliminary Evaluation of H-8 Test Stand Sound Level Data"

4. Memorandum to G. R. Deppe from S. J. Spataro, dated 17 June 1966, Subject: "Sound Pressure Level Data from Test Firing 1.2-05-EHM-001, M-1 Thrust Chamber"

DISTRIBUTION LIST

| | Copies |
|---|---|
| National Aeronautics and Space Administration<br>Lewis Research Center<br>21000 Brookpark Road<br>Cleveland, Ohio 44135 | |
| Attn: I. A. Johnsen<br>M. S. 500-205 | 1 |
| H. W. Douglass<br>M. S. 500-305 | 1 |
| G. J. Widra<br>M. S. 500-305 | 3 |
| W. F. Dankhoff<br>M. S. 3-13 | 1 |
| W. A. Tomazic<br>M. S. 500-305 | 3 |
| R. R. Godman<br>M. S. 21-4 | 1 |
| Library<br>M. S. 60-3 | 1 |
| E. W. Conrad<br>M. S. 100-1 | 2 |
| F. Van Hoff/W. E. Russell<br>M. S. 50-1 | 1 |
| H. M. Henneberry<br>M. S. 501-2 | 2 |
| Major E. H. Karalis (AFSC)<br>M. S. 4-1 | 1 |
| D. L. Nored<br>M.S. 500-209 | 1 |
| T. J. Flanagan<br>M. S. 500-210 | 1 |
| Technical Information Division<br>M. S. 5-5 | 1 |
| National Aeronautics and Space Administration<br>Launch Operations Center<br>Cocoa Beach, Florida | |
| Attn: Library | 1 |
| Air Force Rocket Propulsion Laboratory<br>Edwards Air Force Base<br>Edwards, California | |
| Attn: H. V. Main | 1 |
| NASA Headquarters<br>Washington, D. C. 20546 | |
| Attn: A. O. Tischler<br>Code RP | 1 |
| W. W. Wilcox<br>Code RPX | 1 |
| R. H. Collins<br>Code RPX | 1 |
| National Aeronautics and Space Administration<br>George C. Marshall Space Flight Center<br>Huntsville, Alabama | |
| Attn: J. W. Thomas, Jr. I-E-E | 5 |
| NASA/Rocketdyne<br>Division of North American Aviation, Inc.<br>6633 Canoga Avenue<br>Canoga Park, California | |
| Attn: R. Pease/F. Boffola | 1 |
| Rocketdyne (Library Dept. 586-306)<br>Division of North American Aviation, Inc.<br>6633 Canoga Avenue<br>Canoga Park, California | |
| National Aeronautics and Space Administration<br>600 Independence Avenue, Southwest<br>Washington, D. C. 20546 | |
| Attn: N. J. Gerstein<br>Code NPO | 1 |

| | Copies |
|---|---|
| National Aeronautics and Space Administration<br>Mission Analysis Division<br>OART<br>Moffett Field, California 94035 | |
| Attn: E. W. Gomersall | 1 |
| Jet Propulsion Laboratory<br>4800 Oak Grove Drive<br>Pasadena, California | |
| Attn: L. E. Baughman | 1 |
| Library | 1 |
| National Aeronautics and Space Administration<br>Ames Research Center<br>Moffett Field, California | |
| Attn: Library | 1 |
| National Aeronautics and Space Administration<br>Goddard Space Flight Center<br>Greenbelt, Maryland | |
| Attn: Library | 1 |
| National Aeronautics and Space Administration<br>Langley Research Center<br>Langley Station<br>Hampton, Virginia | |
| Attn: Library | 1 |
| National Aeronautics and Space Administration<br>Manned Spacecraft Center<br>Houston, Texas | |
| Attn: Library | 1 |
| National Air and Space Museum<br>Smithsonian Institute<br>Washington, D. C. 20560 | |
| Attn: F. C. Durant, III | 2 |
| Aerospace Corporation<br>P. O. Box 95085<br>Los Angeles, California | |
| Attn: T. Iura | 1 |
| Chemical Propulsion Information Agency<br>8621 Georgia Avenue<br>Silver Spring, Maryland 20910 | 1 |
| Nasa Scientific & Technical Information Facility<br>Technical Information Abstracting and<br>Dissemination Facility<br>Box 5700<br>Bethesda, Maryland | 1 |
| National Aeronautics and Space Administration<br>Flight Research Center<br>P. O. Box 273<br>Edwards AFB, California 93523 | |
| Attn: Library | |
| National Aeronautics and Space Council<br>Executive Office of the President<br>Executive Office Building<br>Washington, D. C. | |
| Attn: Dr. E. B. Konecci | 1 |
| Pratt & Whitney Aircraft Corporation<br>Florida Research & Development Center<br>P. O. Box 2691<br>West Palm Beach, Florida 33402 | 1 |
| Arnold Engineering Development Center<br>Arnold Air Force Station<br>Tullahoma, Tennessee | 1 |